



HAL
open science

Transport of complex fluids in the human pulmonary airway system

Alireza Kazemi Taskooh

► **To cite this version:**

Alireza Kazemi Taskooh. Transport of complex fluids in the human pulmonary airway system. Other. Université Paris Saclay (COMUE), 2019. English. NNT : 2019SACLX077 . tel-02441821

HAL Id: tel-02441821

<https://theses.hal.science/tel-02441821>

Submitted on 16 Jan 2020

HAL is a multi-disciplinary open access archive for the deposit and dissemination of scientific research documents, whether they are published or not. The documents may come from teaching and research institutions in France or abroad, or from public or private research centers.

L'archive ouverte pluridisciplinaire **HAL**, est destinée au dépôt et à la diffusion de documents scientifiques de niveau recherche, publiés ou non, émanant des établissements d'enseignement et de recherche français ou étrangers, des laboratoires publics ou privés.

Transport of complex fluids in the human pulmonary airway system

Thèse de doctorat de l'Université Paris-Saclay
préparée à l'École Polytechnique

École doctorale n°573 Interfaces : Approches interdisciplinaires,
fondements, applications et innovation (Interfaces)
Spécialité de doctorat : Physique

Thèse présentée et soutenue à Palaiseau, le 17 octobre 2019, par

M. Alireza Kazemi Taskooh

Composition du Jury :

M. Abdul BARAKAT Professeur, Ecole Polytechnique	Président
Mme Annie VIALLAT Professeur, Centre Interdisciplinaire de Nanoscience de Marseille	Rapporteur
M. Benjamin MAUROY Chargé de Recherche, Université de Nice Sophia-Antipolis	Rapporteur
M. Pierre-Henri JARREAU Professeur, Université Paris Descartes	Examineur
M. Jean-François BERRET Professeur, Université Denis Diderot	Examineur
M. Daniel ISABEY Professeur, Université Paris Est Créteil	Examineur
M. MARCEL FILOCHE Professeur, Ecole Polytechnique	Directeur de thèse

Titre : Propagation de bouchons liquides dans les poumons humains

Mots clés : Poumon, Arbre trachéo-bronchique, administration de surfactant, dynamique des fluides

Résumé : La Thérapie par Substitution de Surfactant (TSS), qui opère par instillation d'une solution de surfactant directement dans l'arbre bronchique, est un traitement remarquablement efficace chez les prématurés souffrant de syndrome de détresse respiratoire. À l'inverse, son utilisation s'est avérée inexplicablement décevante chez les adultes atteints du syndrome de détresse respiratoire aigu. Dans cette thèse, nous présentons un modèle numérique de la TSS chez l'animal et chez l'homme.

En simulant la TSS dans des modèles 3D réalistes de poumons, nous démontrons la sensibilité de son efficacité vis-à-vis de l'architecture géométrique, de la taille du sujet et des conditions d'administration, et mettons en évidence en particulier les différences profondes entre les modèles animaux et l'homme. Ces travaux permettent aujourd'hui d'envisager une réouverture de cette voie thérapeutique chez l'adulte, guidée par un véritable outil de prédiction de l'administration individualisée chez le patient.

Title: Propagation of liquid plugs into the human lung

Keywords: Lung, Tracheobronchial tree, Fluid dynamics, Surfactant delivery, SRT

Abstract: Surfactant Replacement Therapy (SRT), which operates by instillation of a surfactant solution directly into the bronchial tree, is a remarkably effective treatment for premature infants with respiratory distress syndrome. Disappointingly, its use in adults for treating acute respiratory distress syndrome (ARDS) experienced initial success followed by failures. In this thesis, we present a numerical model of SRT in animals and humans.

By simulating SRT in realistic 3D lung models, we demonstrate the sensitivity of its effectiveness to geometric architecture, subject size and administration conditions, and highlight in particular the profound differences between animal and human models. These studies now make it possible to consider reopening this therapeutic route in adults, guided by a real tool for predicting individualized administration in patients.

Long résumé

La Thérapie par Substitution de Surfactant (TSS), qui opère par instillation d'une solution de surfactant directement dans l'arbre bronchique, est un traitement essentiel chez les nouveau-nés souffrant de syndrome de détresse respiratoire (SDRN). Cette procédure s'est révélée remarquablement efficace chez les grands prématurés, contribuant à la division par cinq de leur mortalité depuis les années 1980. À l'inverse, son utilisation s'est avérée décevante chez l'adulte dans le traitement du syndrome de détresse respiratoire aigu (SDRA), se soldant par un échec après des premiers essais pourtant prometteurs.

Dans cette thèse, nous présentons un modèle mathématique et numérique de la propagation de bouchons liquides dans le système pulmonaire aérien de mammifères. Dans ce but, nous commençons par créer des modèles d'arbres trachéobronchiques chez le rat, le cochon ou l'homme. Ces modèles sont définis non seulement par leurs propriétés d'échelle mais également par leur structure tridimensionnelle indispensable à la simulation du transport liquidien. Les géométries ainsi créées sont comparées aux données morphométriques de la littérature.

Nous présentons ensuite le modèle mathématique du transport liquidien. La principale propriété de ce modèle réside dans la décomposition de la propagation de bouchons liquides en deux étapes élémentaires fondamentales : (1) le dépôt de liquide sur les parois bronchiques lors de la propagation d'un bouchon, et (2) la division du bouchon liquide à chaque bifurcation de l'arbre. Les équations du processus de séparation sont déduites de la conservation de l'impulsion, pour tout type de bifurcation asymétrique. Cette décomposition en deux étapes élémentaires nous permet de calculer de manière efficace et rapide la propagation du surfactant dans l'intégralité de l'arbre aérien, fournissant ainsi un véritable outil de conception en génie biomédical.

Ce modèle numérique est tout d'abord exploité pour calculer l'administration de surfactant chez le rat. Les rôles respectifs du volume initial, du débit et de l'injection multiple sont examinés. Nos résultats de simulations se révèlent être en bon accord avec les données de la littérature. En particulier, nous mettons en évidence le rôle joué par l'architecture monopodiale du rat qui contribue à la faible homogénéité de la distribution finale de surfactant. On observe également la forte non linéarité de la quantité de surfactant distribuée dans les acini en fonction du volume initial, en raison du dépôt d'une fraction de ce volume sur les parois bronchiques (le *coût de dépôt*). Des simulations de l'administration chez le cochon font apparaître les mêmes propriétés,

avec cette fois une sensibilité accrue à la taille du poumon. Les effets respectifs de la gravité et de la tension de surface ne varient en effet pas suivant les mêmes lois d'échelle, ce qui se traduit par une distribution extrêmement inhomogène à bas débit ou à faible volume.

Enfin, chez l'homme, notre modèle montre que l'origine de l'échec de la TSS chez l'adulte est possiblement à chercher dans la mécanique des fluides, l'accroissement du coût de dépôt aggravant la non-linéarité de l'administration. Cet effet peut être contré soit en instillant le surfactant à plus faible débit (mais au prix d'une distribution finale fortement inhomogène), soit en augmentant le volume initial. Nos résultats montrent en outre que, même pour des tailles comparables, les géométries très différentes de l'homme et du cochon ne permettent pas de traduire directement pour le premier les résultats obtenus chez le second. Un modèle fiable de l'administration est donc indispensable pour prédire l'efficacité de la TSS à partir de modèles animaux.

En conclusion, cette thèse propose un nouvel outil permettant de prédire l'administration de surfactant chez l'animal et chez l'homme, de comprendre le rôle éventuel des modèles animaux, et en définitive de concevoir et d'optimiser de manière individualisée la TSS pour le patient.

Long abstract:

Surfactant Replacement Therapy (SRT), which involves the instillation of a liquid-surfactant mixture directly into the lung airway tree, is a major therapeutic treatment in neonatal patients with respiratory distress syndrome (NRDS). This procedure has proved to be remarkably effective in premature newborns, contributing to a five-fold decrease in mortality since the 1980s. Disappointingly, its use in adults for treating acute respiratory distress syndrome (ARDS) experienced initial success followed by failures.

In this Ph.D. thesis, we present a mathematical and numerical model for the propagation of a liquid plug into the pulmonary airway system of mammals. To that intent, we first create realistic geometrical models of the tracheobronchial trees of mammals, rat, pig, and human, defined not only by their scaling properties but also by their 3D spatial embedding (i.e., branching and rotation angles), a description necessary for simulating liquid transport. The resulting geometries are compared with the available quantitative morphometric measurements found in the literature.

We then introduce the mathematical model describing liquid plug transport. The main feature of this model is to decompose the propagation of liquid plugs in two fundamental elementary steps: (1) liquid deposition onto the airway walls during the propagation of a plug into a single airway, and (2) plug splitting at each bifurcation between two consecutive generations. The equations for the splitting process are derived from momentum conservation considerations, for any type of asymmetric bifurcation and any orientation with respect to gravity. The decomposition of the transport of liquid plugs into these essential steps allows us to compute efficiently and rapidly the propagation of surfactant into the entire airway tree, thus creating a truly biomedical engineering design tool.

This mathematical and numerical model is first used to compute surfactant delivery into realistic asymmetric conducting airway trees of rat lung. The roles of dose volume, flow rate, and multiple aliquot deliveries are investigated. We find that our simulations of surfactant delivery in rat lungs are in good agreement with experimental data. In particular, we show that the monopodial architecture of the rat airway trees plays a major role in surfactant delivery, contributing to the poor homogeneity of the end distribution of surfactant. We also observe that increasing the initial dose volume increases in a nonlinear way the amount of surfactant delivered to the acini after losing a portion to coating the involved airways, the *coating cost volume*. Simulations of

delivery in pig lungs exhibit the same general features, but our model demonstrates that SRT is very sensitive to the lung size. Surface tension and gravity effects do not scale similarly, and the end distribution can become highly nonhomogeneous at lower flow rates or small dose volumes.

Finally, in the human lung, our model shows that the failure of SRT in adults could, in fact, have a fluid mechanical origin that is potentially reversible. The coating cost is predicted to increase in adult lungs, enhancing the nonlinearity of the delivery process. This effect can be countered either by instilling the surfactant mixture at a smaller flow rate (but then the distribution is highly nonhomogeneous) or by using a larger dose volume. In addition, our results show that, even if sizes are comparable, the very different geometrical structures of pig and human lungs do not permit a direct translation of experimental results in pigs to humans, and that a reliable mathematical model of the delivery is absolutely crucial if one wants to predict the efficacy of SRT from animal models.

In conclusion, this thesis provides a tool for predicting surfactant delivery in animals and humans, for understanding how to build animal models of SRT, and finally for engineering and optimizing patient-specific surfactant delivery in complex situations.

INDEX

<u>1</u>	<u>STATE OF THE ART</u>	1
1.1	THE GEOMETRY OF THE PULMONARY AIRWAY TREE	3
1.1.1	THE HUMAN LUNG	3
1.1.2	ANIMAL LUNG	6
1.1.2.1	Rat lung	6
1.1.2.2	Pig lung	7
1.2	LUNG DISEASES	8
1.2.1	ARDS AND NRDS	9
1.3	SURFACTANT REPLACEMENT THERAPY	11
1.4	SURFACTANT PROPERTIES	15
1.4.1	COMPOSITION OF PULMONARY SURFACTANT	15
1.4.2	MECHANICAL PROPERTIES OF SURFACTANT	17
1.4.2.1	Surface tension	17
1.4.2.2	Viscosity	18
1.5	SURFACTANT ADMINISTRATION DELIVERY	21
1.6	CONCLUSION	24
<u>2</u>	<u>GEOMETRICAL MODELS OF THE TRACHEOBRONCHIAL TREE IN MAMMALS</u>	<u>27</u>
2.1	GEOMETRICAL PARAMETERIZATION	29
2.1.1	MODEL OF THE RAT LUNG	30
2.1.2	MODEL OF THE PIG LUNG	38
2.1.3	MODEL OF THE HUMAN LUNG	45
2.1.3.1	Symmetric airways tree (Weibel's model)	46
2.1.3.2	Weibel-based asymmetric airway tree	48
2.1.3.3	Raabe-based asymmetric airways tree	50
<u>3</u>	<u>MATHEMATICAL & NUMERICAL MODEL OF SURFACTANT DELIVERY</u>	<u>55</u>
3.1	MODELING OF PROPAGATION OF THE LIQUID PLUG INTO THE AIRWAY TREE	57
3.1.1	THE COATING LAYER	58
3.1.2	THE SPLITTING RATIO	59
3.1.3	EQUATION ON R_s	62
3.1.3.1	Dimensionless equation	63
3.1.3.2	The splitting factor	64

3.1.3.3	<i>The symmetric bifurcation</i>	65
3.2	MODELING OF MULTIPLE ALIQUOT INSTILLATIONS	66
3.3	ASSESSING THE PERFORMANCE OF SURFACTANT DELIVERY	67
3.4	SURFACTANT PROPERTIES AND INSTILLATION CONDITIONS	68
3.4.1	<i>FLOW RATE</i>	68
3.4.2	<i>DOSE VOLUME AND SURFACTANT PROPERTIES</i>	68
3.4.3	<i>POSTURE</i>	69
3.5	VALIDATION OF THE SPLITTING MODEL	70
3.5.1	<i>EFFECT OF GRAVITY ON LIQUID PLUG SPLITTING AT A BIFURCATION</i>	70
3.5.1.1	<i>Changing ϕ</i>	71
3.5.1.2	<i>Changing γ</i>	72
3.5.1.3	<i>Changing the Bond number</i>	73
3.5.2	<i>EFFECT OF INERTIA AND GRAVITY ON LIQUID PLUG SPLITTING AT A BIFURCATION</i>	74
3.5.2.1	<i>Changing ϕ</i>	74
3.6	VALIDATION OF THE SURFACTANT DELIVERY MODEL IN THE ENTIRE LUNG	77
3.6.1	<i>CHANGING THE DOSE VOLUME: COMPARISON WITH EXPERIMENTAL RESULTS</i>	77
3.6.2	<i>MULTIPLE INSTILLATIONS: COMPARISON WITH EXPERIMENTAL RESULTS</i>	81
4	<u>SIMULATIONS OF SURFACTANT DELIVERY IN RAT, PIG, AND HUMAN PULMONARY AIRWAYS SYSTEMS</u>	85
4.1	A BRIEF HISTORY OF SRT	87
4.2	SURFACTANT DELIVERY IN THE RAT LUNG	89
4.2.1	<i>SYMMETRIC VS. ASYMMETRIC LUNG MODEL</i>	89
4.2.2	<i>FLOW RATE AND DOSE VOLUME</i>	93
4.2.3	<i>ASSESSING THE ROLE OF POSTURE</i>	96
4.2.4	<i>MECHANICAL PROPERTIES OF SURFACTANT</i>	99
4.2.4.1	<i>Viscosity</i>	99
4.2.4.2	<i>Surface tension</i>	100
4.2.5	<i>INSTILLATION TECHNIQUE</i>	102
4.2.6	<i>CONCLUSION</i>	103
4.3	SURFACTANT DELIVERY IN THE PIG LUNG	107
4.3.1	<i>FLOW RATE AND DOSE VOLUME</i>	107
4.3.2	<i>ASSESSING THE ROLE OF POSTURE</i>	110
4.3.3	<i>MECHANICAL PROPERTIES OF SURFACTANT</i>	113
4.3.3.1	<i>Viscosity</i>	113
4.3.3.2	<i>Surface tension</i>	115
4.3.4	<i>INSTILLATION TECHNIQUE</i>	116

4.3.5	CONCLUSION	116
4.4	SRT IN THE HUMAN LUNG	119
4.4.1	NEONATE VS. ADULT	119
4.4.1.1	Flow rate and dose volume	119
4.4.1.2	Assessing the role of posture	126
4.4.1.3	Changing the mechanical properties of surfactant	127
4.4.1.3.1	Viscosity	128
4.4.1.3.2	Surface tension	129
4.4.2	AGE STUDY	131
4.4.3	SYMMETRIC VS. ASYMMETRIC TREE	134
4.4.4	SRT IN THE WEIBEL-BASED ASYMMETRIC TREE	138
4.4.4.1	Assessing the role of posture	138
4.4.4.2	Mechanical properties of surfactant	139
4.4.4.2.1	Viscosity	139
4.4.4.2.2	Surface tension	140
4.4.4.3	Multiple-aliquot Instillation	141
4.4.5	WEIBEL-BASED VS. RAABE-BASED ASYMMETRIC TREES	142
4.4.6	CONCLUSION	145
5	DISCUSSION & CONCLUSION	147
5.1	DISCUSSION	149
5.2	CONCLUSION & PERSPECTIVES	152
6	REFERENCES	155
7	LIST OF FIGURES	170
8	LIST OF TABLES	179

State of the Art

1.1 The geometry of the pulmonary airway tree

1.1.1 The human lung

The human lungs are a paired organ (pyramid-shaped) in charge of gas exchange between air and blood. The lungs are located in the chest on either side of the heart in the rib cage. Because of the position of the heart that shares space with lungs, the two lungs are not the same size: The left lung is more into the heart, while the right lung is shorter, wider, and has a larger volume. Each lung is formed of smaller units called lobes. The right lung consists of three lobes: the superior, middle, and inferior lobes. The left lung consists of two lobes: the superior and inferior lobes [1] (see Figure 1).

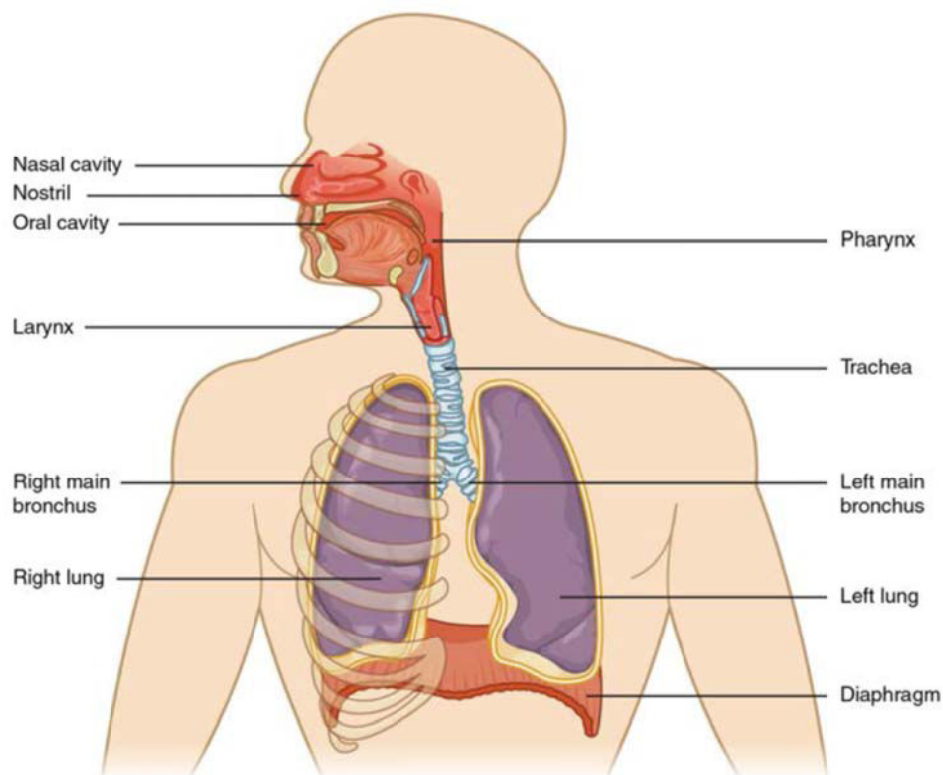


Figure 1: Example of main respiratory structures [1]

Functionally, the pulmonary airway system can be separated into two zones: the conducting zone and the respiratory zone. The conducting zone consists of the structures that are not directly involved in gas exchange [1]. The main functions of the conducting zone are to provide a pathway for incoming and outgoing air, to humidify, to warm, and to remove debris and pathogens from the incoming air. The conducting zone starts from the trachea (windpipe) which extends from the larynx toward the lungs [1]. The trachea branches into the right and left primary bronchi at the carina. Each bronchus bifurcates into two smaller bronchi, iteratively, until they become the

tiny terminal bronchioles which are about 0.5 mm in diameter. Each level of branching is called a *generation*, starting with the trachea as generation $n=0$, the primary bronchi (generation $n=1$), etc... This branching continues until the end of the pulmonary airway system. In an idealized model where each airway would bifurcate perfectly, there would be 2^n airways at generation n . The conducting zone starts from $n=0$ and ends at $n=16$ [2] (see Figure 2).

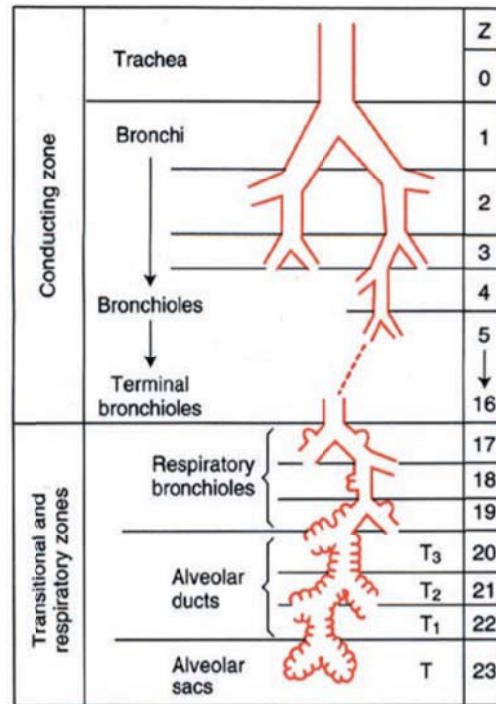


Figure 2: Schematic representation of the pulmonary airway system of the human (Weibel [3]).

The respiratory zone is composed of structures that are directly involved in gas exchange (in contrast to the conducting zone) [1]. The respiratory zone begins where the terminal bronchioles join respiratory bronchioles, the smallest type of bronchiole. The respiratory zone (transitional) starts from $n=17$ to 23 (see Figure 2). The respiratory bronchioles appear between generations 17 and 19. Alveolar ducts are located after the respiratory bronchioles, from generation 20 to 22. The alveolar ducts are made out of smooth muscles and connective tissues. Each lung holds approximately 1.5 to 2 million of them. Surrounding these ducts are small air sacs, called alveoli, designed to maximize gas exchange. The alveoli are surrounded by tiny blood vessels called *capillaries*. Alveolar spaces and capillaries are separated by very thin walls, called the *alveolar-capillary membrane*, which allows the oxygen to transfer from the alveoli to the blood. At generation $n=23$ (end of the respiratory zone), there are no more ducts but clusters of alveoli called *alveolar sacs* [2] (see Figure 3).

The epithelium lining the alveoli forms by two cell types: alveolar type I cells and alveolar type II cells. Alveolar type I cells are extremely flattened (the cell may be as thin as $0.05\ \mu\text{m}$) and forms the bulk (95%) of the surface of the alveolar walls. Alveolar type II cells are irregularly shaped. In 2004, Ochs *et al.* [4] used a design-based stereological approach to estimate the number of alveoli in the human lung. The mean value they found was about 480 million (range: 274–790 million) in six adult human lungs. They also found that the number of alveoli was in direct relation to the total volume of the lung. Their measurements showed that the mean size of an alveolus is $4.2 \times 10^6\ \mu\text{m}^3$ (range: $3.3\text{--}4.8 \times 10^6\ \mu\text{m}^3$) and that it is not related to lung size. An alveolus has an approximate diameter of $200\text{--}300\ \mu\text{m}$ [1].

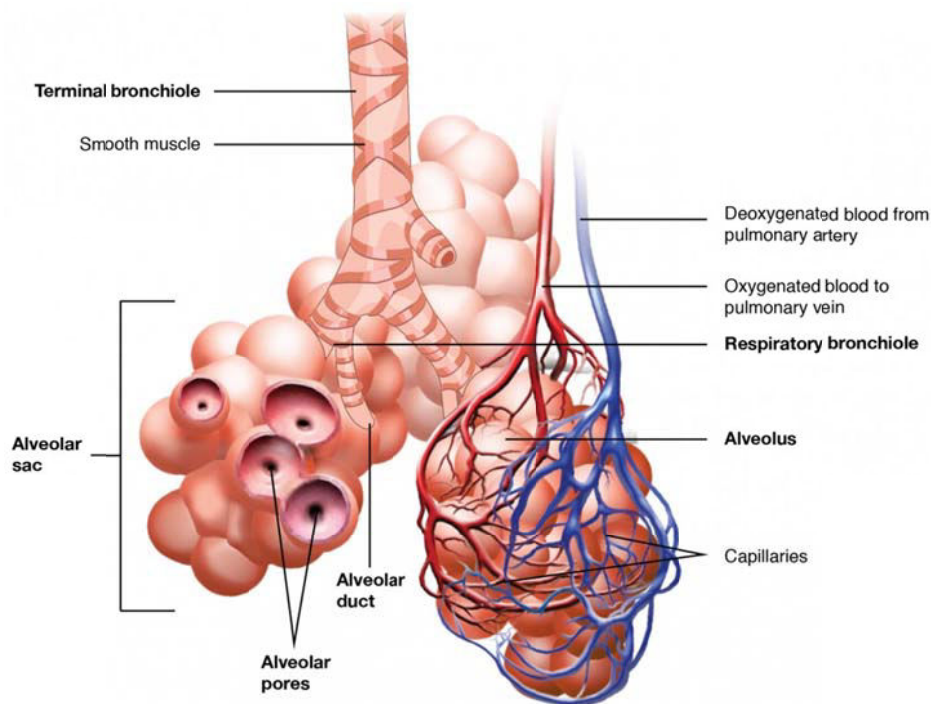


Figure 3: Schematic representation of the respiratory zone, where gas exchange occurs [1].

1.1.2 Animal lung

1.1.2.1 Rat lung

Gas, liquid, and particle transport in the lung are influenced by airway length, diameter, branching¹, and rotational² angles, so a comprehensive description of lung geometry is required to accurately model transport of fluid and particles in pulmonary.

During the last 60 years, a large body of work has been dedicated to the study of the mammalian morphometry of conducting airways, including rat and pig (Weibel *et al.* [3], [5], Raabe *et al.*[6], Phalen *et al.* [7], Menache *et al.* [8], Rodriguez *et al.* [9], Lee *et al.* [10], Oakes *et al.* [11], Horsfield *et al.* [12], Yeh *et al.* [13], Counter *et al.* [14], Azad *et al.* [15], Einstein *et al.* [16]).

In these studies, the lung structure was investigated by creating casts of the pulmonary airways and micro-CT images. They mostly described and simplified the pulmonary airways. Even recent research works as well as published lung geometry and dosimetry model for male Sprague-Dawley rats are simplified [17]. In Miller *et al.* [17] work, they measured the parameters of the tracheobronchial geometry: airway lengths, airway diameters, branching angles, and angles to gravity for 14 generations. The published data provide the average values at each generation, which is enough for building a symmetric model but far from the reality of the rat lung geometry.

In 1987, Rodriguez *et al.* [9] found that the number of generations of conducting airways varies in the different lobes of the rat lung. In the right upper lobe, conducting airways form conducting pathways that extend over 8 to 25 generations, whereas in the right lower lobe they extend over 13 to 32 generations. In 1973, Moreci *et al.* [18] results showed that the mean diameter of 100 sacs at peak inspiration is $66.6 \pm 10.7 \mu\text{m}$ and $59.3 \pm 4.5 \mu\text{m}$ at end-expiration for the Sprague-Dawley rat lung. In 2004, Hyde *et al.* [19] measured the number of alveoli and the average alveolar volume of Wistar rat's lung. The number of alveoli in the rat lung ranged from 17.3×10^6 to 24.6×10^6 , with a mean of 20.1×10^6 . In addition, the right lobe contains 47% more alveoli than the left. The average alveolus volume, $0.5 \times 10^6 \mu\text{m}^3$, was found to be identical on the two sides; it corresponds to a (spherical) diameter of about $100 \mu\text{m}$.

¹ The branching angle is defined as the angle between the two daughter airways after a bifurcation.

² The rotation angles (left and right) are the defined as the angles between the plane of the current bifurcation and the planes of the following bifurcations (starting from the daughter airways, left and right).

1.1.2.2 Pig lung

Pigs have larger lung compared to the rat but have monopodial branching airway similar to the rat [20]. Pig bronchial anatomy has been studied by Nakakuki [21], Dondelinger *et al.* [22], Mouton *et al.* [23], and Maina *et al.* [24]. The bronchial and lobar anatomy of the pig lung is similar to the human lung. The porcine left lung consists of a cranial lobe and a caudal lobe similar to the human lung. In contrast to the human right lung, which has three lobes, the porcine right lung is divided into four lobes (cranial, middle, accessory, and caudal) [25]. One big difference between the pig and human lung anatomy is that the pig right lung has an upper lobe bronchiole that does not exist in the human lung [21] (see Figure 4).

The porcine trachea is notably longer and more cartilaginous than the human trachea. Porcine airways extend over about 23 bronchial generations, identical to humans. Finally, the diameters and lengths of the airways decrease in pig lung, but within a way that is specific to their monopodial branching pattern [26].

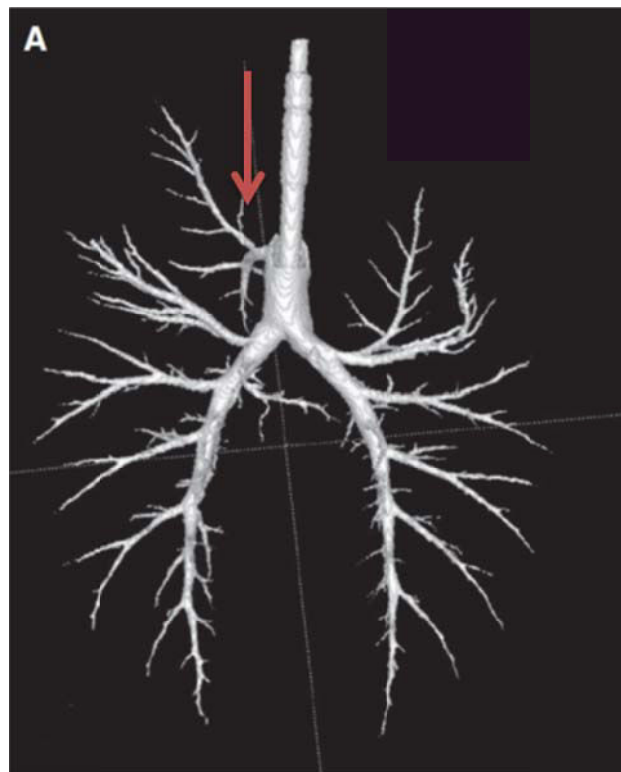


Figure 4: Pig airways extracted from CT images [15]. There is an early airway branching that feeds the top right lung lobe.

The inner layer of the lung of mammalian is coated with a liquid. For the first 16 generations plus trachea (conducting zone), the liquid lining consists of two layers. The

first layer is the watery layer, which calls serous. The serous is near to the airway wall and it includes cilia. The second layer of liquid is on top of the serous layer and call mucus. Mucus has a number of non-Newtonian properties, including viscoelasticity, shear-thinning, and yield stress, while the serous fluid is essentially Newtonian [2]. The entire air-water interface of the respiratory zone is coated by a liquid layer called the pulmonary surfactant, a complex mixture composed of lipids and proteins [27].

1.2 Lung diseases

The term ‘respiratory disease’ refers to any disease or disorder in which the lungs do not function properly. Some of these diseases have genetic origin cause, others are related to pollution and the quality of the air, and some others are related to the bacteria. At least 2 billion people are exposed to indoor toxic smoke, 1 billion inhale outdoor pollutant air, and 1 billion are exposed to tobacco smoke [28].

Lung diseases are defined in six categories:

- Lung diseases affecting the airways

Chronic Obstructive Pulmonary Disease (COPD) (with 3 million death each year [28], 3rd leading cause of death worldwide), asthma (about 334 million people suffer from asthma, the most common chronic disease of childhood affecting 14% of all children globally [28]), chronic bronchitis, acute bronchitis [29].

- Lung diseases affecting the air sacs (alveoli)

Pneumonia (killed 920,136 children aged under 5 years in 2015, accounting for 15% of the deaths in this age group [28]), tuberculosis (over 10 million people develop tuberculosis (TB), and 1.4 million dies from it each year making it the most common lethal infectious disease [28]), acute respiratory distress syndrome (ARDS), and neonatal respiratory distress syndrome (NRDS).

- Lung diseases affecting the interstitium

The interstitium is the microscopically thin, delicate lining between the lungs' air sacs (alveoli). Tiny blood vessels run through the interstitium and allow gas exchange between the alveoli and the blood, like interstitial lung disease (ILD), pneumonia, and pulmonary edemas.

- Lung diseases affecting the blood vessels

The right side of the heart receives low-oxygen blood from the veins. It pumps blood into the lungs through the pulmonary arteries. These blood vessels can suffer from diseases as well, like pulmonary embolism (PE) and pulmonary hypertension.

- Lung diseases affecting the pleura

The pleura is a thin lining that surrounds the lung and lines the inside of the chest wall. A tiny layer of fluid allows the pleura on the lung's surface to slide along the chest wall with each breath, like pleural effusion and pneumothorax.

- Lung diseases affecting the chest wall

The chest wall also plays a vital role in breathing. Muscles connect the ribs to each other, helping the chest to expand. The diaphragm descends with each breath in, also causing chest expansion, like obesity hypoventilation syndrome and neuromuscular disorders.

1.2.1 ARDS and NRDS

ARDS (acute respiratory distress syndrome) is caused by a lack of surface-active compounds, changes in the phospholipid, fatty acid, neutral lipid, and surfactant apoprotein composition, and damage/inhibition of surfactant compounds by inflammatory mediators. The surfactant is coated in a thin film of liquid at the alveolar surface of the lung [30]. ARDS, for the first time described by Ashbaugh *et al.* [31] in 1967, is characterized by an “acute onset of tachypnoea, hypoxemia.” Later in 1994, the American-European Consensus Conference (AECC) defined ARDS as the acute onset of hypoxemia (arterial partial pressure of oxygen to fraction of inspired oxygen, $[\text{PaO}_2/\text{FIO}_2] < 200$ mmHg) with bilateral infiltrates on frontal chest radiograph, and no evidence of left atrial hypertension. They defined acute lung injury (ALI) as the respiratory failure of acute onset with a $[\text{PaO}_2/\text{FIO}_2] < 300$ mmHg [32]. This definition has lots of limitations. In 2012, the Berlin definition (BD) [33] addressed many of these limitations. According to the new BD, ARDS is classified as three categories based on the degree of hypoxemia. Mild ($200 \text{ mmHg} < [\text{PaO}_2/\text{FIO}_2] < 300 \text{ mmHg}$), moderate ($100 \text{ mmHg} < [\text{PaO}_2/\text{FIO}_2] < 200 \text{ mmHg}$), and severe ($[\text{PaO}_2/\text{FIO}_2] < 100 \text{ mmHg}$). The ALI term was not useful and frequently misused, so it is not included in the BD. Both the BD and AECC defined ARDS for adult lung injury and for children have

limitations. At the Pediatric Acute Lung Injury Consensus Conference (PALICC) in 2015 [34], new developed pediatric-specific definitions and recommendations for treatment were stated to cover the BD and AECC definitions for ARDS in children. They mentioned that the onset of pediatric acute respiratory distress syndrome (PARDS) must happen within 7 days of a known clinical insult, and respiratory failure must not be fully explained by cardiac failure or fluid overload. The PALICC used the oxygenation index (OI), and in some conditions, the oxygen saturation index (OSI) instead of the $\text{PaO}_2/\text{FIO}_2$ ratio was used. In Table 1, you can see more details of the PARDS definition of PALICC.

Table 1: Pediatric acute respiratory distress syndrome definition. OI = oxygenation index, OSI = oxygen saturation index [34].

Age	Exclude patients with perinatal related lung disease			
Timing	Within 7 days of known clinical insult			
Origin of Edema	Respiratory failure not fully explained by cardiac failure or fluid overload			
Chest Imaging	Chest imaging findings of new infiltrate(s) consistent with the acute pulmonary parenchymal disease			
Oxygenation	Noninvasive mechanical ventilation	Invasive mechanical ventilation		
	PARDS	Mild	Moderate	Server
	Full face-mask bi-level ventilation	$4 < \text{OI} < 8$	$8 < \text{OI} < 16$	$16 < \text{OI}$
	CPAP $> 5 \text{ cm H}_2\text{O}$ PF ratio < 300 SF ratio < 264	$5 < \text{OSI} < 7.5$	$7.5 < \text{OSI} < 12.3$	$12.3 < \text{OSI}$

The surface area in the human adult lung is $\sim 90\text{m}^2$ involving $274\text{-}790 \times 10^6$ alveoli whose average radius is $\sim 100 \mu\text{m}$. Neonatal lungs have an alveolar surface area of $\sim 3 \text{ m}^2$ for $\sim 24 \times 10^6$ alveoli [35] whose average radius is about $75 \mu\text{m}$. The pressure jump across the air-liquid interface tends to collapse alveolar unless the surface tension is significantly reduced. Reduced surface tension is also needed to increase compliance allowing the lung to inflate much more easily. This role is devoted to pulmonary surfactant [27]. Lack of surfactant can induce airway collapse (atelectasis) and low lung compliance. Its existence was first hypothesized by Von Neergaard, who discovered that more significant pressure was needed to fill the lungs with air compared to saline [36]. In the 1950s, Pattle and Clements described the properties and functions of pulmonary surfactant [37][38][39].

Prematurely born neonates can have a primary surfactant deficiency which stiffens their lungs due to the high surface tensions, making them difficult to inflate. By studying the lung of infants who died from this neonatal respiratory distress syndrome (RDS), Avery and Mead inferred that the cause of death was due to surfactant deficiency from prematurity [40]. Neonatal respiratory distress syndrome (NRDS) is a condition of pulmonary insufficiency that in its natural course commences at or shortly after birth and increases in severity over the first 3 days of life [41]. NRDS is due to a deficiency of alveolar surfactant along with structural immaturity of the lung and it is mainly, but not exclusively, a disease of preterm babies. 10 out of 1000 infants might be born with NRDS [42]. In poor countries, the mortality rate is roughly 10 times higher than in wealthier countries [43].

1.3 Surfactant replacement therapy

Surfactant Replacement Therapy (SRT) consists of instilling a liquid-surfactant mixture directly into the lung airway tree: the surfactant is then transported through pulmonary airways and eventually reaches the alveolar regions. The efficacy of these treatments depends on liquid distribution in the pulmonary airways and delivery to the respiratory zone through the branching airway network. SRT has been applied in different lung diseases:

- Acute respiratory distress syndrome (ARDS).
- Asthma and pneumonia [44]. (A pilot study of natural surfactant showed improved lung function [45], but it was not shown clinical benefit in stable asthma [46]).
- RSV pneumonia [47].
- Stable chronic bronchitis [48]. (Aerosolized synthetic surfactant showed improved pulmonary function in adult patients).
- Immunosuppression.
- Cytokine release [49].
- DNA synthesis of inflammatory mediators [50].
- Lymphocyte proliferation [51].
- Immunoglobulin production [52].
- Expression of adhesion molecules [53].

A more extensive well-controlled study in subjects with respiratory illness needs to confirm these observations [54]. In the 1980s, Fujiwara *et al.* [55] reported the first successful trial of surfactant replacement therapy (SRT) with exogenous surfactant for

treating the preterm infants with RDS. Soon SRT became the standard therapy for these newborn RDS patients. This therapy contributed to a drastic drop in premature neonatal mortality in less than 30 years: from 4,997 deaths in the US in 1980 to 861 in 2005 [56][57]. The mortality rate in Korea plummeted from 56% in the 1980s to 11% in the early 2000s for very low birth weight infants [58][59]. Table 2 shows an overview of case histories and clinical trials demonstrating the benefits of SRT in children/infants/babies with ARDS.

Table 2: Overview of case histories and clinical trials demonstrating the benefits of SRT in children/infants/babies with ARDS [60]

Study	Patients (N)	Surfactant	Outcomes
Fettah <i>et al.</i> [61]	Baby (1)	Curosurf®	Rapid and persistent improvement after 2 doses of Curosurf® (100 mg.kg ⁻¹ body weight, 1.25 mg.kg ⁻¹)
Willson <i>et al.</i> [62]	Children (110)	Infasurf®	No immediate improvement in oxygenation: study stopped at sponsor's request
Willson <i>et al.</i> [63]	Children (152)	Infasurf®	Improved oxygenation and ventilation
Moller <i>et al.</i> [64]	Children (35)	Alveofact®	Improved oxygenation
Hermon <i>et al.</i> [65]	Children (19)	Curosurf®	Improved oxygenation
Lopez-Herce <i>et al.</i> [66]	Children (20)	Curosurf®	Improved oxygenation
Willson <i>et al.</i> [67]	Children (29)	Infasurf®	Improved oxygenation

SRT has also been proposed to treat a related condition affecting both children and adults called *Acute Respiratory Distress Syndrome* (ARDS). SRT was initially successful in ARDS in human adult patients [68], large sheep [69], and later in pediatric patients to age 21 [63].

Anzueto *et al.* [70] in 1996 used an aerosolized surfactant in adults with ARDS. They randomized the patients to receive either Exosurf (364 patients) or 0.45% saline (361 patients). They reported no improvement in oxygenation with the instillation of Exosurf (exogenous surfactant).

In 2001, Kesecioglu *et al.* [71] did a randomized study of 24 patients who received standard therapy plus surfactant (porcine surfactant) and 12 patients who just

received standard treatment. The dosage was from 200 mg phospholipid/kg ideal body weight (up to four doses in case of relapse). Their results presented measures of oxygenation, duration of mechanical ventilation, and the average ICU¹ length of stay, which these results did not differ significantly between the two groups.

Spragg *et al.* in 2003 [72], 2004 [73], and 2011 [74] performed studies on the adult using synthetic surfactant, including recombinant (rSP-C). In the first study with 40 patients, they reported no improvement in oxygenation due to surfactant instillation in the group of patients who received standard therapy plus one of the two doses of exogenous surfactant compared to the group who just received standard treatment. The second study was carried in a bigger group involving 448 patients with ARDS. They compared standard therapy alone with standard treatment plus up to four intratracheal doses of rSP-C-based surfactant. The results showed no improvement in survival due to exogenous surfactant instillation. The third study was included in 843 patients between 12 and 85 years of age with severe impairment of gas exchange administration. The rSP-C surfactant was used at a concentration of 100 mg phospholipid/kg. The results showed no difference in mortality for groups defined by a mechanism of direct lung injury (aspiration or pneumonia). The conclusion was that rSP-C-based surfactant has no clinical benefit in case of severe direct lung injury. Kesecioglu *et al.* in 2009 also concluded that the instillation of a large bolus of exogenous natural porcine, in a group of patients with acute lung injury and ARDS, did not improve the outcome [75].

In parallel to these clinical studies, several groups performed careful experimental studies on liquid plug propagation in the pulmonary airway system. In 1994, Ueda *et al.* investigated surfactant-deficient ventilated preterm lambs [76], showing that surfactant distributions strongly depend on the chosen instillation technique/conditions. In 1998, Espinosa *et al.* showed that rapid injections lead to a more homogenous distribution [77]. Examining the effect of dose and delivery methods on 43-kg adult sheep, Lewis *et al.* observed in all cases an improvement of gas exchange: the larger the dose volume, the more significant the improvement [69]. Moreover, tracheal instillation or administration directly into each lobe under bronchoscopic guidance showed similar results in terms of the lobar distribution of surfactant. Cassidy *et al.* working on rat lung found that the formation of a liquid plug in the trachea before inspiration plays a significant and positive role by creating a

¹ intensive care unit

uniform liquid distribution of surfactant throughout the lung [78]. In 2004, using radiographic image techniques, Bull *et al.* confirmed that the formation of liquid plugs in the large airways, which depend on posture and infusion rate, could result in a more homogeneous liquid distribution than gravity drainage alone [79]. Finally, in 2017, Steffen *et al.* showed that SRT was able to lower alveolar surface tension and that the number of open alveoli was improved significantly in a rat model [80].

Theoretical studies in liquid/surfactant delivery to the lung have also been performed. Halpern *et al.* discovered that both transit and delivery times are strongly influenced by the amount of pre-existing surfactant and by coating the conducting airway surface area treated as a trumpet model [81]. Mathematical modeling and numerical simulations have been used to assess SRT efficacy, which is not only determined by the amount of surfactant delivered to the targeted (alveolar) regions, but also by the homogeneity of the end distribution of delivered surfactant. This distribution in the alveolar region is affected by a number of factors, including physical properties of the liquid (viscosity, density, surface tension), patient posture (prone/supine, left lateral decubitus/right lateral decubitus) airway geometry, instillation method (flow rate), and presence of other plugs in nearby airways from previous instillations [82].

Filoche *et al.* [83] in 2015 simulated SRT in a symmetric 3D structure of the respiratory airway system. Their results showed that an initial instilled dose volume of the surfactant loses a portion of volume V_D to coating the airways. This lost volume is called the *coating cost* V_{CC} . Therefore, the amount actually reaching the acinus is $V_D - V_{CC}$. The successful reduction of V_D/kg in neonates is due to $V_D - V_{CC}$ remaining clinically effective. However, in adults, $V_D - V_{CC}$ was effective at the higher value of V_D/kg , but not at the lower value.

Initial success in applying surfactant to the adult with ARDS [68], large sheep [69], and pediatric patients to age 21 [63] was at a dose volume per kg range $V_D/\text{kg} = 2-4 \text{ mL}\cdot\text{kg}^{-1}$. The field, however, switched to a lower dose volume, $V_D/\text{kg} = 1-1.3 \text{ mL}\cdot\text{kg}^{-1}$, higher concentration strategy that was successful in premature neonates discussed above. However, it led to failure in adults [62][72][73][74][84][70][71] which is in agreement with the findings of Filoche *et al.* [83] in 2015.

1.4 Surfactant properties

1.4.1 Composition of pulmonary surfactant

Alveolar type II cells are responsible for producing pulmonary surfactant. Pulmonary surfactant is composed primarily of lipids and proteins. The lipids account for approximately 90% of the surfactant (in mass), and proteins are around 10% [85][86][87].

- lipids

The main lipids are phospholipids (PL) which are ~80-85% of the surfactant (in mass). PL are amphipathic molecules with a hydrophilic part (polar) and hydrophobic chains (non-polar). The main components of PL are phosphatidylcholine (PC), which is approximately 80% of the lipids. Approximately 10% of the lipid pool is Phosphatidylglycerol (PG), and the rest is composed of small amounts of phosphatidic acid (PA), phosphatidylinositol (PI), phosphatidylethanolamine (PE), phosphatidylserine (PS), sphingomyelin (SPM) and Cholesterol in PL. The component that is responsible for generating a very low surface tension at the interface during compression is Dipalmitoyl-PC (DPPC), and it accounts for at least 50% of PC molecular species. The two saturated acyl chains enable the lipid to form a tightly packed monolayer that can generate these low surface tension values without collapsing [88][89][87]. The combination of lipids depends on the type of surfactant. For example, Curosurf is composed of:

- 1- phosphatidylcholine (PC) or lecithin (1,2-diacyl-sn-glycero-3-phosphorylcholine)
- 2- phosphatidylglycerol (PG) (1,2-diacyl-sn-glycero-3-phosphoryl-1'-sn-glycerol)
- 3- phosphatidylinositol (PI) (1,2-diacyl-sn-glycero-3-phosphoryl-1'-inositol)
- 4- phosphatidylserine (PS) (1,2-diacyl-sn-glycero-3-phosphorylserine)
- 5- phosphatidylethanolamine(PE)(1,2-diacyl-sn-glycero-3-phosphorylethanolamine)
- 6- sphingomyelin (SM) (sphingosine ceramide of phosphorylcholine)
- 7- lysophosphatidylcholine (LPC)

- Proteins

The protein in the surfactant consists of four specific proteins. These proteins are surfactant protein A (SP-A), SP-B, SP-C, and SP-D. Surfactant proteins are in two groups of hydrophobic and hydrophilic. SP-B and SP-C are two small hydrophobic proteins, while SP-A and SP-D are large hydrophilic proteins [90]. Until now, no direct role for SP-A and SP-D in decreasing surface tension of the surfactant has been shown.

However, both in *in vivo* and in *in vitro*, the ability to increase surfactant resistance against inhibition has been observed [91]. SP-B and SP-C by rapid absorbing of phospholipid into the air-liquid interface are involved in lowering the surface tension. Surfactant protein B is a hydrophobic protein that consists of 79 amino acids. Due to its hydrophobicity, SP-B will interact with lipids [85][90]. SP-C is responsible for stabilizes the surface activity of the surfactant film during the expansion and compression involved in breathing [44].

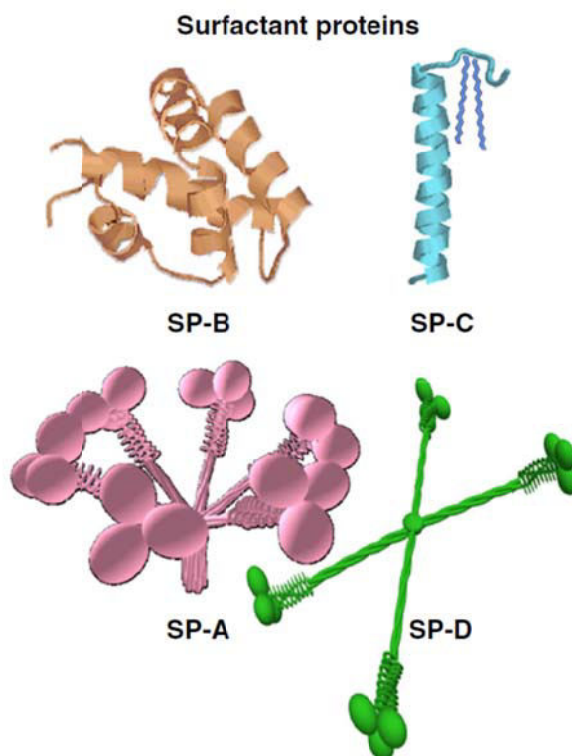


Figure 5: Three-dimensional representation description of surfactant proteins [92]

Two sources of surfactant exist, animal-sourced and synthesized. The synthetic surfactant can be free of proteins or contain proteins. The examples of the synthetic surfactant free of proteins are Pumactant (ALEC®, Britannia Pharmaceuticals, UK), Colfosceril (Exosurf®). The synthetic surfactants that are containing proteins are lucinactant (Surfaxin, Discovery Laboratories, U.S.A) and Pumactant (Venticute, Altana Pharmaceuticals, Germany).

Animal surfactant [93][94] are Bovactant, (Alveofact®, Lyomark, Germany), BLES (BLES®, BLES Biochemicals, Canada), Calfactant (Infasurf®, ONY Inc., U.S.A.), Surfactant-TA (Surfacten®, Tokyo Tanabe, Japan), Beractant (Survanta®, Ross Labs,

U.S.A.) (all extracted from bovine lungs) and Poractant alfa (Curosurf®, Chiesi Farmaceutici, Italy) (from porcine lungs).

1.4.2 Mechanical properties of surfactant

1.4.2.1 Surface tension

Surface tension (σ) is the attractive force applied upon the surface molecules of a liquid by the molecules situated below. This force tends to draw the surface molecules into the bulk of the liquid and makes the liquid assume the shape having the least possible surface area [95]. The forces of attraction acting between molecules of the same type are called cohesive forces and those acting between molecules of different types are called adhesive forces. The molecules at the surface of a liquid see different molecules above and below and therefore are pulled inward. This creates some internal pressure which forces the liquid surface to contract to the minimal area.

In terms of energy, a molecule in contact with a neighbor is in a lower state of energy than if it were alone. Because of missing neighbors, molecules at the boundary have higher energy compared to the interior molecules. The number of higher energy boundary molecules must be minimized to have a minimize energy state. Minimizing the number of boundary molecules results in a minimal surface area. Surface tension can be dimensionally introduced by “energy per area unit” or “force per unit length”: $\sigma = \partial G / \partial A$, where G is the free enthalpy and A is the area. Surface tension is measured in SI units, $\text{J}\cdot\text{m}^{-2}$.

Liquids with weak molecular interactions (for instance when only van der Waals forces exist) have a low surface tension (e.g., for oil $\sigma=20$ mN/m). If interactions are stronger, such as when hydrogen bonding dominates, surface tension is high (e.g., for water $\sigma=73$ mN/m) [96].

The surface tension at the alveolar interface has an influence on lung mechanical properties such as the compliance of lung associated with the elastic work of breathing [97]. Lung geometry dictates that the fractal division of acinar volume between alveoli and alveolar ducts is determined by the balance between two types of force: (i) inward-acting tissue forces in the alveolar entrance ring, and (ii) outward-acting forces arising from septal tissue acting in parallel to surface forces at the air-liquid interface [98].

The changes in the lung volume, the alveolar diameter, and lung compliance are the result of an increase of surface tension in the lung. Such increase generates a

compressive force on capillaries, decreasing capillary volume and compliance, specifically during ARDS [99]. In 2017, Dias *et al.* [100] measured surface tension between air and surfactant (see Figure 6) for different percentages of surfactant varying from 1% to 100% diluted by classical aqueous cell feeding culture medium.

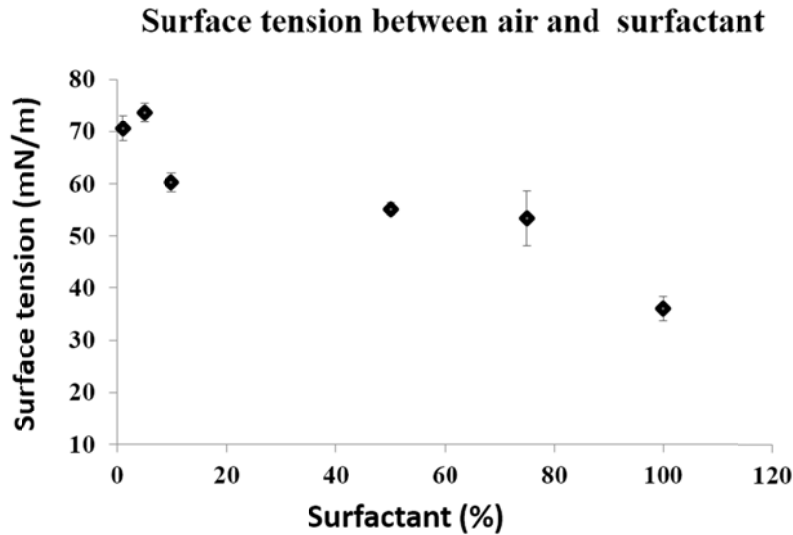


Figure 6: Surface tension (in mN/m) with air for different percentages of surfactant varying from 1% to 100% diluted by classical aqueous cell feeding culture medium (DMEM) [100]

1.4.2.2 Viscosity

The viscosity of a fluid (μ) is a measure of its resistance to gradual deformation by shear stress¹ or tensile stress [101]. Viscosity can be introduced as quantifying the frictional force that arises between two adjacent layers of fluid that are in relative motion. For instance, when a fluid is forced through a tube, the fluid flows more quickly near the tube's axis and more slowly near its walls. In such a case, experiments show that some stress is needed to retain the flow through the tube. This is because a force is required to overcome the friction between the layers of the fluid which are in relative motion; the strength of this force is proportional to the viscosity [101].

For some fluids, the viscosity is constant over a wide range of shear rates (Newtonian fluids) [101]. The fluids whose viscosity is not constant with applied stress are called non-Newtonian fluids. The SI unit of dynamic viscosity is Pa.s or kg.m⁻¹.s⁻¹ [101]. The cgs unit is called the Poise (P).

¹ A shear stress, often denoted τ , is the component of stress coplanar with a material cross section.

Surfactant viscosity depends on the type of surfactant (its microstructure), shear rate (the interactions between components and the environmental conditions), phospholipid concentration, and temperature. Distribution of surfactant in the lungs is believed to be affected by viscosity [102][103][104].

In 2002, King *et al.* [105], using a cone and plate micro viscometer, measured shear viscosities of saline suspensions of lavage calf lung surfactant[®] (LS), Survanta[®], Infasurf[®], and Exosurf[®] at 37 °C. Their results showed that for similar concentration, temperature, and shear rate, Survanta has a higher viscosity and Infasurf[®], LS[®], and Exosurf[®] have smaller viscosity, respectively. For example, Survanta[®] and Infasurf[®] viscosity are 17 and 7 times higher than Exosurf[®] at fixed concentration and shear rate.

Increasing phospholipid concentration and decreasing shear rate shows an increase in the viscosity of all four surfactants. But the dependence of viscosity to temperature is complicated. Increasing the temperature has a different effect on viscosity: it increases viscosity in LS[®] and Infasurf[®] while it leads to a decrease in Survanta[®] and Exosurf[®]. King *et al.* [104] results in 2001 showed that LS[®] at low concentration has a Newtonian behavior but is a Non-Newtonian fluid at higher concentration. Survanta[®] and Infasurf[®] are non-Newtonian at high and low shear rates.

In 2009, Lu *et al.* [106] measured and characterized the viscous properties of Survanta[®] and Infasurf[®]. They focused on kinematic viscosity¹ because of its relevance to the distribution of surfactant in the upper airways. They found that viscosity increased substantially at the higher concentrations of Infasurf[®], 25 or 35 mg/ml. This increase in viscosity was markedly higher at 37 °C than at 23 °C (see Figure 7A, B). The viscosity of Survanta[®] is highly concentration dependent. The largest increase occurring between 12.5 and 25 mg/ml: at 12.5 mg/mL, the viscosity was 8 cSt (CGS unit) at 23 °C and 3 cSt at 37 °C and rises to 90 and 32 cSt, respectively at 25 mg/ml (see Figure 7C, d). Survanta[®] had a consistently higher viscosity than Infasurf[®] at an equal concentration at 23 or 37 °C. At higher concentrations, the viscosity value of Survanta[®] greatly exceeds that of Infasurf[®]. Also, in contrast to Infasurf[®], Survanta[®] viscosity at any concentration is always lower at 37°C than at 23°C and does not change with time at either temperature.

¹ The kinematic viscosity can be converted to dynamic (absolute) viscosity by multiplying by the density of the fluid.

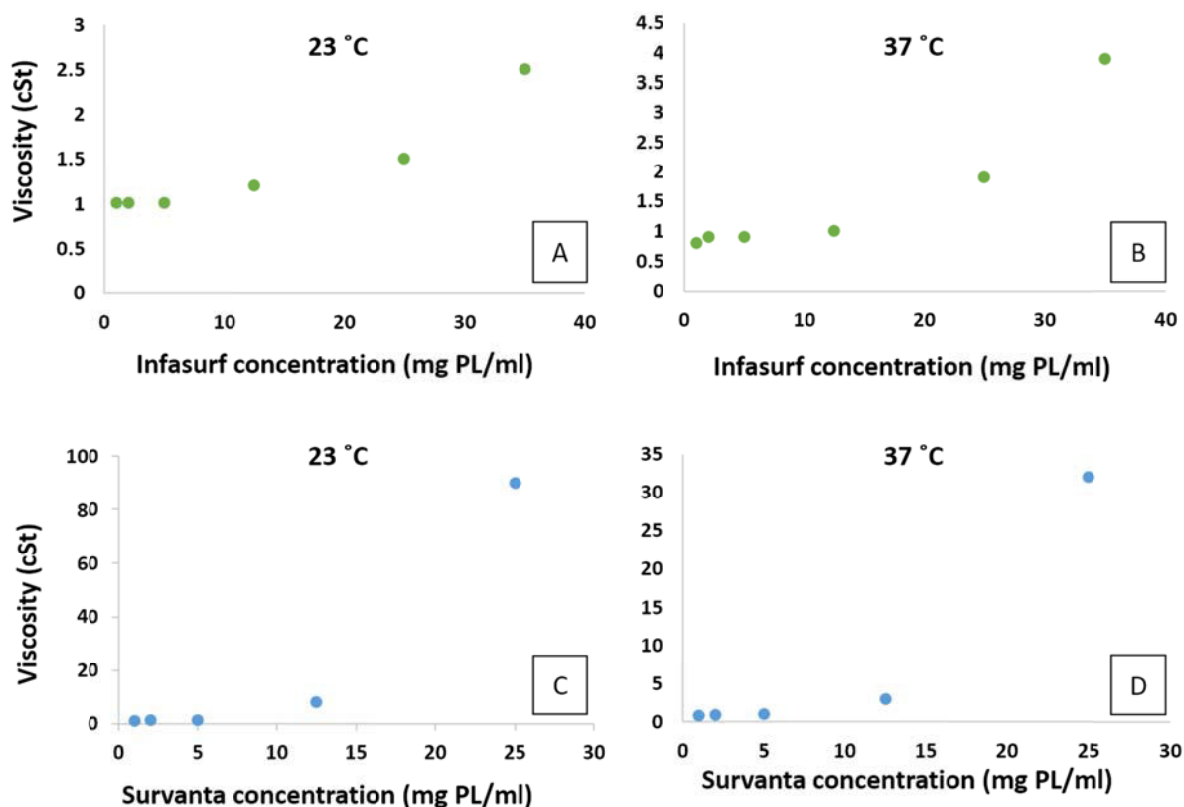


Figure 7: Viscosity of Infasurf® and Survanta® versus phospholipid concentration. A) Infasurf® determined at 23°C. B) Infasurf® at 37°C. C) Survanta® determined at 23°C. D) Survanta® at 37°C. [106]

In these studies, the viscosity is found in the range of 0.9 – 92 cSt. At clinical concentrations and temperatures, the viscosity is in the range of 1.5 – 52 cSt s, indicating a relatively low viscosity fluid [104][105][106].

In 2019, Thai *et al.* using a novel microrheology technique and nanoparticle tracking analysis (NTA) measured the viscosity and volume fraction of Curosurf® [107]. With magnetic rotational spectroscopy (MRS), they submitted it to an external magnetic field at increasing frequency and then calculated the viscosity from the identification of the different wire rotation regimes. They found a linear relation between volume fraction (ϕ) and concentration (c): $\phi = 0.0052 c$, where c is expressed in g.l^{-1} . The static viscosity of Curosurf® at 80 g.l^{-1} of concentration (clinically used) has been measured at 24.5 ± 5 mPa.s by magnetic wire microrheology and at 20 ± 1 mPa.s by cone-and-plate rheology. In Figure 8, we can see the values of static viscosity of Curosurf® as a function of the concentration obtained from magnetic rotational spectroscopy by Thai *et al.* [107].

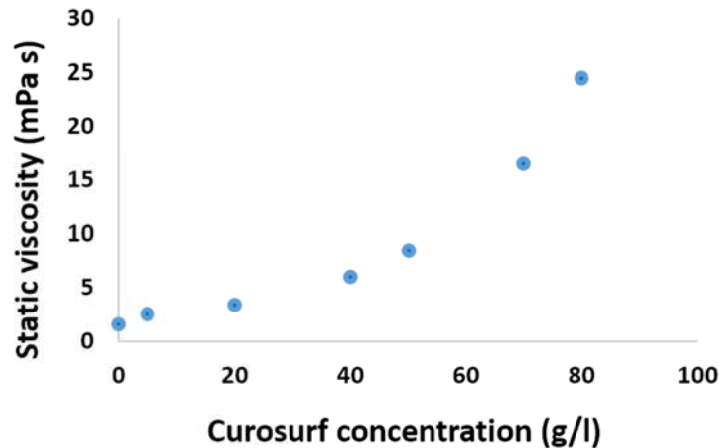


Figure 8: Values of Curosurf[®] static viscosity as a function of the concentration obtained from Magnetic Rotational Spectroscopy [107]

1.5 Surfactant administration delivery

Patients with respiratory distress syndrome (RDS, especially NRDS) and with conditions associated with surfactant deficiency such as meconium aspiration syndrome are a target for SRT. Although most babies with RDS are premature, other factors can influence the chances of developing the disease. These include [108]:

- Previous birth of a baby with RDS
- Cesarean delivery
- Perinatal asphyxia
- Cold stress (a condition that suppresses surfactant production)
- Perinatal infection
- Multiple births (multiple birth babies are often premature)
- Infants of diabetic mothers
- Babies with patent ductus arteriosus

The signs of NRDS are usually noticeable immediately after birth and get worse over the following few days. They can include [108]:

- Respiratory difficulty at birth that gets progressively worse
- Cyanosis (blue-colored lips, fingers, and toes)
- Rapid, shallow breathing
- Flaring of the nostrils
- A grunting sound when breathing
- Chest retractions (pulling in at the ribs and sternum during breathing)

RDS is usually diagnosed by a combination of assessments [108]:

- Appearance, color, and breathing efforts (indicate a baby's need for oxygen)
- Chest X-rays of lungs
- Blood gases (tests for oxygen, carbon dioxide and acid in arterial blood)
- Echocardiography

For the neonate, in the case of ARDS, there are two therapeutic strategies. First, preventive treatment (surfactant is administered at the time of birth), second, rescue treatment (surfactant is applied after the initiation of mechanical ventilation in infants with clinically confirmed RDS) [109][110].

The infants smaller than 24 weeks' gestational age are recommended to be intubated immediately after birth within the first 15 min to 30 min of life. Between intubation and surfactant administration, they have to be ventilated with low tidal volume and pressure. For infants who are older than 24 weeks' gestational age as early treatment can be intubated immediately after birth or initially treated with noninvasive ventilation, and surfactant administration can be done under conditions [111].

Still, 40 years after the introduction of SRT, an optimized way of delivering surfactant to maximize the homogeneity of the distribution while maintaining the efficiency is still lacking. Administration techniques play essential roles in the homogeneity and the efficiency of the delivery. Administration techniques involve issues such as: when to start the therapy, what amount of instilled dose volume, the value of instilled flow rate, the number of repeated doses, the patient position, the ventilation strategies and rates, and the choice of surfactant (because of mechanical properties of surfactant, like viscosity and surface tension), which all have an effect on the surfactant delivery. In this section, we mention some of the current common recommendations for surfactant administration.

First, a physician has to check and give the order for SRT and he or she has to be at the bedside during surfactant administration. A registered respiratory therapist (RRT) is responsible for advising the bedside nurse for SRT. There is a baseline patient assessment, which has to be done by the RRT and registered nurse [111]. The RRT is responsible for administering the surfactant.

The surfactant can be delivered through an in-line catheter with the tip located in the mid-trachea level. However, it can also be delivered by instilling through the nasopharynx [112] or using a nebulizer [113].

The instilled dose volume, V_D , per kilogram used in neonates depends on the surfactant concentration. Different type of surfactant has different concentration. Examples are Survanta[®] ($25 \text{ mg.mL}^{-1} \times 4 \text{ mL.kg}^{-1} = 100 \text{ mg.kg}^{-1}$), Infasurf[®] ($35 \text{ mg.mL}^{-1} \times 3 \text{ mL.kg}^{-1} = 105 \text{ mg.kg}^{-1}$), and Curosurf[®] ($80 \text{ mg.mL}^{-1} \times 1.25 \text{ mL.kg}^{-1} = 100 \text{ mg.kg}^{-1}$) [114] (see Table 3). As it is shown, if we use Survanta[®], Infasurf[®], and Curosurf[®], we need to instill 4, 3, and 1.25 mL.kg^{-1} dose volume. The move to smaller $V_D.\text{kg}^{-1}$, from 4 to 1.25 mL.kg^{-1} , was to reduce the hazards of liquid in the lung while maintaining the molecular dose $\sim 100 \text{ mg.kg}^{-1}$, a goal based on a well-mixed compartment assumption.

Table 3: Surfactant properties [114]

Surfactant	Surfaxin [®]	Exosurf [®]	Survanta [®]	Infasurf [®]	Curosurf [®]	Alveofact [®]
Phospholipid concentration (mg.mL^{-1})	30	13.5	25	35	80	40
Dose volume (mL.kg^{-1})	5.8	5	4	3	1.25 or 2.5	1.2
Dose (mg.kg^{-1})	175	67.5	100	105	100 or 200	50

During surfactant administration, the patient can lay down in one or multi-position. The position could be left lateral decubitus (LLD), right lateral decubitus (RLD), supine (S), prone (P), 45-degree angle (halfway) between supine-LLD (called SL) and the 45-degree angle between supine-RLD positions (SR), and so on. In LLD, the body is lying on the left side and the trachea is horizontal. RLD is similar but on the right side. When these positions are used together (noted L+R), the total dose is divided into 2 half-doses, one half-dose being delivered in RLD position, and the second half in LLD position and so on.

Modes of delivery may have an effect on SRT. Bolus infusion and continuous infusion are two standard methods of surfactant instillation into the trachea. Bolus administration could be in one single dose or in multiple doses. In one single dose, all of the prepared dose volumes are instilled once (10 to 20 s). In multiple doses, the total dose divided into two or more amounts (aliquots). It can be given separately in time, a minimum period of 30 s to 60 s between the aliquots should be used if infants remained stable, or can be instilled in two or more aliquot one after each other between consecutive breaths. Another technique is a continuous infusion, which is a slow administration of the surfactant preparation. A new technique is nebulization. In

this method, a suspension of the surfactant is aerosolized and subsequently inhaled [111][115][116].

1.6 Conclusion

During the last 30 years, the mortality rate in premature newborns with RDS has experienced a drastic drop thanks to the introduction of SRT, although SRT did not alter the mortality rate in adults suffering from ARDS. In fact, this therapy was initially successful in adult patients who received a high dose volume of surfactant ($V_D/kg = 2-4 \text{ mL}\cdot\text{kg}^{-1}$). Changing from high dose volume to low dose volume with higher concentration, a strategy proved successful in premature neonates, led to failure in adults.

Is this failure due to the chemical properties of surfactant and the different nature of the disease in newborns and adults, or should it be attributed to the mechanical properties of surfactant and the delivery methods? To answer this question, we first need to know how surfactant (as a liquid) propagates into the lung under different initial conditions. This requires very detailed knowledge of the 3D structure of the pulmonary airway system.

Most of the investigation on transport into the pulmonary airway system addressed gas transport. For that, one necessarily needs to know only the airway diameters and lengths. Angles bear almost no interest in this case as they have little influence on gas transport. But in order to investigate the propagation of liquid, we need branching angles and rotation angles between successive bifurcation planes as well. One challenge of the current study was to find data for the 4 aforementioned parameters in all the conducting zone.

The animal model in clinical research is the first step to valid therapy. As we saw, the animal (rat and pig) airway pulmonary branching structures are different from the human lung. Rat and pig branching are more monopodial, whereas the human lung branching is rather dichotomous. The lung is designed for gas transport, while in SRT, the liquid is pushed into the lung airway system. Knowing the importance of angles in liquid delivery, can animal models be a reliable model for SRT in humans?

To answer these questions, we develop in the next chapter the first realistic geometrical models of the tracheobronchial tree for rat and pig (the latter being comparable to the human lung in terms of volume). Finally, we develop symmetric and

asymmetric 3D models of the human lung to be able to investigate the propagation of liquid under different applied conditions.

**Geometrical models of the
tracheobronchial tree in
mammals**

The structure of the lower respiratory tract differs among mammals. Rat, pig, and common laboratory rodents exhibit a mainly monopodial branching system (the main axis grows for an indefinite period and during this process, it regularly-produces lateral branches), while dichotomous branching patterns of airways are present in human (branches form as a result of the division of a terminal into two equal daughter branches). To be able to model the propagation of surfactant into the lower respiratory tract, we first need to design realistic models of these tracts that account faithfully for these differences. In this chapter, we first introduce the main features of the geometrical description of the tracheobronchial tree. We then build a realistic asymmetric 3D model of the rat tracheobronchial tree and an asymmetric 3D model of the pig lung. In the end, we developed a symmetric and two asymmetric 3D models of the human lung. Finally, to check the accuracy of our lung models in terms of size, branching, and structure, we compare our respiratory geometrical models with existing pictures of casts and CT-scans.

2.1 Geometrical parameterization

The bronchial tree starts at the trachea and ends in the respiratory terminal bronchioles. In the geometrical description, this airway system is described as an assembly of straight tubes connected by bifurcations, each airway being parameterized by its length (L) and diameter (D). The tree is dichotomous at each bifurcation, and a parent airway divides into two daughter airways. The bifurcations are parameterized by three angles and two dimensionless parameters. The three angles are the branching angle between the two daughter airways (θ) and the two rotation angles (left and right) between the plane of the current bifurcation and the successive bifurcation planes of each daughter airway (ψ). The two dimensionless parameters are the diameter ratios between the daughter airways and the parent airway (λ). Figure 9 displays this geometric description of the airway tree.

The airways are classified by generations, labeling the trachea as generation 0 and increasing by 1 at each bifurcation following Weibel's definition [3] (see Figure 10).

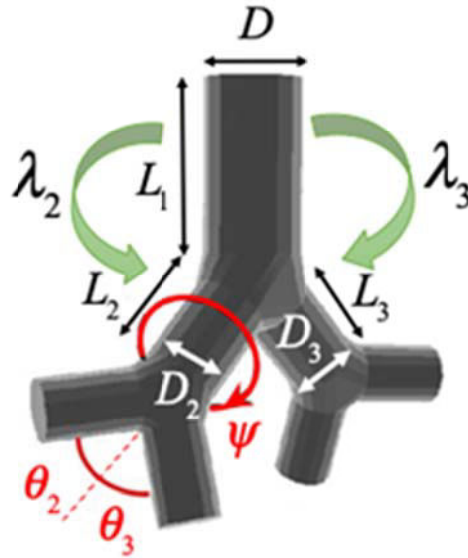


Figure 9: Geometric description of the airway tree: the airways are described by their diameter (D) and length (L). A bifurcation is characterized by its branching angles (θ_2 and θ_3), and the relation between successive bifurcations by the rotation angles between successive bifurcation planes (ψ).

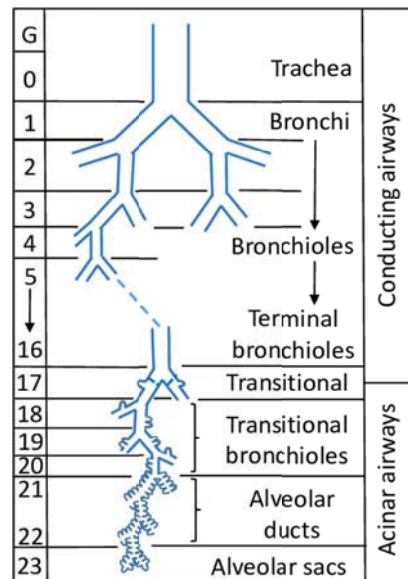


Figure 10: Schematic representation of the geometry in the conductive and transitory zones of the pulmonary airway system [3].

2.1.1 Model of the rat lung

The rat lower respiratory tract is an asymmetrically branching tree. As mentioned earlier, the geometrical description involves length parameters (airway diameter and length) and angle (branching, rotation). These values are obtained from morphometric measurements of Raabe *et al.* performed on the tracheobronchial conducting airways of

the lungs of rat [6]. These morphometric measurements were performed on flexible silicone rubber replica casts at a volume corresponding to end inspiration. The silicone rubber casts were made in lungs that were intact and still within the thorax by an *in situ* method described by Phalen, *et al.* [7]. Raabe *et al.* removed the lungs from the thorax and the tissues digested in sodium hydroxide, leaving only a rubber replica of the air passages. After trimming the flexible replica, the tracheobronchial tree down to terminal bronchioles is left. The diameters of major bronchi are increased by about 15%, whereas the airways length and branching angle changed little during the casting procedure (less than 5%). Raabe *et al.* measured the airway diameters, lengths, branching angles, and angles to normal direction of gravity from the trachea down to the end, including the terminal bronchioles. Five people, who were trained for this work, performed the measurements. The resulting data is used to feed our program to model rat lung structure. Figure 11 displays statistics on the number of branches at each generation as well as the average diameter (D) and length (L). Figure 12A and 12B show histograms of branching angles (θ) and angles to the normal direction of gravity (ϕ) of Raabe measurements, respectively.

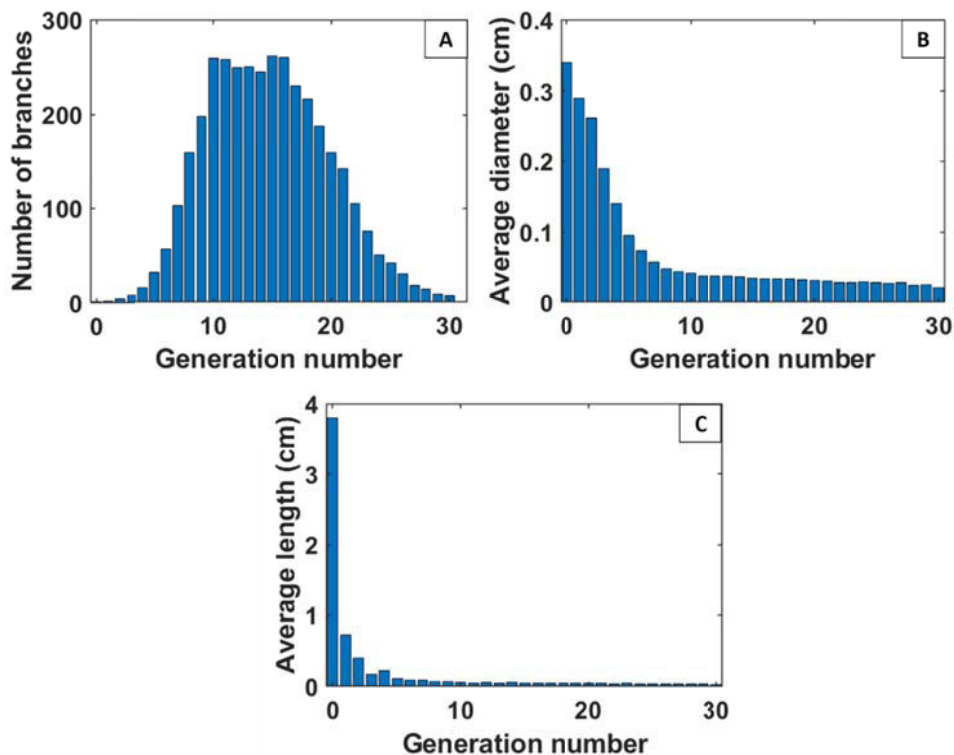


Figure 11: Statistics of the rat lung model built from [6]. A) The number of branches vs. generation. B) Average diameter vs. generation. C) Average length vs. generation.

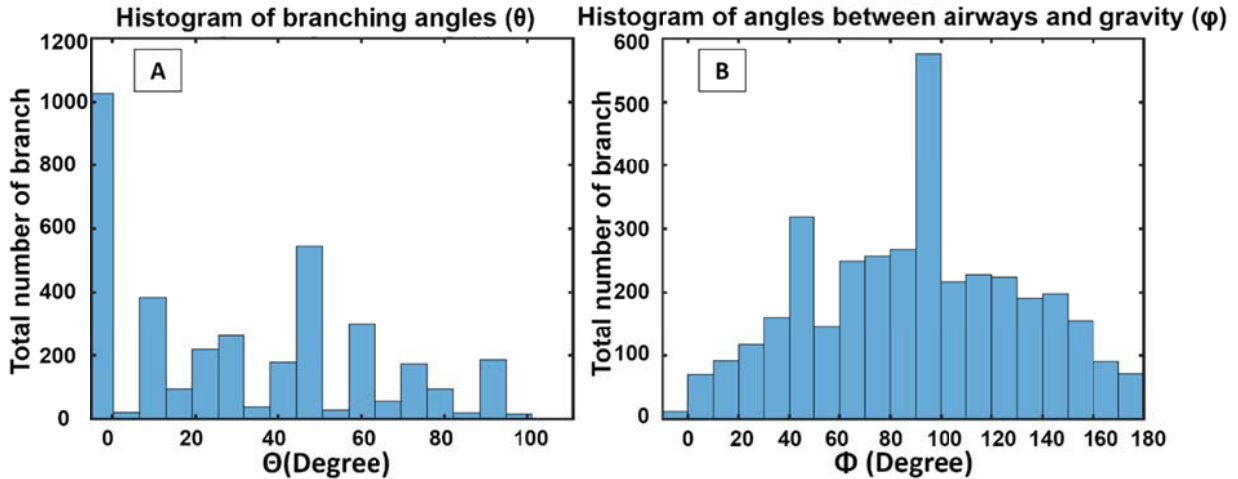


Figure 12: Statistics of the rat lung model built from [6]. A) Histogram of branching angles. B) Histogram of angle to the normal direction of gravity [6].

In experimental studies, Wistar and Sprague-Dawley rats were used. However, we chose to simulate Long-Evans rats respiratory lower tract due to the extensive database on their lung structure (branching angles), and the relative similarity between Long-Evans, Wistar, and Sprague-Dawley lung geometries. This similarity can be exemplified by comparing the respiratory lower tract.

In 2008, Lee *et al.* [10] studied statistics of the branching pattern of six healthy male Sprague-Dawley rats. In their study, automated analyses of computed tomography (CT) images of silicon casts of rat airways are used. In 2012, Oakes *et al.* [11] studied statistics of the branching pattern of Wistar rat and compared their results with Raabe's data for Long-Evans rat and Lee's data for Sprague-Dawley rat [11]. Table 4 displays a comparison between the average values of diameters, lengths, bifurcation angles, and angles to the normal direction of gravity vs. generation obtained from Oakes, Raabe, and Lee studies, respectively. These comparisons show that Wistar rat airway diameters are slightly smaller than Long-Evans and Sprague-Dawley for distal generations (Figure 13A), while lengths are essentially identical (Figure 13B). In Table 4, we can see a general comparison between several parameters of these trees, i.e., angles of airways to gravity, rotation angles, branching angles, body weight, and lung volume. From Figure 13 and Table 4 we can note the similarity between airways trees of these three rat species. This similarity will allow us to use the Long-Evans geometrical model, while Wistar and Sprague rats are used for experiments.

Table 4: Compared lung geometry between Wistar, Long-Evans, and Sprague-Dawley rats modify from [11].

	Raabe 1976 [6]	Oakes 2012 [11]	Lee 2008 [10]
Species	Long-Evans	Wistar	Sprague Dawley
Diameter	Diameters measured in Long-Evans and Sprague-Dawley rats are very similar (see Figure 13). Wistar rat exhibit systematically smaller diameters.		
Length	Airway lengths in all three databases are very similar (see Figure 13).		
Branching Angle	19.3 ± 14.6° for the major airway in the Wistar rat, i.e., 36.7% larger than in the Long-Evans rat, 60.5 ± 19.4° for the minor airway in the Wistar rat, i.e., 4.6% smaller than in the Long-Evans rat		
Angles of airways to gravity	35°-85°	38°-83°	-
Rotation angles	-	24°-53°	20°-50°
Body Weight	330 g	268 g	302 g
Fraction of Total Lung Volume, %			
Right apical	10.4	11.0 ± 1.16	9.2
Right diaphragmatic	28.8	28.0 ± 1.02	31.8
Right intermediate	13.9	13.5 ± 0.36	13.3
Right cardiac	12.1	11.6 ± 0.51	12.5
Left lung	34.8	35.9 ± 1.3	33.3
Right lung (all lobes)	65.2	64.1 ± 1.3	66.8

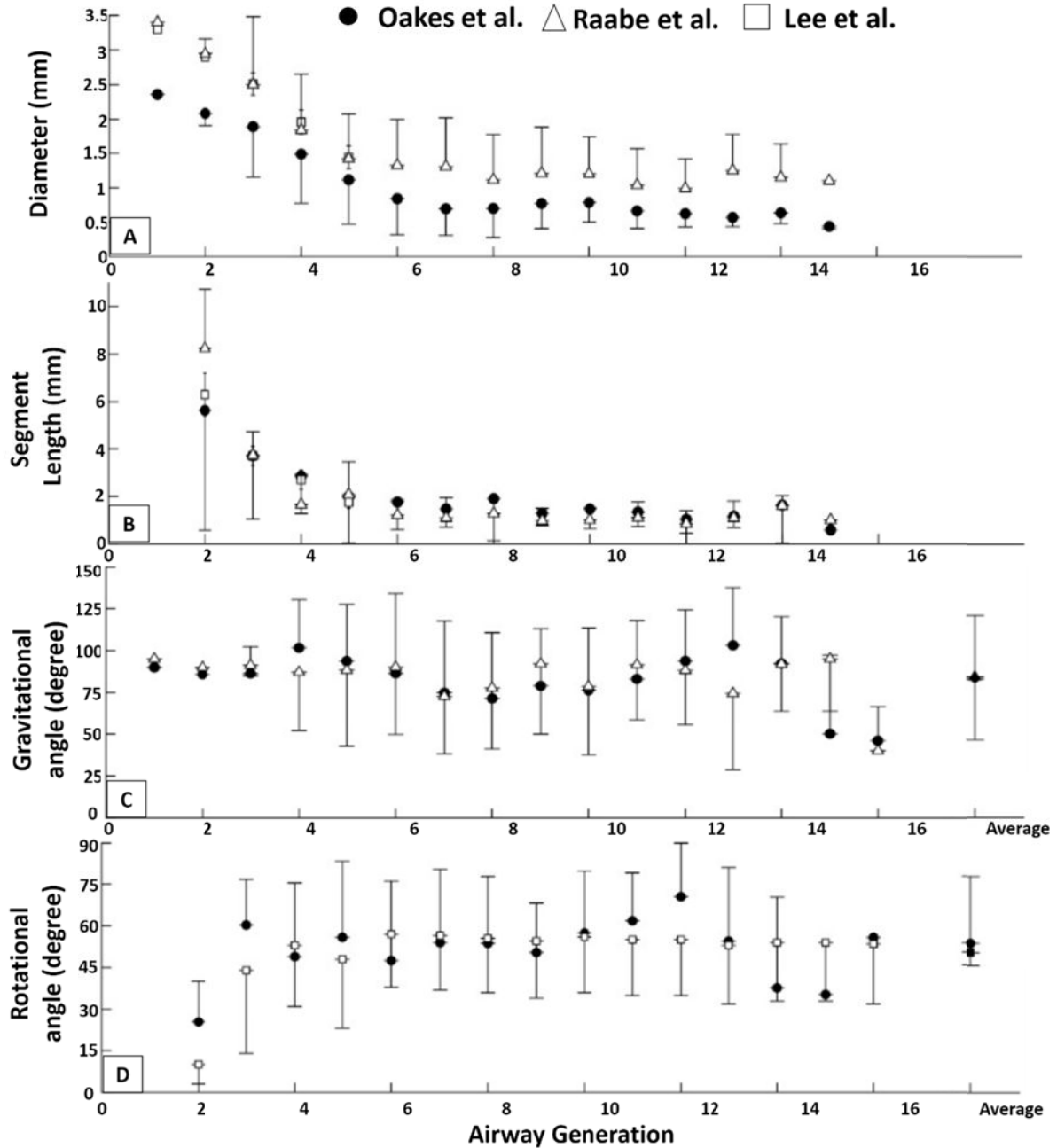


Figure 13: Comparison between measurements of Oakes et al. performed on Wistar rat [11], measurements of Raabe et al. performed on Long-Evans rat [6], and measurements of Lee et al. performed on Sprague-Dawley rat [10] from [11].

Our model of Long-Evans respiratory airway starts from the trachea with a 3.4 mm diameter, contains at most 31 generations along the longest path, and has 1457 terminal branches. Figure 14 shows our Long-Evans rat respiratory airway model in 4 different views. The color-coding represents the airway diameter. Figure 15 shows the same tree, but the color-coding now represents the airways generation number.

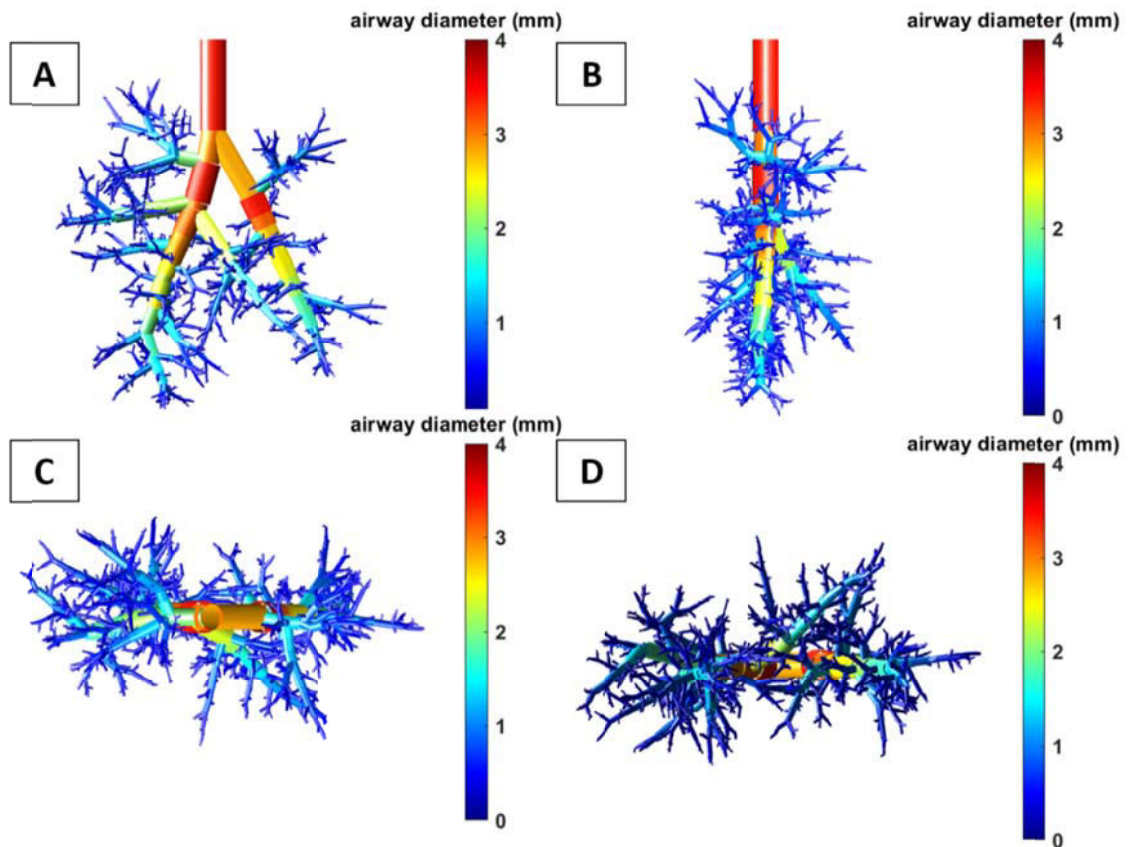


Figure 14: Example of a Long-Evans rat respiratory airway tree (31 generations). The color coding corresponds to the value of the diameter. A) Front view, B) Side view, C) Top view, and D) Bottom view.

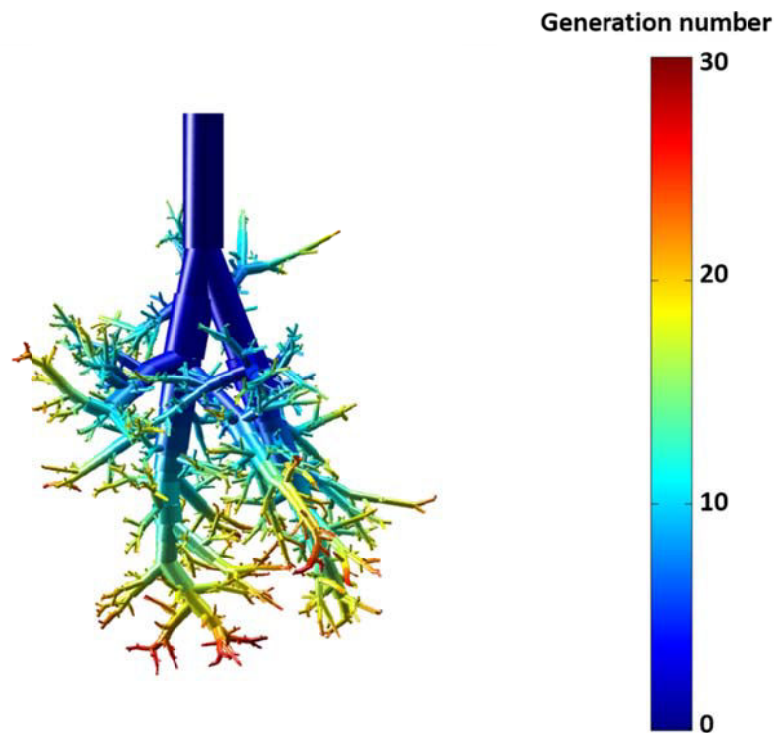


Figure 15: Long-Evans rat pulmonary airway tree. The tree is color-coded according to the generation number.

In the last decade, a number of researchers used casts, CT scans, and magnetic resonance (MR) scanner technique to image the rat pulmonary airways geometry. They used different techniques and these researches are done on different rat species, that makes it difficult to compare the results [11][117][118][16][119][14][120][121]. Authors in [118][16][119][14] [120] investigated airways of Sprague–Dawley, while [11][117] focused on the Wistar rats. Hyde, Einstein, Carson *et al.* worked on silicon cast and Counter, Jacob, Sera, and Barre *et al.* used contrast-enhanced micro-CT, while Oakes used magnetic resonance (MR) scanner. In Table 5, we can see details of recent research works on the morphology of rat conducting airways. Figure 16 displays the results of Barre *et al.* [121] that showed the similarity of the structure of the conducting airways at days 4, 10, 21, 36, and 60 of a Wistar rat in different individuals. The gray color represents the walls of the conducting airways. The colored spheres represent the entrances of the acini. According to their conclusion, the bronchial tree is formed; it stays very constant during lung development as we can see in Figure 16. Figure 17 displays images of the respiratory system for six different rat lungs (see Table 5 for more details). Although none of these six figures show the same picture and each airway tree has a unique shape, we can see the similarity in the monopodial structure and similar trends of branching of rat lung, especially in stem branches.

Table 5: Recent research on the morphology of rat conducting airways

Researcher	Year	Rat species	Method
Sera <i>et al.</i> [117]	2003	Wistar	micro-CT
Hyde <i>et al.</i> [118]	2006	Sprague–Dawley	Cast
Einstein <i>et al.</i> [16]	2008	Sprague–Dawley	Cast
Carson <i>et al.</i> [119]	2010	Sprague–Dawley	Cast
Oakes <i>et al.</i> [11]	2012	Wistar	MR
Counter <i>et al.</i> [14]	2013	Sprague–Dawley	micro-CT
Jacob <i>et al.</i> [120]	2014	Sprague–Dawley	micro-CT
Barre <i>et al.</i> [121]	2016	Wistar	micro-CT

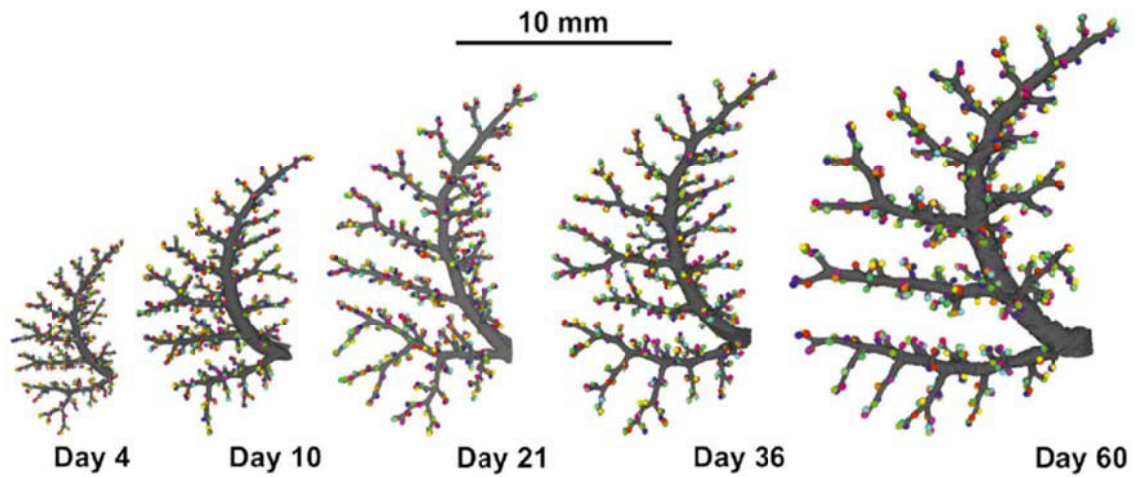


Figure 16: Development of the bronchial tree of the respiratory system of the rat lung at days 4, 10, 21, 36, and 60 [121]. The gray color represents the walls of the conducting airways. The colored spheres represent the entrances of the acini.

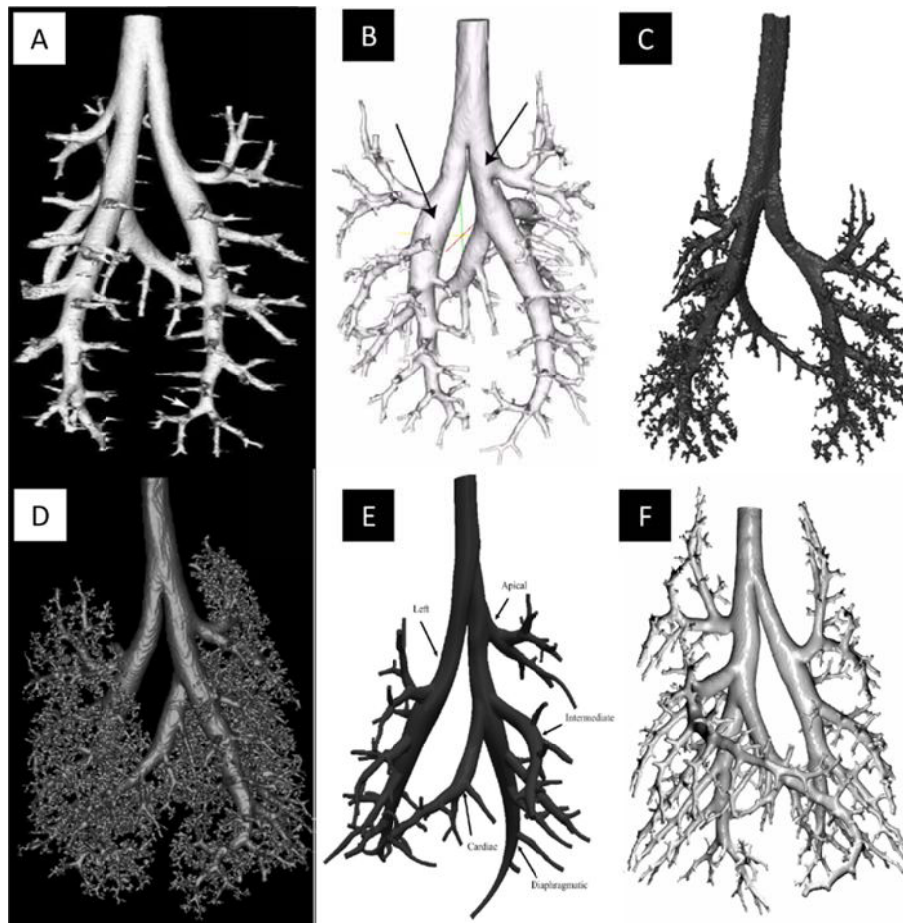


Figure 17: Bronchial trees of the respiratory airway system of rats. A) Sera et al. [117], B) Einstein et al. [16] C) Counter et al. [14] D) Carson et al. [119] E) Oakes et al. [11] F) Jacob et al. [120].

2.1.2 Model of the pig lung

The geometrical model used in the current study to simulate pig lungs is an asymmetric model obtained from morphometric measurements performed by Md. Azad *et al.* [15]. The authors imaged the lungs of six pigs (weight ~40 kg) and used segmentation software tools to extract the geometry of the airway lumen. Airway dimensions were measured for the first 24 airway generations. They showed that the sizes of the airways in the six pigs were similar and that the tracheal diameters are comparable to the typical human adult. However, the diameter, length, and branching angles of other airways are noticeably different from what we can measure in the human lung.

According to this study, the main difference between the pig and human lung respiratory airway systems is the early branching existing in the pig trachea. This branching feeds the top right lung lobe and precedes the main carina. This does not exist in the human respiratory tract. Now a question remains: can the pig airway system be the right candidate for approximating the human airway system and providing an animal model to SRT?

In Table 6, we present statistics from Azad *et al.* [15]. These data are the average airway length per generation and the diameter ratio. Authors showed that two different types of bifurcations coexist in the pig: in-plane and out-of-plane. “In-plane” refers to a bifurcation where the parent branch and the two daughter branches belong to the same plane. “Out-of-plane” refers to a bifurcation where only the parent branch and the major daughter belong to the same plane, the minor daughter being almost perpendicular to this plane [15] (see Figure 18). For some generations, both in-plane and out-of-plane diameter ratios are available. For some others, only one of them is available. Table 6 presents the length (L), the major and minor daughter/parent diameter ratios (d_1/D and d_2/D).

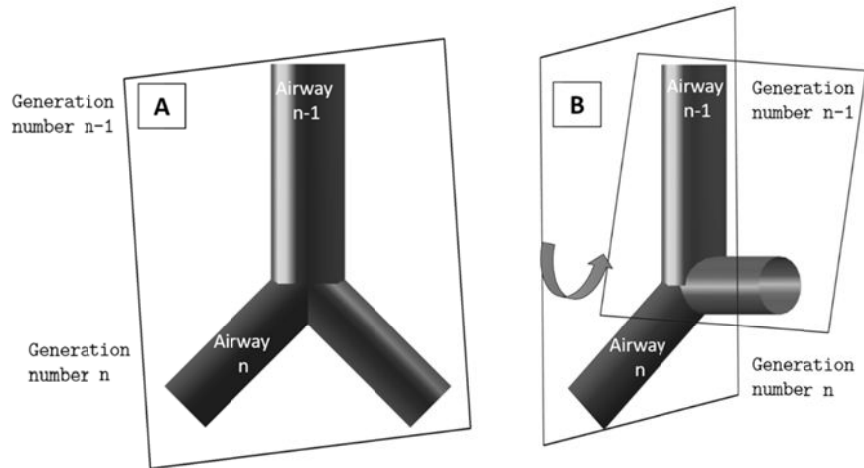


Figure 18: Schematic of an A) in-plane and B) out-of-plane bifurcation.

Table 7 shows the values of the average branching angle and the rotation angle between successive bifurcation planes. In the published data, only the average branching angles per generation are given. However, it is important to have the exact value of the angle of branching, at each generation, for the two main stem bronchi. We used the 2D image of (Figure 1B) the reference [15] to measure the branching angles between the parent branch and the main daughter along the main stem bronchi for all generations. This measurement is performed automatically¹ (Table 8).

¹ With help of klonk image measurement software

Table 6: Airway lengths (cm) and diameter ratios (Md. Azad [15]).

Generation number	L (cm)	d_1/D	Plane	d_2/D	Plane
1	2.95	0.74	Out-of-Plane		Out-of-Plane
			In-Plane	0.73	In-Plane
2	1.04	0.85	Out-of-Plane		Out-of-Plane
			In-Plane	0.44	In-Plane
3	1.71	0.85	Out-of-Plane		Out-of-Plane
			In-Plane	0.59	In-Plane
4	0.638	0.88	Out-of-Plane		Out-of-Plane
			In-Plane	0.26	In-Plane
5	0.694	0.88	Out-of-Plane	0.35	Out-of-Plane
			In-Plane	0.56	In-Plane
6	1.04		Out-of-Plane	0.29	Out-of-Plane
		0.89	In-Plane		In-Plane
7	0.701	0.74	Out-of-Plane	0.25	Out-of-Plane
			In-Plane	0.52	In-Plane
8	0.770	0.85	Out-of-Plane	0.18	Out-of-Plane
			In-Plane	0.49	In-Plane
9	0.404	0.95	Out-of-Plane	0.24	Out-of-Plane
			In-Plane		In-Plane
10	0.813	0.87	Out-of-Plane	0.35	Out-of-Plane
			In-Plane		In-Plane
11	0.703	0.94	Out-of-Plane		Out-of-Plane
			In-Plane	0.55	In-Plane
12	0.604		Out-of-Plane	0.65	Out-of-Plane
		0.78	In-Plane	0.57	In-Plane
13	0.730	0.78	Out-of-Plane		Out-of-Plane
			In-Plane	0.59	In-Plane
14	1.279	0.79	Out-of-Plane	0.32	Out-of-Plane
			In-Plane		In-Plane
15	0.711	0.94	Out-of-Plane		Out-of-Plane
			In-Plane	0.47	In-Plane
16	0.614		Out-of-Plane	0.51	Out-of-Plane
		0.85	In-Plane		In-Plane
17	0.767	0.88	Out-of-Plane		Out-of-Plane
			In-Plane	0.44	In-Plane
18	0.504	0.74	Out-of-Plane	0.43	Out-of-Plane
			In-Plane	0.57	In-Plane
19	0.601		Out-of-Plane	0.55	Out-of-Plane
		0.7	In-Plane		In-Plane
20	0.761	0.72	Out-of-Plane	0.47	Out-of-Plane
			In-Plane	0.57	In-Plane
21	0.990	0.89	Out-of-Plane		Out-of-Plane
		0.6	In-Plane	0.64	In-Plane

Table 7: Branching angles and bifurcation plane angles. By default, all data are taken from Md. Azad [15], pig #3, figure 2 C, D and figure 4 A, B. When data were not available for pig #3, other pig data were used. Red color refers to the lack of data for pig #3 and the green bracket refers to the pig number.

Generations number	Branching angle (degree) θ_1	Plane	Branching angle (degree) θ_2	Plane	Bifurcation plane (degree) Left, ψ_1	Bifurcation plane (degree) Right, ψ_2
1	33	In-Plane	53	In-Plane	-55	-54
2	10 (1)	In-Plane	64	Out-of-Plane	9	9
3	18 (1)	In-Plane	59	Out-of-Plane	3	3
4	10	In-Plane	44	Out-of-Plane	-89	91
5	14	In-Plane	59	Out-of-Plane	-5	-86
6	10	In-Plane	55	Out-of-Plane	-81	-7
7	4.8	In-Plane	59	Out-of-Plane	85	-89
8	4.6	In-Plane	44	Out-of-Plane	-10	81
9	14.7	In-Plane	48	Out-of-Plane	83	5
10	9.7	In-Plane	50	Out-of-Plane	-1	-80
11	14.8	In-Plane	39	Out-of-Plane	-1	80
12	10	In-Plane	33	Out-of-Plane	-89	5
13	15 (4)	In-Plane	79 (1)	Out-of-Plane	-5 (1)	-77 (1)
14	10	In-Plane	48	Out-of-Plane	9	-89
15	4.7	In-Plane	45	Out-of-Plane	78	81
16	19.45	In-Plane	40	Out-of-Plane	1	5
17	19.68 (1)	In-Plane	53	Out-of-Plane	0	-50 (2)
18	9.8 (1)	In-Plane	48	Out-of-Plane	-90	0
19	9.38	In-Plane	43	Out-of-Plane	0	-90
20	14	In-Plane	48 (1)	Out-of-Plane	0	90
21	14.6 (2)	In-Plane	53	Out-of-Plane	90	0

Table 8: Branching angles for daughter one (θ_1) for main stem bronchi.

Generation number	Branching angle (degree) θ_1
1	25
2	10
3	7
4	6
5	6
6	5
7	3
8-10	2
11-21	1

Figure 19 displays statistics of the pig lung such as the number of branches at each generation, as well as the average diameters and lengths.

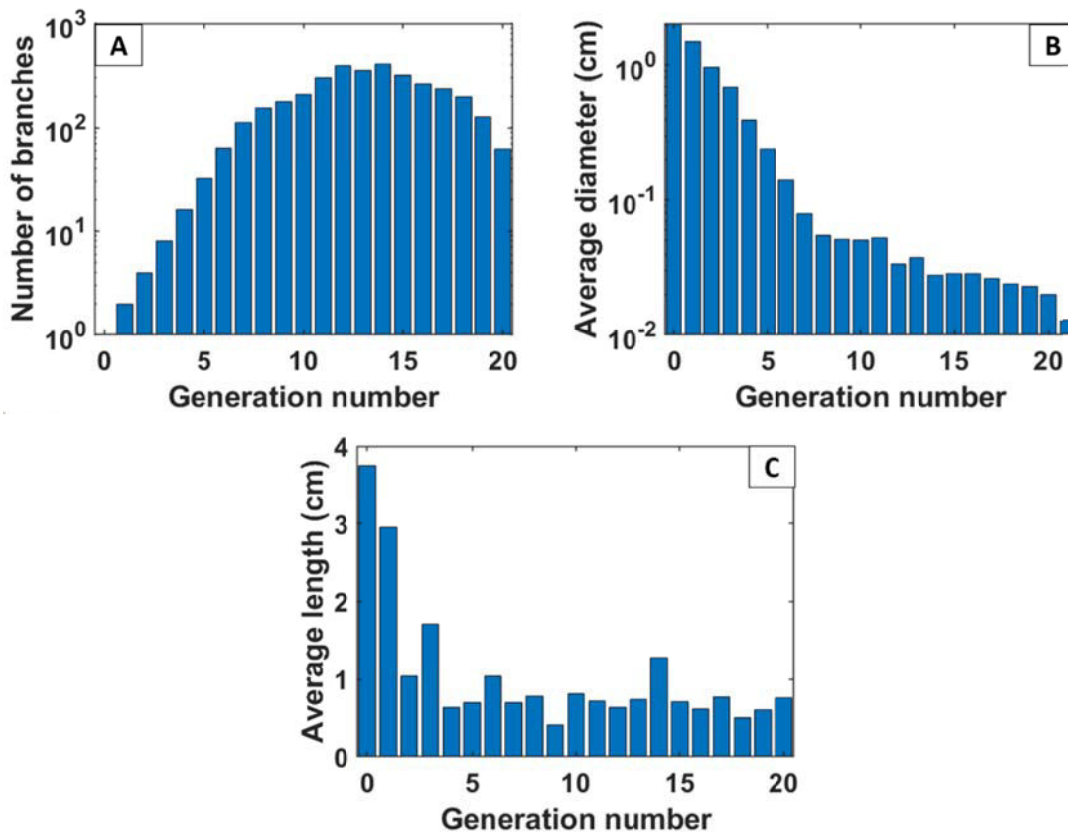


Figure 19: Statistics of the geometry of the pig lung model based on Azad *et al.* data [15]. A) The number of branches vs. generation. B) Average diameters vs. generation. C) Average length vs. generation.

To visualize in three dimensions the pig airway system, we plotted the geometry based on Azad *et al.* published data. Figure 20 is a front view of the generated airway tree containing 22 generations. The tracheal diameter is 20.3 mm and the diameters of all terminal bronchioles are 0.26 mm [122]. Figure 21 shows the same tree as in Figure 20, but the color-coding of the tree now represents the airway generation number. In 10 first generations, the major daughter direction is close to the parent direction and the minor daughters have a large angle to the parent direction, which leads to the current monopodial structure of the pig lung.

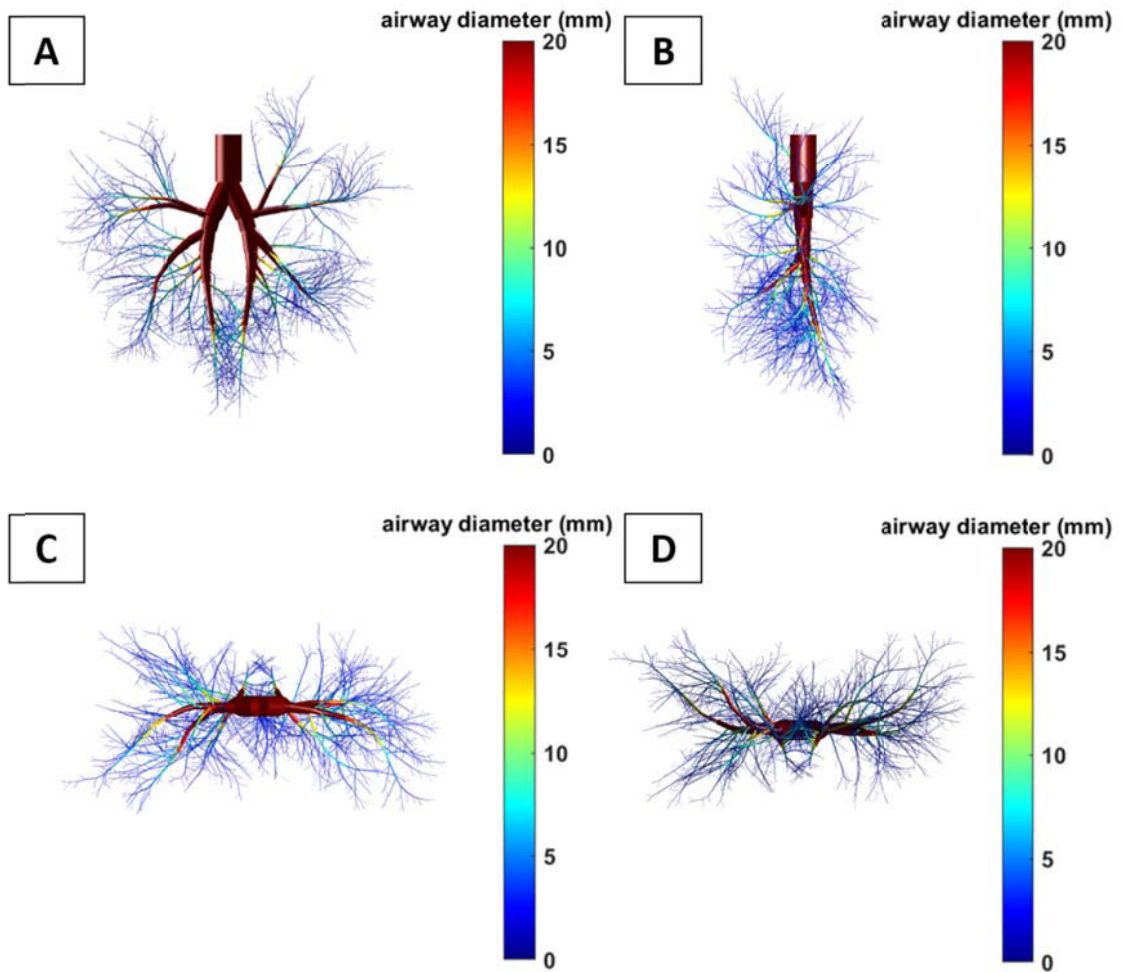


Figure 20: Example of a pig pulmonary airway tree (22 generations) based on Azad *et al.* [15]. The color-coding represents the diameter value. A) Front view, B) Side view, C) Top view, and D) Bottom view.

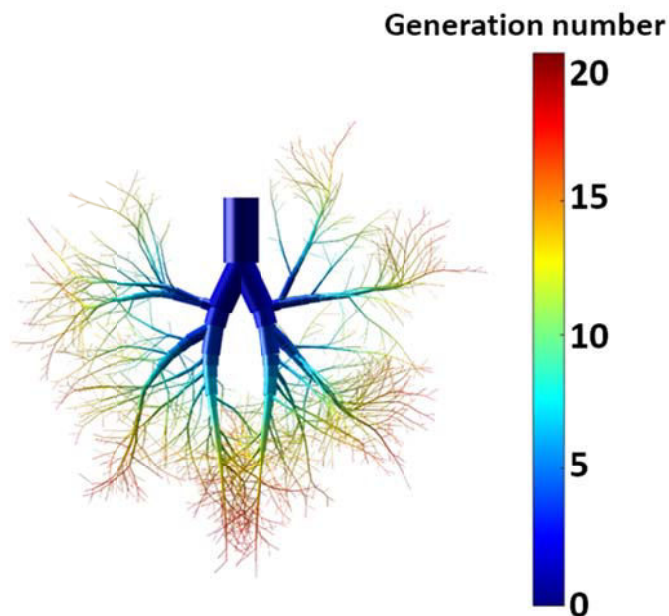


Figure 21: Example of a pig pulmonary airway tree (22 generations) based on Azad *et al.* [15]. The color-coding represents the generation number.

In the last 20 years, a number of researchers imaged and measured the monopodial structure of pig pulmonary system [15][24][123][26][124]. Authors used different techniques to reconstruct the shape of the pig lung such as cast, CT scan, and acoustic techniques (see Table 9).

Table 9: Recent research on the morphology of pig conducting airways

Researcher	Year	Method	Weight (kg)
Maina <i>et al.</i> [24]	2001	Cast	155
Monteiro <i>et al.</i> [123]	2014	Cast	30
Judge <i>et al.</i> [26]	2014	Photograph	105
Asgharian <i>et al.</i> [124]	2016	CT scan	27
Azad <i>et al.</i> [15]	2016	CT scan	40

Figure 22 displays a schematic and a dorsal photo of pig lungs by Monteiro *et al.* [123] and Judge *et al.* [26], respectively. The schematic (A) depicts the trachea (cranial lobar), the main bronchi (right and left), lateral (l1, l2, l3, l4, l5), dorsal (d1, d2, d3, d4), ventral (v1, v2, v3, v4, v5), and medial (m1, m2). The photo (B) includes the trachea (a), the carina (b), the left lung (c), the right lung (d), and the cranial lobe bronchus (e) of a 105 kg pig. In both pictures, we can see an early-branching from the trachea that feeds the top right lung lobe and precedes the main carina, called “tracheal bronchus.” In human and rat lungs, we do not observe these early branches.

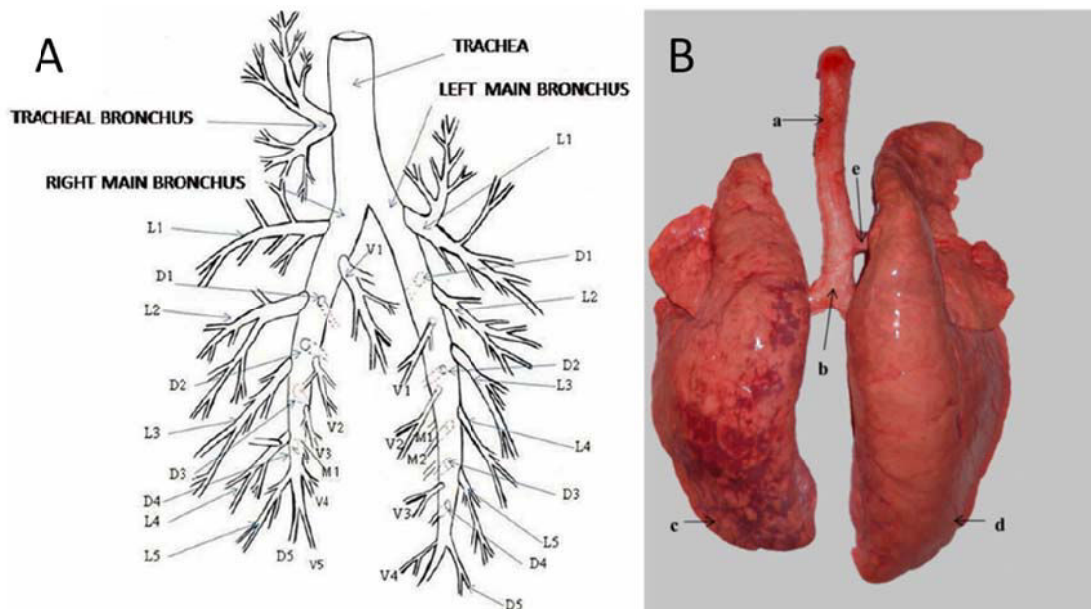


Figure 22: A) Schematic and nomenclature of the pig bronchial tree (Monteiro *et al.* [123]). B) Photograph (dorsal aspect) of a 105 kg pig (trachea (a), carina (b), left lung (c), right lung (d), and cranial lobe bronchus (e)) (Judge *et al.* [26])

To check the accuracy of our model of pig conducting airways based on Azad *et al.* morphology results [15], we displayed 4 different pig airways pictures in Figure 23. Although none of these pictures show the exact same branching angles, we can observe the similarity in branching, sizes, and early cranial lobe bronchus.

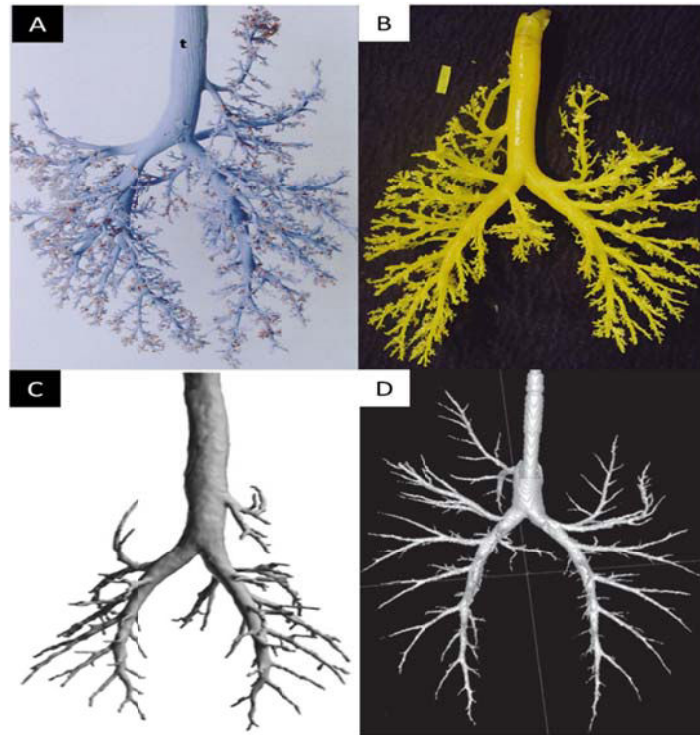


Figure 23: Pig conducting airways. A) Maina *et al.* [24] B) Monteiro *et al.* [123] C) Asgharian *et al.* [124] D) Azad *et al.* [15].

2.1.3 Model of the human lung

In 1985, Phalen *et al.* used a replica cast of the morphometric measurements of human lungs [125] to measure lengths and diameters of the airways. From the extracted data they formulated an equation to compute the lengths and diameters from the trachea until generation 15 based on body height. However, they did not measure the branching and rotation angles.

In 2008, Menache *et al.* used data from Utah biomedical test laboratory lung cast [126] to determine lengths, diameters, branching, and gravity angles for subjects ranging from a 3-month baby to 21-year old. Based on these cast measurements, they computed the average value of each generation. By providing one value per generation, Menache's data build a model that is intrinsically symmetric. Another symmetric model is the famous Weibel's 'C' model [9]. In our work, three geometrical models of the tracheobronchial tree are used. The first and most simplified symmetric model is

Weibel's C model [9], the second model is an asymmetrized version of Weibel's airway tree, and the third model is an asymmetric model based of Raabe's measurements [6].

2.1.3.1 Symmetric airways tree (Weibel's model)

The Weibel's symmetric model has symmetric branching at each bifurcation. The two daughter airways have equal diameter and length, and branch symmetrically on both sides of the parent airway with equal and opposite rotation angles. In our model, the branching angle 2θ is 90° , while the rotation angles are always equal to 90° (Figure 24). All airways belonging to the same generation have therefore the same diameter which is indexed by the generation number n , called D_n . The diameter ratio between successive generations remains constant throughout the tree, $D_{n+1}/D_n = h_0 = 2^{-1/3} \approx 0.79$ following Murray-Hess law [127][128]. The airway tree is therefore *scale-invariant* and satisfies: $D_n = D_0 \cdot 2^{-n/3}$ [5]. The same property holds for the airway lengths, all airways having a similar aspect ratio: $L_n = 3D_n$. (see Figure 24)

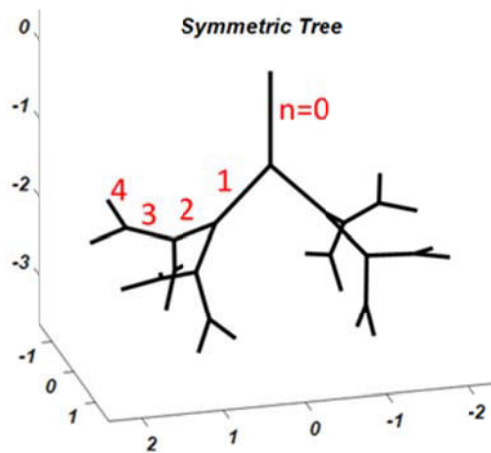


Figure 24: Symmetric model of the human pulmonary airway tree, four generations plus trachea.

In Figure 25, the number of branches, average diameter, and average length in each generation is reported for a total of 15 generations. The symmetric airway tree stems from the trachea ($n=0$), which means that the tracheal diameter is now the sole parameter entirely controlling the size of the tree [129] (see Figure 26). Figure 27 shows the same tree as in Figure 26, but the color-coding represents the airways generation number.

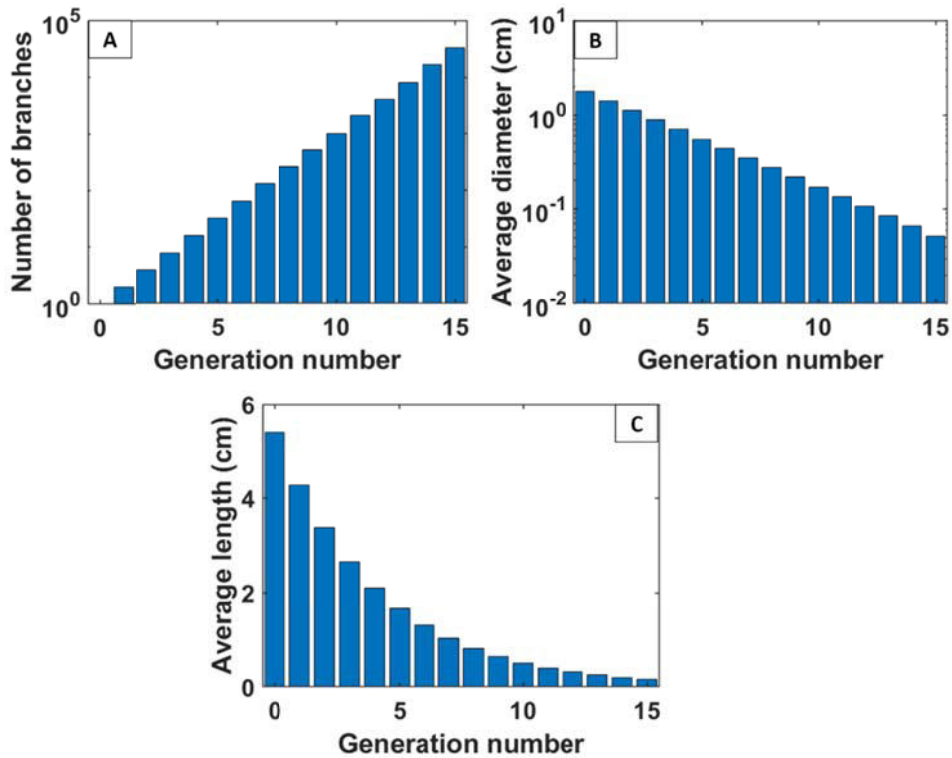


Figure 25: Statistics of the human lung model based on the Weibel symmetric model. A) The number of branches vs. generation. B) Average diameter vs. generation. C) Average length vs. generation.

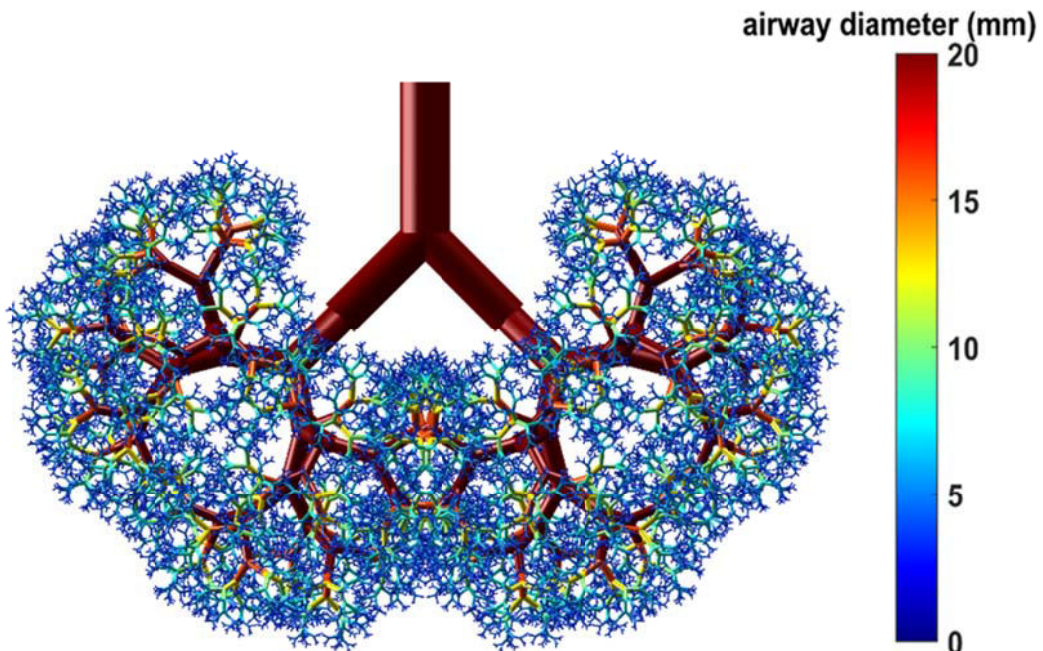


Figure 26: Symmetric human pulmonary airway tree based on Weibel's symmetric model [9]. The color coding represents the diameter value.

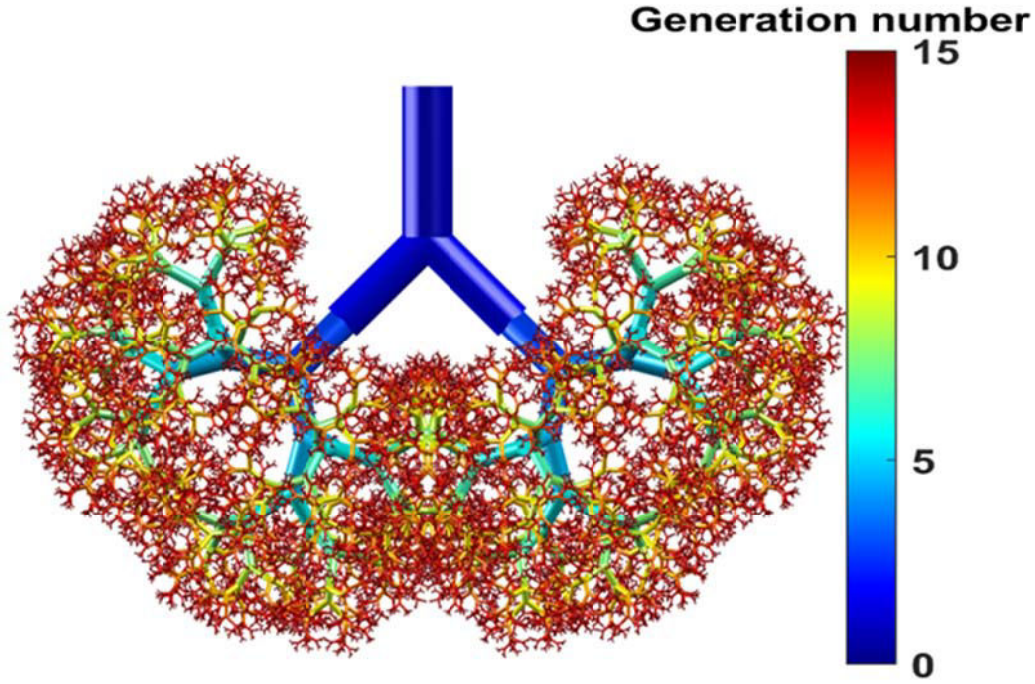


Figure 27: Symmetric human pulmonary airway tree with 15 generations. The color coding represents the diameter value.

2.1.3.2 Weibel-based asymmetric airway tree

In this first model of our asymmetric airway tree, the branching and rotation angles are identical to the Weibel's symmetric model, but the two daughter airways always exhibit different diameters and lengths, determined by two different diameter ratios $h_1 = D_{\text{daughter1}}/D_{\text{parent}}$ and $h_2 = D_{\text{daughter2}}/D_{\text{parent}}$ at each bifurcation. We assume that the diameters at each bifurcation follow the Murray-Hess law [127][128], i.e., $D_{\text{parent}}^3 = D_{\text{daughter1}}^3 + D_{\text{daughter2}}^3$. Even in the asymmetric case, the sizes of the conducting airways abide by the Hess-Murray law, as it was measured on a plastic cast of a human airway tree [130][131]. This implies that $h_1^3 + h_2^3 = 1$. It is therefore convenient to define these two ratios with one asymmetry parameter ε such that

$$h_1 = h_0(1+\varepsilon)^{1/3}, \quad h_2 = h_0(1-\varepsilon)^{1/3} \quad \text{with} \quad h_0 = 2^{-1/3} \quad (2.1)$$

In this asymmetric model, the airway tree is entirely determined by the trachea diameter D_0 and the asymmetry parameter ε . The default values for these parameters are 1.8 cm and 0.2, respectively. Figure 28 displays a 3D view of this asymmetric model of the human pulmonary airway tree, the color-coding representing the diameter values.

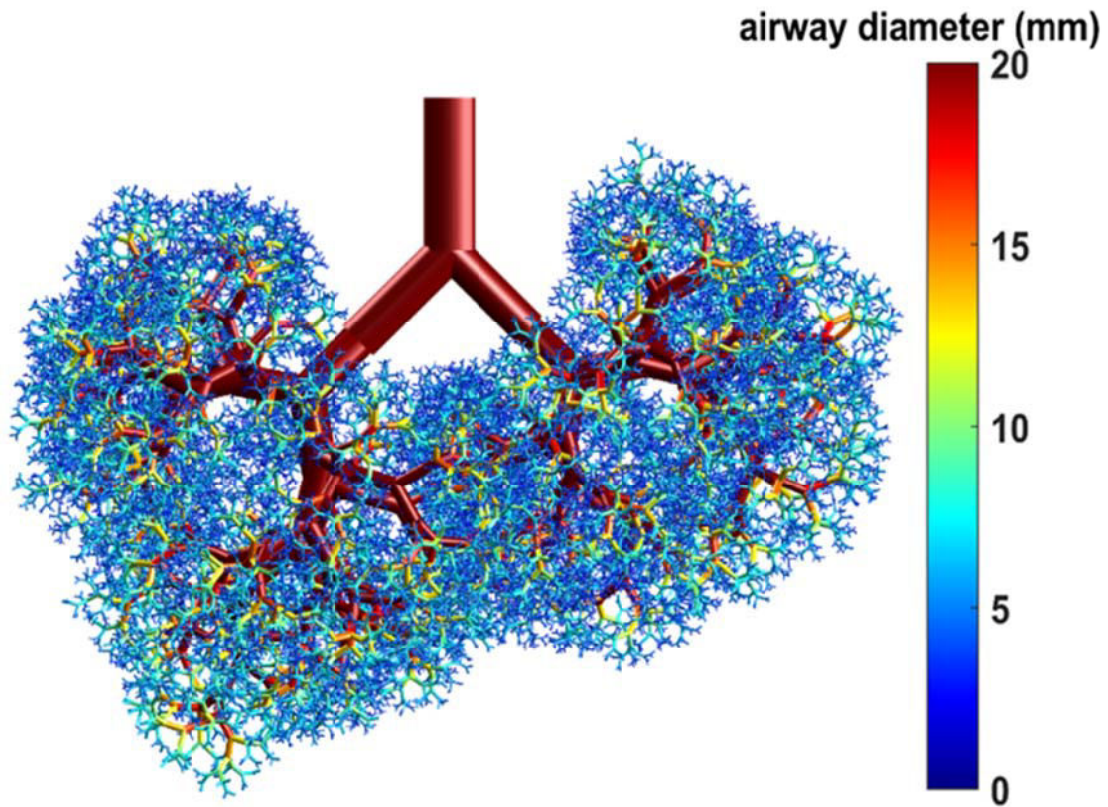


Figure 28: Asymmetric model of the human pulmonary airway tree. The color coding represents the diameter value.

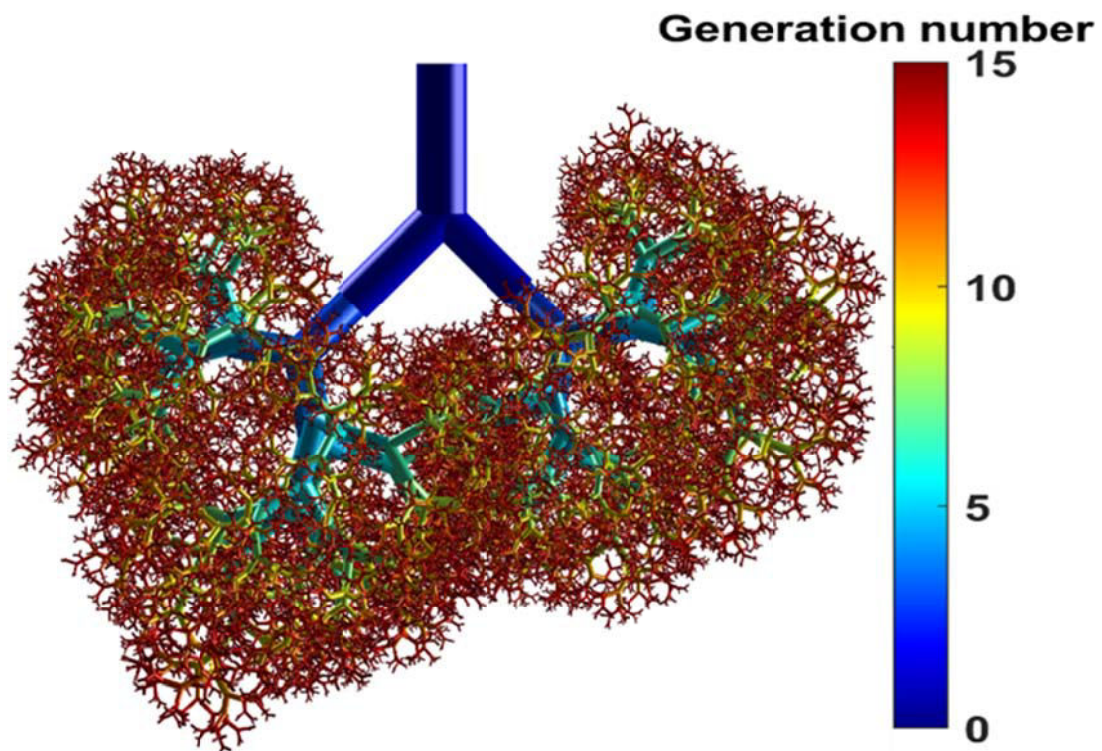


Figure 29: Asymmetric model of the human pulmonary airway tree with a maximum of 15 generations. The color-coding represents the Generation number.

2.1.3.3 Raabe-based asymmetric airways tree

In 1976, Raabe *et al.* prepared replica casts of human lungs [6]. The authors elaborated on an asymmetric model (Figure 30) using input measured parameters including the parent and daughter segment lengths, diameters, branching angles, and angles to the direction of gravity from the trachea down to end, including the terminal bronchioles. These morphometric measurements were performed on flexible silicone rubber replica casts at a volume corresponding to end inspiration.

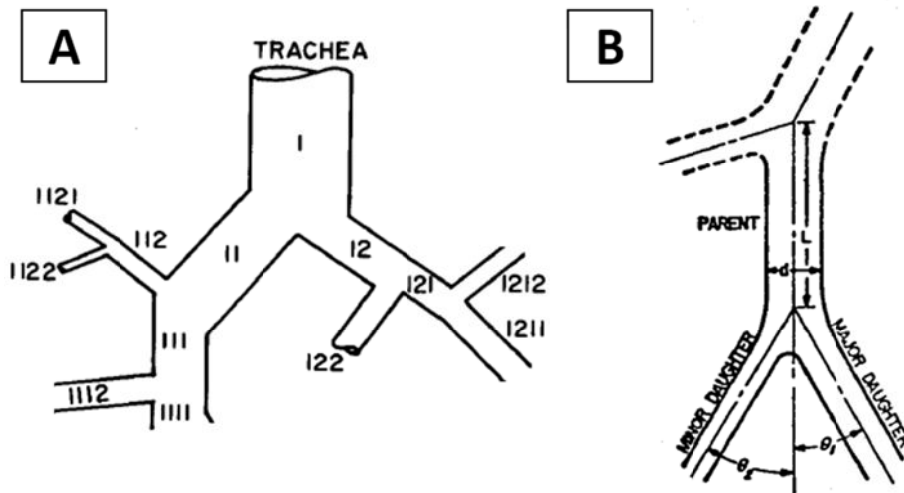


Figure 30: A) Raabe's lung airways tree, first three generations plus trachea. B) The asymmetric model of tracheobronchial bifurcation [6].

Figure 31 displays statistics of the number of branches, average diameters, lengths, and the number of terminals at each generation.

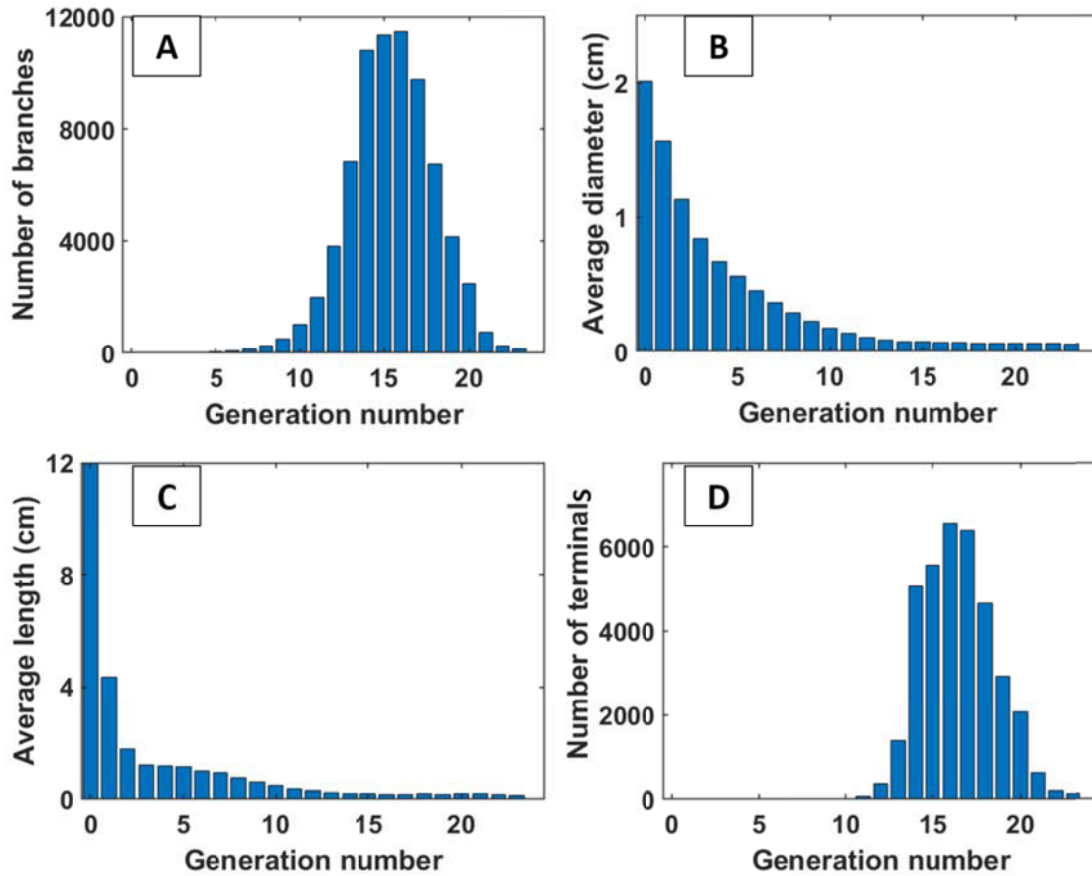


Figure 31: Statistics of Raabe's human lung model [6]. A) The number of branches vs. generation. B) Average diameter vs. generation. C) Average length vs. generation. D) The number of terminals vs. generation.

The Raabe's human asymmetric tree used in our simulations starts from a trachea with a 20 mm diameter, contains at most 22 generations along the longest path, and has 36,043 terminal branches. Figure 32 shows our lung model based on Raabe's data in the front view. The color-coding represents airway diameter. Figure 33 displays the same tree, but the color-coded tree now represents the generation number.

Table 10 describes the techniques used in works for studying the morphology of the human conducting airways. Figure 34 represents the results of these studies.

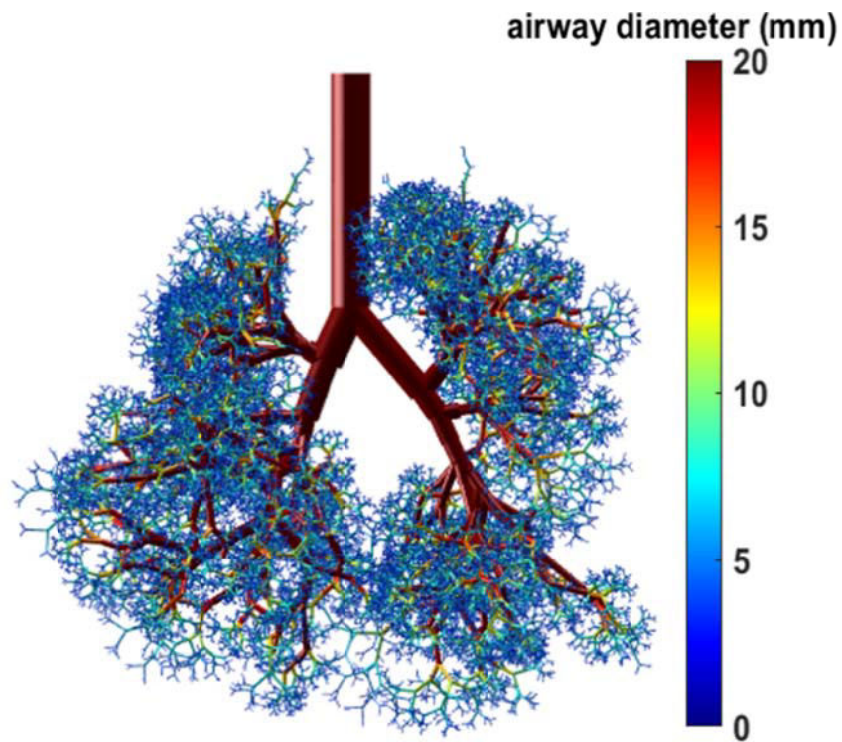


Figure 32: Raabe-based lung airway tree. The color coding corresponds to the value of the diameter.

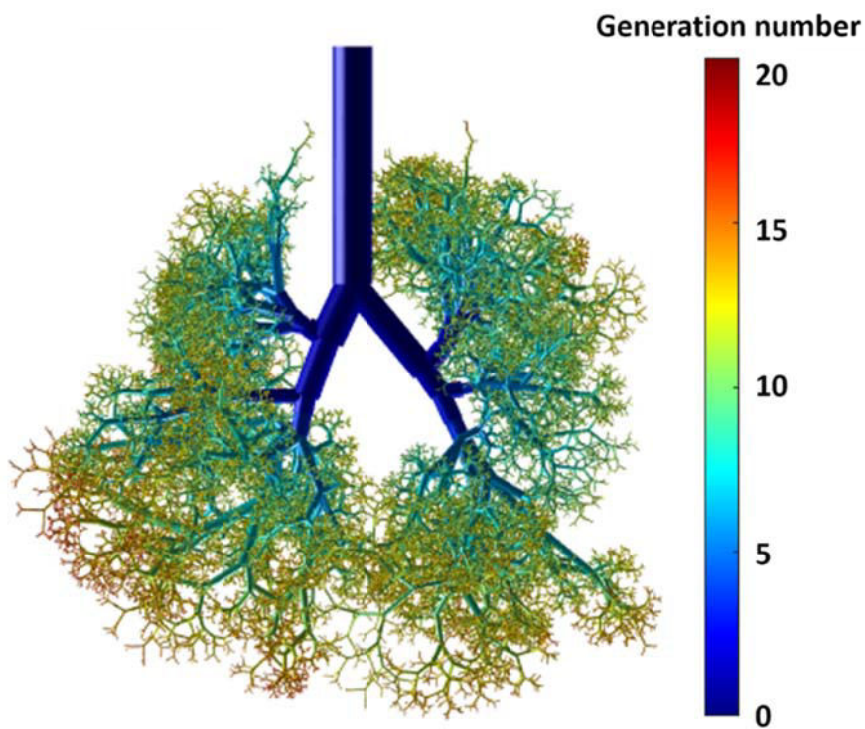


Figure 33: Raabe-based lung airway tree. The color-coding tree representing the generation number.

Table 10: Research on the morphology of human conducting airways

Researcher	Year	Method
Phalen et al. [125]	1985	Cast
Schmidt et al. [132]	2004	computer tomography
Tawhai et al. [133]	2004	computer tomography
Monteiro at al. [123]	2014	Cast

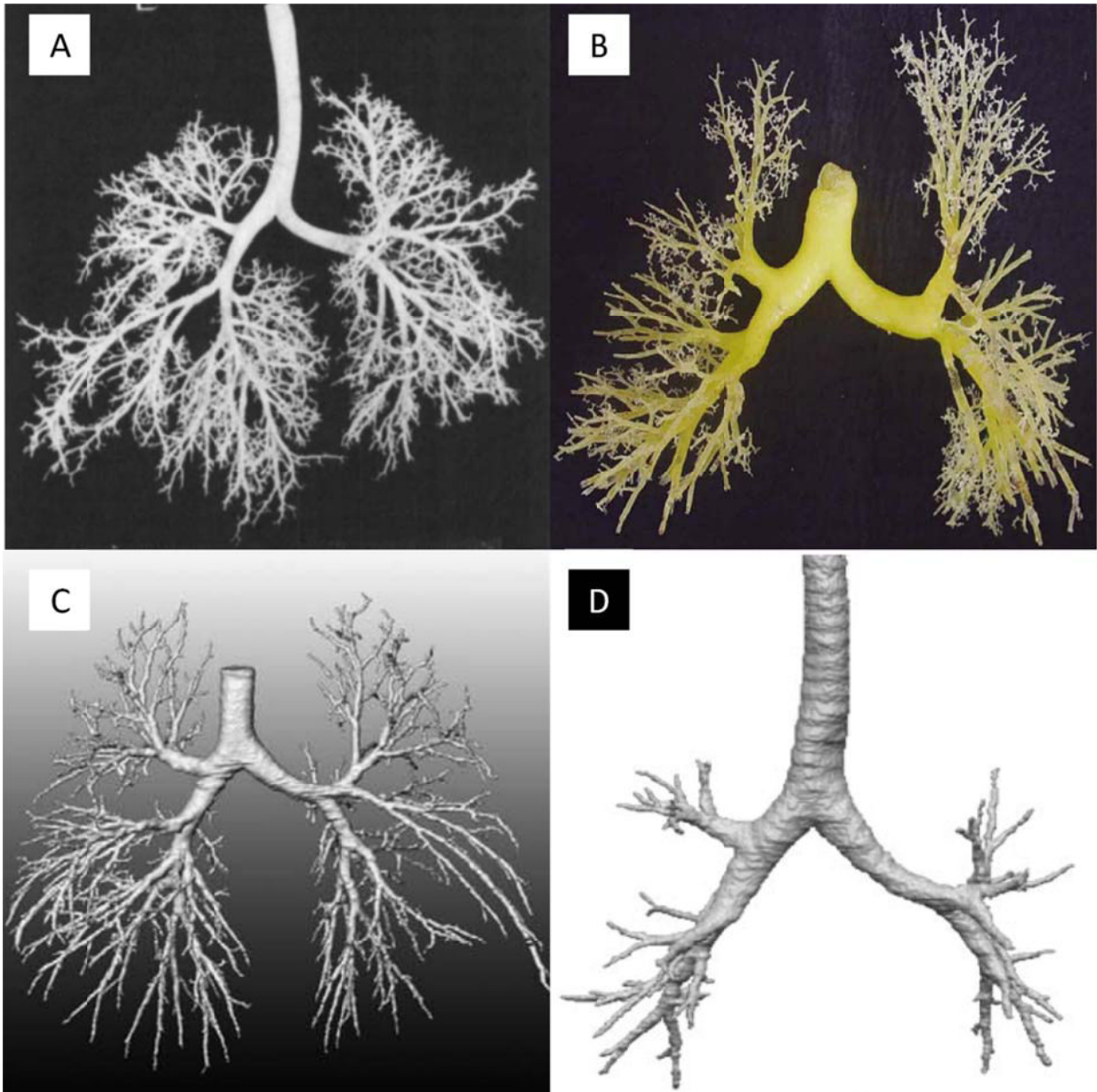


Figure 34: Human airways image and cast. A) Phalen *et al.* [125] B) Monteiro at al. [123] C) Schmidt *et al.* [132] D) Tawhai *et al.* [133]

In conclusion, in this chapter, we presented models of rat, pig, and human lower respiratory tract. The aim of this work is to create accurate models for investigating the propagation of liquid in SRT. To model the human lung, we first started using geometrical data based on Phalen *et al.* [125] and Menache *et al.* [126]. The Phalen-based model does not contain any branching angle or gravity angle. On the contrary, the Menache-based model is interesting because it provides data for lengths, diameters, branching, and gravity angles for a wide range of ages. Both Phalen-based and Menache-based models of the airway tree are symmetric because the published data are averaged for each generation. To model a human symmetric airway tree, we finally opted for the well-known Weibel symmetric tree because it provides a mathematical formula for computing the lengths and diameters, and is easy to work with. In a second step, we developed an asymmetric model based on Weibel symmetric model and Raabe published data. In the following chapter, we now turn to the propagation of a liquid plug into our geometrical model. We describe the mathematical and numerical model of surfactant delivery and compare it with two experiments.

Mathematical & numerical model of surfactant delivery

In the previous chapter, we have presented models of rat, pig, and human lower respiratory airway systems. In this chapter, we will introduce the mathematical models that will allow us to set up the numerical simulations of liquid plug propagation into these airway systems. First, we describe the propagation of a liquid plug into a single branch and the coating mechanism that goes with it. Then we derive equations for the splitting of this plug at a bifurcation. In this model, surfactant delivery is entirely determined by the geometry of the airway tree, the surfactant properties, and the instillation conditions. To characterize the overall performance of the delivery inside the entire airway tree, we define two dimensionless quantities, namely the *efficiency* and the *homogeneity* indices. These indices allow us to compare the results of our surfactant delivery model with actual experimental data.

3.1 Modeling of propagation of the liquid plug into the airway tree

In SRT, a surfactant mixture is instilled at the trachea. Very rapidly, a liquid plug forms, travels, splits, and distributes along the branches of the pulmonary airway system towards the acinar region. The efficacy of SRT depends crucially on delivering the right amount of surfactant to targeted regions of the lung. Consequently, understanding how the liquid plug splits at airway bifurcations and distributes throughout the airway system is key to improve SRT. Many parameters influence the final distribution of liquid in the lung:

- The physical properties of the liquid: viscosity, density, and surface tension at the air-liquid interface [134].
- The delivery conditions: initial instilled dose volume or plug size [135], flow rate or propagation speed [103], patient position, gravitational orientation [79], instillation method [102], redosing, and presence of other plugs in nearby airways from previous instillations [78]
- The patient morphology: airway geometry, lengths, diameters, and angles.

The dynamics of propagation of a liquid plug in the airway tree structure is complicated. However, we can simplify this propagation by decomposing it according to two separate fundamental steps. The first step is the propagation of a plug along an individual airway, accompanied by the deposition of a trailing film onto the airway walls (the coating layer). The second step is the splitting of a plug at one bifurcation of the pulmonary airway tree. We now examine these two fundamental mechanisms and derive mathematical equations to describing them.

3.1.1 The coating layer

Let us consider a plug of volume V_0 entering an airway. During its journey towards the end of the airway, this plug loses part of its mass (or volume) by depositing a fraction of it on the airway walls. Let us call V_1 the volume of liquid that reaches the end of the airway, i.e., the next bifurcation. The difference between V_0 and V_1 is called the *coating volume* V_C (see Figure 35):

$$V_1 = V_0 - V_C \quad (3.1)$$

Numerical studies [81] have shown that the thickness (h) of the coated layer left behind the plug essentially depends on the average velocity of the fluid at the rear meniscus (U_p) through the capillary number:

$$H = \frac{h}{a} = 0.36 \left(1 - e^{-2Ca_P^{0.523}} \right) \quad (3.2)$$

where a is the airway radius, and Ca_p is the capillary number ($Ca = \mu U / \sigma$) that represents the ratio of viscous forces to surface tension force (μ : viscosity, U : velocity, σ : surface tension). Eq. (3.1) means that the volume V_1 that is finally delivered to the daughter airways is deduced from V_0 (the volume of the plug initially entering the parent airway) through:

$$V_1 = V_0 - \pi \left[a_1^2 - (a_1 - h)^2 \right] L_a = V_0 - V_a \left[1 - \left(1 - \frac{h}{a_1} \right)^2 \right] \quad (3.3)$$

with the help of Eq. (3.2):

$$V_1 = V_0 - V_a \left[1 - \left(0.64 + 0.36 e^{-2Ca_p^{0.523}} \right)^2 \right] \quad (3.4)$$

L_a and V_a being the length and the volume of the parent airway, respectively. The velocity of the rear meniscus U_p which appears in the capillary number is related to the velocity U_1 of the front meniscus of the liquid plug, when it reaches the bifurcation, through conservation of the flow rate:

$$Q_1 = \pi a_1^2 U_1 = \pi (a_1 - h)^2 U_p, \quad U_1 = \left(1 - \frac{h}{a_1} \right)^2 U_p, \quad \text{and} \quad Ca_1 = \left(1 - \frac{h}{a_1} \right)^2 Ca_p \quad (3.5)$$

3.1.2 The splitting ratio

The second fundamental step in describing the propagation of liquid into the pulmonary airway tree is the splitting of a liquid plug when passing a bifurcation. This process is characterized by a quantity called the *splitting ratio*, R_s , defined as the ratio of the volume of liquid entering the upper daughter, V_2 , to the volume entering the lower daughter, V_3 (see Figure 35). A value of $R_s=1$ means that the plug splits equally while $R_s=0$ or $R_s=+\infty$ means that the entire plug flows down into one of the daughter's airways.

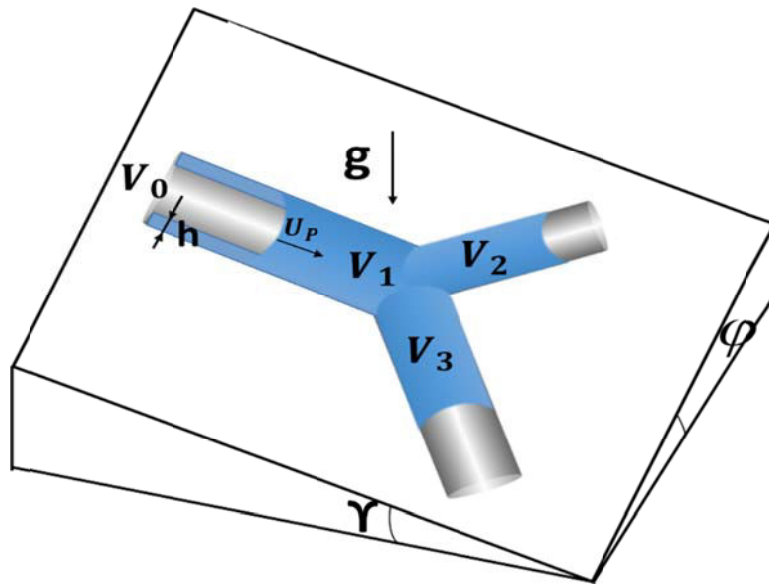


Figure 35: Splitting of a liquid plug across one single bifurcation: the spatial orientation of the bifurcation is characterized by two angles: the rolling angle (ϕ), and the pitch angle (γ). The roll angle and pitch angle describe the orientation of the bifurcation plates with respect to gravity. A plug of volume V_0 entering the parent branch leaves behind a trailing film of thickness h . The volumes entering the daughter branches are V_2 and V_3 such that $V_2 + V_3 < V_0$.

The splitting ratio is obtained by considering momentum conservation at the bifurcation, assuming that the downstream pressures in both daughter airways are equal. The pressure difference between the upstream pressure P_1 in the parent branch and the downstream pressures P_2 and P_3 in the daughter branches 2 and 3 are sums of several contributions (see Figure 36). These contributions are the pressures drop across front and back meniscus, and the pressure drops due to friction and gravity in the parent and daughter airways:

$$\begin{aligned} P_1 - P_2 &= (P_1 - \pi_1) + (\pi_1 - \pi_0) + (\pi_0 - \pi_2) + (\pi_2 - P_2) \\ P_1 - P_3 &= (P_1 - \pi_1) + (\pi_1 - \pi_0) + (\pi_0 - \pi_3) + (\pi_3 - P_3) \end{aligned} \quad (3.6)$$

where π_1, π_0, π_2 , and π_3 are the pressures inside the plug, right at the rear meniscus in parent tube, bifurcation point, upper daughter, and lower daughter, respectively. To solve these equations, we assess the pressure drops in 4 zones:

- 1- across the rear meniscus,
- 2- in the parent branch,
- 3- in the daughter branches,
- 4- at the front menisci in the daughter's branches.

Figure 36 displays these 4 zones. We now examine the pressure drops in each zone closely.

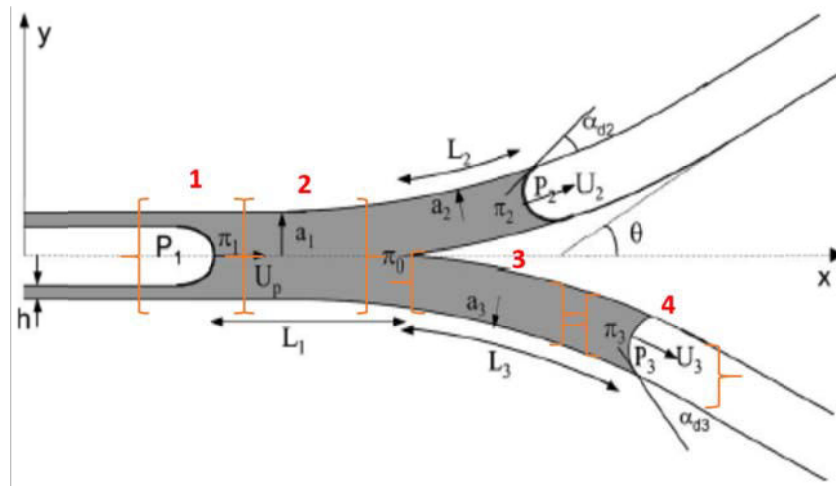


Figure 36: Schematic of the pressure difference between the upstream pressure P_1 in the parent branch and the downstream pressures P_2 and P_3 . Taken from [82].

- The pressure drop across the rear meniscus.

First, we assess the pressure drop at the rear meniscus in the parent airway by using the Young-Laplace law which gives the capillary pressure jump across a static hemispherical interface. We neglect here the viscous effects since the meniscus velocity is small. The difference between the air pressure P_1 and the liquid pressure π_1 at the rear meniscus is, therefore, equal to:

$$P_1 - \pi_1 = \frac{2\sigma}{a_1 - h} \quad (3.7)$$

- The pressure drop in the parent branch: viscous (Poiseuille) drop + hydrostatic pressure drop + inertia term.

The pressure drop is approximated using the Poiseuille law, a valid assumption in the case of small capillary numbers. The entrance effects and the secondary flows when the liquid passes the bifurcation are neglected. These features do not have a substantial effect on the splitting ratio, especially at low velocity and small capillary number [82]. Also, we have to consider a second hydrostatic pressure drop due to gravity. The pressure drop inside the liquid plug in the parent airway finally reads:

$$\pi_1 - \pi_0 = \frac{8\mu L_1}{\pi a_1^4} Q_1 - \rho g \sin \gamma L_1 + \frac{1}{2} \rho \left(\frac{Q_1}{\pi a_1^2} \right)^2 - \frac{1}{2} \rho \left(\frac{Q_0}{\pi a_1^2} \right)^2 \quad (3.8)$$

where L_1 , Q_1 , Q_0 , γ , ρ , and g are the length of the plug in the parent airway right before splitting, the flow rate in the parent airway corresponding to the surfactant that is transferred to the daughter airways, the flow rate in the entrance of parent airway, the pitch angle (see Figure 36), the surfactant density, and the standard gravity, respectively [129][82][136].

- The pressure drop in the daughter branch: viscous (Poiseuille) drop + hydrostatic pressure + inertia term.

The pressure drop in the daughter airway includes the same terms already seen in the parent airway (Eq. (3.8)). For daughter 2, this pressure is:

$$\pi_0 - \pi_2 = \frac{8\mu L_2}{\pi a_2^4} Q_2 + \rho g [\sin \theta_2 \sin \varphi - \cos \theta_2 \sin \gamma] L_2 + \frac{1}{2} \rho \left(\frac{Q_2}{\pi a_2^2} \right)^2 - \frac{1}{2} \rho \left(\frac{Q_1}{\pi a_1^2} \right)^2 \quad (3.9)$$

while for daughter 3, it is:

$$\pi_0 - \pi_3 = \frac{8\mu L_3}{\pi a_3^4} Q_3 + \rho g [\sin \theta_3 \sin \varphi - \cos \theta_3 \sin \gamma] L_3 + \frac{1}{2} \rho \left(\frac{Q_3}{\pi a_3^2} \right)^2 - \frac{1}{2} \rho \left(\frac{Q_1}{\pi a_1^2} \right)^2 \quad (3.10)$$

where L_i , Q_i , a_i , θ_i , and φ for ($i=2,3$) are the lengths of the plugs in the daughter airways, the flow rates of surfactant in the daughter airways, the radius of the daughter airways, the half-branching angles, and the roll angle (see Figure 36) [129][82][136]. One introduces also the quantities f_2 and f_3 defined as:

$$\begin{aligned} f_2 &= \sin \theta_2 \sin \varphi - \cos \theta_2 \sin \gamma \\ f_3 &= \sin \theta_3 \sin \varphi - \cos \theta_3 \sin \gamma \end{aligned} \quad (3.11)$$

- The pressure drops across the front meniscus in daughters 2 and 3.

At the air-liquid-solid interfaces in the daughter tubes, the capillary jumps are given by

$$\pi_2 - P_2 = -\frac{2\sigma}{a_2}, \quad \pi_3 - P_3 = -\frac{2\sigma}{a_3} \quad (3.12)$$

When the plug has entirely passed the bifurcation, the rear meniscus is located at π_0 . This means that $L_1=0$. Since the two new plugs in both daughter branches have crossed the bifurcation during the same duration, we can infer that:

$$\frac{L_2}{U_2} = \frac{L_3}{U_3}, \text{ hence } \frac{L_2}{\frac{Q_2}{\pi a_2^2}} = \frac{L_3}{\frac{Q_3}{\pi a_3^2}} \quad (3.13)$$

The splitting of the plug is characterized by the splitting ratio $R_s = V_2/V_3$. From Eq. (3.13), one deduces the ratio between flow rates Q_2 and Q_3 :

$$\frac{Q_2}{Q_3} = \frac{\pi a_2^2 L_2}{\pi a_3^2 L_3} = \frac{V_2}{V_3} = R_s \quad (3.14)$$

Finally, conservation of matter tells us that $V_2 + V_3 = V_1$ and $Q_2 + Q_3 = Q_1$.

3.1.3 Equation on R_s

The value of the splitting ratio R_s is obtained by stating that both downstream pressures are equal, $P_2 = P_3$, or that both pressure drops are equal, $\pi_0 - P_2 = \pi_0 - P_3$. It follows that

$$\frac{8\mu}{\pi a_2^4} L_2 Q_2 + \rho g f_2 L_2 + \frac{1}{2} \rho \left(\frac{Q_2}{\pi a_2^2} \right)^2 - \frac{2\sigma}{a_2} = \frac{8\mu}{\pi a_3^4} L_3 Q_3 + \rho g f_3 L_3 + \frac{1}{2} \rho \left(\frac{Q_3}{\pi a_3^2} \right)^2 - \frac{2\sigma}{a_3} \quad (3.15)$$

Rewriting this equation in terms of volumes leads to:

$$\frac{8\mu}{\pi a_2^6} V_2 Q_2 + \rho g f_2 \frac{V_2}{\pi a_2^2} + \frac{1}{2} \rho \left(\frac{Q_2}{\pi a_2^2} \right)^2 - \frac{2\sigma}{a_2} = \frac{8\mu}{\pi a_3^6} V_3 Q_3 + \rho g f_3 \frac{V_3}{\pi a_3^2} + \frac{1}{2} \rho \left(\frac{Q_3}{\pi a_3^2} \right)^2 - \frac{2\sigma}{a_3} \quad (3.16)$$

All volumes and flow rates in the daughter branches are now expressed in term of the parent branch:

$$\begin{aligned}
& \frac{8\mu}{\pi^2 a_2^6} \left(\frac{R_s}{1+R_s}\right)^2 V_1 Q_1 + \rho g f_2 \frac{V_1}{\pi a_2^2} \frac{R_s}{1+R_s} + \frac{1}{2} \rho \left(\frac{Q_1}{\pi a_2^2}\right)^2 \left(\frac{R_s}{1+R_s}\right)^2 - \frac{2\sigma}{a_2} \\
& = \frac{8\mu}{\pi^2 a_3^6} \left(\frac{1}{1+R_s}\right)^2 V_1 Q_1 + \rho g f_3 \frac{V_1}{\pi a_3^2} \frac{1}{1+R_s} + \frac{1}{2} \rho \left(\frac{Q_1}{\pi a_3^2}\right)^2 \left(\frac{1}{1+R_s}\right)^2 - \frac{2\sigma}{a_3}
\end{aligned} \tag{3.17}$$

Multiplying by $(1+R_s)^2$ on both sides yields:

$$\begin{aligned}
& \frac{8\mu}{\pi^2 a_2^6} R_s^2 V_1 Q_1 + \rho g f_2 \frac{V_1}{\pi a_2^2} R_s (1+R_s) + \frac{1}{2} \rho \left(\frac{Q_1}{\pi a_2^2}\right)^2 R_s^2 - \frac{2\sigma}{a_2} (1+R_s)^2 \\
& = \frac{8\mu}{\pi^2 a_3^6} V_1 Q_1 + \rho g f_3 \frac{V_1}{\pi a_3^2} (1+R_s) + \frac{1}{2} \rho \left(\frac{Q_1}{\pi a_3^2}\right)^2 - \frac{2\sigma}{a_3} (1+R_s)^2
\end{aligned} \tag{3.18}$$

One finally rewrites the equation in R_s as a second-order equation: $A R_s^2 + B R_s + C = 0$ where the coefficients A , B , and C are defined by:

$$\begin{cases}
A = \frac{8\mu}{\pi^2 a_2^6} V_1 Q_1 + \rho g f_2 \frac{V_1}{\pi a_2^2} + \frac{1}{2} \rho \left(\frac{Q_1}{\pi a_2^2}\right)^2 - 2\sigma(1/a_2 - 1/a_3) \\
B = \rho g f_2 \frac{V_1}{\pi a_2^2} - \rho g f_3 \frac{V_1}{\pi a_3^2} - 4\sigma(1/a_2 - 1/a_3) \\
C = -\frac{8\mu}{\pi^2 a_3^6} V_1 Q_1 - \rho g f_3 \frac{V_1}{\pi a_3^2} - \frac{1}{2} \rho \left(\frac{Q_1}{\pi a_3^2}\right)^2 - 2\sigma(1/a_2 - 1/a_3)
\end{cases} \tag{3.19}$$

3.1.3.1 Dimensionless equation

The quantities A , B , and C can be reformulated using the dimensionless numbers Re (Reynold number), Ca (capillary number), and Bo (Bond number):

$$Re = \frac{\rho U_1 a_1}{\mu}, \quad Ca = \frac{\mu U_1}{\sigma}, \quad Bo = \frac{\rho g a_1^2}{\sigma} \tag{3.20}$$

where Re represents the ratio of inertial to viscous forces, Bo represents the ratio of gravitational forces to surface tension force and Ca is the aforementioned capillary number. Then

$$\begin{aligned}
\frac{8\mu}{\pi^2 a_2^6} V_1 Q_1 &= \frac{8\mu}{\pi^2 a_2^6} \pi a_1^3 \left(\frac{V_1}{\pi a_1^3}\right) \pi a_1^2 U_1 = \frac{8\mu}{a_1 \lambda_2^6} \left(\frac{V_1}{\pi a_1^3}\right) U_1 = \frac{8\tilde{V}_1 Ca}{\lambda_2^6} \frac{\sigma}{a_1} \\
\rho g f_2 \frac{V_1}{\pi a_2^2} &= \frac{\sigma Bo}{a_1^2} f_2 \left(\frac{\pi a_1^3}{\pi a_2^2}\right) \tilde{V}_1 = \frac{f_2 \tilde{V}_1 Bo}{\lambda_2^2} \frac{\sigma}{a_1} \\
\frac{1}{2} \rho \left(\frac{Q_1}{\pi a_2^2}\right)^2 &= \frac{1}{2} \rho \frac{\pi^2 a_1^4 U_1^2}{\pi^2 a_2^2} = \frac{Re Ca}{2\lambda_2^4} \frac{\sigma}{a_1} \\
2\delta(1/a_2 - 1/a_3) &= 2(1/\lambda_2 - 1/\lambda_3) \frac{\sigma}{a_1}
\end{aligned} \tag{3.21}$$

where $\tilde{V}_1 = V_1/\pi a^3$ is the dimensionless dose volume, V_1 being the actual dose volume reaching the bifurcation and λ is diameter ratio. The dimensionless equation R_s is thus obtained by dividing all A, B, C coefficients by σ/a_1 :

$$\begin{cases} A' = \frac{a_1 A}{\sigma} = +\frac{\text{Re Ca}}{\lambda_2^4} + 16\frac{\text{Ca}\tilde{V}_1}{\lambda_2^6} + 2\text{Bo}\tilde{V}_1\frac{f_2}{\lambda_2^2} + 4(1/\lambda_3 - 1/\lambda_2) \\ B' = \frac{a_1 B}{\sigma} = 2\text{Bo}\tilde{V}_1(f_2/\lambda_2^2 - f_3/\lambda_3^2) + 8(1/\lambda_3 - 1/\lambda_2) \\ C' = \frac{a_1 C}{\sigma} = -\frac{\text{Re Ca}}{\lambda_3^4} - 16\frac{\text{Ca}\tilde{V}_1}{\lambda_3^6} - 2\text{Bo}\tilde{V}_1\frac{f_3}{\lambda_3^2} + 4(1/\lambda_3 - 1/\lambda_2) \end{cases} \quad (3.22)$$

3.1.3.2 The splitting factor

The splitting ratio is a dimensionless parameter that ranges from 0 to $+\infty$, whether the entire plug goes to one daughter branch or the other. To handle more conveniently a measurable parameter, we introduce from now the splitting factor α such that $V_2 = \alpha V$ and $V_3 = (1 - \alpha)V$. It follows immediately that

$$R_s = \frac{\alpha}{1 - \alpha} \quad \text{and} \quad \alpha = \frac{R_s}{1 + R_s} \quad (3.23)$$

α ranges from 0 to 1. Value $\alpha = 0.5$ means that the plug splits equally between both daughter airways while values 0 and 1 correspond an entirely uneven splitting. α satisfies a second-order equation which is obtained from the dimensionless equation in R_s :

$$A' \left(\frac{\alpha}{1 - \alpha} \right)^2 + B' \frac{\alpha}{1 - \alpha} + C' = 0 \quad (3.24)$$

Hence

$$A_1 \alpha^2 + B_1 \alpha + C_1 = 0 \quad \text{with} \quad \begin{cases} A_1 = A' - B' + C' \\ B_1 = B' - 2C' \\ C_1 = C' \end{cases} \quad (3.25)$$

Consequently, the coefficients $A_1, B_1,$ and C_1 are:

$$\begin{cases} A_1 = ReCa(1/\lambda_2^4 - 1/\lambda_3^4) + 16\tilde{V}_1Ca(1/\lambda_2^6 - 1/\lambda_3^6) \\ B_1 = 2\tilde{V}_1Bo(f_2/\lambda_2^2 - f_3/\lambda_3^2) + \frac{2ReCa}{\lambda_3^4} + \frac{32\tilde{V}_1Ca}{\lambda_3^6} \\ C_1 = -\frac{ReCa}{\lambda_3^4} - \frac{16\tilde{V}_1Ca}{\lambda_3^6} - \frac{2\tilde{V}_1Bof_3}{\lambda_3^2} + 4(1/\lambda_3 - 1/\lambda_2) \end{cases} \quad (3.26)$$

3.1.3.3 The symmetric bifurcation

In a symmetric bifurcation $\lambda_2 = \lambda_3 = \lambda$, $L_2 = L_3$, and $\theta_3 = -\theta_2$. This simplifies the expression of A_1 , B_1 , and C_1 to:

$$\begin{cases} A_1 = 0 \\ B_1 = \frac{2\tilde{V}_1Bo}{\lambda^2}(f_2 + f_3) + \frac{2ReCa}{\lambda^4} + \frac{32\tilde{V}_1Ca}{\lambda^6} \\ C_1 = -\frac{2\tilde{V}_1Bof_3}{\lambda^2} - \frac{ReCa}{\lambda^4} - \frac{16\tilde{V}_1Ca}{\lambda^6} \end{cases} \quad (3.27)$$

The equation in α therefore becomes a first-order equation whose solution is:

$$a = \frac{1}{2} \left(\frac{ReCa\lambda^2 + 16Ca\tilde{V}_1 - 2Bo\tilde{V}_1(\sin\theta\sin\varphi + \cos\theta\sin\gamma)\lambda^4}{ReCa\lambda^2 + 16Ca\tilde{V}_1 - 2Bo\tilde{V}_1\cos\theta\sin\gamma\lambda^4} \right) \quad (3.28)$$

Introducing the dimensionless quantity $X = \frac{2Bo\tilde{V}_1\lambda^4}{(Re\lambda^2 + 16\tilde{V}_1)Ca}$, one can finally express

the splitting factor for a symmetric bifurcation:

$$\alpha = \frac{1}{2} \left(1 - \frac{X\sin\theta\sin\varphi}{1 - X\cos\theta\sin\gamma} \right) \quad (3.29)$$

In summary, when a plug of volume V_0 enters an airway at a given velocity, the first computation step consists in assessing the thickness of the trailing film and thus the maximal volume V_C of surfactant that will be left lining the parent airway. If this coated volume is smaller than the volume of the plug, then $V_1 = V_0 - V_C$ is the volume of the surfactant available for splitting. The second step consists in calculating the splitting ratio of the liquid plug through the bifurcation, which gives two new volumes entering both daughter airways. The process is then iterated in the daughter's airways, until reaching the acini or exhausting the liquid plug.

3.2 Modeling of multiple aliquot instillations

As we mentioned before, the surfactant can be delivered into the lung either in one single or through multiple instillations. In the latter case, the initial dose volume is divided into equal aliquots, one per breath. With this technique, the final instilled volume is the sum of the volumes of the aliquots. When instilling the first aliquot, a plug forms which propagates along the branches of the pulmonary airway system. In each airway tube, the plug loses a part of its volume. This volume of liquid remains coating the walls of the airways (Figure 37A and B). The following aliquots form new plugs that therefore propagate through airways already lined with surfactant.

The effect of a precursor (preexisting) film on the coating layer and plug length has been studied by Cassidy *et al.* [78]. Results showed that the trailing film thickness depends upon the plug capillary number (Ca), but not on the precursor film thickness. The film thickness depends strongly on Ca but is a weak function of L_P and Re . We have implemented this property in our model by assuming that the new plug does not lose any volume when passing through airways that are already coated with a precursor film (from previous plugs). Therefore, a new plug starts losing a fraction of its volume only when it reaches airways that were never coated previously (Figure 37C and 3D). Our numerical model accounts for this specific feature of the multiple aliquot deliveries.

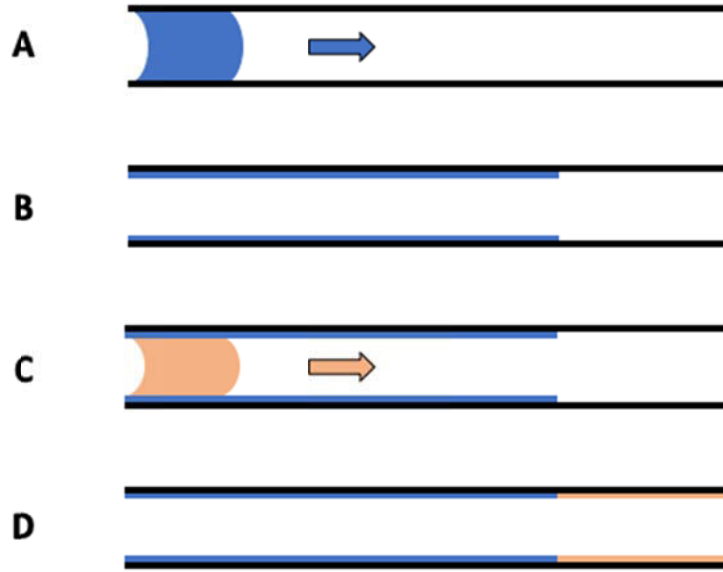


Figure 37: Sketch of the multiple aliquot deliveries. A and B: a liquid plug propagating in an airway with dry walls leaves a trailing film and may end up being entirely deposited on the airway wall. C and D: the same plug propagating into an airway whose walls are already coated with surfactant proceeds without losing its mass, and starts leaving a trailing film only when it reaches the dry portions of the walls.

3.3 Assessing the performance of surfactant delivery

To assess the performance of the delivery, we introduce two indices called *efficiency index* and *homogeneity index* [129]. These indices are dimensionless and allow us to compare the delivery performance of various surfactants for different delivery conditions. The efficiency index η is defined as the percentage of the initially instilled dose volume V_D that actually reaches the ends of the terminal airways:

$$\eta = 100 \times \frac{\sum_{i=1}^M V_i}{V_D}, \quad (3.30)$$

M being the number of terminal airways and V_i being the volume of surfactant mixture reaching terminal airway $\#i$. The homogeneity index HI is defined as the reciprocal of the standard deviation of the normalized distribution of V_i :

$$HI = \left(\langle V_{N,i}^2 \rangle - \langle V_{N,i} \rangle^2 \right)^{-1/2} = \left(\frac{M \sum_{i=1}^M V_i^2}{\left(\sum_{i=1}^M V_i \right)^2} - 1 \right)^{-1/2} \quad \text{where} \quad V_{N,i} = \frac{V_i}{\frac{1}{M} \sum_{j=1}^M V_j} \quad (3.31)$$

A vanishing standard deviation, hence an infinite value of HI , means that the delivery is entirely homogeneous. A value of HI smaller than 1 corresponds to a poorly homogeneous distribution. The smallest homogeneity is achieved when the entire delivered volume goes to one terminal airway only, in which case $HI = 1/\sqrt{M-1}$.

3.4 Surfactant properties and instillation conditions

Simulations of surfactant delivery have been performed for various instillation conditions, flow rate, dose volume, surfactant properties, and posture. We examine here how these conditions are determined.

3.4.1 Flow rate

The flow rate depends strongly on the breathing frequency. For rats, this breathing frequency depends on the species. The frequency used in the Long-Evans rat simulations is 70 min^{-1} and the inspiration time is 0.3 s. The tidal volume is about 9 mL.kg^{-1} , which is moderate [137]. Such tidal volume inspired during 0.3 seconds corresponds to a flow rate of $30 \text{ mL.kg}^{-1}.\text{s}^{-1}$. The tidal volumes for Sprague-Dawley and Wistar rats are 8 mL.kg^{-1} and 6 mL.kg^{-1} , respectively. Such tidal volumes with their frequencies and I:E⁷ ratios correspond in our simulations to flow rates of 26.8 and $6 \text{ mL.kg}^{-1}.\text{s}^{-1}$, respectively.

The pig tidal volume is 10 mL.kg^{-1} , the breathing frequency is 12 min^{-1} [138], (using a 1:2 ratio of inspiratory to expiratory duration), and the flow rates range from 1 to $6 \text{ mL.kg}^{-1}.\text{s}^{-1}$.

Typical human tidal volume and breathing frequency at rest are $7\text{-}8 \text{ mL.kg}^{-1}$ [139][140] and 12 min^{-1} , respectively, which corresponds to a $5\text{-}6 \text{ mL.kg}^{-1}.\text{s}^{-1}$ flow rate. Flow rates ranging from 1 to $6 \text{ mL.kg}^{-1}.\text{s}^{-1}$ were used in human simulations.

3.4.2 Dose volume and surfactant properties

Simulations are also run for a wide range of dose volumes per kilogram, from 1 to 8 mL.kg^{-1} [135][63] [141][142][143]. The recommended instilled dose volume per kg of body weight depends on the type of surfactant and its phospholipid concentration [114]. In Table 11, we display the phospholipid concentration, dose volume/kg, and molecular dose of 6 commonly-used surfactants.

⁷ Inspiratory : Expiratory ratio

Table 11: Surfactant properties [105][144]

Surfactant	Surfaxin	Exosurf	Survanta	Infasurf	Curosurf	Alveofact
Phospholipid concentration (mg.mL ⁻¹)	30	13.5	25	35	80	40
Dose volume/kg (mL.kg ⁻¹)	5.8	5	4	3	1.25 or 2.5	1.2
Dose (mg.kg ⁻¹)	175	67.5	100	105	100 or 200	50

Surfactant viscosity (Survanta®, Infasurf®, and Curosurf®) is taken equal to $\mu=30$ cP [105][144], and density is water-like in all cases, i.e., 1 g.mL⁻¹. The surface tension of the air-liquid interface also has a strong influence on lung mechanical properties [97]. The default surface tension is set at $\sigma = 30$ dyn.cm⁻¹ [34] [35] unless mentioned otherwise. In 2018, Thai et al. [107] exhibited a linear relationship between the volume fraction ϕ and the surfactant concentration: $\phi = 0.0052c$, where c is given in g.L⁻¹. It means that for Curosurf® at 80 g.L⁻¹ concentration, the volume fraction is $\phi = 0.42$.

3.4.3 Posture

We have simulated surfactant delivery for various animal and human postures: left lateral decubitus (LLD), right lateral decubitus (RLD), supine (S), prone (P), 45-degree angle (halfway) between supine-LLD (called SL) and 45-degree angle between supine-RLD postures (SR) (see Figure 38). When two postures are used together, the total dose volume is divided into 2 half-doses, one half-dose being delivered in the first posture and the second half in the second posture. When three postures are used, the total dose volume is divided into 3 equal dose volumes and each dose volume is instilled in one position. In multiple instillations, all dose volumes are instilled in one position.

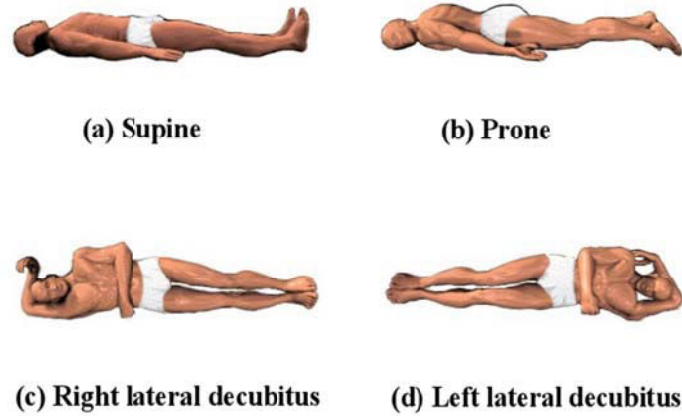


Figure 38: Patient positions. Taken from [145].

3.5 Validation of the splitting model

We now test the validity of our fluid mechanical model to reproduce the splitting of liquid plugs at bifurcations. As already mentioned, when the surfactant is instilled in a sufficient amount into the pulmonary airway tree, a liquid plug forms and propagates along the branches of the pulmonary airway system. Gravity, viscous (Poiseuille) drop, hydrostatic pressure drop, and inertia all influence this propagation, and in particular the splitting at each bifurcation. In this section, we first compare the predictions of our theoretical model of the splitting factor with the experimental results obtained by Zheng *et al.* [82][136] in 2005 and 2006. In a second step, we compare the results of the surfactant delivery of our full delivery model with two experiments performed in rat lungs.

3.5.1 Effect of gravity on liquid plug splitting at a bifurcation

In 2005, Zheng *et al.* [82] used a bench-top model of a symmetrically bifurcating airway to investigate the effect of gravity and surface tension forces in the distribution of instilled liquid at the bifurcation. Figure 39 displays a schematic of their experimental setup which consists of one parent tube and two daughter tubes that are connected through a symmetric bifurcation. The diameter of the parent tube is 0.4 cm while the diameter of each daughter tube is 0.32 cm. The branching angle between the two daughter tubes is 60 degrees ($\theta=30^\circ$). The total cross-sectional area increases by 28% from the parent to the daughters and the tube sizes correspond to airways in the 5-7 generation of the human respiratory system. The authors described the orientation to the gravity of the setup through a roll angle (ϕ) and pitch angle (γ). When $\phi = \gamma = 0$, the direction of gravity is normal to the plane of the bifurcation plate; when $\phi > 0$, the daughter tubes are asymmetrically oriented with respect to the gravity.

When $\gamma > 0$, gravity favors the liquid motion in the daughter tube. With the help of a syringe and pump, the authors instilled a plug of liquid into the parent tube and recorded by video camera the plug motion to measure the fluid volumes entering the upper and lower daughters.

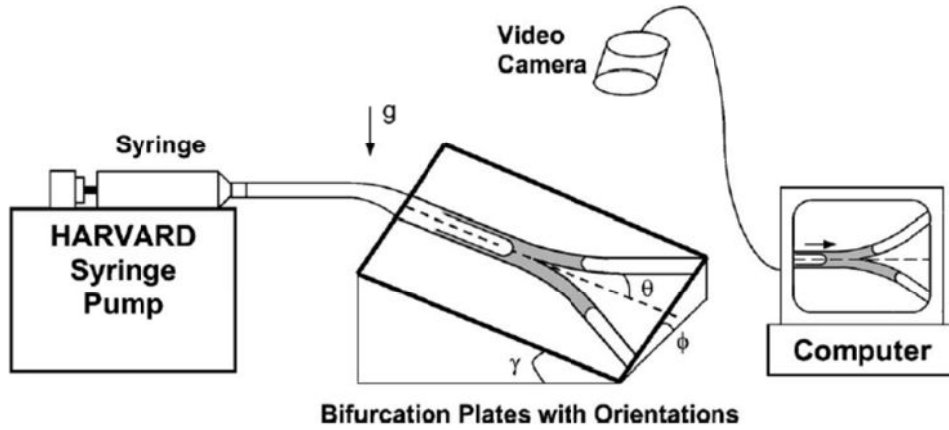


Figure 39: Schematic of the experimental setup. The roll angle (ϕ) and pitch angle (γ) describe the orientation of the bifurcation plates with respect to the gravity. The branching angle of the daughter tube with respect to the parent tube is indicated by θ . Taken from [82].

In this section, we run our model in the same geometry and applied conditions than the experiments of Zheng *et al.* [82]. Two different liquids are used to investigate the effect of gravity on the splitting ratio. Table 12 shows the mechanical properties of these two liquids and the experimental conditions.

Table 12: Mechanical properties of liquids and experimental conditions

Property	LB-400-X	Glycerin
μ (g/cm/s)	1.51	9.6
ρ (g/cm ³)	0.989	1.26
σ (dyn/cm)	30.7	63.4
Bo	1.26	0.78
Ca_p	0.001-0.11	0.005-0.11
Re_p	0.0027-0.3	0.0008-0.024

3.5.1.1 Changing ϕ

In the experiment in 2005, Zheng *et al.* [82] first studied the splitting for a pitch angle $\gamma = 0$ and a roll angle $\phi = 15^\circ, 30^\circ, 60^\circ$. They plotted R_s against Ca_p for Ca_p in the [0.001;0.11] range (see Figure 40). They found the existence of a critical value of the capillary number (Ca_c), below which $R_s = 0$. A vanishing value of R_s means all liquid

goes to the lower daughter while $R_s=+\infty$ means all liquid goes to the upper daughter. $R_s=1$ corresponds to an equal splitting between both daughter tubes. They concluded that minimum pressure is required for the liquid to overcome gravity and enter the upper daughter after the bifurcation. They also found that R_s increases with Ca_p but decreases with ϕ . They also tested very low-speed instillations in order to remove the effect of inertia. We have mimicked the same delivery conditions to be able to compare their data with the results of our theoretical model.

Figure 40 displays a comparison of the splitting factor measured experimentally (symbols) and obtained with our model (plain lines) for different values of Ca_p . We find similar trends: as in the experiments, we observe the existence of a critical capillary number, an increase of R_s with Ca_p and a decrease of R_s with ϕ . The agreement between theory and experiment is also better for smaller values of ϕ .

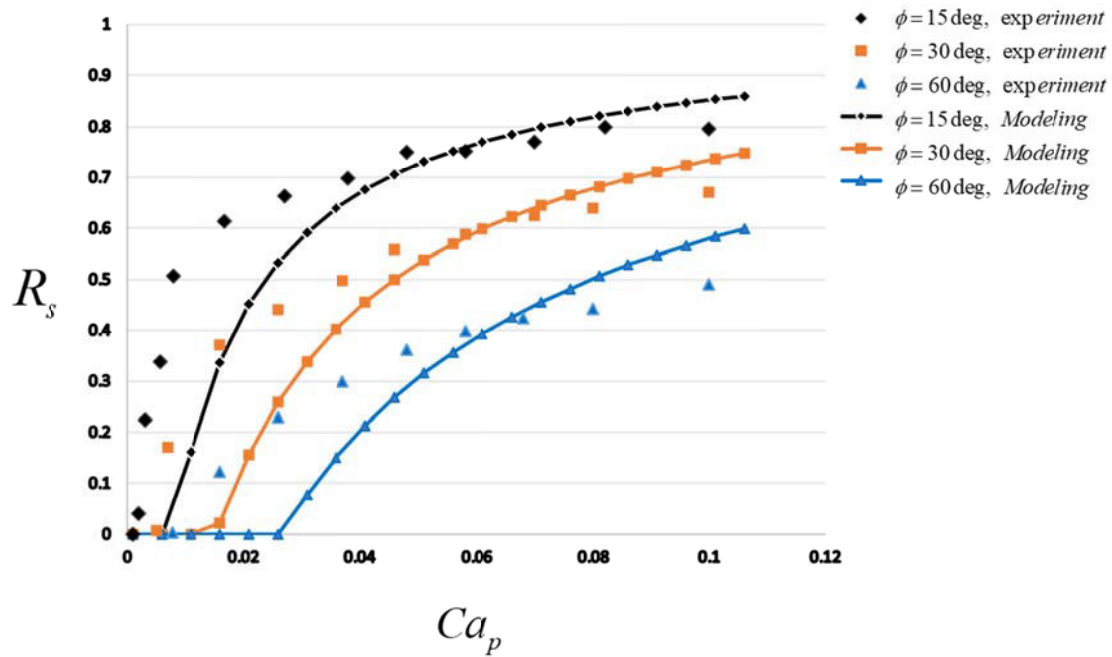


Figure 40: Comparison of R_s vs. Ca_p for $\gamma=0^\circ$ and $\phi=15^\circ$ (experiments: black diamonds, model: black line), $\phi=30^\circ$ (experiments: orange squares, model: orange line), and $\phi=60^\circ$ (experiments: blue triangles, diamond, model: blue line). Experimental data are extracted from [82].

3.5.1.2 Changing γ

The second parameter that can control the orientation of the bifurcation with respect to gravity is the pitch angle γ . Figure 41 shows a comparison of the splitting factor between experimental data (symbols) and theoretical computations (lines) for three

different values γ (and $\phi = 30^\circ$). As previously, the computed curves of R_s vs. Ca_p reproduce the same aspect as the experimental data. R_s increases with Ca_p and decreases with γ .

At smaller Ca_p , our model, however, consistently underestimates the splitting ratio R_s compared to the experimental values while it is the opposite at larger values of Ca_p . The discrepancy between theory and experiments increases with γ . The discrepancy between experiment and theory results from the simplification of the fluid dynamics in the theoretical analysis and approximations to the geometry of the model.

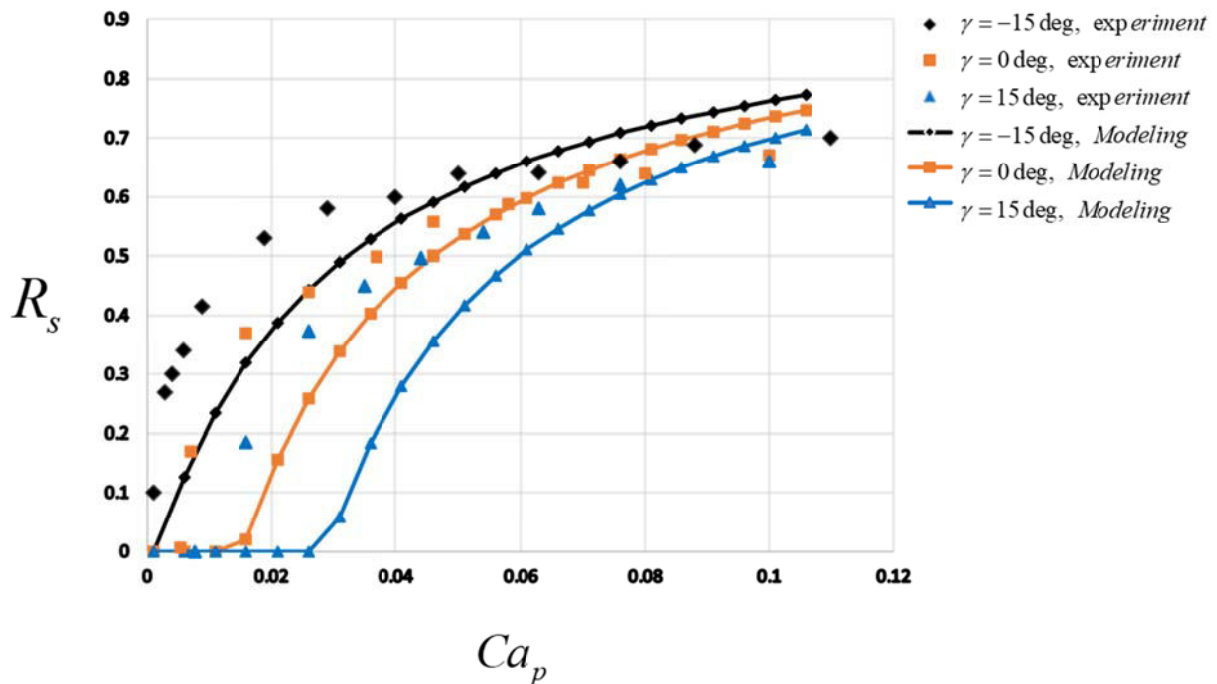


Figure 41: Comparison of R_s vs. Ca_p for $\phi = 30^\circ$ and $\gamma = -15^\circ$ (experiments: black diamonds, model: black line), $\gamma = 0^\circ$ (experiments: orange squares, model: orange line), and $\gamma = 15^\circ$ (experiments: blue triangles, model: blue line). Experimental data are extracted from [82].

3.5.1.3 Changing the Bond number

In Figure 42, we have compared theoretical and experimental results for different Bond numbers. The theory follows the experiments, increasing Ca_p or decreasing Bo leading in both cases to an increase in R_s . As when changing γ , the theoretical values of R_s appear smaller than the experimental ones at smaller Ca_p numbers, and more significant for larger Ca_p numbers.

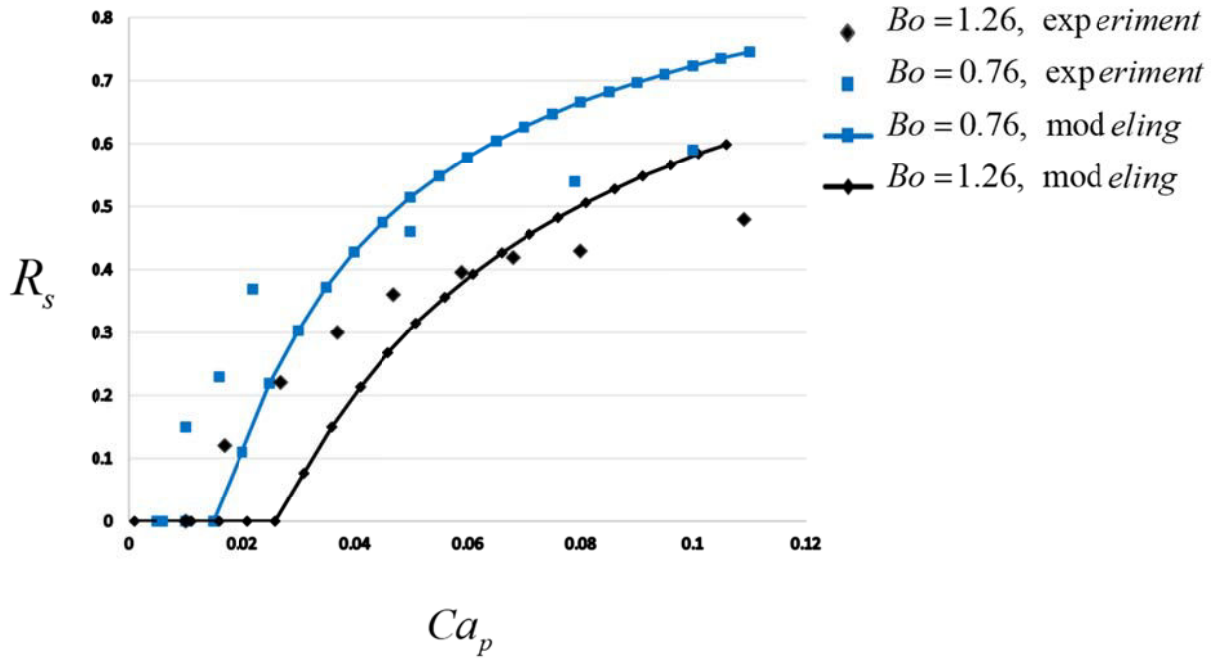


Figure 42: Comparison of R_s vs. Ca_p for different values of the Bond number Bo (angles are $\phi = 60^\circ$ and $\gamma = 0^\circ$): $Bo=1.26$ (experiments: black diamonds, model: black line), and $Bo=0.76$ (experiments: blue triangles, model: blue line). Experimental data are extracted from [82].

The real pulmonary airways have a rounded carina in the bifurcation region, while Zheng *et al.* experimental setups had sharp corners. Consequently, the pressure drop across this region may be different. Also on the experiments, the plug is installed manually into the parent tube and the plug length varies between experimental runs.

3.5.2 Effect of inertia and gravity on liquid plug splitting at a bifurcation

3.5.2.1 Changing ϕ

In 2006, Zheng *et al.* [136] set up an experiment to assess the effect of inertia and gravity on liquid plug splitting at a bifurcation individually. The sizes and dimensions of the setup were similar to their experiment used for comparison in the previous section [82]. The main difference between these two studies consisted of investigating the effect of inertia. In their experimental results, they presented R_s vs. Re_p for various experimental conditions. Re_p ranged from 5 to 300 while the capillary number varied between 2×10^{-5} and 3×10^{-3} . The pitch angle is $\gamma = 0^\circ$ and the roll angles are $\phi = 30^\circ$ and $\phi = 60^\circ$ in Zheng *et al.* [136]. Table 13 shows the mechanical properties of the liquids and the experimental conditions used in these experiments.

Table 13: Mechanical properties of the liquid and experimental conditions

Property	Water
ρ (g/cm/s)	0.01
ρ (g/cm ³)	1
σ (dyn/cm)	72.4
Bo	0.54
Ca_P	$2 \cdot 10^{-5}$ - $3 \cdot 10^{-3}$
Re_P	2 – 300

The authors plotted R_s vs. Re_P for values of Re_P ranging from 2 to 300 (see Figure 43). They found the existence of a critical value of the Reynolds number (Re_c) below which the splitting ratio R_s vanishes, meaning that all liquid goes to the lower daughter. They also observed that R_s increases with Re_P while in contrast, an increase in the value of ϕ a lead to a decrease in R_s and an increase in Re_c . In the following, we simulate with our numerical model precisely the same conditions used in these experiments.

Figure 43 displays comparisons of the splitting factor measured experimentally (symbols) with our theoretical predictions (lines) for different values of Re_P . Again, our simulation results have captured the trends of the experimental data. We observe here a critical Reynolds number and an increase in the R_s with an increase of Re_P and decrease of ϕ .

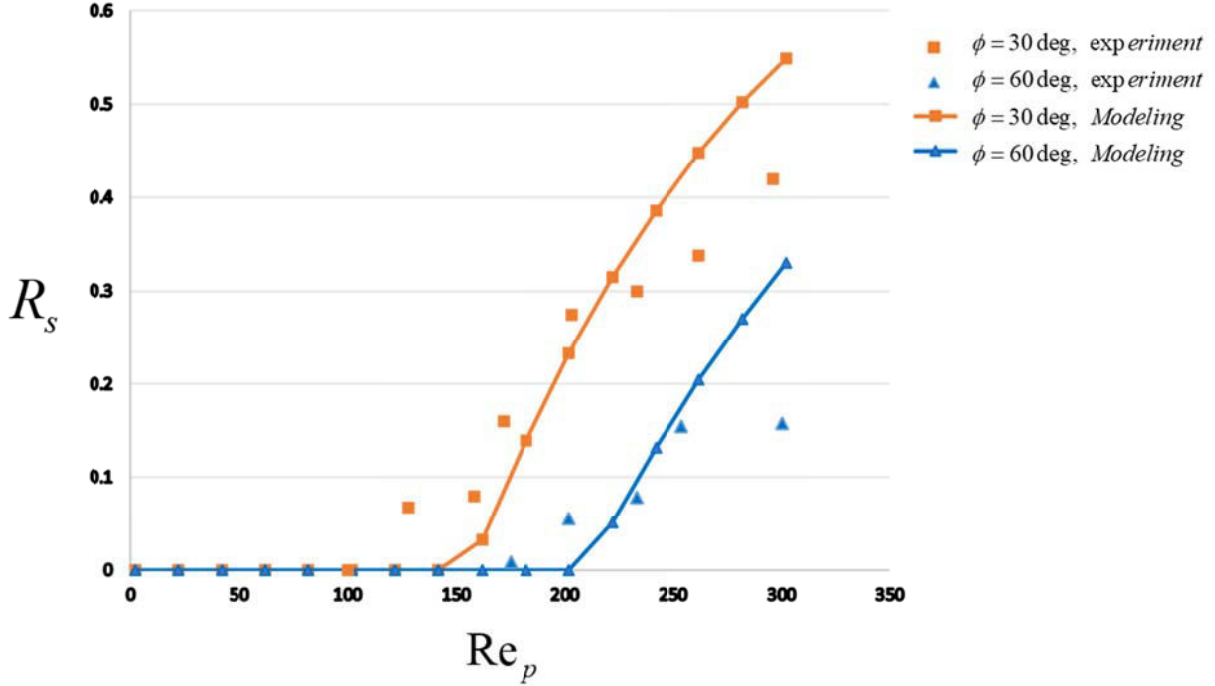


Figure 43: R_s vs. Re_p for $\gamma = 0^\circ$ and $\phi = 30^\circ$ (experiments: orange squares, model: orange line) and $\phi = 60^\circ$ (experiments: blue triangles, model: blue line). Data are extracted from [136]

Our theoretical analysis and our numerical model are based on some simplifying assumptions. First, we do not account for the specificity of the contact angles in the capillary jumps at the air-liquid-solid interfaces in the daughter tubes. This angle is assumed to be zero. Also, the geometrical model does not account for the precise geometry of the transition region at the bifurcation. In some cases, the effects due to the transition from parent to daughter airways can be significant (if the carina is not smooth, for instance), but our model cannot see this. The input velocity profiles in each daughter's tubes are assumed to be identical, i.e., flat and uniform. Also, the downstream pressures in both daughter airways might slightly differ while they are supposed to be identical in our model. All unsteady effects are neglected and we used Poiseuille flow for assessing the pressure drops in the liquid. Zheng *et al.* [136] showed that the frictional pressure drop can be much higher than the Poiseuille pressure drop. This assumption is only valid for a long plug in the parent tube. Finally, the effects of biphasic flow are neglected. All of these simplifications and approximations can explain the discrepancies observed between theory and experiment. Future improvements in our model should try to remove these simplifying hypotheses.

3.6 Validation of the surfactant delivery model in the entire lung

In this section, we verify and validate our computer simulation models with two animal experiments surfactant delivery. The first experiment explores the propagation of surfactant for various dose volumes and the second for multiple instillations.

3.6.1 Changing the dose volume: comparison with experimental results

To validate our model, we have compared it with experimental results obtained by Gary Nieman's team (State University of New York Upstate Medical University) in rats when testing different dose volumes. All experiments were conducted with approval from the State University of New York Upstate Medical University Institutional Animal Care and Use Committee.

For the experiments, three male Sprague-Dawley rats weighing ~ 450 g were anesthetized with 1 mL.kg^{-1} of Ketamine/Xylazine I.P. and surgically prepared with a tracheotomy. Rats were then mechanically ventilated with a 6 mL.kg^{-1} tidal volume (V_t), 2 positive end-expiratory pressure (PEEP), 21% inspiratory oxygen fractionation (FiO_2), and a frequency of 20 breaths per minute (Dräger Medical, Evita Infinity V500) [103]. The animal was disconnected from the ventilator and positioned in left lateral decubitus and reverse Trendelenburg (L+R). One half of the surfactant/dye mixture was distributed by sliding a catheter into the endotracheal tube and forming a plug [102]. After 20 mechanical breaths, the animal was put in right lateral decubitus and reverse Trendelenburg and the procedure repeated. The lung was then clamped at inspiration, and the lungs were excised and immersed in 10% formalin for histological examination.

Infasurf® surfactant (210 mg) was tagged with Green Tissue Marking Dye® (Green Dye: WAK-Chemie Medical GmbH, Germany) at a concentration of 1% of the total volume of surfactant [146]. Three dose volumes per kg of surfactant 1.125, 2.5, and 5.8 mL.kg^{-1} were tested for experiments. The dye and surfactant mixture was incubated at 37°C until the time of distribution. Figure 44 shows the results for these different three-dose volumes per kg into the rat lung.

There is a marked visual difference in surfactant distribution between the three-dose volumes per kg (Figure 44A-C). The low dose volume per kg (1.125 mL.kg^{-1}) exhibits a scattered heterogeneous distribution in both right and left lungs. Increasing the instilled dose volume per kg to 2.5 mL.kg^{-1} resulted in a higher concentration of surfactant in the caudal portions of both lungs. For the highest instilled dose volume

per kg (5.8 mL.kg^{-1}), an even distribution of surfactant in the caudal portion of both lungs was observed while the remaining lung showed no surface distribution at all. In summary, the low dose volume per kg resulted in small areas of heterogeneous surfactant distribution whereas the high dose volume per kg induced a more locally homogeneous distribution isolated to the caudal portion of both lungs, indicating regional-scale heterogeneity.

Of course, the heterogeneity observed here lies at the outer surface of the pulmonary airway system, which corresponds to the most distal part of the external acini. It is reasonable to assume that having surfactant reaching this surface implies that the corresponding acini are also filled with surfactant and this heterogeneity reflects the 3D patchy distribution of surfactant in the lung volume. Our simulations (Figure 44D-F) support this assumption.

We have then carried out numerical simulations using our model in the same conditions. Figure 45A, B, and C present 3D views of the end distributions of surfactant in a rat lung after a double instillation in L+R posture, with instilled dose volumes per kg = 1.125 mL.kg^{-1} , 2.5 mL.kg^{-1} , and 5.8 mL.kg^{-1} , respectively. The surfactant viscosity is $\mu=30 \text{ cP}$, and the flow rate per kg is $6 \text{ mL.kg}^{-1}.\text{s}^{-1}$. This corresponds to the experiments presented in Figure 44, with 20 breathes per minute, a tidal volume per kg of 6 mL.kg^{-1} , and a ratio between inspiration and exhalation times I:E=1:2. One observes that increasing the instilled dose volume allows more surfactant to reach the terminal regions. Indeed, the efficiency is raised from 5.9% to 45.6% and 76%, respectively, while the homogeneity index remains very poor, about 0.2 to 0.29. The amount of surfactant left coating the airways is displayed for all dose volumes per kg in Figure 45D, E, and F. In the two last cases, the coating cost V_C is about 0.45 mL, only 30% more than the one found for a 1.125 mL.kg^{-1} instilled dose volume per kg, whereas the amount of instilled dose volume per kg is 2 and 5 times larger, respectively. V_C reaches a plateau above a given initial dose volume per kg. As we can see, the end distributions of surfactant in rat lungs are very poor, both in our simulations and in the experiments. However, apart from the clinical result, the results of our simulations have the same trend as experiments.

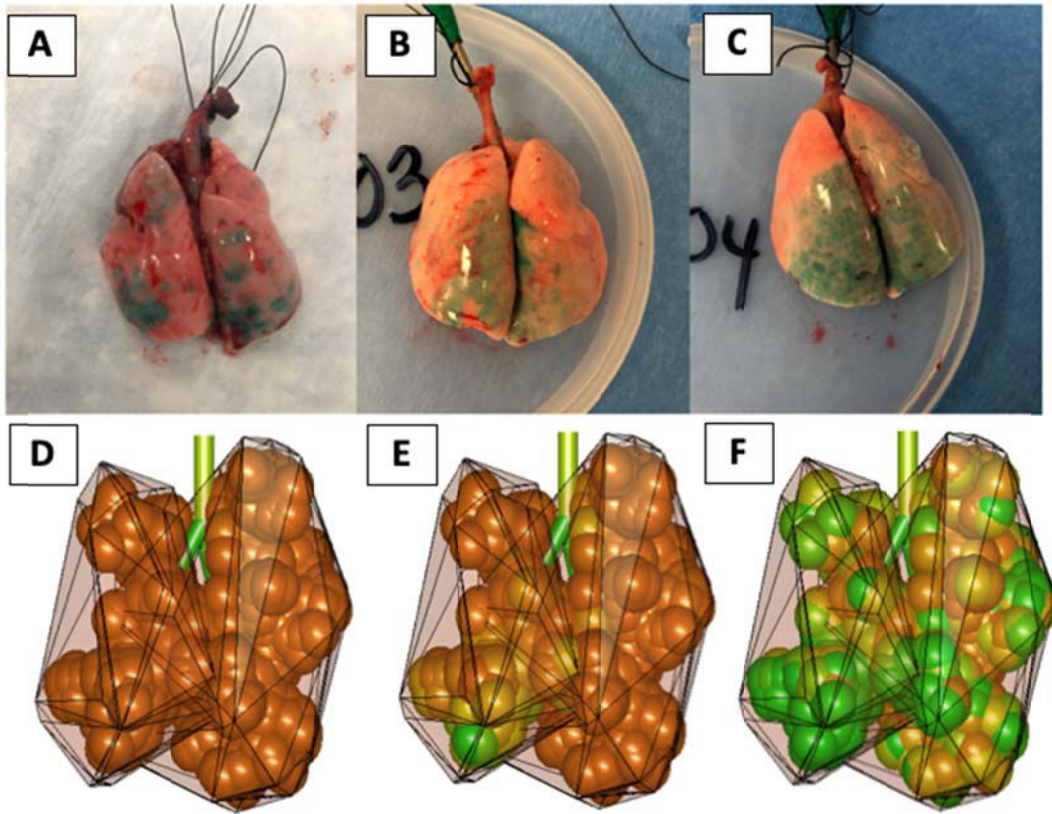


Figure 44: Delivery of three surfactant dose volumes into a rat lung (L+R posture). Surfactant (Infasurf®) was tagged with Green Tissue Marking Dye. A) Dose volume per kg = $1.125 \text{ mL}\cdot\text{kg}^{-1}$, B) Dose volume per kg = $2.5 \text{ mL}\cdot\text{kg}^{-1}$, and C) Dose volume per kg = $5.8 \text{ mL}\cdot\text{kg}^{-1}$.

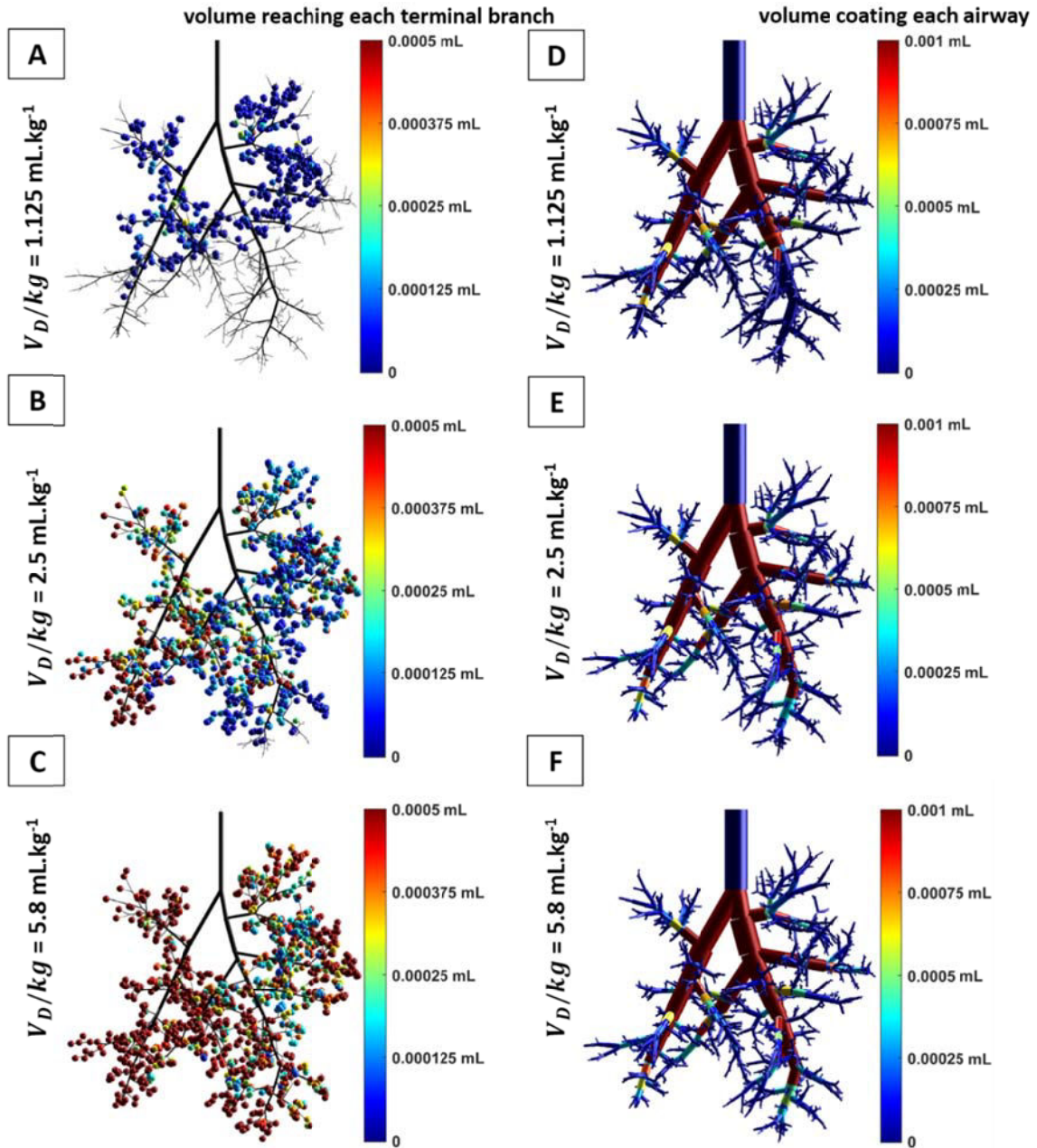


Figure 45: Simulated distributions of surfactant in the rat. A) 3D Front view representing the distribution of volumes reaching the terminal branches for $V_D=1.125 \text{ mL}\cdot\text{kg}^{-1}$. The efficiency index is $\eta=5.9\%$. B) The same figure, for $V_D=2.5 \text{ mL}\cdot\text{kg}^{-1}$ with $\eta=45.6\%$ and C) the same figure, for $V_D=5.8 \text{ mL}\cdot\text{kg}^{-1}$ with $\eta=76\%$. D) 3D front view displaying the amount of surfactant left coating the airways, in simulation (A). The color-coding represents the left coating volume of each airway. The homogeneity index is $HI=0.2$. E) The same figure as (D), corresponding to simulation (B) with $HI=0.29$, and F) the same figure as (D), corresponding to simulation (C) with $HI=0.28$.

3.6.2 Multiple instillations: comparison with experimental results

In this section, we compare the results of numerical simulations of surfactant delivery with experimental results obtained by Cassidy *et al.* [102] in 2001 on Wistar rats. Surfactant viscosity and surface tension were 12.2 cP and 54 dyn.cm⁻¹, respectively. Wistar rats were laid down in a vertical position for instilling surfactant. Simulations of surfactant delivery have been carried out with our model using similar viscosity, surface tension, volume, posture, and velocity than in the experiments (see Table 14).

Table 14: Properties and condition of instilled surfactant in simulations and experiments [102].

	Simulation (Long_Evans)	Experiment (Wistar)
Viscosity (cP)	12.2	12.2
Surface tension (dyn.cm ⁻¹)	54	54
Density (g.cm ⁻³)	1.22	1.22
Flow rate (mL.kg ⁻¹ .s ⁻¹)	26.8	16
Dose (mL.kg ⁻¹)	1 per breath (10 breaths)	1 per breath (10 breaths)
Position	Vertical	Vertical
Capillary Number (Trachea)	0.22	0.22
Bond Number (Trachea)	0.64	0.58
Reynolds Number (Trachea)	165	160
Trachea diameter (cm)	0.34	0.324
Velocity (cm.s ⁻¹) (Trachea)	97	97
Rat weight (kg)	0.330	0.500

The surfactant is being delivered in multiple aliquots, 0.053 mL per breath (0.1 mL.kg⁻¹) during the first 10 breaths (which amounts to 1 mL.kg⁻¹ in total). At the end of each inspiration, images of the lung were captured. Figure 46 shows a comparison between the end distributions of surfactant mixture observed experimentally (A-D), and in our simulations (E-H) after the 1st, 3rd, 6th, and 10th breath. In both cases, one can observe that the liquid plugs propagate increasingly deeper down the airway tree during each successive breath. This is particularly striking in Figure 47, which displays the surfactant delivered during the 10th breath. The efficiency of the delivery is about 59%, which is quite good. This high efficiency is due to the pre-existing film lining the airways that allow the plugs to propagate without losing most of their mass.

In their experiments, Cassidy *et al.* defined the homogeneity of the end distribution of surfactant to analyze their results [102], which differs from ours. They divided the lung into four main quadrants; in each quadrant, the two-dimensional area reached by the liquid would be measured. Each of these areas would be then divided by the total

surface area of the quadrant (AR), and the homogeneity index defined for each image as the smallest value of AR divided by its largest one. To avoid any confusion in what follows, we call this quantity comprised between 0 and 1 the “quadrant homogeneity index” (QHI). A value $QHI=1$ corresponds to a perfectly homogeneous distribution (at the level of a quadrant) while a vanishing QHI means a strongly inhomogeneous distribution. This QHI index differs from the homogeneity index (HI) introduced later in [129] and defined by Eq. (3.31), which is more general and captures more details about the distribution homogeneity. To allow a direct comparison between experiments and our model, we have computed a tentative estimate of the QHI from our simulations. To that end, simulated images of the lung are created by placing a sphere around each terminal branch of the bronchial tree (see Figure 48). The size of the sphere is constant and corresponds to the average size of an acinus. The sphere is colored on a grayscale, a white color meaning that no surfactant has reached the acinus and while black means that the amount of the surfactant reaching the acinus is sufficient to coat the entire acinar surface. Table 15 displays the efficiency and the homogeneity indices computed from our simulations and the QHI obtained measured in the experiments, and the $SQHI$ (simulated QHI) computed from our simulations. We see that the efficiency rises at each breath, from 0% to 59% in the 10th breath. The homogeneity also increases, whether measured by our HI index or by the original quadrant-based index. We can observe that QHI and $SQHI$ follow very similar curves, with a slight shift that is probably due to a difference in the initial tracheal coating, difficult to estimate from the original images.

Table 15: Simulated efficiency and homogeneity indices compared with the homogeneity index measured in Cassidy *et al.* [102].

Breath number	1	2	3	4	5	6	7	8	9	10
Efficiency (%)	0	0	2	10	20	31	41	48	54	59
Homogeneity Index (HI)	0	0	0.19	0.39	0.53	0.65	0.72	0.76	0.78	0.8
Quadrant Homogeneity Index (QHI) (%) [102]	5	7	17	29	37	49	56	58	63	65
Simulated Quadrant Homogeneity Index ($SQHI$) (%)	0	0	3.1	8.2	24.2	34.3	40.8	49.9	51.8	52

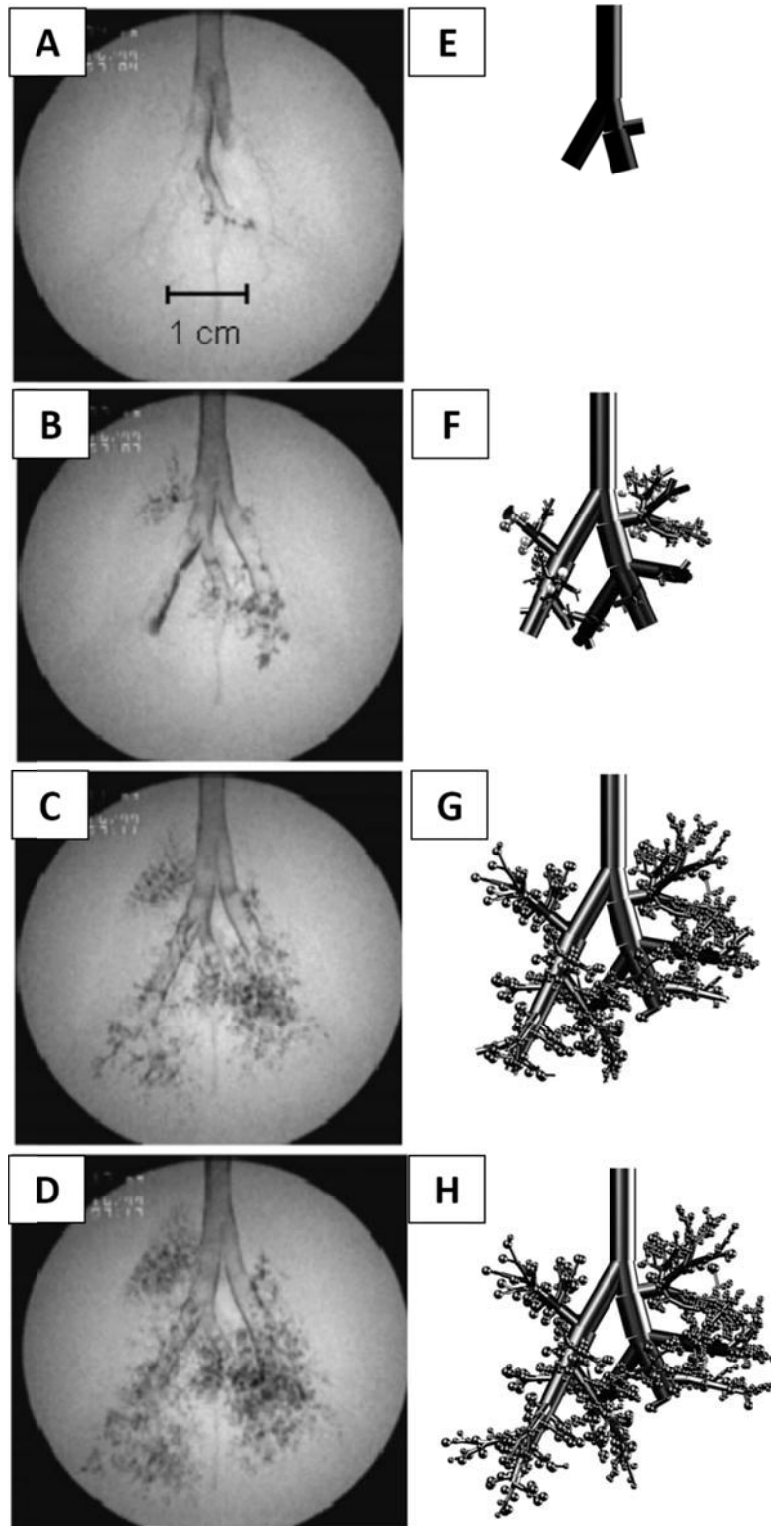


Figure 46: Images of sample experiments (A-D) [102] and our surfactant delivery simulation (E-H) at the end-inspiration. 1st (A, E), 3rd (B, F), 6th (C, G), and 10th (D, H) aliquot.

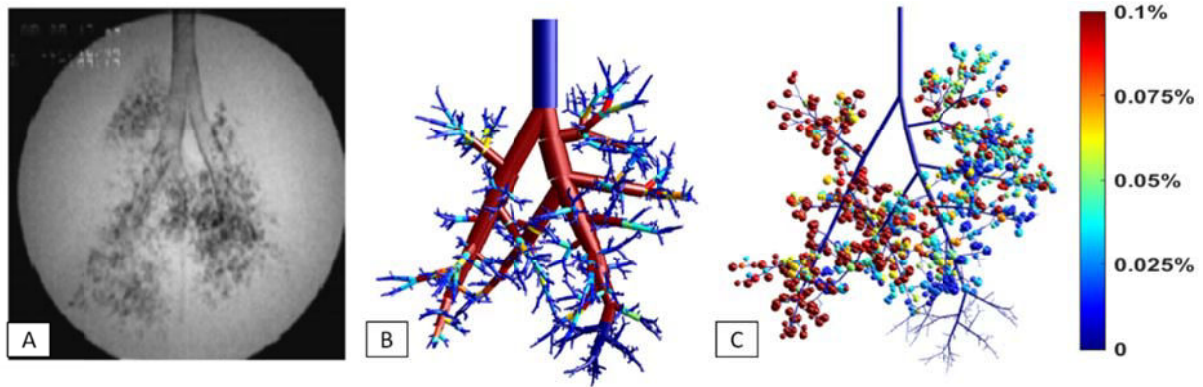


Figure 47: A) Liquid dose volume distribution during the 10th breath [102]. (B) Front view of the simulated end distribution of surfactant in a 3D model of rat lung. The color-coding represents the volume coating each airway divided by the initial instilled dose volume. C) The delivered surfactant to the terminal airways. The color of each bubble corresponds to the percentage of the initial dose volume, reaching each terminal airway.

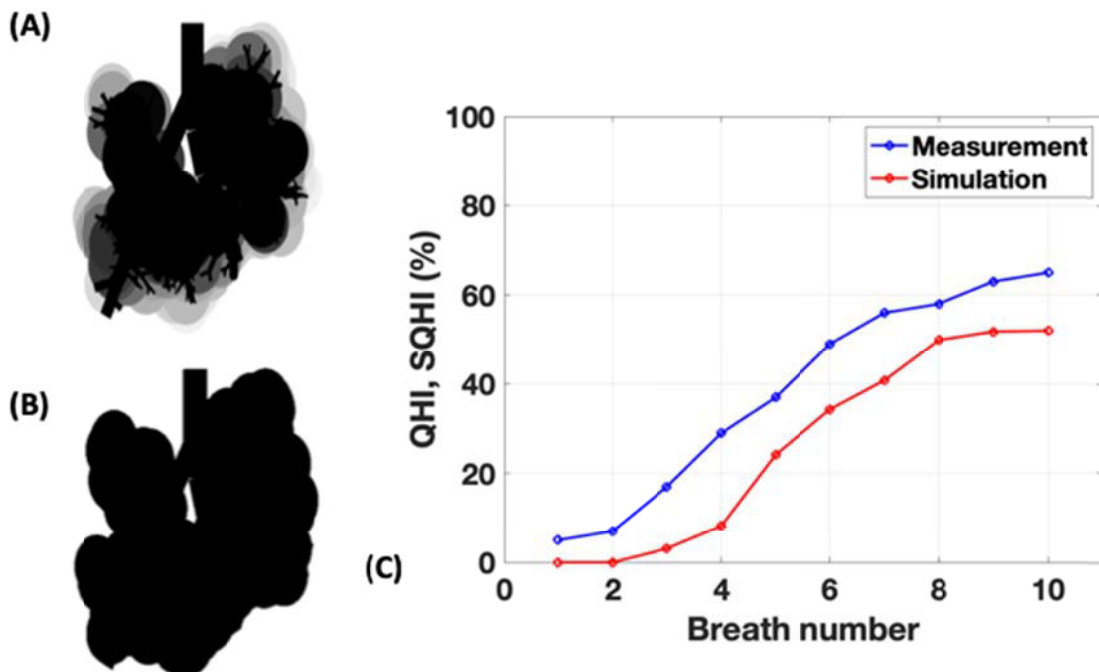


Figure 48: Comparison between measured Quadrant Homogeneity Index (QHI) (1) and simulated Quadrant Homogeneity Index (SQHI). A) Image computed from the numerical simulation to mimic the images of Figure 46. A sphere is plotted around each terminal branch. Its grayscale goes from white (no surfactant) to black (fully coated). When two spheres superimpose, their grey levels are added. B) The image obtained in the frame (A) is thresholded to obtain a black and white image (threshold is 90% grey), on which the SQHI can be computed as in [102]. C) Comparison of measured QHI and simulated QHI ($SQHI$) on 10 consecutive breaths.

Simulations of surfactant
delivery in rat, pig, and
human pulmonary airways
systems

4.1 A brief history of SRT

Surfactant replacement therapy has been introduced as a treatment for severe forms of respiratory distresses, namely the Newborn Respiratory Distress Syndrome (NRDS, also called IRDS for Infantile Respiratory Distress Syndrome) and the Acute Respiratory Distress Syndrome (ARDS).

Ashbaugh *et al.* [31] were the first in 1967 to report ARDS as a form of acute respiratory failure characterized by a diffuse, progressive inflammatory lung disease. In the last two decades, the definition of ARDS will be modified several times. In 1994, the American-European Consensus Conference (AECC) defined ARDS as the acute onset of hypoxemia and in 2012, the Berlin definition (BD) [33] addressed many of AECC limitations. In this definition, ARDS was categorized according to 3 terms, mild, moderate, and severe. In 2015, in the Pediatric Acute Lung Injury Consensus Conference (PALICC) [34], new developed pediatric-specific definitions and recommendations for treatment were introduced to cover the BD and AECC definitions for ARDS in children.

ARDS occurs in adult and children groups and affects males and females equally [147]. However, the occurrence of ARDS in children is 5–8 times less than in adults [148]. The incidence of children is about 0.003-0.128 % per year [149][150]. The published data show that the mortality rate has remained unchanged in the last two decades. Based on the AAEC definition of ARDS [32], 32 studies reported a mortality rate of 33.7% in children for ARDS. The mortality in western countries is reported between 4.3%-30.5% [151][152], and studies from Asia reported mortality as high as 61% [153]. In general, it is perceived that the mortality in children is lower than in adults.

NRDS is a different condition that affects specifically premature newborns. It is caused by a deficiency in surfactant production. The lack of surfactant results in non-homogeneous inflation of the pulmonary air spaces and stiff lungs, impairing the oxygen supply. Fujiwara *et al.* [55] reported the first successful trial of exogenous surfactant replacement therapy (SRT) in the 1980s to treat NRDS and after, SRT became a standard therapy for the newborn baby with RDS. With the help of this therapy, premature neonatal mortality drastically dropped in less than 30 years [56][57][58][59].

Despite being successful in premature infants, studies at this stage showed that routine surfactant administration is not recommended for treating ARDS in adults. Yet, due

to differences in surfactant preparations and delivery methods, a precise comparison of results among studies is complicated. In fact, SRT was initially successful in ARDS in adult patients and large sheep as well [68][69], and later in pediatric patients to age 21 [63]. These studies were at high dose volume per kg. Later a lower dose volume with a higher concentration strategy was applied that was successful in premature neonates, but it led to failure in adults [62][72][73][74][84][70][71].

One can wonder what is the origin of this difference. First, there are obvious differences between adult, children and neonate's lungs. Infants and young children have approximately 20 million alveoli after birth, while there are around 300 million alveoli by the age of 8 years. But it is not only a matter of number. Infants have also smaller alveolus. The size (diameter) of each alveolus is about 150–180 μm for children vs. 250–300 μm for adults [147]. If we consider just a symmetric tree, like Weibel's model of the lung, we can see that the airway surface area of a neonate, which has ~ 8 conducting airway generations, is $\sim 40\text{cm}^2$ while that of an adult, with ~ 15 generations, is $\sim 4,500\text{cm}^2$. The difference in airway surface area is a $\sim 110:1$ ratio that does not scale with weight since it significantly exceeds the kg weight ratio of $\sim 70:1$ adult to the neonate in this patient population [129][83][154]. Based on these two facts, the surface area that is available for gas exchange in children is smaller than the adult. This anatomic variation is prevalent until approximately 8 years of age. In addition to the sizing, the mechanical properties of the lungs of children and infants are different from adults too. We believe that these differences in size and mechanical properties affect the result of SRT, and we cannot just scale surfactant instilled dose volume per weight for adult and neonate. To have a successful outcome and see higher efficiency and homogeneity, we need to apply a higher dose volume per kg in adults compared to the neonates.

In 2015, Filoche *et al.* [129] published the first 3D structural model of SRT for the human symmetric airways system and simulated the delivery of a liquid bolus of surfactant mixture into the entire tracheobronchial tree [129]. They showed that a fraction of instilled dose volume is lost coating the airways. Therefore, the amount reaching the acinus is less than the instilled dose volume. In neonates' lung after reduction of instilled dose volume, SRT still reminds successful in clinical cases due to the relative smaller surface of the conduction airways. However, in adults, because of the lost coating layer at the low dose volume, SRT is not efficient at small instilled dose volumes. The significant difference influencing reminded dose volume in neonates compared to adults is the airway surface area available for coated volume.

What is the minimum initial instilled dose volume per kg for an adult to have optimal efficiency and homogeneity is still unclear. To address this question, we started to investigate the propagation of liquid (surfactant) in small animals and then moved to a bigger animal (pig) which is comparable to the human adult lung. At the last step, we modeled SRT in humans. Our human model includes symmetric and asymmetric for a big range of ages from neonate to adults and is based on the celebrated Weibel model [131] and on Raabe *et al.* [6] published data.

In our study, we simulated the final distribution of the surfactant into the rat, pig, and human lungs. In this chapter, we present the results of these simulations. In particular, we use these computations to assess the respective effects of lung asymmetry, dose volumes, flow rates, posture, mechanical properties, and instillation techniques like single, double, and repetitive dosing.

4.2 Surfactant delivery in the rat lung

4.2.1 Symmetric vs. asymmetric lung model

The asymmetric monopodial structure of the rat lung is one of the main factors that are likely to influence the delivery and inhomogeneity of the end distribution of surfactant. To investigate the effect of this asymmetry structure, we have first compared our model with a symmetric version of the rat airway tree. To create a symmetric airway tree, we used the average value of Raabe *et al.* [6] asymmetric tree measurement in each generation. In this symmetrized version of the tracheobronchial tree, all airways belonging to the same generation share the same diameter and length, which are the average length and diameter of the corresponding asymmetric airway tree. In addition, each bifurcation is symmetric. The rotation angles between successive bifurcation planes are equal and opposite ($+90^\circ$ and -90°). The branching angle θ is 45° . An interesting feature of these two models (symmetric and asymmetric) is that they both have almost the same total surface area.

In Figure 49A, the 3D geometry of this symmetric tree is presented. The color-coding represents the diameter value. Figure 49B displays a 3D color-coded view of the end distribution of surfactant for a single instillation delivery in the supine position. The color of each bubble corresponds to the volume of the surfactant reaching each terminal branch. The mechanical properties of Curosurf[®] and Survanta[®] are considered for this simulation ($\mu=30$ cP, $\sigma=30$ yn.cm⁻¹), see Table 16 for more details.

Table 16: Properties and condition of instilled surfactant in simulations

	Figure 49	Figure 50
Dose volume per kg (mL.kg ⁻¹)	1	1
Flow rate (mL.kg ⁻¹ .s ⁻¹)	30	30
Viscosity (cP)	30	30
Surface tension (dyn.cm ⁻¹)	30	30
Density (g.cm ⁻³)	1	1
Position	Supine	Supine
Lung model	Rat, symmetric	Rat, asymmetric

To be able to compare the results, we computed efficiency and homogeneity indices. The computed efficiency index for the symmetric tree is $\eta = 26.8\%$ and the homogeneity index of this distribution is $HI = 7.45$.

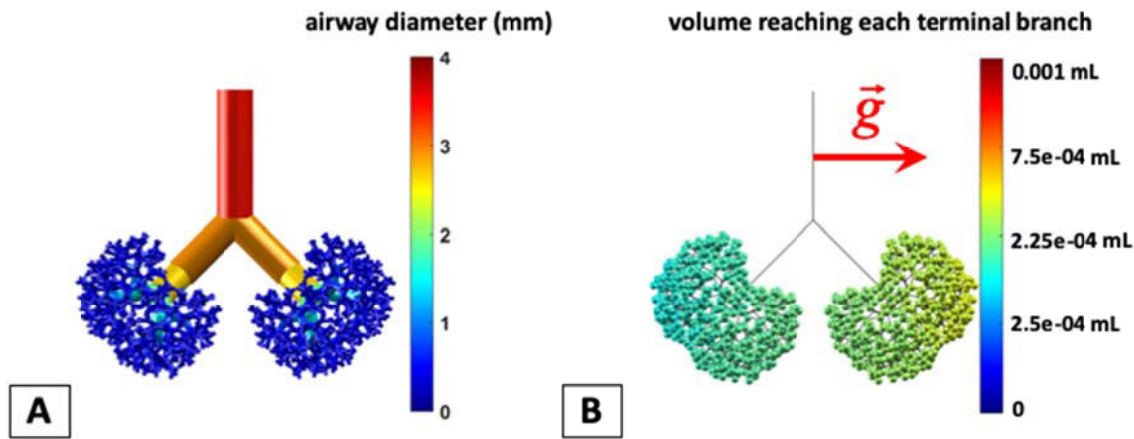


Figure 49: Simulation of surfactant delivery in a symmetric model of the rat airway tree. The simulation is performed on a 0.330-kg rat in the supine position. Surfactant viscosity is $\mu = 30$ cP, dose volume per kg is 1 mL.kg⁻¹, and flow rate per kg is 30 mL.kg⁻¹.s⁻¹. A) Front view of the symmetric model of the rat conducting airways. The color-coding represents the diameter value. B) 3D representation of the delivery (gravity is signaled by the red arrow). The color of each bubble corresponds to the volume of the surfactant reaching each terminal branch. The computed efficiency index is $\eta = 26.8\%$ and the homogeneity index of this distribution is $HI = 7.45$.

We compared this simulation to another simulation of delivery carried out in the same conditions (see Table 16) in a realistic asymmetric model of the rat pulmonary airway tree. Figure 50 presents the result of a single instillation at the end of the trachea of a 1 mL.kg⁻¹ dose volume per kg in the supine posture. Figure 50A displays the front view of a 3D tree with 1457 terminal airways. At the end of each of these airways, a sphere

is color-coded according to the fraction of the initial dose delivered to this specific end (delivered dose divided by the initial instilled dose volume). The computed efficiency index is $\eta = 4.9\%$. Figure 50B presents a 3D view of the surfactant left coating the airways for the same simulation, the color-coding representing this time the ratio of volume coating each airway to the initial instilled plug volume. The coating cost (the total volume left on the airway walls) is 0.32 mL (95% of the initial instilled volume).

Moreover, the end distribution of surfactant is far from being homogenous. As we can see, many terminal airways do not receive any surfactant at all. Figure 50C shows the end distribution of normalized delivered volumes (for each terminal airway, the volume of surfactant at the end of this airway divided by the sum of all end volumes). Figure 50D shows the histogram of these normalized volumes. The histogram confirms the highly non-homogeneous distribution, characterized by a very low homogeneity index $HI = 0.32$.

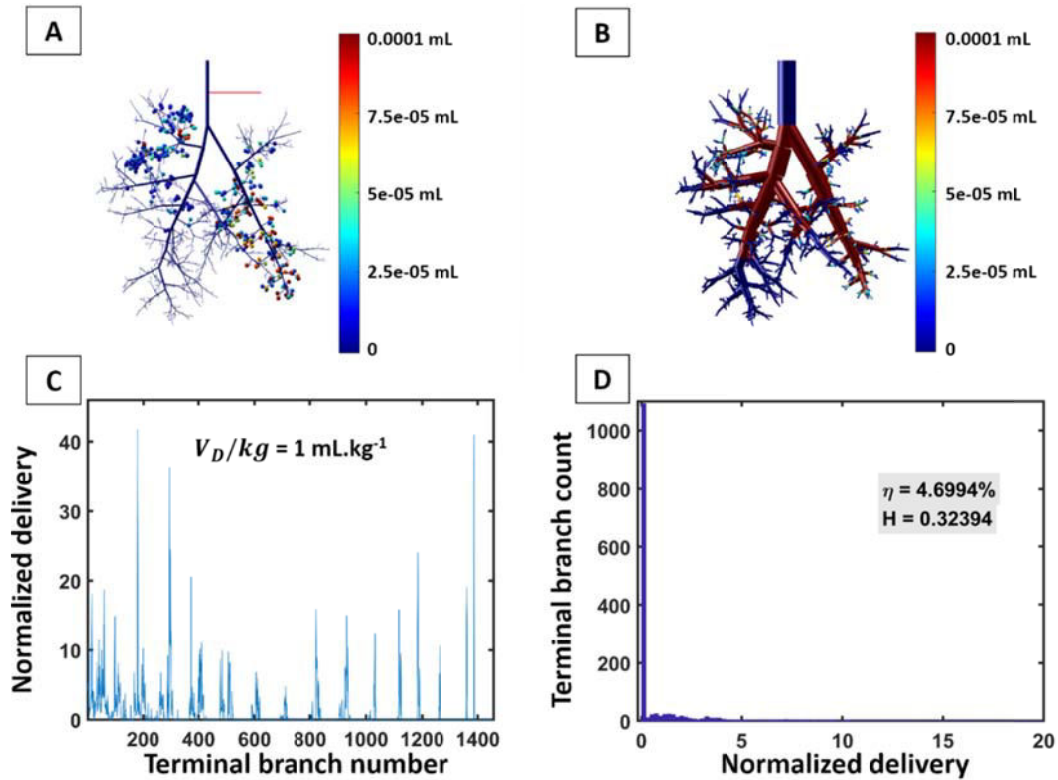


Figure 50: Simulation of surfactant delivery in a realistic model of the rat airway tree. The delivery is performed on a 0.330-kg rat in the supine position. Surfactant viscosity is $\mu = 30$ cP, dose volume per kg is 1 mL.kg^{-1} , and flow rate per kg is $30 \text{ mL.kg}^{-1}.\text{s}^{-1}$. The airway tree model has 31 generations and 1457 terminal branches. (A) 3D representation of the delivery. Each bubble represents a terminal branch, and the color of each bubble corresponds to the volume of the surfactant reaching the corresponding terminal branch. The computed efficiency index is $\eta = 4.9\%$. (B) Coating in the tree. The color-coding represents the volume coating each airway. (C) Normalized delivery $V_N(i)$ plotted vs. the terminal branch number. (D) Histogram of normalized delivery. The homogeneity index of this distribution is $HI = 0.32$, which corresponds to a highly inhomogeneous distribution.

In summary, the efficiency and the homogeneity indices (η and HI) of the symmetric tree are about 5.5 and 23 times larger than the ones found for the asymmetric tree, respectively (see Table 17). Moreover, all acini of the symmetric tree receive surfactant, which is not at all the case in the asymmetric tree. This comparison underlines the importance of accurately accounting for the asymmetrical monopodial structure of the airway tree when dealing with fluid transport.

Table 17: Computed efficiency and homogeneity indices of instilled surfactant

	Figure 49	Figure 50
Efficiency index (%)	26.8	4.9
Homogeneity index	7.45	0.32

4.2.2 Flow rate and dose volume

Using the asymmetric model of the rat conducting airways developed and tested above, we now explore the role of the initial dose volume V_D . Figure 51A and Figure 51B present 3D views of the end distributions of surfactant in a rat lung after a single instillation in the supine posture, with $V_D = 2 \text{ mL.kg}^{-1}$ and 5 mL.kg^{-1} , respectively (Table 18). One observes that increasing V_D reduces almost proportionally the coating cost, allowing now enough surfactant to reach the terminal regions. Indeed, the efficiency is raised from 4.9% to 41% and 76%, respectively, whereas the homogeneity index remains very poor, about 0.47 and 0.54. The amount of surfactant left coating the airways is displayed for both dose volumes (2 mL.kg^{-1} and 5 mL.kg^{-1}) in Figure 51C and Figure 51D. In both cases, the coating cost V_C is about 0.38 mL, only 15% more than the one found for a 1 mL.kg^{-1} instilled dose volume, whereas the amount of instilled dose volume is 2 and 5 times larger, respectively. V_C reaches a plateau above a given initial dose volume.

Table 18: Properties and condition of instilled surfactant

	Figure 51A	Figure 51B	Figure 52
Dose volume per kg (mL.kg^{-1})	2	5	1 - 8
Flow rate ($\text{mL.kg}^{-1}.\text{s}^{-1}$)	30	30	10 - 50
Viscosity (cP)	30	30	30
Surface tension (dyn.cm^{-1})	30	30	30
Density (g.cm^{-3})	1	1	1
Position	Supine	Supine	Supine
Lung model	Rat, asymmetric	Rat, asymmetric	Rat, asymmetric

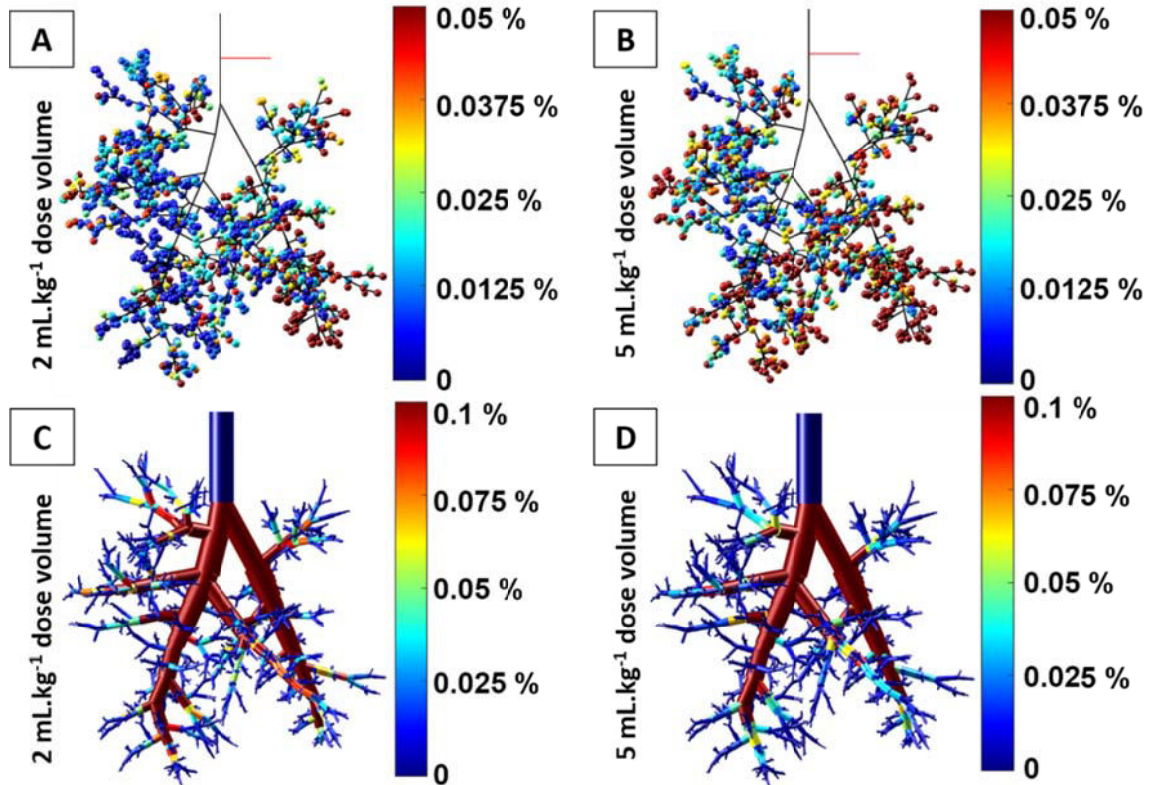


Figure 51: Simulated distributions of surfactant delivery in a 0.330-kg rat in the supine position. A) 3D Front view representing the distribution of volumes reaching the acini, for a dose volume of 2 mL.kg⁻¹. The efficiency index is $\eta = 41\%$. B) Same figure, for a dose volume of 5 mL.kg⁻¹. The efficiency index is $\eta = 76\%$. C) 3D front view displaying the amount of surfactant left coating the airways, in simulation (A). The color-coding represents the volume left coating each airway divided by the initial instilled dose volume. The homogeneity index is $HI=0.47$, D) Same figure as (C), corresponding to simulation (B). The homogeneity index is $HI=0.54$.

Table 19: Computed efficiency and homogeneity indices of instilled surfactant

	Figure 50	Figure 51A	Figure 51B
Efficiency index (%)	4.9	41	76
Homogeneity indices	0.32	0.47	0.54

Figure 52 shows the efficiency index (solid line, filled symbols) and homogeneity index (dashed line, open symbols) for a wide range of dose volumes per kg (1-8) for tracheal flow rates of 10, 20, 30, 40, and 50 mL.kg⁻¹.s⁻¹. As we already mentioned, increasing the dose volume increases efficiency. In contrast, changing the flow rate in the simulations does not significantly alter the efficiency and coating cost, as shown in Figure 52

(efficiency), Figure 53A (absolute amount), and Figure 53B (fraction of the initial volume). Figure 53A illustrates that, for a given flow rate, the total coating volume is almost identical for different doses. Figure 53B shows that the ratio V_C/V_D slowly increases with the flow rate. This is due to the thicker trailing film left by the plugs propagating through the tree. At the same time, due to the increased velocity, the influence of gravity decreases and the splitting factor gets closer to 0.5. However, if V_D is too small, only a small number of terminal airways are adequately supplied with the surfactant, which means that both efficiency and homogeneity plummet, independently of the velocity.

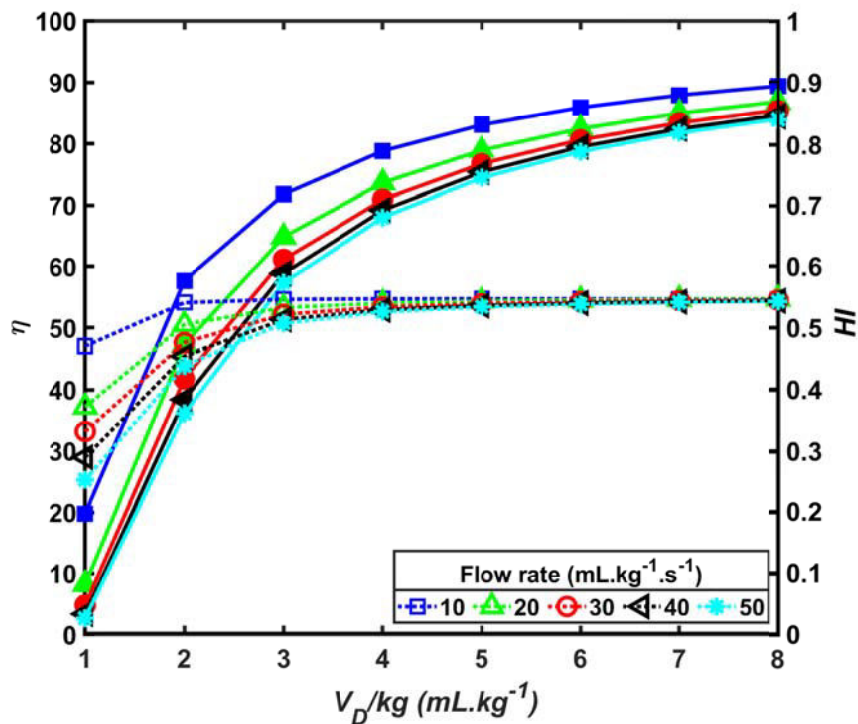


Figure 52: Efficiency index η (solid line, filled symbols) and homogeneity index HI (dashed line, open symbols) vs. dose volume per kg for tracheal flow rates of 10, 20, 30, 40, and 50 mL.kg⁻¹.s⁻¹ in the rat lung.

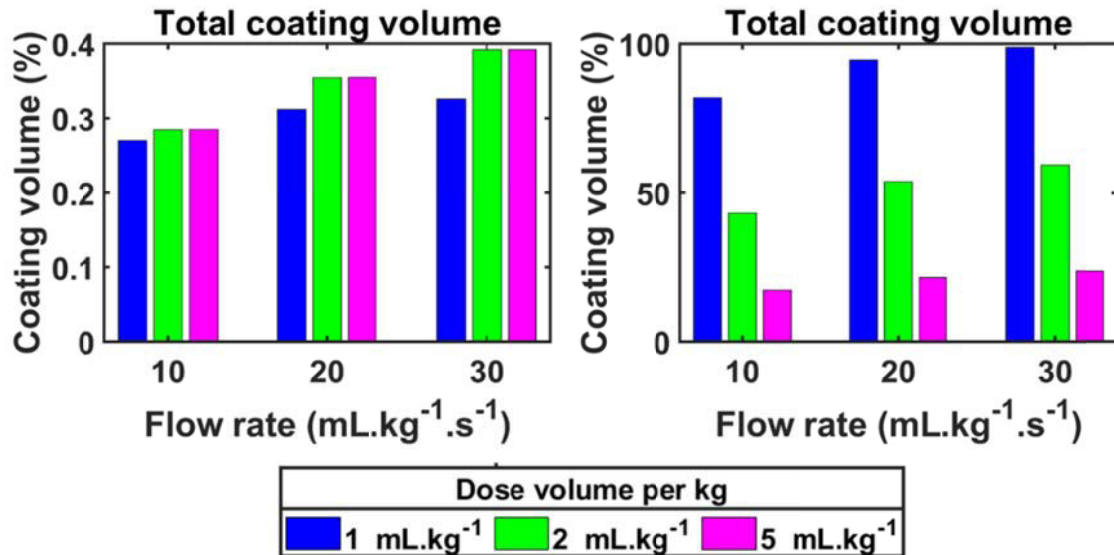


Figure 53: Total coating cost vs. flow rate for a 0.330-kg rat lung in the supine position. A) The absolute amount of coating volume in the entire tree, B) coating volume divided by the initial instilled dose volume.

All simulations in this section were performed in supine position but with our model, it is possible to simulate the instillation of surfactant in other postures. In the next section, we investigate the effect of posture on efficiency and homogeneity indices.

4.2.3 Assessing the role of posture

Simulations of surfactant delivery have been performed for various body postures: left lateral decubitus (LLD), right lateral decubitus (RLD), supine (S), prone (P), 45-degree angle (halfway) between supine-LLD (called SL) and the 45-degree angle between supine-RLD positions (SR). Figure 54 displays the behavior of the efficiency index η (open symbols) and homogeneity index HI (filled symbols) in different postures. The results are presented for a range of dose volumes, for 3 different flow rates and 6 different postures: 4 are single instillation, i.e., LLD, RLD, supine, prone, and 2 are multiple instillations, i.e., $\frac{1}{2}$ supine + $\frac{1}{2}$ prone (called S+P), $\frac{1}{3}$ supine/LLD + $\frac{1}{3}$ supine/RLD + $\frac{1}{3}$ prone (called SL+SR+P) (see Table 20). In all cases, the homogeneity remains stable at a low level, with HI below 1, the signature of a highly non-homogeneous delivery. In all cases also, the efficiency increases with the dose volume and slightly decreases with the flow rate. As one can see in Figure 54A-D, the efficiency and the homogeneity indices do not seem to depend much on the posture for a single instillation. In these cases, for volume doses per kg larger than 2 mL.kg⁻¹, the efficiency reaches a plateau and remains larger than 50 %. If one goes below this threshold dose volume, the efficiency-dose plot exhibits a steep slope and

decreases significantly. When the surfactant is instilled in 2 and 3 dose volumes on the contrary (in S+P and SL+SR+P postures), both efficiency and homogeneity decrease as compared to the single instillation situation. This reduction is even aggravated for a more significant number of injections (see Figure 54F). For multiple instillations, one also observes an increase in the threshold volume dose. This can be easily understood: splitting the initial dose volume into several smaller doses, in order to inject in different postures, is detrimental to the efficiency.

Table 20: Properties and condition of instilled surfactant

Figure 54	A	B	C	D	E	F
Dose volume per kg (mL.kg ⁻¹)	1-8	1-8	1-8	1-8	1-8	1-8
Flow rate (mL.kg ⁻¹ .s ⁻¹)	30	30	30	30	30	30
Viscosity (cP)	30	30	30	30	30	30
Surface tension (dyn.cm ⁻¹)	30	30	30	30	30	30
Density (g.cm ⁻³)	1	1	1	1	1	1
Position	LLD	RLD	Supine	Prone	S+P	SL+SR+P

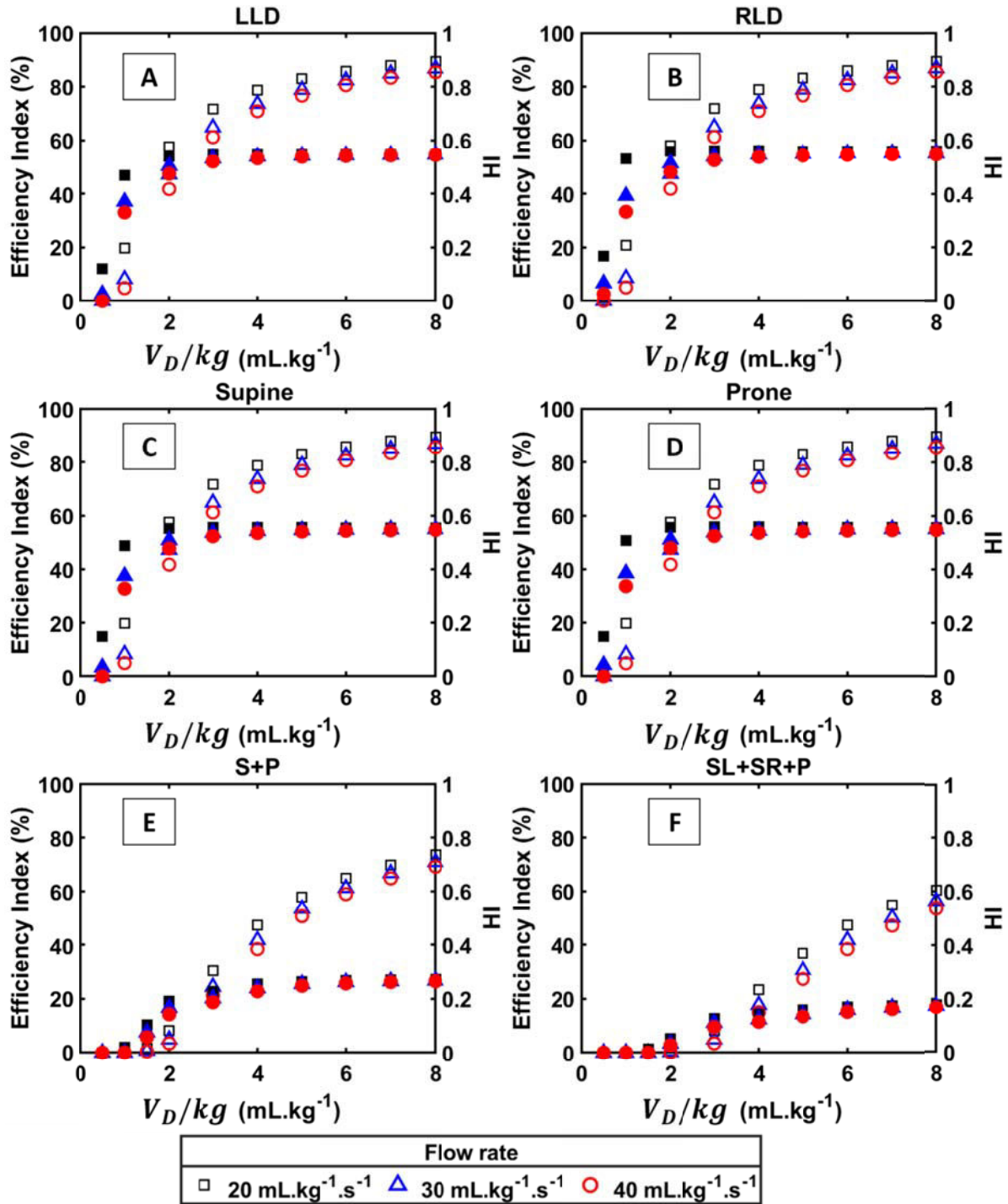


Figure 54: Efficiency index η (open symbols) and homogeneity index HI (filled symbols) as a function of dose volume, computed in a 0.330-kg rat lung, for three different flow rates, (viscosity $\mu = 30$ cP). A) Single instillation in the LLD position. B) Single instillation in the RLD position. C) Single instillation in the supine position. D) Single instillation in the prone position. E) Double instillation in supine and prone positions (S+P). F) Three instillations, one-half way between LLD and supine, one-half way between RL and supine, and one in prone posture (SL+SR+P).

4.2.4 Mechanical properties of surfactant

As mentioned earlier, several clinical trials of SRT in adults have shown no significant improvement in the number of survival of ARDS/ALI [62][72][73][74][84][70][71]. The question then arises of the origin of this failure: might it be due to the type of surfactant that was used, to its phospholipid concentration, or is there some mechanical origin in which not only the dose volume per (mL.kg^{-1}) but also the surfactant properties (density, viscosity, and surface tension) would play the primary role. To shed light on this issue, we have performed simulations of delivery for various types of surfactant.

4.2.4.1 Viscosity

A critical parameter in fluid transport is the fluid viscosity. The surfactant viscosity depends on the type of surfactant, on the phospholipid concentration, on shear rate and temperature. For example, for a concentration of 35 mg of PL/ml, a shear rate of 300 s^{-1} , and a body temperature of 37°C , Survanta and Infasurf viscosities are 25.3 cP and 10.4 cP, 17 and 7 times larger than the low Exosurf viscosity, respectively (Exosurf viscosity being 1 cP at a clinical concentration of 13.5 mg of phospholipid/ml). The temperature dependence of viscosity is also complicated and there are distinct differences between Survanta and Infasurf: a temperature increase leads to an increase of viscosity in Survanta while it decreases the viscosity of Infasurf at a fixed shear rate [104][105]. As one can see, the range of values is vast. For Survanta, viscosity can typically vary from 9 to 52 cP [105].

Figure 55 shows the computed efficiency and homogeneity indices vs. dose volume (LLD posture, $30 \text{ mL.kg}^{-1}.\text{s}^{-1}$ flow rate, 1-4 mL.kg^{-1} dose volume per kg), for the smallest and largest values of the viscosity of Survanta (Table 21). A larger viscosity increases the thickness of the trailing film left by the propagating plugs and lowers the efficiency, especially at low dose volume. A larger viscosity reduces the homogeneity as well.

Table 21: Properties and condition of instilled surfactant

	Figure 55
Dose volume per kg (mL.kg^{-1})	1-4
Flow rate ($\text{mL.kg}^{-1}.\text{s}^{-1}$)	30
Viscosity (cP)	9 and 52
Surface tension (dyn.cm^{-1})	30
Density (g.cm^{-3})	1
Position	LLD
Lung model	Rat, asymmetric

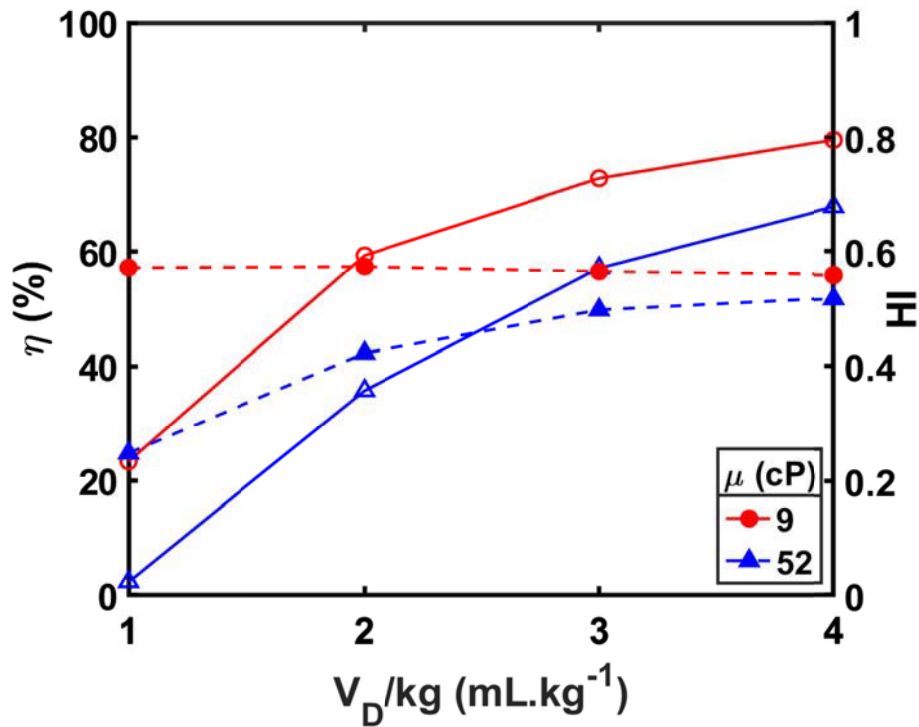


Figure 55: Efficiency index η (open symbols with solid line) and homogeneity index HI (filled symbols with the dashed line) as functions of the dose volume for Survanta with two viscosity, 9 cP (concentration: 25 mg of PL/ml, 770 s^{-1} shear rate and $37 \text{ }^\circ\text{C}$) and 52 cP (concentration: 35 mg of PL/ml, 70 s^{-1} shear rate and $37 \text{ }^\circ\text{C}$).

4.2.4.2 Surface tension

The surfactant instilled in SRT is in reality inside a solution. The surface tension changes with the concentration of surfactant in solution: it decreases at a higher concentration of surfactant molecules. In addition, different surfactants have different surface tensions. In this section, we investigate the effect of surface tension on the efficiency and homogeneity indices. We run the simulation for three different surface tension (3, 30, and 90 dyn.cm^{-1}) in the same conditions (see Table 22). In Figure 56,

we can see the evolution of the efficiency index η (open symbols with solid line) and of the homogeneity index HI (filled symbols with the dashed line). Increasing the surface tension leads to an increase in both efficiency and homogeneity for all applied dose volumes. In all applied conditions, the homogeneity index is smaller than 1 which is the sign of a highly non-homogeneous delivery. For higher values of the surface tension, the homogeneity index tends to explore a narrower range: for example, for the surface tension of 90 dyn.cm⁻¹, the index varies between 0.49 and 0.55.

Table 22: Properties and condition of instilled surfactant

	Figure 56
Dose volume per kg (mL.kg ⁻¹)	1-4
Flow rate (mL.kg ⁻¹ .s ⁻¹)	30
Viscosity (cP)	30
Surface tension (dyn.cm ⁻¹)	3, 30, 90
Density (g.cm ⁻³)	1
Position	LLD
Lung model	Rat, asymmetric

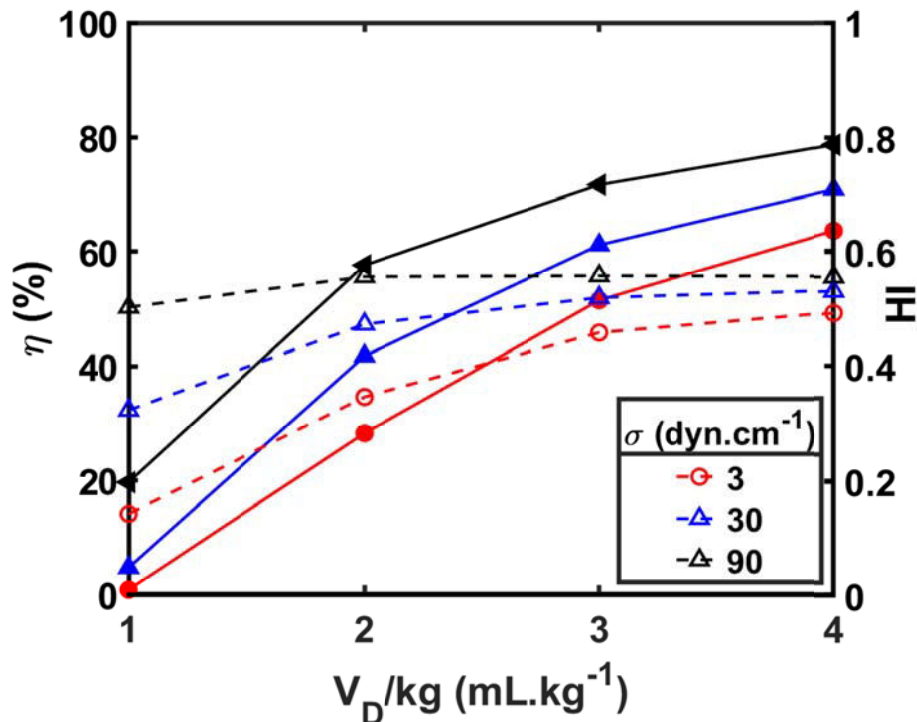


Figure 56: Efficiency index η (solid line) and homogeneity index HI (dashed line) as functions of the dose volume for 3 different values of the surface tension.

4.2.5 Instillation technique

There are different ways to instill surfactant into the trachea. A first possibility consists of instilling the totality of the surfactant in one single volume. One can also insert the dose volume in 2 or 3 times, for different postures (as we already simulated). Another interesting option for improving the efficiency of surfactant delivery is multiple aliquot approaches. In this approach, we can instill the surfactant in 10 or more aliquots in the same posture during successive breaths. In the chapter of the mathematical and numerical model of surfactant delivery section 3.6, we have compared numerical simulations performed using our model with experimental results obtained by Cassidy *et al.* on Wistar rats [102]. Simulations of surfactant delivery have been carried out using the same viscosity, surface tension, volume, posture, and velocity of experiments. In the experiments, the surfactant was being delivered in multiple aliquots, 0.053 mL per breath (0.1 mL.kg^{-1}) during the first 10 breaths.

In both cases, we could observe that the liquid plugs propagate increasingly deeper down the airway tree at each successive breath. The total efficiency of the simulated delivery is about 59%, a much better result than the efficiency of the single-instillation delivery simulation in the same conditions which is close to 5%. This high efficiency is due to the pre-existing film lining the airways.

We now study using our model the effect of increasing the initial dose volume per kg, from 1 to 2 mL.kg^{-1} (Table 23). Figure 57 presents the efficiency and homogeneity indices computed for 1, 5, 10, and 15 aliquots, respectively. We observe an apparent increase in both indices for a larger number of aliquots. However, the homogeneity index remains always smaller than 1 which indicates very poorly homogeneous distributions. This poor homogeneity is confirmed visually in the experiments, at all dose volumes. The origin of this relative insensitivity of the inhomogeneity to the dose volume is to be found in the monopodial airway structure (i.e., the strong branching asymmetry): increasing the dose volume simply increases the delivery to the already favored alveoli.

Table 23: Properties and condition of instilled surfactant

	Figure 57
Dose volume per kg (mL.kg^{-1})	2
Flow rate ($\text{mL.kg}^{-1}.\text{s}^{-1}$)	30
Viscosity (cP)	30
Surface tension (dyn.cm^{-1})	30
Density (g.cm^{-3})	1
Position	LLD

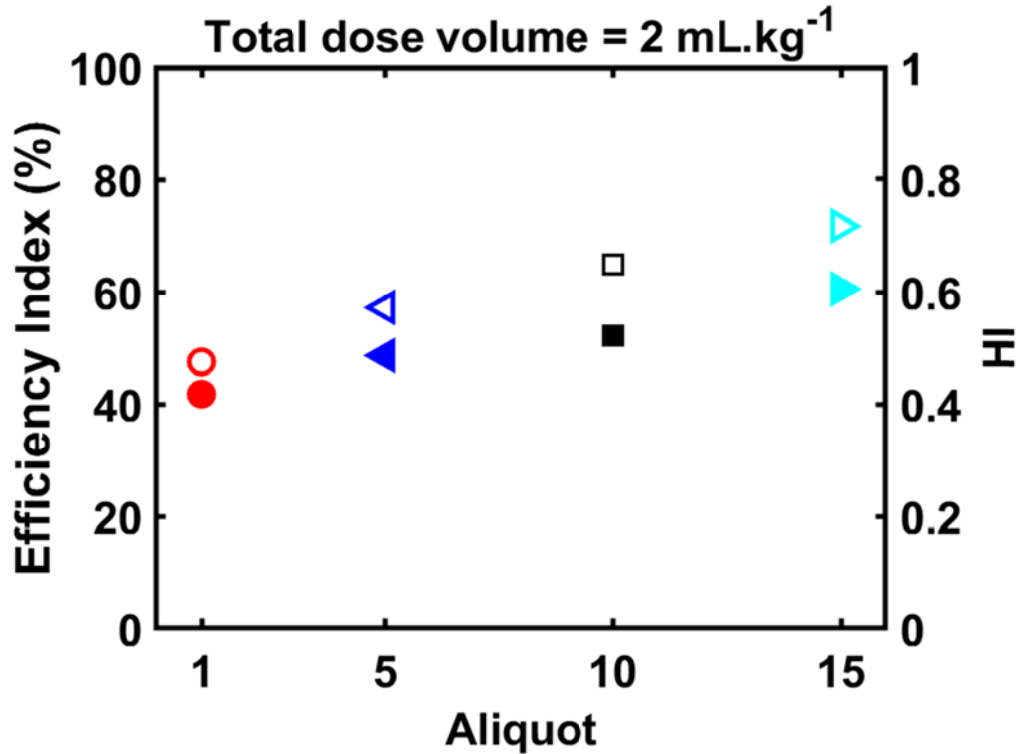


Figure 57: Efficiency index η (filled symbols) and homogeneity index HI (open symbols) computed when changing the number of aliquots for a given initial dose volume, in a 0.330-kg rat lung, (total dose volume: 2 mL.kg^{-1} , flow rate: $30 \text{ mL.kg}^{-1}.\text{s}^{-1}$, LLD, viscosity $\mu = 30 \text{ cP}$).

4.2.6 Conclusion

In the previous chapter, we have shown that the rat respiratory airway system has an asymmetric structure. To assess the importance of using a realistic geometrical model, we have compared the efficiency and homogeneity indices of the symmetric model with the asymmetric model. Our results showed that the efficiency and the homogeneity indices of the symmetric tree are about 5.5 and 23 times larger than the ones found for the asymmetric tree, respectively. In addition, in the asymmetric tree, more than half of the acini do not receive surfactant while all acini receive surfactant in the case of a

symmetric tree. This comparison underlines the importance of accurately accounting for the asymmetrical monopodial structure of the airway tree in fluid transport. On the other hand, the mechanical properties of the surfactant and the instillation condition also have a substantial effect on the end distribution of surfactant in the lung. Table 24 shows the effect of these parameters on the efficiency and homogeneity indices. Increasing the dose volume and the viscosity leads to an increase in both indices while increasing the flow rate and the surface tension resulted in a decrease of these indices.

If one now fixes the dose volume, the viscosity, the flow rate, and the surface tension, changing the posture (supine, prone, LLD, and RLD) for a single instillation does not significantly modify the efficiency and homogeneity (see Figure 54), whereas going to multiple aliquot instillation leads to a significant increase in efficiency and homogeneity. Table 24 provides a general overview of these trends. To give an example and show the importance of the effect of the combination of these parameters in Figure 58, we plotted the normalized delivery of terminal branches in two different conditions. In Figure 58A, the surfactant is instilled in 10 aliquots (multiple instillation) at 4 mL.kg⁻¹ dose volume per kg while in Figure 58B the delivery is performed in one single instillation in LLD posture and for dose volume per kg of 1 mL.kg⁻¹ (see Table 25 for full details on the applied conditions). The efficiency and homogeneity computed in Figure 58A are $\eta = 93.1\%$ and $HI = 0.75$, while in Figure 58B they are about 93 and 4.7 times smaller, respectively.

Table 24: The efficiency and homogeneity in different applied conditions

		Efficiency (η)	Homogeneity (HI)
Flow rate	↑	↓	↓
Dose volume	↑	↑	↑
Viscosity	↑	↓	↓
Surface tension	↑	↑	↑
Multiple instillation	↑	↑	↑
Posture		Same in supine, prone, LLD, and RLD	

Table 25: Properties and condition of instilled surfactant

	Figure 58A	Figure 58B
Dose volume per kg (mL.kg^{-1})	4	1
Flow rate ($\text{mL.kg}^{-1}.\text{s}^{-1}$)	10	40
Viscosity (cP)	10	40
Surface tension (dyn.cm^{-1})	40	10
Density (g.cm^{-3})	1	1
Position	LLD	LLD
Instillation technique	10 aliquot	Single instillation

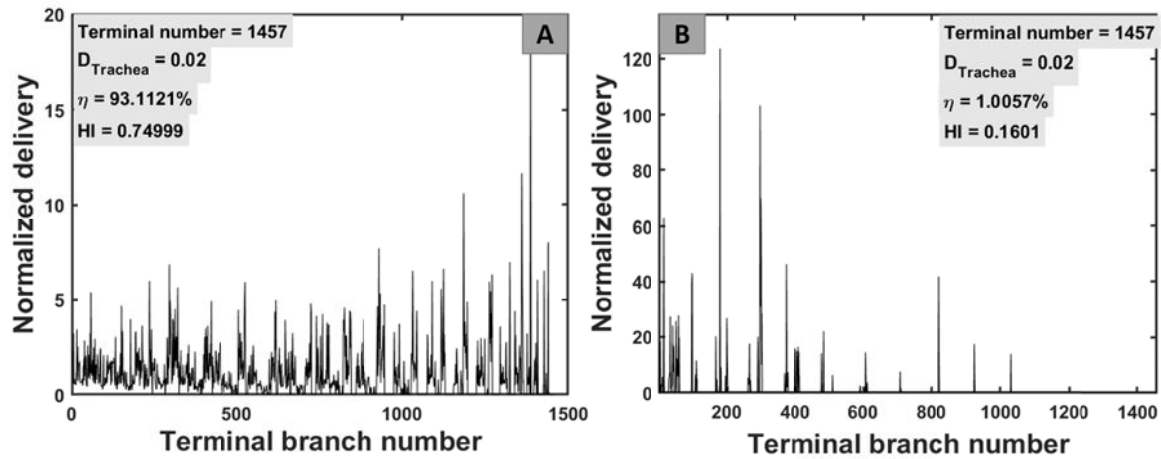


Figure 58: Normalized deliver vs. terminal branches. A) 4 mL.kg^{-1} dose volume per kg, 10 $\text{mL.kg}^{-1}.\text{s}^{-1}$ flow rate, and 10 cP viscosity in LLD position. B) 1 mL.kg^{-1} dose volume per kg, 40 $\text{mL.kg}^{-1}.\text{s}^{-1}$ flow rate, and 40 cP viscosity in LLD position.

Our simulations also show that the instilled dose volume is a critical parameter. The coating cost in the asymmetric lung of the rat increases at first when increasing the instilled dose volume, but it saturates to a fixed value above a critical initial dose volume. Therefore it is always crucial to instill an initial quantity of surfactant much larger than this critical dose volume to have enough liquid reaching the alveolar region. In addition, we have seen that the coating cost at saturation (and consequently the ratio of the coating volume to the initial plug volume) is almost independent of the flow rate.

In this section, we have seen that the efficiency and homogeneity indices depend on the initial applied condition and mechanical properties of the surfactant. As a consequence, the resulting efficiency can range from 0 to almost 100% (Figure 58). We now turn to a bigger animal, the pig. Indeed, the model developed in 2015 by Filoche, Tai, and Grotberg showed that the overall size of the lung plays an essential role in determining

the features of the final surfactant distribution [129]. Any experimental animal model should, therefore, have a size comparable to the human adult lung, which is the case for the pig. However, the pig pulmonary airway system is very specific, different from the human because it has a monopodial branching structure similar to the rat lung [20], and different from the rat in terms of design, overall structure, and surface area.

4.3 Surfactant delivery in the pig lung

The pig lung is comparable to the adult human lung in terms of volume but has a monopodial branching structure similar to the rat [20]. To investigate the propagation of the surfactant in the pig respiratory airway, we have built an asymmetric model based on the morphometric measurements performed by Md. Azad *et al.* [15]. This geometrical model of the pig bronchial tree starts at the trachea and ends in the respiratory bronchioles. Its volume is 45 times bigger than the rat lung, and its surface area is about 12 times bigger. The first question that comes to mind is therefore: is the propagation of surfactant similar to the rat? Or do the specific structure and size of the pig lung significantly modify the results we have seen so far? To answer these questions, we examine hereafter the respective effects of dose volume, flow rate, posture, mechanical properties, and instillation technique on surfactant delivery in the pig and compare them with the previous results obtained on the rat lung.

4.3.1 Flow rate and dose volume

First, we compare the propagation and coating layer for low vs. high dose volumes ($V_D = 1 \text{ mL.kg}^{-1}$ vs. $V_D = 4 \text{ mL.kg}^{-1}$) in Figure 59 (see Table 26 for the details of the delivery conditions). The pig airway tree model contains 21 generations and 1712 terminal branches. Figure 59A displays a 3D front view of the distribution of volumes reaching the acini, for an initial dose volume per kg of 1 mL.kg^{-1} while Figure 59B presents the same figure for a higher value (4 mL.kg^{-1}). The computed efficiency indices are $\eta = 60\%$ and $\eta = 90\%$, respectively. Each sphere represents a terminal branch that has received surfactant, and the color of the sphere corresponds to the volume of surfactant reaching the corresponding terminal branch. Figure 59C shows a 3D front view of the amount of surfactant left coating the airways in simulation (A). The color-coding represents the volume left coating each airway divided by the initial instilled dose volume. Figure 59D shows the same figure as (C) corresponding to simulation (B). In the first case (low dose volume), the coating cost V_C is about 13.33 mL while in the second case, it is 14.69 mL, i.e., only 10% more whereas the amount of initial instilled dose volume is 4 times larger. Figure 59E illustrates the normalized delivery $V_N(i)$ plotted vs. the terminal branch number of simulation (A), and Figure 59F is the same plot for simulation (B). The homogeneity index is 0.31 in the low dose volume case and 0.30 in the high dose volume one.

Table 26: Properties and conditions of instilled surfactant

	Figure 59A	Figure 59B	Figure 60
Dose volume per kg (mL.kg^{-1})	1	4	1, 2, 3, 4
Flow rate ($\text{mL.kg}^{-1}.\text{s}^{-1}$)	4	4	1, 3, 6
Viscosity (cP)	30	30	30
Surface tension (dyn.cm^{-1})	30	30	30
Density (g.cm^{-3})	1	1	1
Position	LLD	LLD	Supine
Lung model	Pig, asymmetric	Pig, asymmetric	Pig, asymmetric

One observes that increasing V_D reduces almost proportionally the coating cost, allowing now enough surfactant to reach the terminal regions. Indeed, the efficiency is raised from 60% to 90%, whereas the homogeneity index remains very poor, about 0.3. Delivery of surfactant in terms of efficiency for low dose volume is very high compared to the rat lung. In our simulations in rat lung, the efficiency was about 5% for 1 mL.kg^{-1} while it is 60% for the pig. This observation is reverse to what we expected based on the size of the lung. It shows that the lung volume is not the only parameter that we must take into account for understanding the scaling properties of SRT. The explanation for this specific behavior of the delivery in pig lung lies in the lung structure. This lung structure plays an essential role when it comes to liquid delivery and we cannot compare directly the results in different species. We can note also that despite exhibiting very different efficiencies, the homogeneity index is very similar (about 0.3) in both animals.

Figure 60 displays the efficiency index (solid line, filled symbols) and the homogeneity index (dashed line, open symbols) for a realistic range of dose volumes per kg ($1\text{-}4 \text{ mL.kg}^{-1}$) and for various tracheal flow rates, 1, 3, and 6 $\text{mL.kg}^{-1}.\text{s}^{-1}$. As already mentioned, increasing the dose volume increases efficiency. Increasing the flow rate has a moderate impact on efficiency: it leads to a decrease in efficiency of about 10% at a low flow rate and does not significantly alter the efficiency at higher flow rates. One interesting point though is that neither the dose volume or the flow rate seems to have any impact on the homogeneity of the end distribution of surfactant.

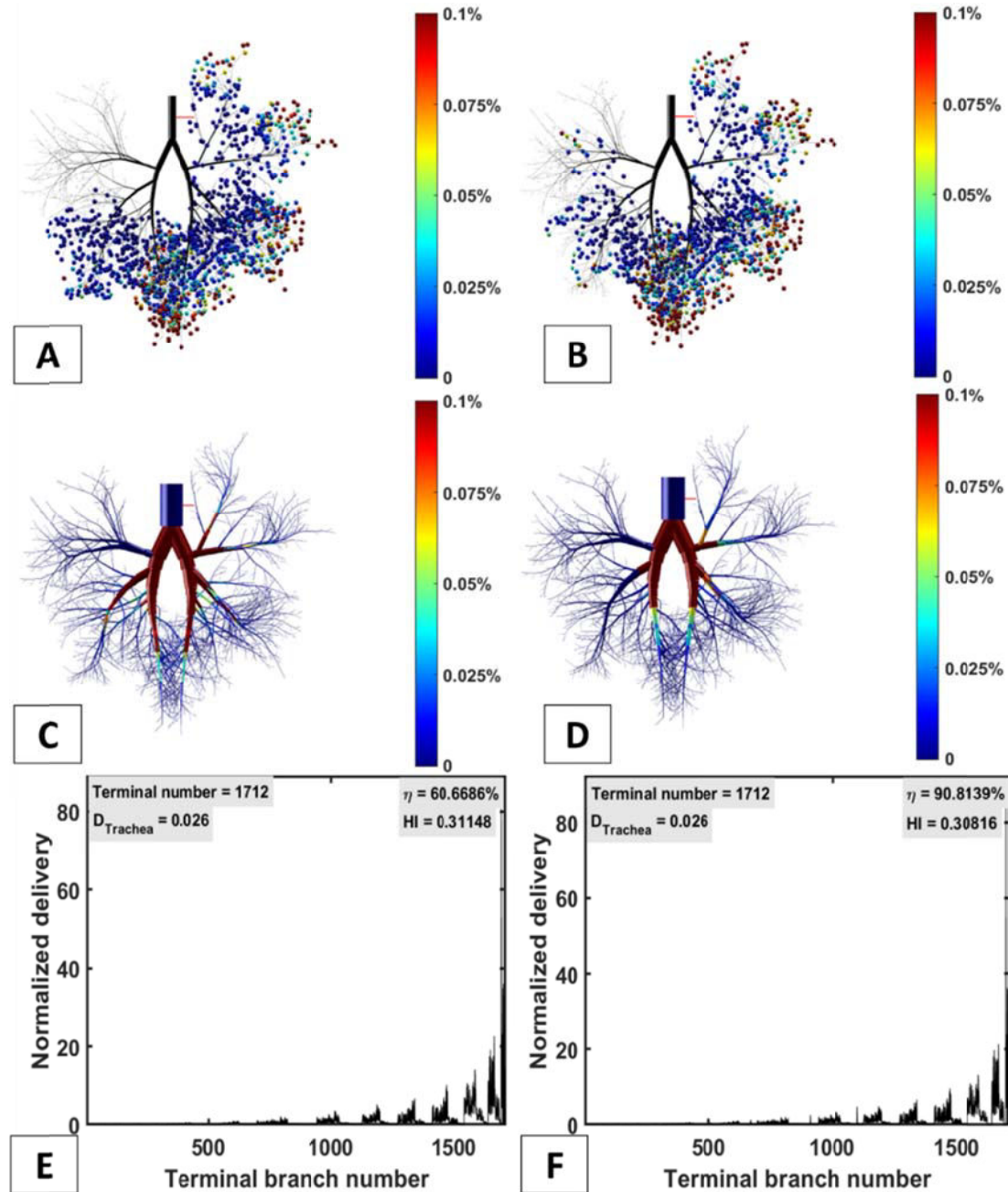


Figure 59: Simulation of surfactant delivery in the pig airway system. (A) 3D Front view representing the distribution of volumes reaching the acini, for a dose volume per kg of 1 mL.kg⁻¹. The computed efficiency index is $\eta = 60\%$. (B) Same figure, for a dose volume per kg of 4 mL.kg⁻¹. The calculated efficiency index is $\eta = 90\%$. Each sphere represents a terminal branch, and the color of the sphere gives the volume of surfactant reaching the corresponding terminal branch. (C) 3D front view displaying the amount of surfactant left coating the airways, in simulation (A). The color-coding represents the volume left coating each airway divided by the initial instilled dose volume. (D) Same figure as (C), corresponding to simulation (B). (E) Normalized delivery $V_N(i)$ plotted vs. the terminal branch number of simulation (A). (F) Same figure as (F) plotted for simulation (B).

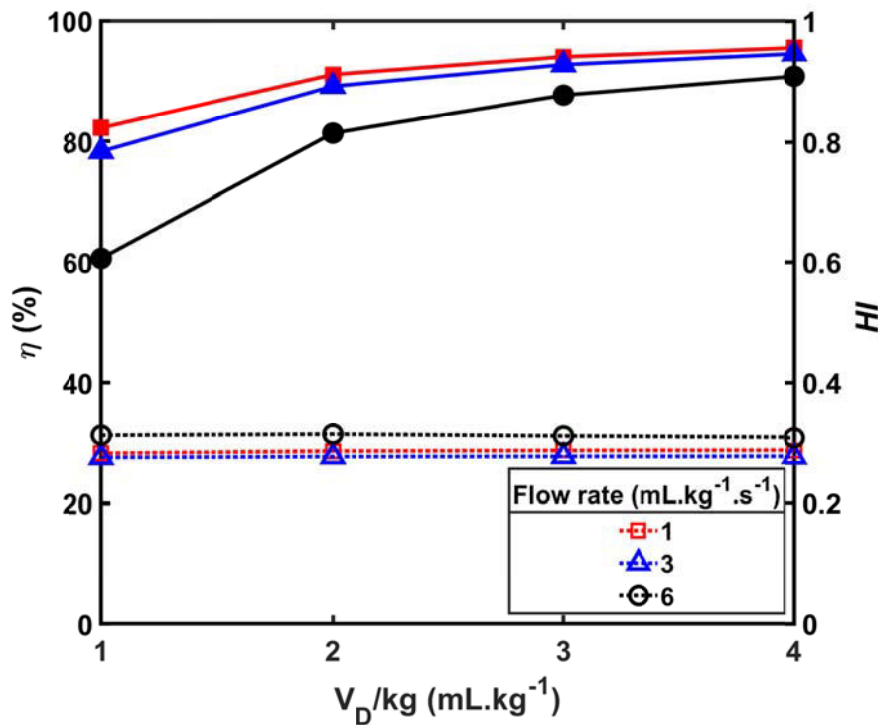


Figure 60: Efficiency index (solid line, filled symbols) and homogeneity index (dashed line, open symbols) vs. the dose volume per kg for tracheal flow rates of 1, 2, 3, and 4 mL.kg⁻¹.s⁻¹ in the pig lung. All deliveries are performed in the supine position.

4.3.2 Assessing the role of posture

As in the rat study, several positions have been tested. Figure 61 displays the behavior of the efficiency index (solid line) and homogeneity index (dashed line) for different postures. The results are presented for a range of dose volumes, for 3 different flow rates and 5 different postures. The delivery is achieved through 2 single instillations in LLD and supine position, 2 double instillations, 1/2 supine + 1/2 prone (called S+P) and 1/2 LLD + 1/2 RLD (called L+R), and finally one triple instillation in 1/3 supine/LLD + 1/3 supine/RLD + 1/3 prone (called SL+SR+P).

Also similar to the rat simulations, the surfactant delivery performed in one single instillation exhibits a higher efficiency. The efficiency indices vs. flow rate and dose volume are found similar in the (S+P) and (L+R) cases, only slightly better in the L+R case. As observed in the simulations of surfactant delivery in rat lungs, increasing the dose volume or decreasing the flow rate leads in both cases to an increase in the delivery efficiency. However, unlike in the rat lungs, we observe that the efficiency

computed in (S+P) position is smaller than the one in (L+R): e.g., 40% lower for a 1 mL.kg⁻¹ dose volume.

In the case of the rat, we have seen that for dose volumes per kg larger than 2 mL.kg⁻¹, the efficiency reaches a plateau and remains larger than 50 % above a certain critical value of the dose volume. Below this value, the efficiency-dose plot exhibits a steep slope and decreases significantly. In contrast, we do observe see this threshold in the pig lung for a single instillation.

When the surfactant is instilled in 2 and 3 dose volumes (in S+P, L+R, and SL+SR+P postures), both efficiency and homogeneity decrease compared to the single instillation situation (same as the results obtained in rats). This reduction is even more significant for a larger number of injections (see Figure 61E). For 2 and 3 instilled dose volumes, we can now note the existence of a threshold dose volume, this one being larger for 3 instillations than for 2.

In all cases, the homogeneity remains stable at a low level, with *HI* below 0.4, the signature of a highly non-homogeneous delivery. As one can see in Figure 61A and B, the homogeneity index does not seem to depend much on the posture for a single instillation. Figure 62 shows a color-coded view of the fraction of the surfactant exiting the terminal airways (i.e., the amount arriving at the end divided by the initial instilled dose volume). Comparing (S+P) and (L+R), we can see that several terminal bronchioles (876) do not receive any surfactant at all in the former condition. This is very different from the (L+R) situation where only 241 branches do not receive surfactant. The LLD position always appears to be the most favorable position compared to (L+R), (S+P), or (SL+SR+P).

Table 27: Properties and conditions of instilled surfactant

	Figure 61	Figure 62
Dose volume per kg (mL.kg ⁻¹)	1-4	4
Flow rate (mL.kg ⁻¹ .s ⁻¹)	4	6
Viscosity (cP)	30	30
Surface tension (dyn.cm ⁻¹)	30	30
Density (g.cm ⁻³)	1	1
Position	LLD, S, L+R, S+p, SL+SR+P	L+R, S+P
Lung model	Pig, asymmetric	Pig, asymmetric

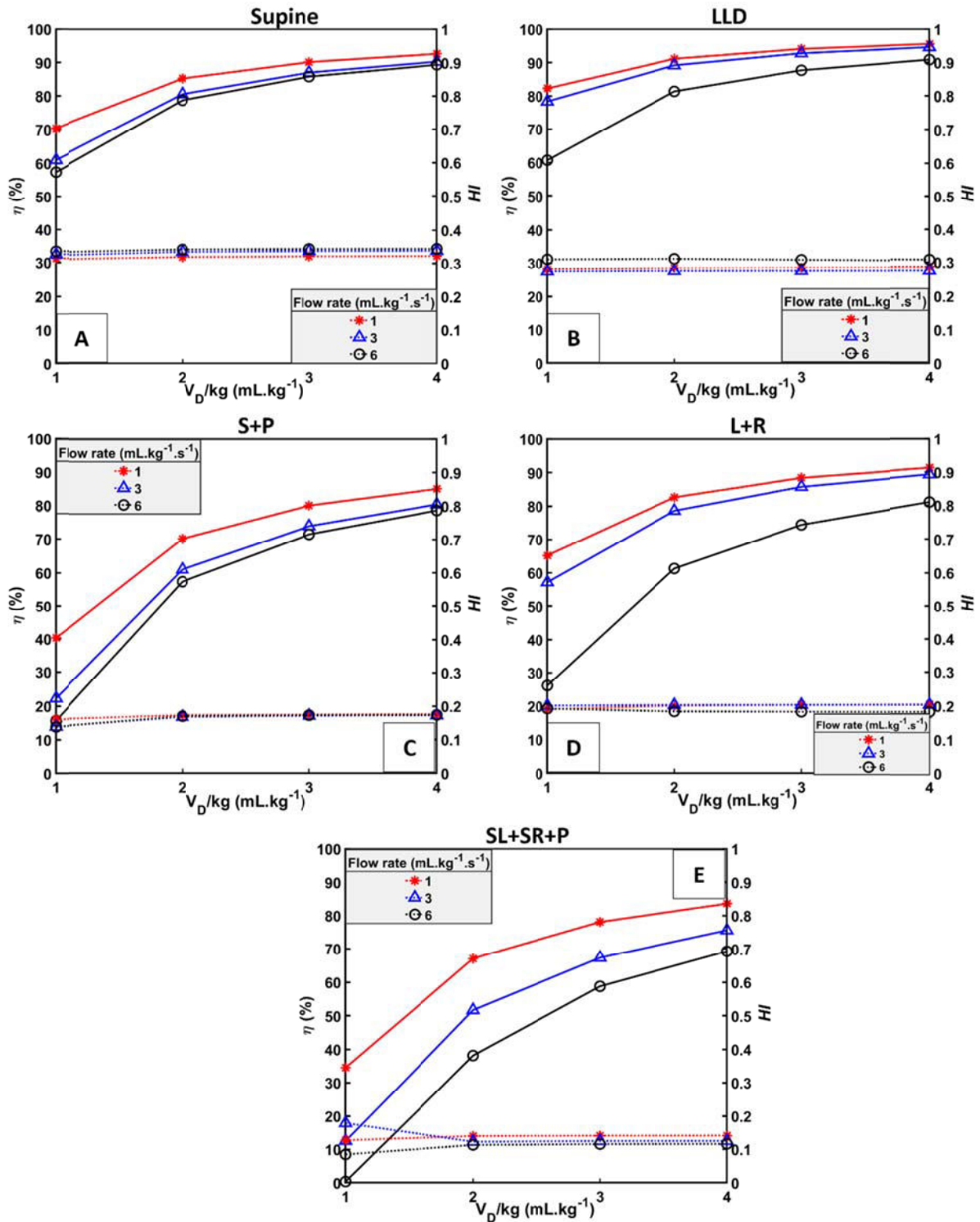


Figure 61: Efficiency index (solid line) and homogeneity index (dashed line) vs. the dose volume, computed in a 40-kg pig lung for three different flow rates, (viscosity $\mu = 30$ cP). A) Single instillation in the supine position. B) Single instillation in the LLD position. C) Double instillation in supine and prone positions (S+P). D) Double instillation in LLD and RLD positions (L+R). E) Three instillations, one-half way between LLD and supine, one-half way between RL and supine, and one in prone posture (SL+SR+P).

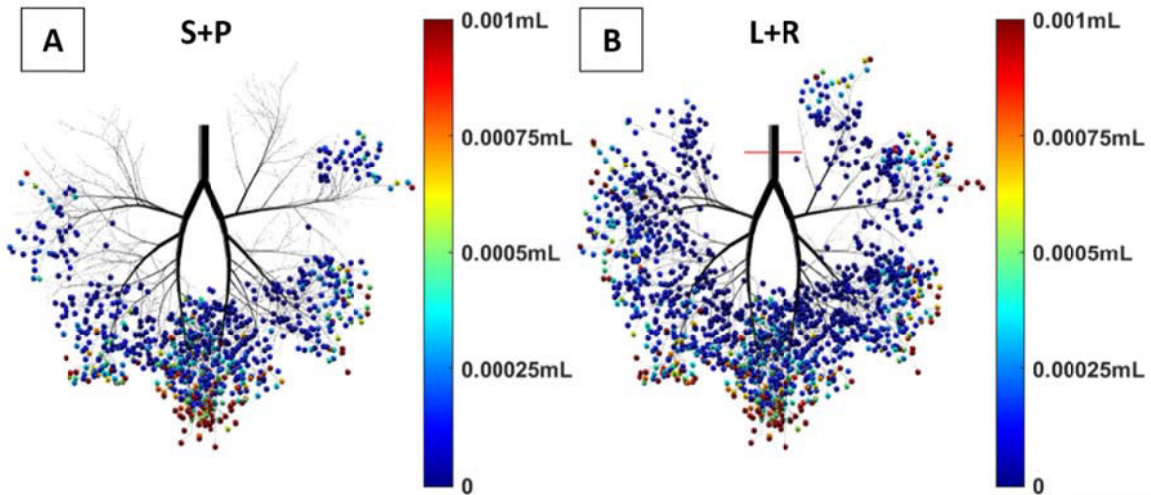


Figure 62: Simulated delivery in a 40-kg pig (viscosity $\mu = 30$ cP). The airway tree is asymmetric with 21 generations and 1712 acini. The two front views display the fraction of the initial dose volume delivered to each acinus. A) Half-supine and half-prone position (S+P). The computed efficiency index is $\eta = 15\%$ and the homogeneity index is $HI = 0.13$. 876 out of 1712 acini do not receive any surfactant B) Half-LLD and half-RLD positions (L+R). The efficiency index is $\eta = 26\%$ and the homogeneity index is $HI = 0.19$. 241 out of 1712 acini do not receive any surfactant.

Although pig lungs are large and comparable in size with human lungs, they share with the rat a respiratory tract with the monopodial pattern which is intrinsically different from the human tracheobronchial tree (which is closer to a symmetrical homothetic pattern).

4.3.3 Mechanical properties of surfactant

4.3.3.1 Viscosity

The molecular composition of the surfactant, the microstructure, the interaction between the components and the environmental conditions all contribute to modify the surfactant viscosity in the lung. As we have seen and expected from the equation of the splitting ratio, viscosity influences the rate and the homogeneity of the end distribution of surfactant in the lung, a result which is supported by previous studies [102][103][104]. For instance, we expect that a lower value of viscosity would induce a more uniform and rapid distribution of the instilled surfactant with a smaller coasting cost in the upper airways. To shed light on this issue, we have performed simulations of delivery for various types of surfactant.

Figure 63 shows the computed efficiency (solid line, filled symbols) and homogeneity (dashed line, open symbols) indices vs. dose volume (LLD posture, 4 mL.kg⁻¹.s⁻¹ flow rate, 1-4 mL.kg⁻¹ dose volume per kg), for the smallest and largest values of the viscosity of Survanta (Table 28). A larger viscosity increases the thickness of the trailing film left by the propagating plugs and lowers the efficiency, especially at low dose volume. A larger viscosity reduces the homogeneity as well.

Table 28: Properties and condition of instilled surfactant

	Figure 63	Figure 64	Figure 65
Dose volume per kg (mL.kg ⁻¹)	1-4	1-4	1 and 4
Flow rate (mL.kg ⁻¹ .s ⁻¹)	4	4	4
Viscosity (cP)	9 and 52	30	30
Surface tension (dyn.cm ⁻¹)	30	3, 30, 90	30
Density (g.cm ⁻³)	1	1	1
Position	LLD	LLD	LLD
Lung model	Pis, asymmetric	Pig, asymmetric	Pig, asymmetric

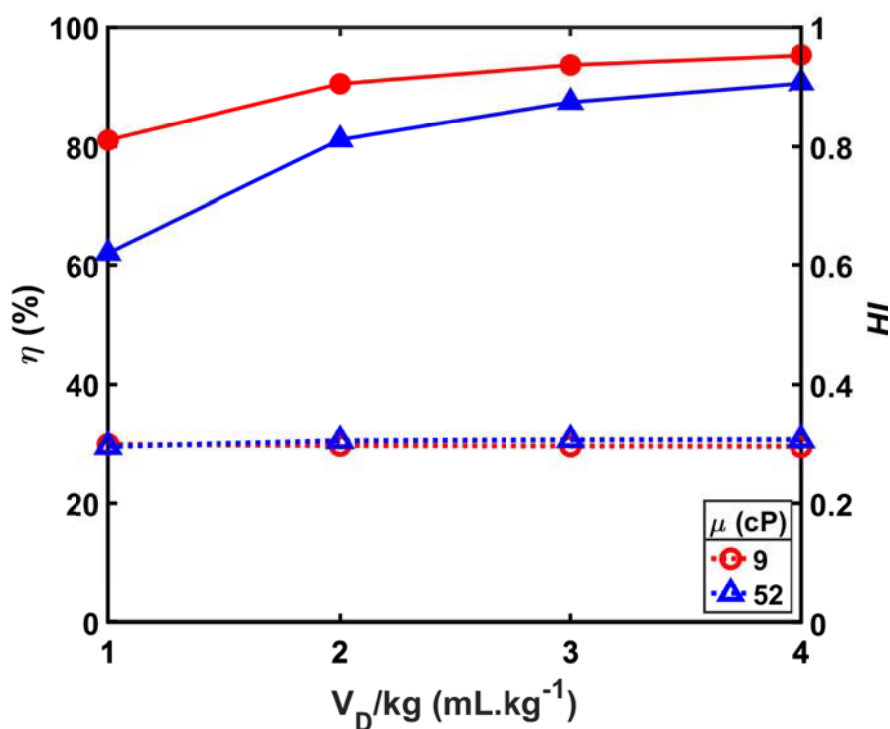


Figure 63: Efficiency index (solid line, filled symbols) and homogeneity index (dashed line, open symbols) vs. dose volume for Survanta with two values of the viscosity, 9 cP (Concentration: 25 mg of PL/ml, 770 s⁻¹ shear rate and 37 °C) and 52 cP (Concentration: 35 mg of PL/ml, 70 s⁻¹ shear rate and 37 °C).

4.3.3.2 Surface tension

The surface tension at the alveolar interface has an influence on several lung mechanical properties such as lung compliance associated with the elastic work of breathing [97]. Surface tension decreases when increasing the concentration of surfactant molecules in solution. Moreover, different surfactants have different surface tensions. In this section, we investigate the effect of surface tension on the efficiency and homogeneity indices. The simulations are run for three different values of the surface tension values (3, 30, and 90 dyn.cm^{-1}) for the same applied conditions (see Table 28). Figure 64 displays the efficiency index (solid line, filled symbols) and the homogeneity index (dashed line, open symbols). As we can see, increasing the surface tension leads to a small increase (less than 5%) in efficiency. However, changing the surface tension does not seem to have any impact on the homogeneity index, for all studied dose volumes. In all cases, the homogeneity index remains around 0.30, an indication of a highly non-homogeneous delivery.

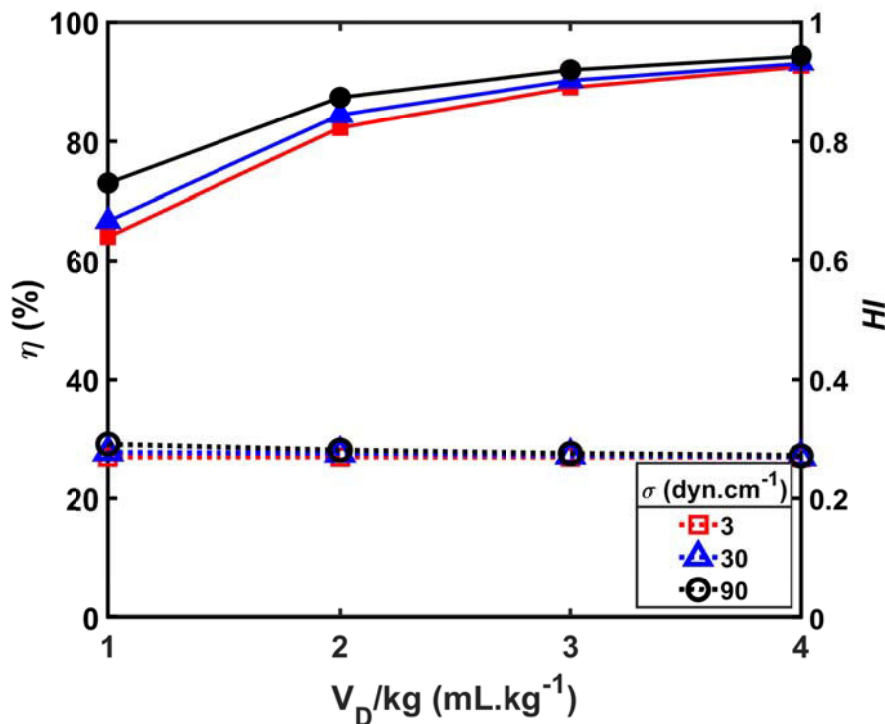


Figure 64: Efficiency index (solid line, filled symbols) and homogeneity index (dashed line, open symbols) vs. dose volume for 3 different values of the surface tension.

4.3.4 Instillation technique

In this section, we investigate the role of the instillation technique by simulating the delivery for one, 2, or 3 instillations in different postures. Later on, we study the multiple aliquot deliveries in which the surfactant is instilled in 10 or more aliquots in the same posture during successive breaths.

The simulations are run for low and high initial dose volumes, for a flow rate of 4 mL.kg⁻¹.s⁻¹ (see Table 28 for the applied conditions). Figure 65 displays the efficiency (open symbols) and homogeneity (filled symbols) indices computed for 1, 5, 10, and 15 aliquots, respectively. At both low and high flow rates, the overall efficiency does not seem to depend heavily on the number of aliquots. But the homogeneity index is slightly increasing for both cases in higher aliquot. However, the homogeneity index remains always smaller than 0.5, which indicates very poor homogeneous distributions. The reason for this inhomogeneity is very likely to be the monopodial structure of the pig airway system.

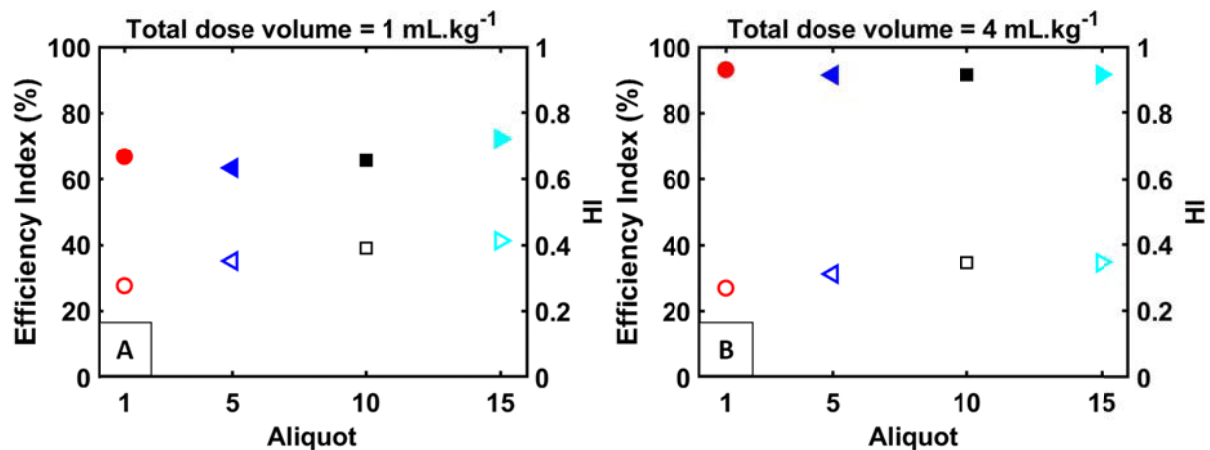


Figure 65: Efficiency index (filled symbols) and homogeneity index (open symbols) computed in a multiple aliquot delivery with the same initial dose volume, in a 40-kg pig lung, (flow rate: 30 mL.kg⁻¹.s⁻¹, posture LLD, viscosity $\mu = 30$ cP). A) Total dose volume = 1 mL.kg⁻¹, B) total dose volume = 4 mL.kg⁻¹.

4.3.5 Conclusion

We have performed numerical simulations of surfactant delivery in a small animal (rat) and in a larger one (pig). The simulation of surfactant delivery in the rat lung (supine position, 1 mL.kg⁻¹ dose volume, and single instillation) has shown a 5% efficiency index and homogeneity index of 0.32 while the pig results were 60% and

0.32, respectively. A previous study of Filoche *et al.* [28] on the neonate and the adult had demonstrated that the neonatal airway tree behaves as a well-mixed compartment whereas the adult airway tree is not, the difference is essentially due to the lung size. Nevertheless, after comparing surfactant delivery in rats and pigs, we see that the smaller lung (rat) does not behave either as a well-mixed compartment, the reason lying in the architecture of the lung airway system. Indeed, if we were to compare simulations of surfactant delivery among the same species, with the same lung structure, the smaller lung would exhibit higher efficiency than the bigger one. However, we cannot compare directly different sizes for lungs coming from two different species. Size matters, but the geometrical structure of the lungs is crucial too. In the pig lung, due to its particular geometry, we never observed the efficiency index smaller than 57% while the homogeneity index was always in the [0.31-0.34] range for all simulations performed with a single instillation. This is very different from what was found in the rat simulations.

However, one trend remains identical. The effect of the dose volume on the efficiency index is similar in both species: increasing the dose volume leads to an increase of the efficiency index independently of the flow rate, in the rat and pig respiratory systems. On the contrary, changing the dose volume bears no effect on the homogeneity index which remains stable for all simulated dose volumes.

Another difference between rat and pig surfactant delivery models is the effect of flow rate on the homogeneity index. Simulations of surfactant delivery in rat and pig lungs show a slight decrease in the efficiency index when increasing the flow rate. This effect is especially marked at low dose volume.

In contrast to the rat results, the mechanical properties of the surfactant do not seem to have a substantial effect on the homogeneity index of surfactant delivery into the respiratory airway system of the pig. The homogeneity index remains fairly stable when viscosity and surface tension are modified. The efficiency index decreases by about 20% (from 9 to 52 cP), and increases by less than 10% (from 3 to 90 dyn.cm⁻¹).

Generally speaking, the homogeneity index has shown to be remarkably stable across all applied conditions. To have a quick overview of these variations, please refer to Table 29.

Table 29: The efficiency and homogeneity in different applied conditions

		Efficiency (η)	Homogeneity (HI)
Flow rate	↑	↓	↔
Dose volume	↑	↑	↔
Viscosity	↑	↓	↔
Surface tension	↑	↑	↔
Multiple instillation	↑	↔	↑
Posture		Depend on position	↔

4.4 SRT in the human lung

4.4.1 Neonate vs. adult

4.4.1.1 Flow rate and dose volume

To investigate the effect of flow rate and dose volume in SRT in the human lower respiratory tract, we have first reproduced the results of the study by Filoche, Tai & Grotberg [129], i.e., we have simulated and compared the propagation and the final distribution surfactant in a 1-kg premature neonate (8 generations + trachea, 256 acini) with a 70-kg adult (12 generations + trachea, 4096 acini). The surfactant bolus starts as a plug in the distal trachea for both because that would generally be the location of the outlet of an endotracheal tube. The surfactant is delivered in the LLD position. Figure 66A and Figure 66B show a 3D front view of the neonatal and adult respiratory lower tract, respectively. Figure 66C illustrates the normalized delivery $V_N(i) = V_i / \text{mean}(V_i)$ plotted vs. the terminal branch number of the neonate, while Figure 66D provides the same plot for an adult and an initial dose volume of 1 mL.kg⁻¹ dose volume per kg. The mixture viscosity is $\mu = 30$ cP, which is typical of Survanta® (to see more details on the delivery conditions refer to Table 30). Clearly, the second half of the neonate acinus ($129 \leq i \leq 256$) receives more surfactant due to the LLD position. The efficiency index is $\eta = 52.8\%$. It means that 47.2%, i.e., almost half of the instilled volume is lost lining the airway walls. Very different from the neonate, we can note that the right lung in the adult case does not receive any surfactant at all. The efficiency index is $\eta = 15.7\%$. Figure 66E displays a histogram of Figure 66A and Figure 66F is the same plot for Figure 66B. The calculated homogeneity index is about 5.7 for the neonate lung and 0.73 for the adult lung.

Table 30: Properties and conditions of instilled surfactant

	Figure 66
Dose volume per kg (mL.kg ⁻¹)	1
Flow rate (mL.kg ⁻¹ .s ⁻¹)	6
Viscosity (cP)	30
Surface tension (dyn.cm ⁻¹)	30
Density (g.cm ⁻³)	1
Position	LLD
Lung model	Human, symmetric

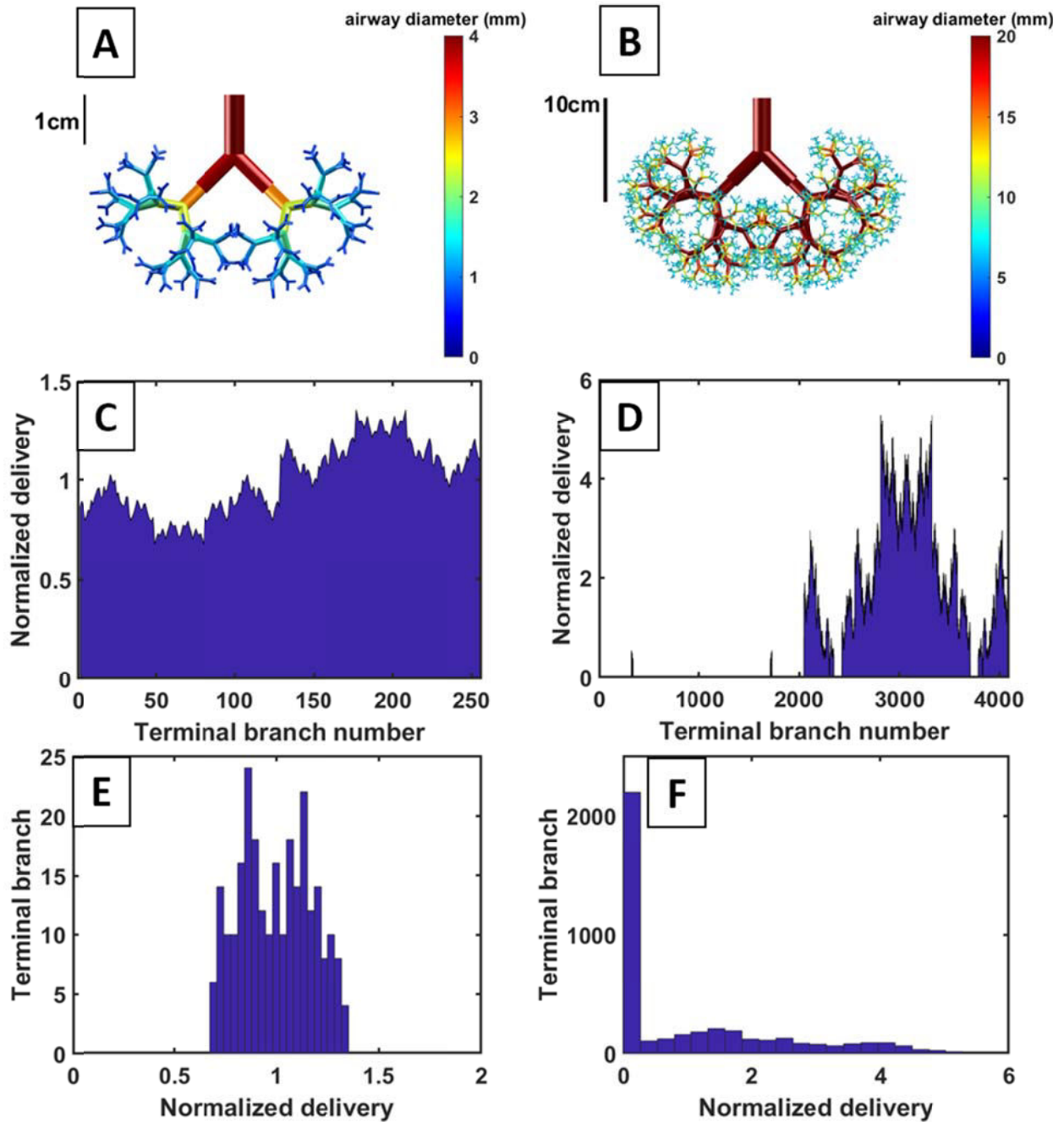


Figure 66: A) Front view of the 1-kg neonatal respiratory lower tract. B) Front view of the 70-kg adult respiratory lower tract. C) Normalized delivery of terminals of neonate's lung. D) Normalized delivery of terminals of the Adult lung. E) Histogram of normalized delivery of neonate's lung. F) Histogram of normalized delivery of adult lung.

The next step consists of comparing the neonate and adult models in a large variety of delivery conditions [68][73]. Figure 67 displays the efficiency index η (line, filled symbols) and the homogeneity index HI (dashed line, open symbols) as functions of the tracheal flow rate. Delivery of dose volumes per kg of 1, 2, 3, and 4 mL.kg⁻¹ are

computed in a 1-kg neonate lung for flow rates ranging from 1 to 6 mL.kg⁻¹.s⁻¹ (see Figure 67 for details of delivery conditions). The dose volume is administered in two half doses (LLD and RLD positions successively). Our results show that increasing the flow rate has two opposite effects on efficiency and homogeneity. The efficiency decreases with increasing flow rate due to the presence of a thicker trailing films coating the airway walls whereas the homogeneity increases because the splitting factor at each bifurcation is shifted toward 0.5. In other words, we see here a fundamental contradiction regarding the flow rate: a higher flow rate achieves a better homogeneity but a smaller flow rate leads to better efficiency.

Increasing the dose volume increases both efficiency and homogeneity at any given flow rate because the additional available volume reduces the number of plug rupture events. For a dose volume per kg of 1 mL.kg⁻¹, the efficiency is found in the [6%-56%] range and the homogeneity is in the [1.1-13.7] range. If we now examine the results for a 4 mL.kg⁻¹ dose volume per kg, the range of efficiency is [76%-89%] while the range of homogeneity is [4-164].

Table 31: Properties and conditions of instilled surfactant

	Figure 67 and Figure 71
Dose volume per kg (mL.kg ⁻¹)	1-4
Flow rate (mL.kg ⁻¹ .s ⁻¹)	1-6
Viscosity (cP)	30
Surface tension (dyn.cm ⁻¹)	30
Density (g.cm ⁻³)	1
Position	L+R
Lung model	Neonate and adult symmetric

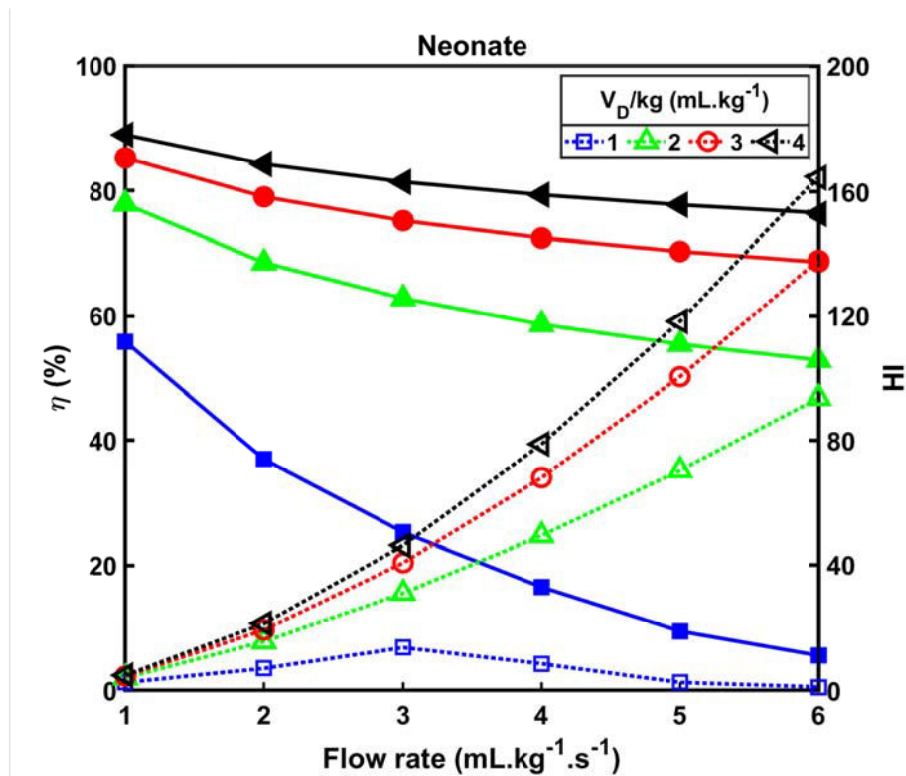


Figure 67: Efficiency index η (line, filled symbols) and homogeneity index HI (dashed line, open symbols) vs. tracheal flow rate for total dose volumes per kg of 1, 2, 3, and 4 mL.kg^{-1} in the 1-kg neonate lung. For each given dose volume, one-half is delivered in RLD and the other in LLD.

Figure 68A displays bar diagrams of the absolute amount of coating volume in the entire tree while Figure 68B displays bar diagrams of the ratio of the coating volume to the initial dose volume. Figure 68A illustrates that, for a given flow rate, the total coating volume is almost identical for different doses. Figure 68B shows that the ratio V_C/V_D increases with the flow rate. This is due to the thicker trailing film left by the plugs propagating through the tree. At the same time, due to the increased velocity, the influence of gravity decreases and the splitting factor gets closer to 0.5. However, if V_D is too small, only a small number of terminal airways are adequately supplied with the surfactant, which means that both efficiency and homogeneity plummet, independently of the velocity.

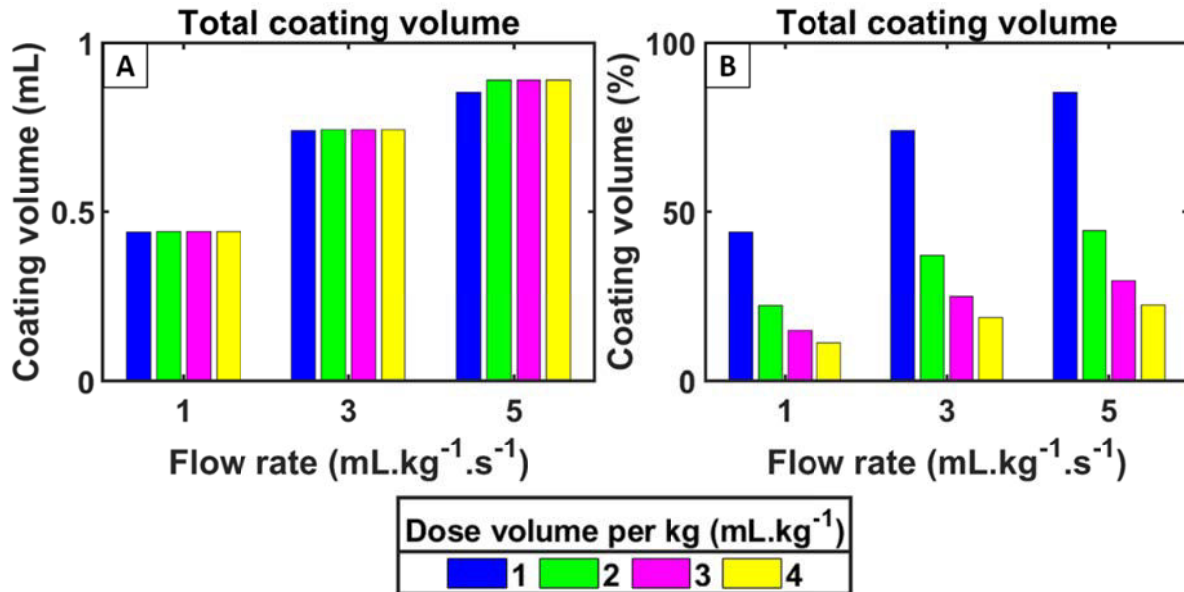


Figure 68: Total coating cost vs. flow rate for a 1-kg neonate lung in the L+R position. A) The absolute amount of coating volume in the entire tree, B) coating volume divided by the initial instilled dose volume.

Figure 69 shows the trailing film ratio thickness to radius for two different flow rates per kg (1 and 6 mL.kg⁻¹.s⁻¹). As one can see, the larger flow rate per kg (6 mL.kg⁻¹.s⁻¹) leaves a coating layer of about 2.5 times thicker on average in all branches than the lower flow rate.

Figure 70 shows the splitting factor for two different flow rates per kg (1 and 6 mL.kg⁻¹.s⁻¹). As mentioned before, the homogeneity increases with the flow rate. Figure 70 shows that at larger flow rates, the splitting factor is closer to 0.5, which means an equal partition between the two daughter airways.

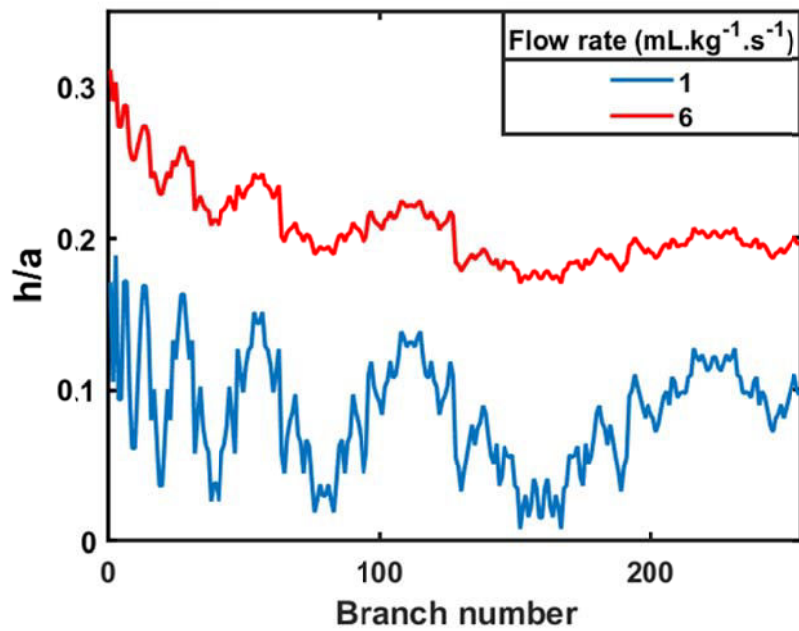


Figure 69: Trailing film ratio thickness to the radius at low (blue) and high (red) flow rate in 1 mL.kg^{-1} dose volume per kg

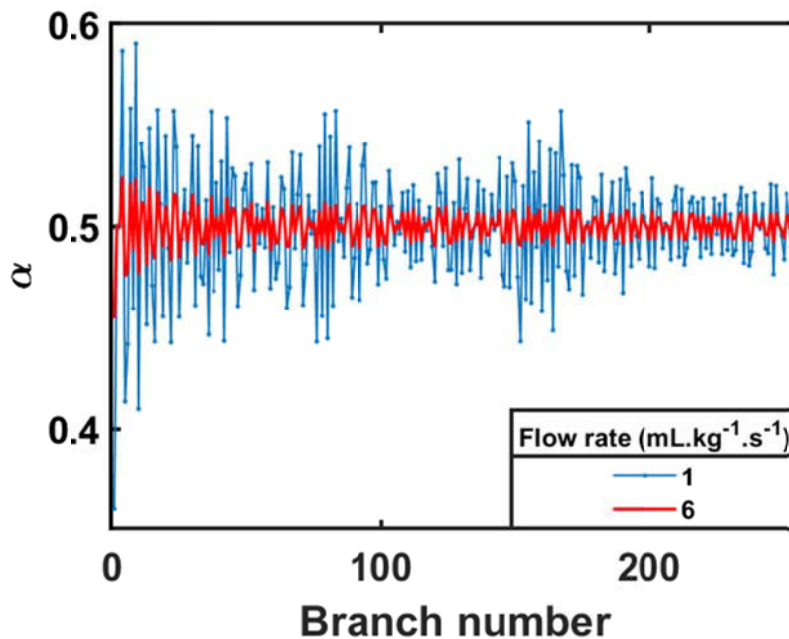


Figure 70: Splitting factor at low (blue) and high (red) flow rate in 1 mL.kg^{-1} dose volume per kg

In stark contrast, Figure 71 exhibit very different behaviors between the adult and the neonate's lungs. First, both efficiency and homogeneity are smaller in adults than in neonates for a wide range of flow rates per kg (from 1 to $6 \text{ mL.kg}^{-1}.\text{s}^{-1}$). As shown in Figure 71, increasing the flow rate reduces the efficiency and increases the

homogeneity, except for a 1 mL.kg^{-1} dose volume per kg. At higher doses volume per kg (4 mL.kg^{-1}), the efficiency is comprised between 54% and 87%, and the homogeneity is comprised between 0.4 and 4.3 for flow rates per kg in the $[1-6 \text{ mL.kg}^{-1}.\text{s}^{-1}]$ range. For a lower dose volume per kg (1 mL.kg^{-1}), the efficiency ranges from 0% to 49% (it vanishes around $4 \text{ mL.kg}^{-1}.\text{s}^{-1}$) and the homogeneity ranges from 0 to 0.38.

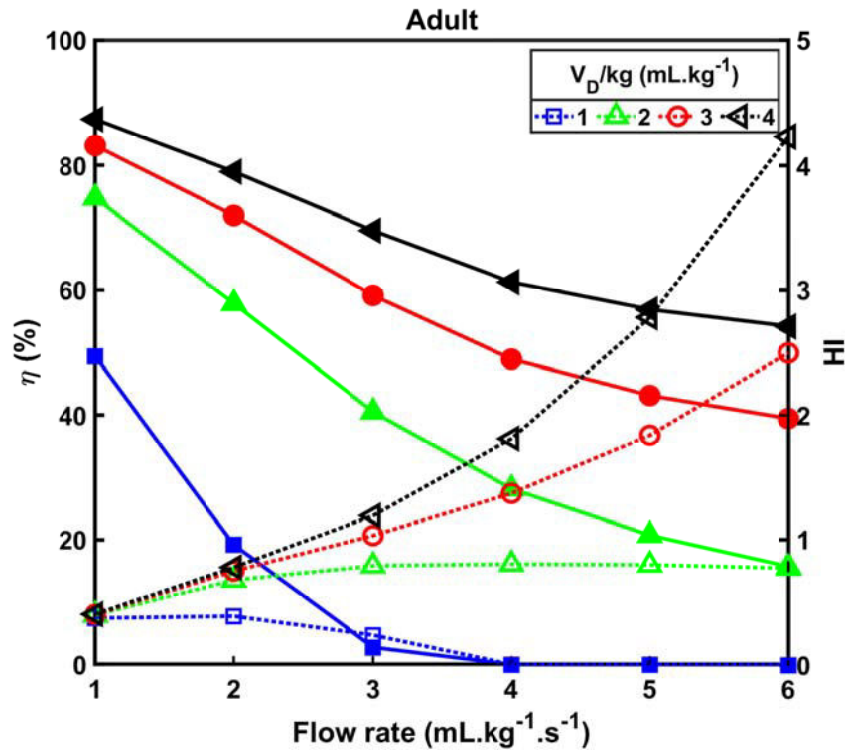


Figure 71: Efficiency index (solid line, filled symbols) and homogeneity index (dashed line, open symbols) vs. the tracheal flow rate for total dose volumes per kg of 1, 2, 3, and 4 mL.kg^{-1} in the 70-kg adult lung. For each value of the dose volume, one-half is delivered in RLD and the other in LLD.

Figure 72A (absolute amount) illustrates that, for a given flow rate, the total coating volume is almost identical for different doses while Figure 72B (fraction of the initial volume) shows that the ratio V_C/V_D increases with the flow rate, as we have already seen for the neonate's lung.

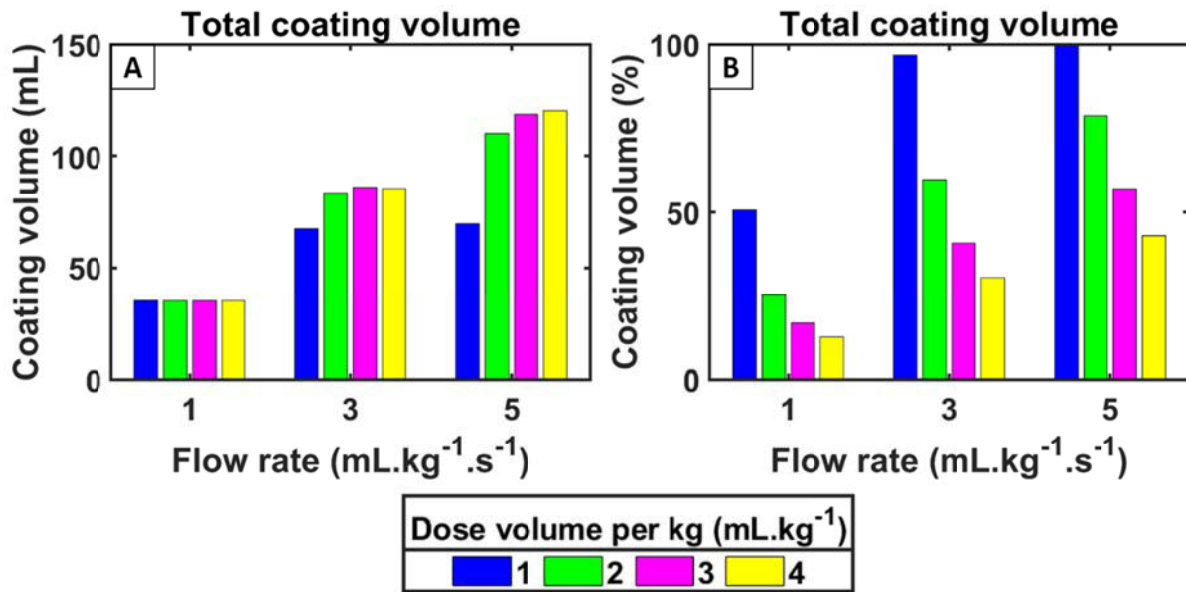


Figure 72: Total coating cost vs. flow rate for a 70-kg adult lung in the L+R position. A) The absolute amount of coating volume in the entire tree, B) coating volume divided by the initial instilled dose volume.

4.4.1.2 Assessing the role of posture

Figure 73 displays the behavior of the efficiency index (solid line, filled symbols) and the homogeneity index (dashed line, open symbols) in different postures. The results are presented for a range of dose volumes, flow rates, and 4 different postures: 2 are single instillation, i.e., LLD, supine, and 2 are multiple instillations, i.e., $\frac{1}{2}$ prone + $\frac{1}{2}$ supine (called L+R), and $\frac{1}{2}$ supine + $\frac{1}{2}$ prone (called S+P). In all cases, the efficiency increases with the dose volume and decreases with the flow rate. However, the homogeneity increases with both flow rate and dose volume (except for 1 mL.kg⁻¹). As one can see in Figure 73A-B, the efficiency and the homogeneity indices do not seem to depend strongly on the posture for a single instillation. In addition, LLD shows better efficiency, and supine shows a small improvement in homogeneity.

On the contrary, when the surfactant is instilled in 2 doses (in L+R and S+P postures), the efficiency decreases and the homogeneity increases as compared to the single instillation situation. For multiple instillations, one observes an increase in the threshold volume dose. This can be easily understood: splitting the initial volume into several smaller doses in order to instill in different postures improves the homogeneity, but this is detrimental to the efficiency. Each instillation sees now a smaller plug expanding through a new route inside the airway tree. Consequently, the coating cost increases, leading to a significant reduction in efficiency.

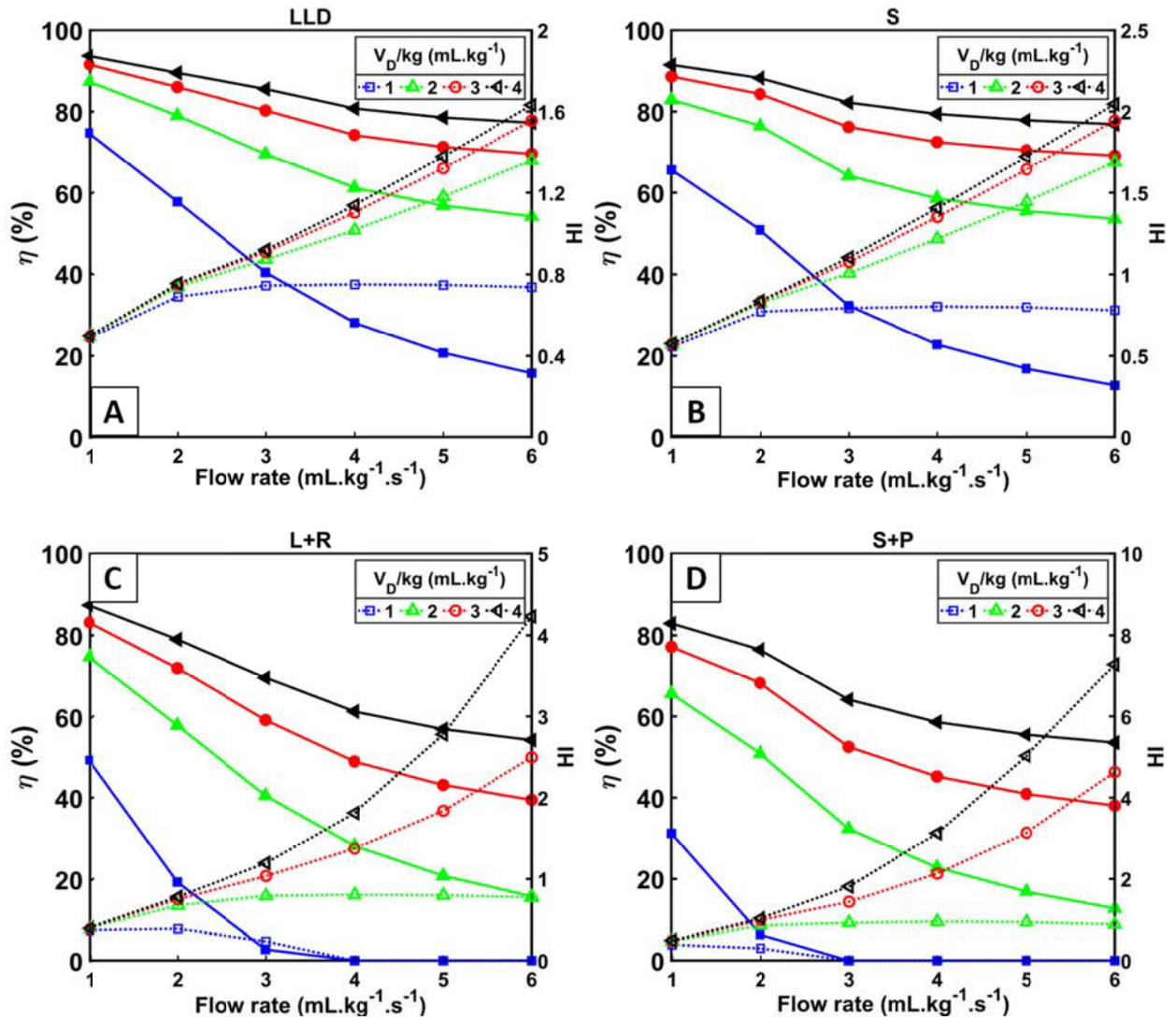


Figure 73: Efficiency index η (solid line, filled symbols) and homogeneity index HI (dashed line, open symbols) as a function of the flow rate, computed in a human adult lung. A) Single instillation in the LLD position. B) Single instillation in the supine position. C) Double instillation in LLD and RLD positions (L+R). D) Double instillation in supine and prone positions (S+P).

4.4.1.3 Changing the mechanical properties of surfactant

As we have seen for the rat and pig lungs, the mechanical properties of the fluid influence the final distribution of surfactant. To assess this influence (through viscosity and surface tension), we have performed simulations for various types of surfactants in a symmetric adult model.

4.4.1.3.1 Viscosity

The surfactant viscosity depends on the type of surfactant, the phospholipid concentration, the shear rate, and the temperature. Similarly to what we did with the rat and the pig models in this section, we investigate the effect of surfactant viscosity on the final distribution of Survanta® (9 and 52 cP [105]). Figure 74 shows the computed efficiency index (solid line, filled symbols) and the homogeneity index (dashed line, open symbols) vs. the dose volume (see Table 32). A larger viscosity increases the thickness of the trailing film left by the propagating plugs and lowers the efficiency, especially at low dose volume. For lower viscosity, the homogeneity remains fairly stable, but a higher viscosity induces a positive dependency between homogeneity and dose volume.

Table 32: Properties and condition of instilled surfactant

	Figure 74
Dose volume per kg (mL.kg ⁻¹)	1-4
Flow rate (mL.kg ⁻¹ .s ⁻¹)	4
Viscosity (cP)	9 and 52
Surface tension (dyn.cm ⁻¹)	30
Density (g.cm ⁻³)	1
Position	LLD
Lung model	Adult, symmetric

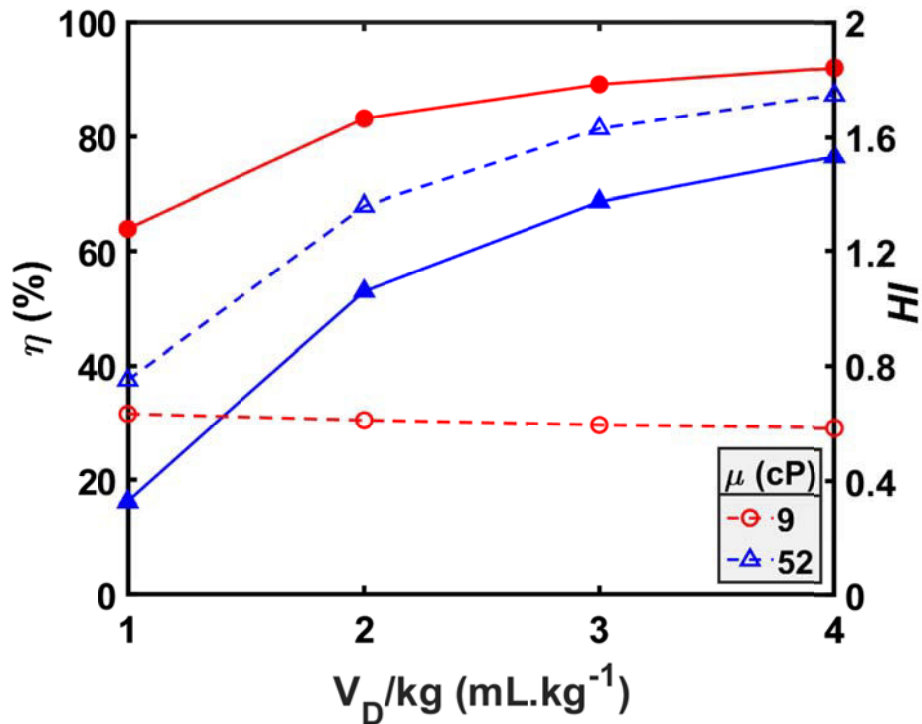


Figure 74: Efficiency index η (solid line, filled symbols) and homogeneity index HI (dashed line, open symbols) vs. the dose volume for Survanta® with two different values of the viscosity, 9 cP (concentration: 25 mg of PL/ml, 770 s⁻¹ shear rate and 37°C) and 52 cP (concentration: 35 mg of PL/ml, 70 s⁻¹ shear rate and 37°C).

4.4.1.3.2 Surface tension

The surface tension of the surfactant solution decreases with the concentration of surfactant molecules. We have run simulations for three different values of the surface tension, i.e., 3, 30, and 90 dyn.cm⁻¹ in the same conditions (see Table 33) to assess the influence of surface tension on SRT in the human adult lung. In Figure 75, we can observe the efficiency index (solid line, filled symbols) and the homogeneity index (dashed line, open symbols). As can be seen in the figure, increasing the surface tension leads to an increase in both efficiency and homogeneity for all tested dose volumes. The homogeneity for all applied conditions is always smaller than 1.2, a sign of a very non-homogeneous delivery. Please refer to Table 34 to see the summary of the effects of different applied conditions on the neonatal and adult lung models.

Table 33: Properties and condition of instilled surfactant

	Figure 75
Dose volume per kg (mL.kg^{-1})	1-4
Flow rate ($\text{mL.kg}^{-1}.\text{s}^{-1}$)	4
Viscosity (cP)	30
Surface tension (dyn.cm^{-1})	3, 30, and 90
Density (g.cm^{-3})	1
Position	LLD
Lung model	Adult, asymmetric

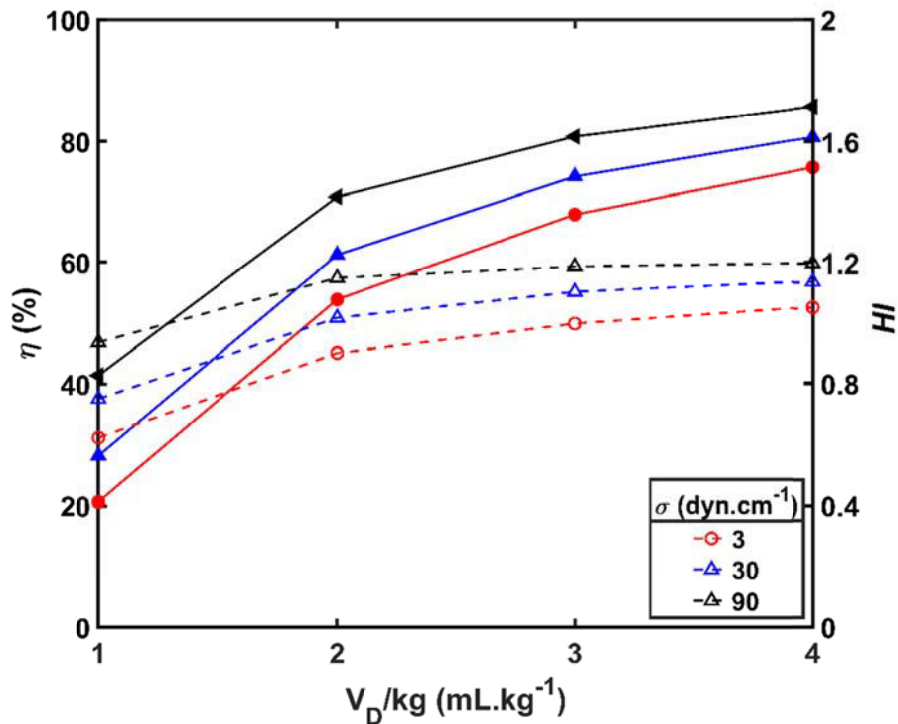


Figure 75: Efficiency index η (solid line, filled symbols) and homogeneity index HI (dashed line, open symbols) vs. the dose volume for 3 different values of the surface tension.

Table 34: The efficiency and homogeneity in different applied conditions

	Efficiency (η)	Homogeneity (HI)
Flow rate \uparrow	\downarrow	\uparrow
Dose volume \uparrow	\uparrow	\uparrow
Viscosity \uparrow	\downarrow	\uparrow
Surface tension \uparrow	\uparrow	\uparrow
Posture	LLD, $S > L+R$, S+P	LLD, $S < L+R$, S+P

4.4.2 Age study

We have seen that neonate and adult lungs perform very differently in SRT due to their size difference. In this section, we investigate how the performance of SRT evolves with age, as the lung size progressively increases. To model age-dependent geometry, we used the Weibel-based symmetric tree. The symmetric airway tree stems from the trachea ($n=0$), and as we saw in section 2.1.3.1, the tracheal diameter is the sole parameter entirely controlling the size of the tree.

Figure 76 displays the efficiency index (solid line, filled symbols) and the homogeneity index (dashed line, open symbols) vs. the age from 1 to 19 years. The flow rate per kg is kept constant throughout the simulations ($6 \text{ mL}\cdot\text{kg}^{-1}\cdot\text{s}^{-1}$), which means that, at each age, the flow rate is proportional to the patient weight. The delivery is simulated for 4 different values of the total dose volume per kg of 1, 2, 3, and 4 $\text{mL}\cdot\text{kg}^{-1}$, respectively, administered in two half-doses in RLD then LLD position (refer to Table 35 for the details of delivery conditions). Figure 76 shows a decrease in efficiency with age due to the increase of the tracheobronchial tree size. From ages 1 to 9, the efficiency drops at an almost constant rate, but from 11-13 and at a higher age, the drop becomes even sharper. We see here the direct influence of the lung size. The age-dependent model of the lung geometry contains about 15 generations from 1 to 13 years, and 16 from 15 to 19 years (see Table 36) [155]. At all ages, however, we conserve the classical trend, which is increasing the dose volume increases the efficiency, in agreement with our previous results in neonate and adult. For 1 to 9 years, the efficiency index remains high for dose volumes per kg larger than $1 \text{ mL}\cdot\text{kg}^{-1}$. Above 9 years, the efficiency index drops or requires a higher initial dose volume to remain above 50%. At a smaller dose volume per kg ($1 \text{ mL}\cdot\text{kg}^{-1}$), the efficiency is comprised between 0 and 48% while for a larger dose volume per kg ($4 \text{ mL}\cdot\text{kg}^{-1}$), the efficiency is in the [45%-86%] range. As for efficiency, the homogeneity decreases with increasing age.

Table 35: Properties and conditions of instilled surfactant

	Figure 76	Figure 77
Dose volume per kg (mL.kg ⁻¹)	1-4	1-4
Flow rate (mL.kg ⁻¹ .s ⁻¹)	6	1
Viscosity (cP)	30	30
Surface tension (dyn.cm ⁻¹)	30	30
Density (g.cm ⁻³)	1	1
Position	LLD+RLD	LLD+RLD
Age (year)	1-19	1-19
Lung model	Human, symmetric	Human, symmetric

Table 36: Age-dependent lung size and body weight

Age (year)	Trachea diameter (cm) [155]	Terminals diameter (cm)	Number of generations	Weight (Kg) [156]
1	0.5	0.0184	15	1
3	0.7	0.0258	15	7
5	0.8	0.0295	15	14
7	0.9	0.0332	15	18
9	1	0.0369	15	23
11	1.2	0.0443	15	28
13	1.3	0.0479	15	36
15	1.5	0.0437	16	56
17	1.7	0.0495	16	65
19	1.8	0.0524	16	69

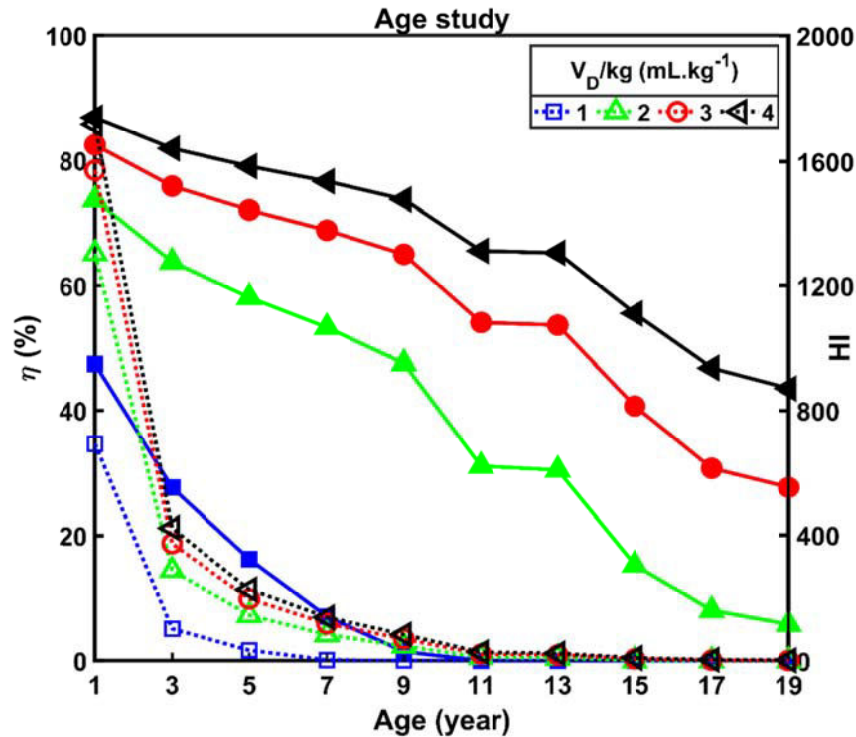


Figure 76: Efficiency index (solid line, filled symbols) and homogeneity index (dashed line, open symbols) vs. age for 4 different values of the dose volume, at for a $6 \text{ mL.kg}^{-1}.\text{s}^{-1}$ flow rate per kg.

We now perform new simulations at a lower flow rate while keeping it still proportional to body weight ($1 \text{ mL.kg}^{-1}.\text{s}^{-1}$). Figure 77 shows the efficiency index (solid line, filled symbols) and the homogeneity index (dashed line, open symbols) vs. age in the same conditions as Figure 76. We can see that the efficiency drop with age is more marked at a higher flow rate ($6 \text{ mL.kg}^{-1}.\text{s}^{-1}$ which it is 48% to 0 for $6 \text{ mL.kg}^{-1}.\text{s}^{-1}$), especially for a small dose volume per kg (1 mL.kg^{-1} , compare the blue lines for efficiency in Figure 76 vs. Figure 77): the efficiency index drops from 48% to 0 between ages 1 and 19 in the former case, while the drop is only from 67% to 39% in the latter. For dose volumes per kg larger than 2 mL.kg^{-1} , the efficiency index remains always above 70% at all ages at a low flow rate (Figure 77).

What is striking in all cases is that the homogeneity index experiences a sharp drop from the beginning and falls under 5 above 9-year-old. This homogeneity appears here as the main issue for adults, which suggests that a multiple posture delivery should be more adapted for increasing the efficacy of SRT in this case.

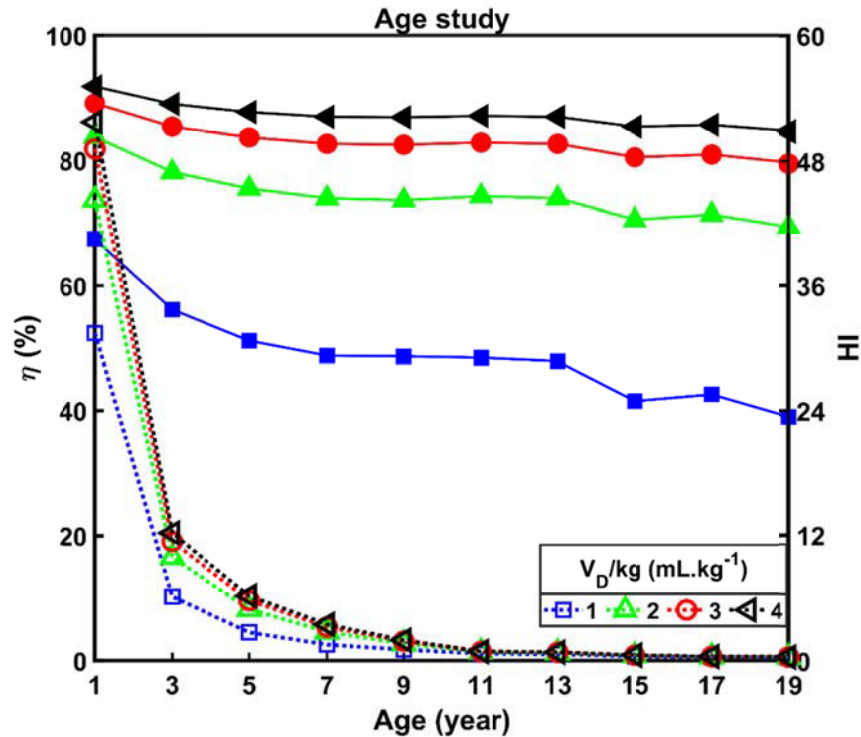


Figure 77: Efficiency (solid line, filled symbols) and homogeneity (dashed line, open symbols) vs. age at 4 dose volumes in 1 mL.kg⁻¹.s⁻¹ flow rate per kg.

4.4.3 Symmetric vs. asymmetric tree

We have seen in animal models that the monopodial structure of the lung plays a fundamental role in determining the properties of the end distribution of surfactant. The structure of the human pulmonary airway system is much closer to a symmetrically branching tree but still bears some asymmetry. To investigate the role of this asymmetry, we have performed simulations of surfactant delivery in symmetric vs. asymmetric models of the human tracheobronchial tree. These trees are both based on the celebrated Weibel's. For a detailed description of both models, please refer to Section 2.1.3.

Figure 78A displays a front view of the symmetric model of the human conducting airways, while Figure 78B illustrates the same data for the asymmetric model. The color-coding represents the diameter value. Figure 78C shows a 3D front view of the amount of surfactant left coating the airways in simulation (A). The color-coding represents the volume left coating each airway divided by the initial instilled dose volume. Figure 78D shows the same figure as (C), corresponding to simulation (B). Figure 78E shows a 3D front view of the distribution of volumes reaching the acini of the symmetric model while Figure 78F is the same figure for the asymmetric model.

The computed efficiency and homogeneity indices are $\eta = 55.5\%$ and $HI = 0.86$ for the symmetric tree, and $\eta = 54.8\%$ and $HI = 0.61$ for the asymmetric one. Each sphere represents a terminal branch that received surfactant, and the color of the sphere corresponds to the volume of surfactant reaching the corresponding terminal branch. Table 37 and Table 38 provide the properties of the surfactant and instillation conditions. Figure 79 shows a comparison of the efficiency index (solid line, filled symbols) and the homogeneity index (dashed line, open symbols) between the symmetric and the asymmetric trees vs. tracheal flow rate, for 4 different dose volumes. Interestingly, both trees exhibit similar trends, the homogeneity index of the symmetric tree being only slightly higher and its efficiency slightly lower than the asymmetric version.

Table 37: Properties and conditions of instilled surfactant

	Figure 78	Figure 79
Viscosity (cP)	30	30
Surface tension (dyn.cm ⁻¹)	30	30
Density (g.cm ⁻³)	1	1
Flow rate (mL.kg ⁻¹ .s ⁻¹)	4	1-6
Dose volume per kg (mL.kg ⁻¹)	2	1-4
Position	LLD	LLD
Lung model	Human, symmetric	Human, asymmetric

Table 38: Model size and body weight

	Figure 78A	Figure 78B
Trachea diameter (cm)	1.8	1.8
Terminals diameter (cm)	0.05	0.05
Number of generations	16	maximum 16
Weight (Kg)	69	69
Number of terminals	32,768	29,202

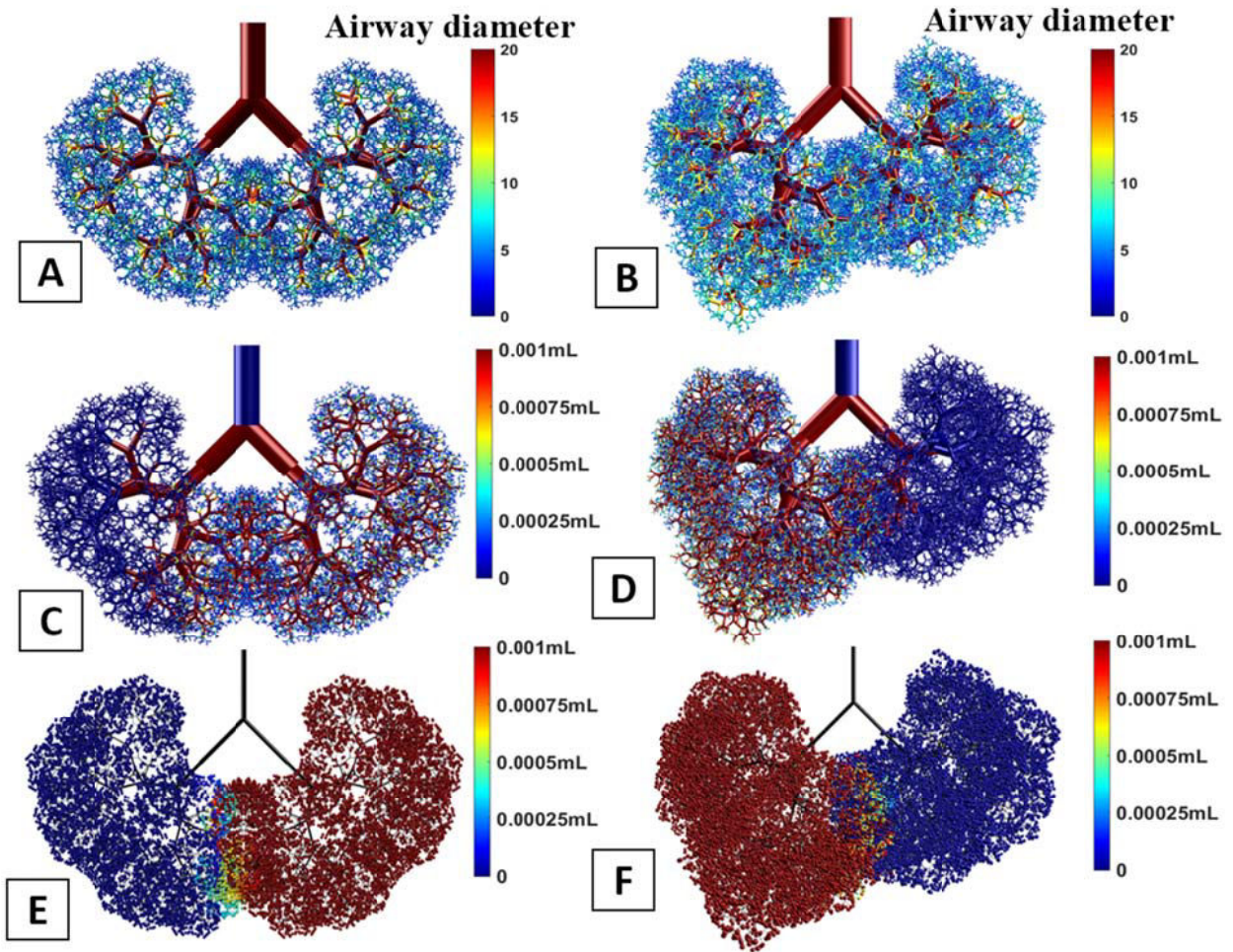


Figure 78: Simulation of surfactant delivery in a symmetric and asymmetric models of the human airway tree. A) Front view of the symmetric model of the human conducting airways. B) Front view of the asymmetric model of the human conducting airways. The color-coding represents the diameter value. C) 3D front view displaying the amount of surfactant left coating the airways, in simulation (A). The color-coding represents the volume left coating each airway divided by the initial instilled dose volume. D) Same figure as (C), corresponding to simulation (B). E) 3D Front view representing the distribution of volumes reaching the acini. F) Same figure, for the asymmetric tree.

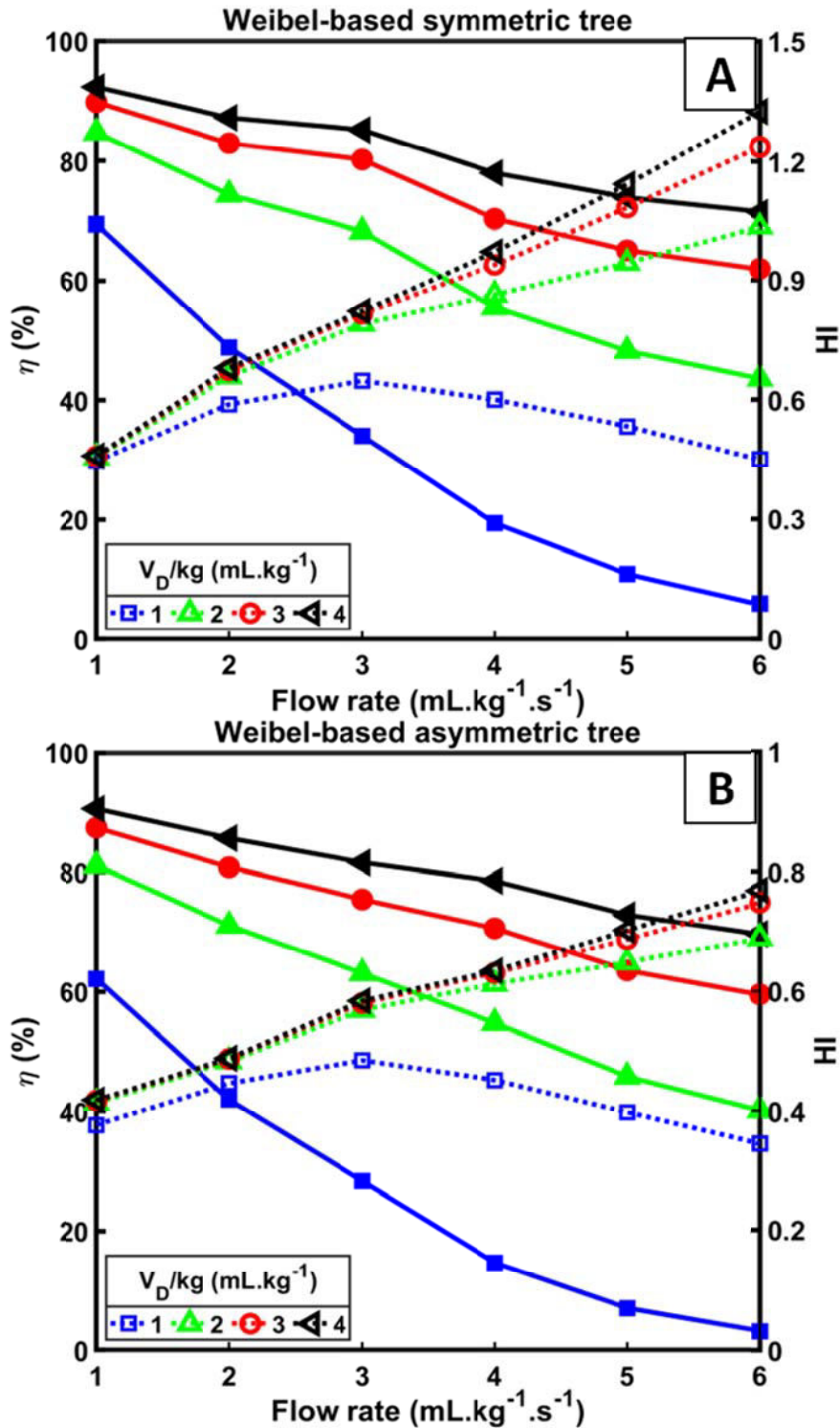


Figure 79: Efficiency index (solid line, filled symbols) and homogeneity index (dashed line, open symbols) vs. tracheal flow rate for total dose volumes per kg of 1, 2, 3, and 4 mL.kg^{-1} . A) Weibel-based symmetric respiratory airways tree. B) Weibel-based asymmetric respiratory airways tree.

4.4.4 SRT in the Weibel-based asymmetric tree

In the Weibel-based asymmetric airway tree, the branching and rotation angles are identical to the Weibel's symmetric model, but the two daughter airways always exhibit different diameters and lengths determined by two different diameter ratios at each bifurcation. In this section, we investigate the influence of posture, viscosity, surface tension, and multiple instillations on the final distribution of surfactant delivery.

4.4.4.1 Assessing the role of posture

Simulations of SRT have been performed for LLD, L+R, supine, and S+P positions. Figure 80 displays the behavior of the efficiency index (solid line, filled symbols) and the homogeneity index (dashed line, open symbols) in different postures. The results are presented for a range of dose volumes in $4 \text{ mL.kg}^{-1}.\text{s}^{-1}$ flow rates and 4 different postures: 2 are single instillation, i.e., LLD, supine, and 2 are multiple instillations, i.e., $\frac{1}{2}$ LLD + $\frac{1}{2}$ RLD (L+R) and $\frac{1}{2}$ supine + $\frac{1}{2}$ prone (S+P) (see Table 39 for details of applied conditions). In all cases, the efficiency increases with the dose volume. As one can see in Figure 80, the efficiency and the homogeneity indices do not seem to depend much on the posture for a single instillation. In these cases, for dose volumes per kg bigger than 2 mL.kg^{-1} , the efficiency remains bigger than 50 %. If one goes below this threshold dose volume, the efficiency-dose plot exhibits a steep slope and decreases significantly. When the surfactant is instilled in 2 dose volumes, on the contrary, both efficiency and homogeneity decrease as compared to the single instillation situation. For multiple instillations, one also observes an increase in the threshold volume dose and it due to splitting the initial volume into several smaller doses in order to instill in different postures detrimental to the efficiency.

Table 39: Properties and condition of instilled surfactant

	Figure 80	Figure 81	Figure 82	Figure 83	Figure 84
Dose volume per kg (mL.kg^{-1})	4	1-4	1-4	4	1-4
Flow rate ($\text{mL.kg}^{-1}.\text{s}^{-1}$)	4	4	4	4	1-6
Viscosity (cP)	30	9 and 52	30	30	30
Surface tension (dyn.cm^{-1})	30	30	3, 30, 90	30	30
Density (g.cm^{-3})	1	1	1	1	1
Position	LLD, L+R, S, S+P	LLD	LLD	LLD	LLD
Lung model	asymmetric	asymmetric	asymmetric	asymmetric	asymmetric

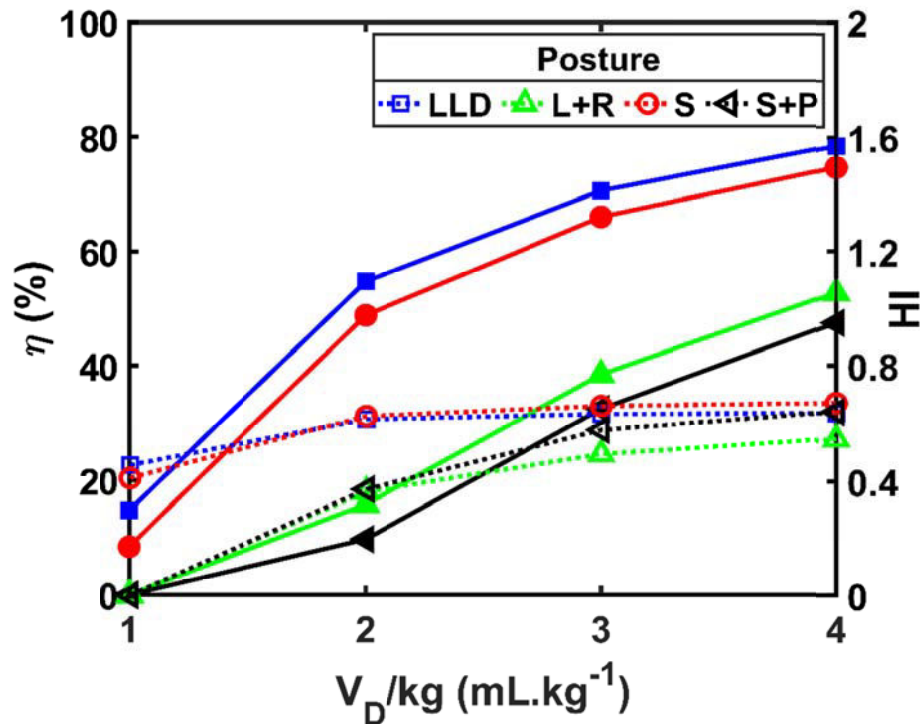


Figure 80: Efficiency index η (solid line, filled symbols) and homogeneity index HI (line, open symbols) vs. dose volume, computed in a 70-kg human lung, at a 4 mL.kg⁻¹.s⁻¹ the flow rate in two single (LLD and supine) and two double (L+R and S+P) instillation.

4.4.4.2 Mechanical properties of surfactant

4.4.4.2.1 Viscosity

As we have seen (and expected from the equation of splitting ratio), the viscosity of the instilled fluid influences the end distribution of surfactant in the lungs. To see the effect of viscosity on the final distribution in the Weibel-based asymmetric model, we have performed simulations of delivery for various types of surfactants. Figure 81 shows the computed efficiency index (solid line, filled symbols) and homogeneity index (dashed line, open symbols) indices vs. dose volume for various values of the viscosity of Survanta® (Table 39). A larger viscosity increases the thickness of the trailing film left by the propagating plugs and lowers the efficiency, especially at low dose volume. This observation is consistent with what we already saw in rat and pig simulations. We do not see any noticeable changes in the homogeneity, especially at low dose volume. The distribution is strongly non-homogenous for both cases.

4.4.4.2.2 Surface tension

Simulations are run for 3 different values of the surface tension (3, 30, and 90 dyn.cm⁻¹) for the same initial applied conditions (see Table 39). Figure 82 displays the efficiency index η (solid line, filled symbols) and the homogeneity index HI (dashed line, open symbols). We can see that increasing surface tension leads to an increase in the efficiency and homogeneity for all values of the initial dose volume. The homogeneity is always smaller than 1, once again a sign of a highly non-homogeneous delivery.

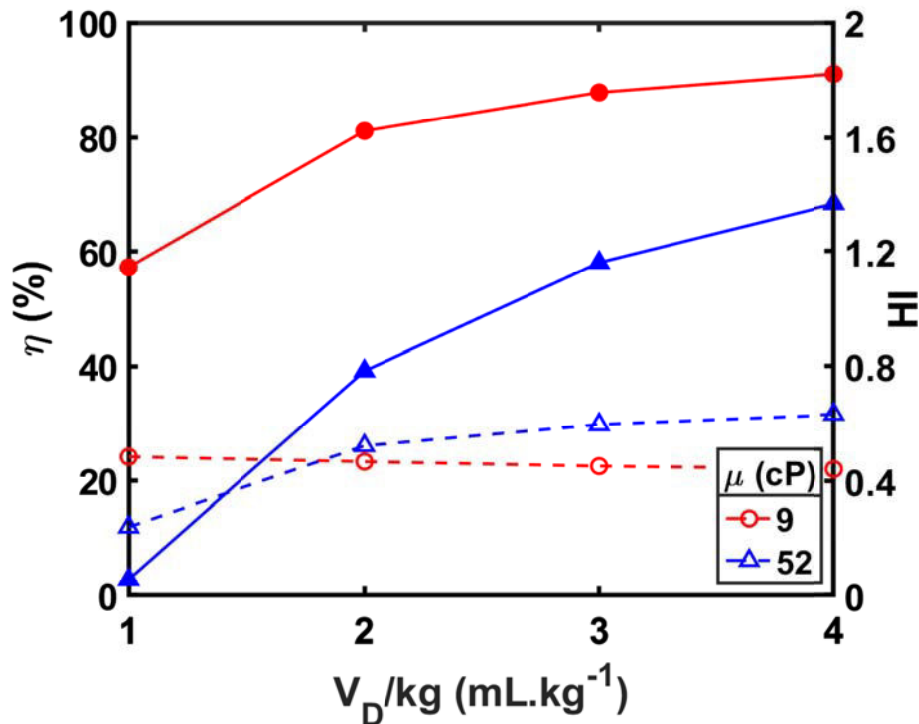


Figure 81: Efficiency index η (solid line, filled symbols) and homogeneity index HI (dashed line, open symbols) vs. dose volume for Survanta® for two different values of the viscosity, 9 cP (Concentration: 25 mg of PL/ml, 770 s⁻¹ shear rate and 37 °C) and 52 cP (Concentration: 35 mg of PL/ml, 70 s⁻¹ shear rate and 37 °C).

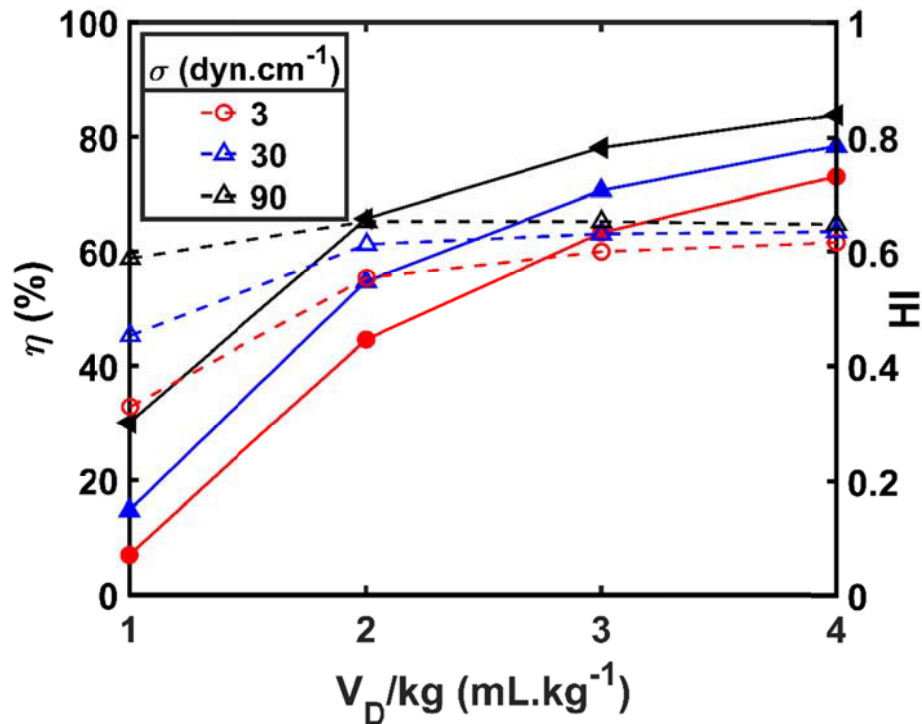


Figure 82: Efficiency index η (solid line, filled symbols) and homogeneity index HI (dashed line, open symbols) vs. dose volume for 3 different values of the surface tension.

4.4.4.3 Multiple-aliquot Instillation

In this section, we run our model to simulate SRT in the case of a multiple-aliquot delivery. As we have already observed in rat and pig simulations, multiple-aliquot instillation improved the efficiency and the homogeneity indices. However, this instillation technique did not exhibit any benefit in terms of homogeneity for surfactant delivery in the pig lung. Figure 83 displays the efficiency index (filled symbols) and the homogeneity index (open symbols) computed for 1, 5, 10, and 15 aliquots, respectively. We observe no improvement of the efficiency with the number of aliquots, but a slight increase of the homogeneity index which remains in all cases smaller than 1, the sign of a non-homogeneous distributions (see Table 39 for applied conditions).

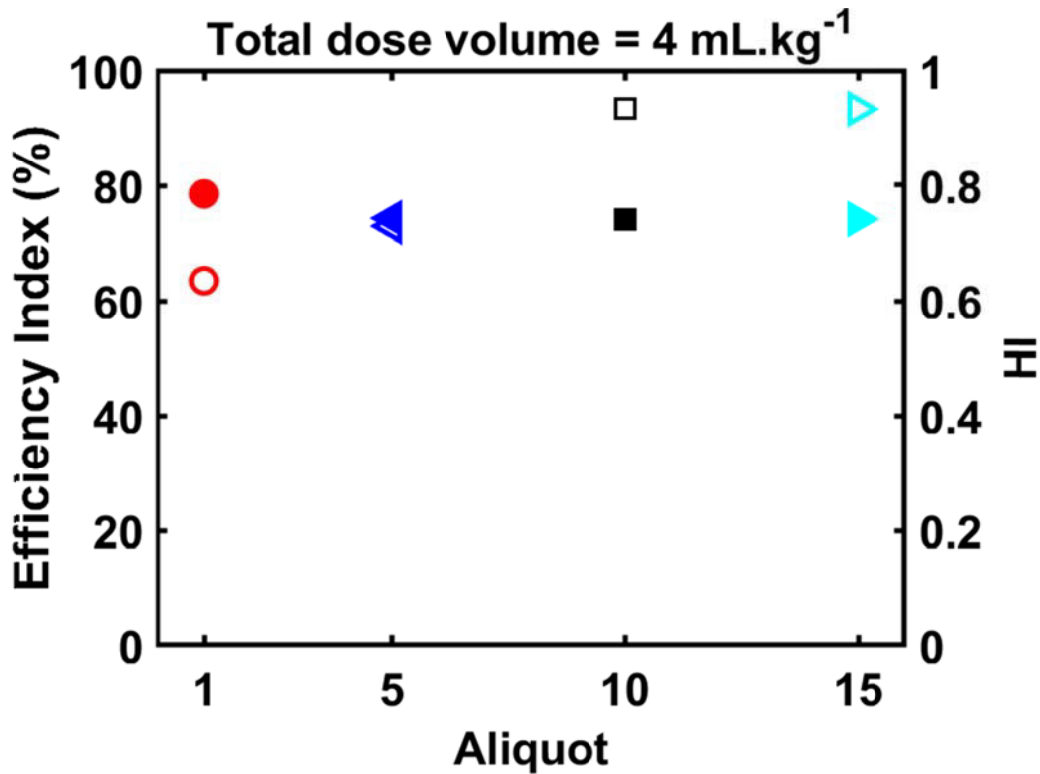


Figure 83: Efficiency index η (filled symbols) and homogeneity index HI (open symbols) vs. the number of aliquots in a multiple-aliquot delivery.

4.4.5 Weibel-based vs. Raabe-based asymmetric trees

In order to check how sensitive are our results with respect to the geometrical model of the lung that we used, we will compare in this section two asymmetric models of the human pulmonary airway system. The first is the Weibel-based asymmetric model (that we already compared with the symmetric version in Section 4.4.3). The second is the Raabe-based model.

Figure 84 displays the efficiency index (solid line, filled symbols) and the homogeneity index (dashed line, open symbols) computed in those models (see Table 39 for the details of applied conditions) vs. flow rate, for 4 different values of the initial dose volume per kg. As expected, the efficiency and homogeneity indices follow the same general pattern. In all cases, we observe a decrease of the efficiency index vs. flow rate and a simultaneous increase of the homogeneity index. Increasing the dose volume corresponds in all cases to an increase of both efficiency and homogeneity indices. The efficiency index in the Raabe-based model is only slightly higher than the Weibel-Based asymmetric model, while the homogeneity index is slightly lower.

In summary, Figure 84 shows that the two models are quite similar in terms of distribution and delivery of surfactant. The simulation results are robust, the trends are similar, and the only differences originate from the small differences in the details of the geometry. In the next section, we use the Raabe-based asymmetric model to investigate the effect of posture, surface tension, viscosity, and aliquot instillation.

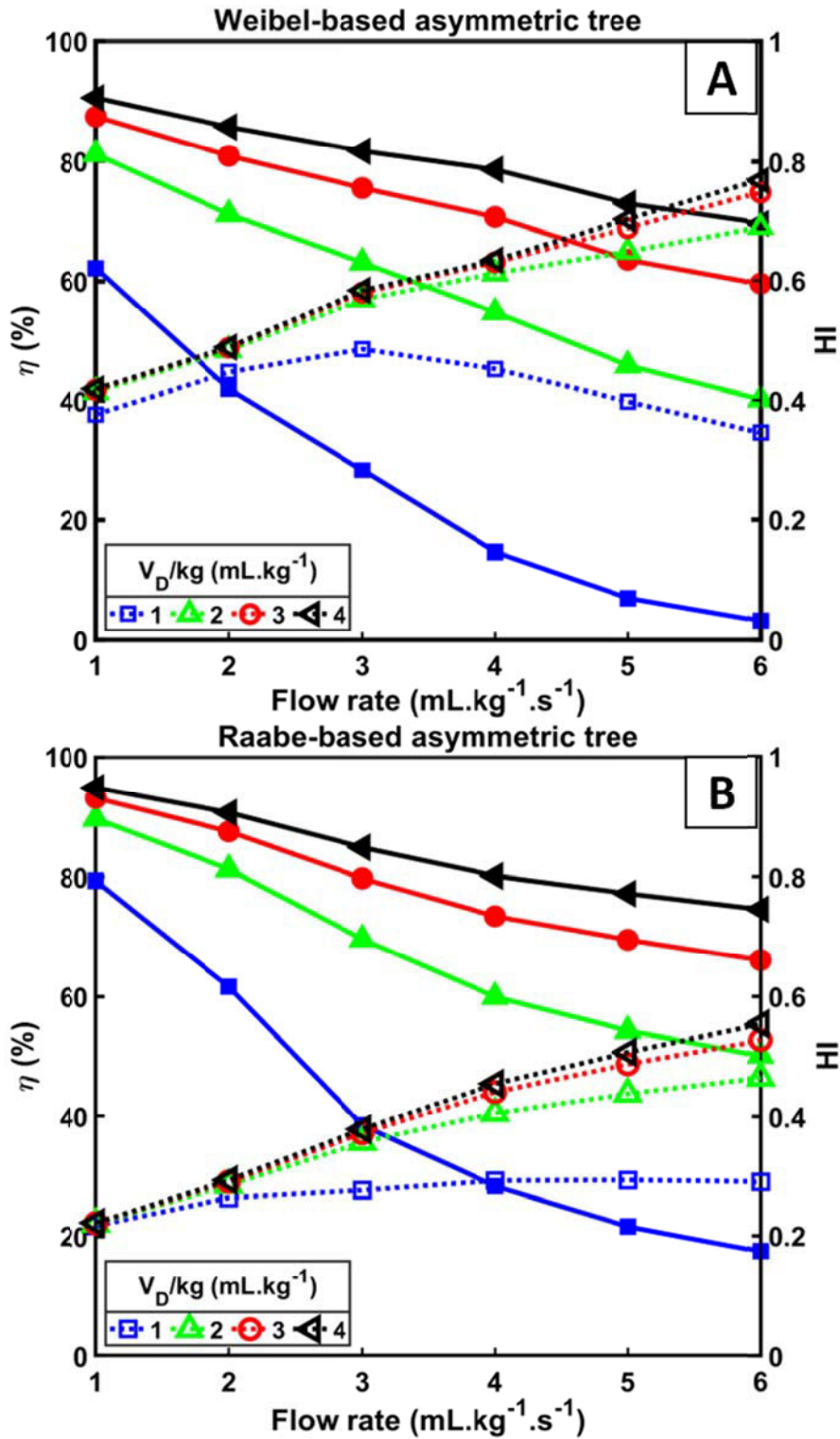


Figure 84: Efficiency index η (solid line, filled symbols) and homogeneity index HI (dashed line, open symbols) as functions of the tracheal flow rate for total dose volumes per kg of 1, 2, 3, and 4 mL.kg⁻¹. A) Weibel-based asymmetric model. B) Raabe-based asymmetric model.

4.4.6 Conclusion

In this chapter, we have simulated SRT in several models of the human pulmonary airway system. We have first compared symmetric models of neonate and adult and recovered the results of Filoche *et al.* [129] showing that the neonate's lung acts as a well-mixed compartment while the adult lung does not. However, both models share similarities: in all cases, increasing the dose volume leads to an increase of both efficiency and homogeneity indices, for any given flow rate because the larger available volume reduces the number of plug ruptures during the propagation of surfactant into the lung airway system. On the contrary, the increasing flow rate has the opposite effects on efficiency and homogeneity. On the one hand, the efficiency decreases with increasing flow rate due to the thicker trailing films coating the airway walls left behind by the plug during their propagation. On the other hand, the homogeneity increases due to the more even spitting at each bifurcation at a higher flow rate.

We have then studied how the efficiency and the homogeneity drop progressively with age. For this age study, a Weibel-based symmetric model has been used, from ages 1 to 19. This age study has shown that due to the increase of the lung volume and surface area, both efficiency and homogeneity drop dramatically above age 9-10, except at a very low flow rate.

The next step has consisted in assessing the role of the geometrical asymmetry by comparing the Weibel-based symmetric model with its asymmetric version, for adult lung. We have shown that, although the main features remain identical the same, there are some numerical differences, especially with respect to the computed values of the homogeneity index.

Finally, we have tested the robustness of our model of surfactant delivery in comparing a Raabe-based asymmetric model of the human pulmonary airway system with the Weibel-based version. The efficiency and homogeneity indices for Weibel symmetric and asymmetric based tree and Raabe-based tree follow the same trends, and both indices are very close in all cases. We conclude from that that we can safely use either one or the other model for assessing the efficacy of SRT in the human lung.

Discussion & conclusion

5.1 Discussion

This study is the first attempt to run a fast and reliable numerical and mathematical model of surfactant delivery in realistic large animal and human lung models and to validate it with experimental data. Many studies have investigated the plug or semi-infinite bubble propagations in straight channels to see the effect of different applied conditions, but very few have studied the final distribution of liquid resulting from plug propagation and splitting in the lungs. The lower respiratory tract in mammals is a highly hierarchical branching tree, and thus understanding liquid delivery and propagation through its branches and bifurcations bears a great interest for lung function and lung treatment.

To this end, we have developed realistic 3D models of rat, pig, and human tracheobronchial trees, accounting in particular for the branching asymmetry which is crucial for reliable computation of liquid plug propagation. Our mathematical model avoids solving the Navier-Stokes equation in two-phase flow and is based instead on describing the liquid plug propagation as a two-step process: step A, propagation of the plug along an individual airway and deposition of a trailing film onto the airway walls; step B, plug splitting at the bifurcation. These two steps are then repeated in the daughter's airways and so on through the airway tree. Step A essentially governs the efficiency of the delivery, defined as the fraction of the initial plug volume reaching the terminal region, while step B mostly governs the homogeneity of the final distribution. The computation of step A is achieved through an empirical equation deduced from CFD studies while step B relies instead on rate equations for computing the splitting factor at each bifurcation of the pulmonary airway tree.

The initial numerical study of SRT in humans using a similar model by Filoche *et al.* [129] had shown that, contrary to the adult lung, the neonate's lung is a well-mixed compartment for surfactant delivery. Due to the respective scaling of gravity force vs. surface tension and to the much larger surface of airway walls in the adult human lung than in the neonate (more than 3000 cm² for the adult and about 1500 cm² for the 3-month old neonate), the coating cost becomes vastly larger than delivered dose in the adult.

Our new simulations of surfactant delivery in rat and pig lungs presented here to offer a different and more complex picture. Despite the small size of the rat lung (smaller than the human neonate), simulations of delivery under realistic conditions result in a poor efficiency index (e.g. 4.69%) and a very small homogeneity index (0.32), overall a

very poor performance. At the same time, the pig whose lung has a size comparable to the human adult lung exhibits a higher efficiency (around 60%) and almost the same homogeneity (0.31). This seems to contradict our preceding explanation based on the size. The reason for this discrepancy can be found in the asymmetric structure of the airway pulmonary tree of the rat. Our computations emphasize that, beyond its size, the detailed geometrical structure of the lung airways plays a crucial role in distributing fluid to the alveolar region. The splitting factor at a bifurcation depends on asymmetries due to orientation with gravity and also geometry. For the rat lung, this geometric asymmetry dominates liquid transport. It is interesting on this topic to point out that the descriptions of the rat or pig pulmonary airway tree found in the literature are generally not suited for simulating liquid transport. These descriptions are usually used for simulating

1. Air and gas transport, for which one essentially needs only the airway diameters and lengths. For this entire airway tree, it is even more efficient to store the diameter and length of the trachea, then the ratios between successive generations of these parameters. Angles are almost of no interest as they have little influence on gas transport.
2. Aerosol deposition, for which not only the airway diameters and lengths are needed, but also the branching angles at each bifurcation. Deposition by impaction occurs mostly at the bifurcation carina, which explains the role played by the branching angle. On the contrary, rotation angles between successive bifurcation planes play a very little role [157]. Angles to gravity need only to be stored statistically, as they are involved in sedimentation.

Simulating liquid delivery in the tracheobronchial tree is a two-phase flow problem that is far more demanding in terms of knowledge of geometry. One needs now of course airway diameters and lengths, but also precise values of the angles to gravity for each airway and each bifurcation. These parameters are not usually found in the literature or in the commonly available lung airway models, hence the need to develop original 3D models of the mammalian pulmonary airway trees. Our simulations show for instance that the delivery reflects the craniocaudal asymmetry of the rat lung, a conclusion qualitatively consistent with the experimental data [158].

More generally, our results underline the crucial role played by the detailed 3D geometrical structure: it appears as one of the important determinants of the end distribution of surfactant (especially when moving from a symmetric to an asymmetric

model). In particular, despite the small size of the animals, the end distributions of surfactant in rat lungs are very non-homogeneous, both in our simulations and in the experiments. This high inhomogeneity is mainly due to the asymmetric architecture of the rat and pig airway trees, very different from that of the human. A cautionary note is that pig and sheep lungs, having monopodial lung architecture, have been used for SRT experimentation [15][133]. Thus, generalizing results of surfactant delivery between different species might be misleading, even for mammals of similar size or weight. The specific geometry of the studied species has to be accounted for in order to under the precise quantitative results obtained from numerical models. Also, material properties of the surfactant such as viscosity and surface tension may drastically alter the efficiency. This dependency makes it more complicated to compare results of trials performed with different surfactants. Preliminary data on surfactant dose volume distribution in rats confirm our computational findings.

Our model also suggests that one could customize the delivery for each patient by accounting precisely for the branching asymmetry in the first few generations, either to improve the final homogeneity or to reach one lobar or sub-lobar region. It therefore opens the way of engineering the delivery to target specific regions of the lung by tuning the initial dose volume, the flow rate, and the patient posture.

In addition to underlying the role played by the asymmetry in the pulmonary airway systems, our simulations confirmed that the instilled dose volume is a crucial parameter. This observation was corroborated with the biologic data of surfactant distribution in rat lungs. For dose volumes per kg ranging from 1 to 8 mL.kg⁻¹, the coating cost (the amount of surfactant left lining the walls of the airways) is very stable, about 0.32-0.76 mL in the asymmetric rat lung (L+R posture). When increasing even more the initial dose volume, the coating cost reaches a plateau. Once this plateau is reached, the efficiency of the delivery improves for larger dose volumes. This phenomenon seems to be universal and consistent with what has been already observed in our first computation in the human lung. However, a way to overcome this coating cost is not necessarily to increase the dose volume.

Indeed, a new feature of the model presented here is the possibility to simulate for the first time multiple-aliquot delivery. A plug traveling over a previously coated airway (by a previous plug) will not lose its mass until it reaches regions of the lung that were not attained by the preceding plugs. Our simulations clearly show that resorting to multiple aliquot deliveries without changing the posture increases the efficiency.

Increasing the homogeneity would require changing posture, but then the benefit of the multiple aliquot deliveries is partially lost, the subsequent plugs entering parts of the lung which have never been visited during the preceding instillations.

5.2 Conclusion & perspectives

In summary, this thesis investigates the transport of liquid plugs through the lower respiratory tract in order to understand the fundamental fluid mechanics in respiratory distress syndromes. Liquid instillation into the lungs is indeed required in many clinical therapies, such as liquid ventilation, drug delivery, and surfactant replacement therapy (SRT). Understanding how liquids distribute in the lungs is the primary key to the efficacy of these treatments. The current clinical practice is mostly based on empirical knowledge, both for determining the patient postures, the delivery conditions, or the type solution and surfactant. The work presented here provides new insights into the physical mechanisms of liquid plug dynamics inside the pulmonary airways during liquid instillation.

We have thus presented a numerical model of surfactant plug propagation into the pulmonary airway system. To that end, we have developed original 3D asymmetric geometrical models of rat, pig, and human conducting airways, based on morphometric measurements and dedicated to fluid transport. Using these models, we have assessed the effects of dose volume, flow rate, and multiple aliquot deliveries, and observed the existence of a threshold dose volume under which the coating cost represents 100% of the initial dose volume, which means that no surfactant reaches the acinar region at all. Moving from single to multiple instillations for a given total dose volume allows us to overcome partially the constraint of the coating cost and to globally improve the efficiency.

The liquid distribution is also affected by a number of factors, including physical properties of the liquid (viscosity, density, surface tension), patient posture (prone/supine, left lateral decubitus/right lateral decubitus) airway geometry, instillation method (flow rate), and presence of other plugs in nearby airways from previous instillation. We have studied the influence of all these factors and compared the results when it was possible to experimental data available on rats.

Based on this collection of results, one could wonder what the best strategies for successful delivery are. We have seen the major role played by the dose volume. It is therefore natural to use this tuning parameter to target specifically some regions of the

lung. If the region to be treated is the conducting airways, then a small initial dose volume V_D and a high flow rate would optimally distribute the surfactant everywhere in the lung while maximizing the deposition on the airway walls. If on the contrary the target is located distally within a well-defined lobe, one will favor a larger V_D and a smaller flow rate, able to propagate the liquid plugs for a long time without losing too much of their masses along the way. The dependence of homogeneity and efficiency, indices vs. the dose volume remains, however similar to the symmetric case.

We can envision further improvements to our model in several directions. While we have studied so far the detailed effects of surfactant on liquid plug propagation, trailing film thickness, and rupture in a single tube or channel [136][159][160][161], accounting for surface-active effects, fluid inertia in the deposition process would be the next steps when dealing with a branching tree geometry. The fate of surfactant, once it coats the airways or has entered the acinus, is also a challenging field of study. Understanding how surfactant will progressively coat the entire complex acinar surface requires accounting for the dynamics of alveolar recruitment during the breathing cycle [162], the mechanics of the compliant distal airways [163], and the complex motion of surfactant plugs in the rough-walled acinar ducts [164]. Accurately modeling this step should provide valuable insights into the delivery process, the final distribution of surfactant on the alveolar walls, and the global efficiency of SRT.

References

- [1] J. G. Betts *et al.*, *Anatomy and Physiology*. CNX: OpenStax, 2013.
- [2] J. B. Grotberg, “Respiratory fluid mechanics,” *Phys. Fluids*, vol. 23, no. 2, pp. 1–16, 2011.
- [3] E. R. Weibel, *Morphometry of the Human Lung*, 1st ed. Berlin and New York: Springer-Verlag, 1963.
- [4] M. Ochs *et al.*, “The Number of Alveoli in the Human Lung,” *Am J Respir Crit Care Med*, vol. 169, pp. 120–124, 2004.
- [5] E. R. Weibel and D. M. Gomez, “Architecture of the Human Lung,” *Science (80-.)*, vol. 137, pp. 577–85, 1962.
- [6] O. G. Raabe, H. C. Yeh, G. M. Schum, and R. F. Phalen, “Tracheobronchial geometry; Human, Dog, Rat, Hamster,” 1976.
- [7] R. F. Phalen, H.-C. Yeh, O. G. Raabe, and D. J. Velzasquez, “Casting the Lungs In-situ ROBERT,” *Anat. Rec.*, vol. 177, pp. 255–263, 1973.
- [8] M. Menache, W. Hofmann, and B. Asgharian, “Airway Geometry models of children’s lungs for use in dosimetry modeling,” vol. 20, pp. 101–126, 2008.
- [9] M. Rodriguez, S. Bur, A. Favre, and E. R. Weibel, “Pulmonary Acinus : Geometry and Morphometry of the Peripheral Airway System in Rat and Rabbit,” *Am. J. Anat.*, vol. 180, pp. 143–155, 1987.
- [10] D. Lee, M. V. Fanucchi, C. G. Plopper, J. Fung, and A. S. Wexler, “Pulmonary Architecture in the Conducting Regions of Six Rats,” *Anat Rec.*, vol. 291, pp. 916–926, 2008.
- [11] J. M. Oakes, M. Scadeng, E. C. Breen, A. L. Marsden, and C. Darquenne, “Rat airway morphometry measured from in situ MRI-based geometric models,” *J Appl Physiol*, vol. 112, no. 11, pp. 1921–1931, 2012.
- [12] K. Horsfield, “The relation between structure and function in the airways of the lung,” *Brit. J. Dis. Ches*, vol. 68, pp. 145–160, 1974.
- [13] C. Yeh, G. M. Schum, and M. T. Duggan, “Anatomic Models of the Tracheobronchial and Pulmonary Regions of the Rat,” *Anat. Rec.*, vol. 195, pp.

- 483–492, 1979.
- [14] W. B. Counter, I. Q. Wang, T. H. Farncombe, and N. R. Labiris, “Airway and pulmonary vascular measurements using contrast-enhanced micro-CT in rodents,” *Am J Physiol Lung Cell Mol Physiol*, vol. 304, pp. 831–843, 2013.
 - [15] M. K. Azad, H. A. Mansy, and P. T. Gamage, “Geometric features of pig airways using computed tomography,” *Physiol Rep.*, vol. 4, p. e12995, 2016.
 - [16] D. R. Einstein *et al.*, “An Automated Self-similarity Analysis of the Pulmonary Tree of the Sprague-Dawley Rat Daniel,” *Anat Rec.*, vol. 291, no. 12, pp. 1628–1648, 2009.
 - [17] F. J. Miller *et al.*, “Respiratory tract lung geometry and dosimetry model for male Sprague-Dawley rats,” *Inhal. Toxicol.*, vol. 8378, no. 9, pp. 524–544, 2014.
 - [18] A. P. Moreci and J. C. Norman, “Measurements of alveolar sac diameters by incident-light photomicrography. Effects of positive-pressure respiration.,” *Ann. Thorac. Surg.*, vol. 15, no. 2, pp. 179–186, 1973.
 - [19] D. M. Hyde, N. K. Tyler, L. F. Puteny, P. Singh, and H. J. G. Gundersen, “Total Number and Mean Size of Alveoli in Mammalian Lung Estimated Using Fractionator Sampling and Unbiased Estimates of the Euler Characteristic of Alveolar Openings,” *Anat Rec.*, vol. 274, pp. 216–226, 2004.
 - [20] P. B. Noble *et al.*, “Distribution of airway narrowing responses across generations and at branching points, assessed in vitro by anatomical optical coherence tomography,” *Respir Res*, vol. 11, pp. 1–12, 2010.
 - [21] S. Nakakuki, “The New Interpretation of Bronchial Tree,” *Proc. Japan Acad.*, vol. 51, pp. 342–346, 1975.
 - [22] R. F. Dondelinger *et al.*, “Relevant radiological anatomy of the pig as a training model in interventional radiology,” *Eur. Radiol.*, vol. 1273, pp. 1254–1273, 1998.
 - [23] W. Mouton, J. Pfitzner, J. Bessell, and G. Maddern, “Bronchial anatomy and single-lung ventilation in the pig,” *CAN .J. ANESTH.*, vol. 46, pp. 701–703, 1999.
 - [24] J. N. Maina and P. V. Gils, “Morphometric characterization of the airway and vascular systems of the lung of the domestic pig, *Sus scrofa*: comparison of the airway, arterial and venous systems,” *Comp. Biochem. Physiol.*, vol. 130, pp. 781–798, 2001.

- [25] S. Nakakuki, "Bronchial tree, lobular division and blood vessels of the pig lung," *J Vet Med Sci.*, vol. 56, pp. 685–689, 1994.
- [26] E. P. Judge, J. M. L. Hughes, J. J. Egan, M. Maguire, E. L. Molloy, and S. O. Dea, "Anatomy and Bronchoscopy of the Porcine Lung A Model for Translational Respiratory Medicine," *Am. J. Respir. Cell Mol. Biol.*, vol. 51, no. 3, pp. 334–343, 2014.
- [27] L. a Creuwels, L. M. van Golde, and H. P. Haagsman, "The pulmonary surfactant system: biochemical and clinical aspects.," *Lung*, vol. 175, no. 1, pp. 1–39, 1997.
- [28] Forum of International Respiratory Societies, "The Global Impact of Respiratory Disease," Sheffield, 2017.
- [29] A. Sharafkhaneh, N. A. Hanania, and V. Kim, "Pathogenesis of Emphysema: From the Bench to the Bedside," *Proc. Am. Thorac. Soc.*, vol. 5, no. 4, pp. 475–477, 2008.
- [30] J. Bastacky *et al.*, "Alveolar lining layer is thin and continuous : scanning electron microscopy of rat lung," pp. 1615–1628, 2018.
- [31] D. Ashbaugh, D. Boyd Bigelow, T. Petty, and B. Levine, "Acute Respiratory Distress in Adults," *Lancet*, vol. 290, no. 7511, pp. 319–323, 1967.
- [32] G. R. Bernard *et al.*, "Definitions, Mechanisms, Relevant Outcomes, and Clinical Trial Coordination," *Crit. Care Med.*, vol. 149, pp. 818–824, 1994.
- [33] V. M. Ranieri *et al.*, "Acute respiratory distress syndrome: The Berlin definition," *JAMA - J. Am. Med. Assoc.*, vol. 307, no. 23, pp. 2526–2533, 2012.
- [34] P. Jouvret *et al.*, "Pediatric Acute Respiratory Distress Syndrome: Consensus Recommendations from the Pediatric Acute Lung Injury Consensus Conference," *Pediatr. Crit. Care Med.*, vol. 16, no. 5, pp. 428–439, 2015.
- [35] M. S. Dunnill, "POSTNATAL GROWTH OF THE LUNG," *Thorax*, vol. 17, pp. 329–333, 1962.
- [36] K. von Neergard, "Neue Auffassungen uber einen Grundbegriff der Atemmechanik. Die Retraktionskraft der Lunge, abhangig von der Oberflachenspannung in den Alveolen," *T Gesamte Exp Med*, vol. 66, pp. 374–394, 1929.
- [37] R. E. Pattle, "Properties, function, and origin of the alveolar lining layer,"

- Nature*, vol. 175, no. 4469, pp. 1125–1126, 1955.
- [38] J. A. Clements, “Surface tension of lung extracts,” *Proc Soc Exp Biol Med*, vol. 95, pp. 170–172, 1957.
- [39] J. A. Clements, E. S. Brown, and R. P. Johnson, “Pulmonary Surface Tension and the Mucus Lining of the Lungs: Some Theoretical Considerations,” *J Appl Physiol*, vol. 12, pp. 262–268, 1958.
- [40] M. E. Avery and J. Mead, “Surface properties in relation to atelectasis and hyaline,” *AMA Am J Dis Child*, vol. 97, pp. 517–523, 1959.
- [41] C. Long, W. Li, L. Wanwei, L. Jie, and S. Yuan, “Noninvasive Ventilation with Heliox for Respiratory Distress Syndrome in Preterm Infant: A Systematic Review and Meta-Analysis,” *Can. Respir. J.*, vol. 2016, pp. 1–8, 2016.
- [42] P. A. Dargaville and B. Copnell, “The Epidemiology of Meconium Aspiration Syndrome: Incidence, Risk Factors, Therapies, and Outcome,” *Pediatrics*, vol. 117, no. 5, pp. 1712–1721, 2006.
- [43] R. M. Hubbard, K. M. Choudhury, and G. Lim, “Treatment Patterns and Clinical Outcomes in Neonates Diagnosed With Respiratory Distress Syndrome in a Low-Income Country: A Report From Bangladesh,” *Anesth Analg*, vol. 5, no. 126, pp. 1684–1686, 2018.
- [44] M. Griese, “Pulmonary surfactant in health and human lung diseases : state of the art,” *Eur Respir J.*, vol. 13, pp. 1455–1476, 1999.
- [45] K. Kurashima, H. Ogawa, T. Ohka, M. Fujimura, T. Matsuda, and T. Kobayashi, “A pilot study of surfactant inhalation in the treatment of asthmatic attack,” *Arerugi.*, vol. 40, pp. 160–163, 1991.
- [46] S. B. Oetomo *et al.*, “Surfactant Nebulization does not Alter Airflow Obstruction and Bronchial Responsiveness to Histamine in Asthmatic Children,” *Am J Respir Crit Care Med.*, vol. 153, pp. 1148–1152, 1996.
- [47] G. D. Vos, M. N. Rijtema, and C. E. Blanco, “Treatment of Respiratory Failure due to Respiratory Syncytial Virus Pneumonia With Natural Surfactant,” *Pediatr Pulmonol.*, vol. 415, pp. 412–415, 1996.
- [48] A. Anzueto *et al.*, “Effects of Aerosolized Surfactant in Patients With Stable Chronic Bronchitis,” *JAMA.*, vol. 278, pp. 1426–1431, 1997.
- [49] J. Allen, S. Moore, A. Pope-Harman, C. Marsh, and M. Wewers,

- “Immunosuppressive properties of surfactant and plasma on alveolar macrophages,” *J Lab Clin Med.*, vol. 125, pp. 356–369, 1995.
- [50] J. M. Antal, L. T. Divis, S. C. Erzurum, H. P. Wiedemann, and M. J. Thomassen, “Surfactant Suppresses NF-KB Activation in Human Monocytic Cells,” *Am J Respir Cell Mol Biol.*, vol. 14, pp. 374–379, 1996.
- [51] P. Bartmann, L. Gortner, F. Pohlandt, and L. Gortner, “Immunogenicity and immunomodulatory activity of bovine surfactant (SF-RI 1),” *Acta Paediatr.*, vol. 81, pp. 383–388, 1992.
- [52] P. Bartmann, L. Gortner, F. Pohlandt, and H. Jaeger, “In vitro lymphocyte functions in the presence of bovine surfactant and its phospholipid fractions.,” *J Perinat Med.*, vol. 20, pp. 189–196, 1992.
- [53] M. D. Roth, M. Pinto, S. H. Golub, and H. Shau, “Pulmonary Surfactant Inhibits Interleukin-2-induced Proliferation and the Generation of Lymphokine-activated Killer Cells,” *Am J Respir Cell Mol Biol.*, vol. 9, pp. 652–658, 1993.
- [54] S. Han and R. K. Mallampalli, “The Role of Surfactant in Lung Disease and Host Defense against Pulmonary Infections,” *Ann Am Thorac Soc.*, vol. 12, no. 5, pp. 765–774, 2015.
- [55] T. Fujiwara, S. Chida, Y. Watabe, H. Maeta, T. Morita, and T. Abe, “Saturday I2 January I980 ARTIFICIAL SURFACTANT THERAPY IN HYALINE-MEMBRANE DISEASE,” no. 2, pp. 2–6.
- [56] M. Barber and C. J. Blaisdell, “Respiratory causes of infant mortality: Progress and challenges,” *Am. J. Perinatol.*, vol. 27, no. 7, pp. 549–558, 2010.
- [57] H. L. Halliday, “History of surfactant from 1980,” *Biol. Neonate*, vol. 87, no. 4, pp. 317–322, 2005.
- [58] Y. M. Bae and C. W. Bae, “The Changes in the Mortality Rates of Low Birth Weight Infant and Very Low Birth Weight Infant in Korea over the Past 40 Years,” *J. Korean Med. Sci.*, vol. 19, no. 1, pp. 27–31, 2004.
- [59] C. W. Bae and W. H. Hahn, “Surfactant therapy for neonatal respiratory distress syndrome: A review of Korean experiences over 17 years,” *J. Korean Med. Sci.*, vol. 24, no. 6, pp. 1110–1118, 2009.
- [60] A. Amigoni, A. Pettenazzo, V. Stritoni, and M. Circelli, “Surfactants in Acute Respiratory Distress Syndrome in Infants and Children: Past, Present and Future,” *Clin. Drug Investig.*, vol. 37, no. 8, pp. 1–8, 2017.

- [61] N. Fettah, D. Dilli, S. Beken, A. Zenciroglu, and N. Okumuş, “Surfactant for acute respiratory distress syndrome caused by near drowning in a newborn,” *Pediatr. Emerg. Care*, vol. 30, no. 3, pp. 180–181, 2014.
- [62] D. F. Willson *et al.*, “Pediatric calfactant in acute respiratory distress syndrome trial,” *Pediatr. Crit. Care Med.*, vol. 14, no. 7, pp. 657–665, 2013.
- [63] D. Willson *et al.*, “Effect of Exogenous Surfactant (Calfactant) in Pediatric Acute Lung Injury,” *Jama*, vol. 293, no. 4, pp. 470–476, 2005.
- [64] J. C. Möller *et al.*, “Treatment with bovine surfactant in severe acute respiratory distress syndrome in children: A randomized multicenter study,” *Intensive Care Med.*, vol. 29, no. 3, pp. 437–446, 2003.
- [65] M. M. Hermon *et al.*, “Surfactant Therapy In Infants And Children : Three Years Experience In A Pediatric Intensive Care Unit,” *Shock*, vol. 17, no. 4, pp. 247–251, 2002.
- [66] J. López-Herce, N. De Lucas, A. Carrillo, A. Bustinza, and R. Moral, “Surfactant treatment for acute respiratory distress syndrome,” *Arch. Dis. Child.*, vol. 80, no. 3, pp. 248–252, 1999.
- [67] D. F. F. Willson *et al.*, “Instillation of calf lung surfactant extract (calfactant) is beneficial in pediatric acute hypoxemic respiratory failure. Members of the Mid-Atlantic Pediatric Critical Care Network.,” *Crit. Care Med.*, vol. 27, no. 1, pp. 188–195, 1999.
- [68] T. J. Gregory *et al.*, “Bovine surfactant therapy for patients with acute respiratory distress syndrome,” *Am. J. Respir. Crit. Care Med.*, vol. 155, no. 4, pp. 1309–1315, 1997.
- [69] I. M. Lewis, L. M. C. Caig, D. Häfner, R. Spragg, R. Veldhuizen, and C. Kerr, “Dosing and Delivery of a Recombinant Surfactant in Lung-injured Adult Sheep Induction of Lung Injury.”
- [70] A. Anzueto, R. Baughman, K. Guntupalli, J. Weg, and P. Wiedemann, “AEROSOLIZED SURFACTANT IN ADULTS WITH SEPSIS-INDUCED ACUTE RESPIRATORY DISTRESS SYNDROME,” *N Engl J Med.*, vol. 334, no. 22, 1996.
- [71] J. Kesecioglu, M. Schultz, and D. Lundberg, “Treatment of acute lung injury (ALI/ARDS) with surfactant,” *Am J Respir Crit Care Med*, vol. 163, p. A819, 2001.

- [72] R. G. Spragg *et al.*, “Treatment of Acute Respiratory Distress Syndrome with Recombinant Surfactant Protein C Surfactant,” *Am. J. Respir. Crit. Care Med.*, vol. 167, no. 11, pp. 1562–1566, 2003.
- [73] R. G. Spragg *et al.*, “Effect of Recombinant Surfactant Protein C–Based Surfactant on the Acute Respiratory Distress Syndrome,” *N. Engl. J. Med.*, vol. 351, no. 9, pp. 884–892, 2004.
- [74] R. G. Spragg *et al.*, “Recombinant Surfactant Protein C – based Surfactant for Patients with Severe Direct Lung Injury,” *Am. J. Respir. Crit. Care Med.*, vol. 183, pp. 1055–1061, 2011.
- [75] J. Kesecioglu *et al.*, “Exogenous Natural Surfactant for Treatment of Acute Lung Injury and the Acute Respiratory Distress Syndrome,” *Am J Respir Crit Care Med.*, vol. 180, pp. 989–994, 2009.
- [76] T. Ueda, M. Ikegami, E. D. Rider, and A. H. Jobe, “Distribution of surfactant and ventilation in surfactant-treated preterm lambs,” *J Appl Physiol*, vol. 76, no. 1, pp. 45–55, 1994.
- [77] F. F. Espinosa and R. D. Kamm, “Meniscus formation during tracheal instillation of surfactant,” *Am. Physiol. Soc.*, vol. 85, no. 1, pp. 266–272, 1998.
- [78] K. J. Cassidy, N. Gavriely, and J. B. Grotberg, “Liquid Plug Flow in Straight and Bifurcating Tubes,” *J. Biomech. Eng.*, vol. 123, no. 6, p. 580, 2001.
- [79] J. L. Bull, S. Tredici, E. Komori, D. O. Brant, J. B. Grotberg, and R. B. Hirschl, “Distribution dynamics of perfluorocarbon delivery to the lungs: an intact rabbit model,” *Am. Physiol. Soc.*, vol. 96, no. December 2003, pp. 1633–1642, 2004.
- [80] L. Steffen *et al.*, “Surfactant replacement therapy reduces acute lung injury and collapse induration related lung remodeling in the bleomycin model,” *Am. J. Physiol. - Lung Cell. Mol. Physiol.*, vol. 313, pp. 313–327, 2017.
- [81] D. Halpern, O. E. Jensen, and J. B. Grotberg, “A theoretical study of surfactant and liquid delivery into the lung,” *J. Appl. Physiol*, vol. 85, pp. 333–352, 1998.
- [82] Y. Zheng, J. C. Anderson, V. Suresh, and J. B. Grotberg, “Effect of gravity on liquid plug transport through an airway bifurcation model,” *J. Biomech. Eng. Asme*, vol. 127, no. 5, pp. 798–806, 2005.
- [83] C. F. Tai, B. L. Vaughan, M. Florens, M. Filoche, and J. B. Grotberg, “Liquid and drug delivery into a 3D lung tree,” *Am. J. Respir. Crit. Care Med.*, vol.

- 183, no. 1 Meeting Abstracts, pp. 2–3, 2011.
- [84] D. F. Willson, J. D. Truwit, M. R. Conaway, C. S. Traul, and E. E. Egan, “The adult calfactant in acute respiratory distress syndrome trial,” *Chest*, vol. 148, no. 2, pp. 356–364, 2015.
- [85] E. Lopez-Rodriguez and J. Pérez-Gil, “Structure-function relationships in pulmonary surfactant membranes: From biophysics to therapy,” *Biochim. Biophys. Acta - Biomembr.*, vol. 1838, no. 6, pp. 1568–1585, 2014.
- [86] S. Orgeig, J. L. Morrison, and C. B. Daniels, “Prenatal Development of the Pulmonary Surfactant System and the Influence of Hypoxia,” *Respir. Physiol. Neurobiol.*, 2011.
- [87] W. Bernhard *et al.*, “Conductive Airway Surfactant: Surface-tension Function, Biochemical Composition, and Possible Alveolar Origin,” *Am. J. Respir. Cell Mol. Biol.*, vol. 17, no. 1, pp. 41–50, 1997.
- [88] E. J. A. Veldhuizen and H. P. Haagsman, “Role of pulmonary surfactant components in surface film formation and dynamics,” *Biochim. Biophys. Acta - Biomembr.*, vol. 1467, pp. 255–270, 2000.
- [89] N. El-Gendy, A. Kaviratna, C. Berkland, and P. Dhar, “Delivery and performance of surfactant replacement therapies to treat pulmonary disorders,” *Ther. Deliv.*, vol. 4, no. 8, pp. 951–980, 2013.
- [90] U. Christmann, V. Buechner-Maxwell, S. G. Witonsky, and R. D. Hite, “Role of Lung Surfactant in Respiratory Disease: Current Knowledge Large Animal Medicine,” *J Vet Intern Med*, vol. 23, pp. 227–242, 2009.
- [91] A. Almlén, “Synthetic pulmonary surfactant : Effects of surfactant proteins B and C and their analogues,” Stockholm, Sweden, 2010.
- [92] C. Casals and O. Cañadas, “Biochimica et Biophysica Acta Role of lipid ordered/disordered phase coexistence in pulmonary surfactant function,” *BBA - Biomembr.*, vol. 1818, no. 11, pp. 2550–2562, 2012.
- [93] D. Sweet *et al.*, “European consensus guidelines on the management of neonatal respiratory distress syndrome,” *J. Perinat. Med.*, vol. 35, no. 3, pp. 175–186, 2007.
- [94] Y. Y. Zuo, R. A. W. Veldhuizen, A. W. Neumann, N. O. Petersen, and F. Possmayer, “Current perspectives in pulmonary surfactant - Inhibition, enhancement and evaluation,” *Biochim. Biophys. Acta - Biomembr.*, vol. 1778,

- no. 10, pp. 1947–1977, 2008.
- [95] Merriam-Webster.com, “surface tension,” 2019. [Online]. Available: www.merriam-webster.com/dictionary.
- [96] D. K. Owens and R. C. Wendt, “Estimation of the surface free energy of polymers,” *J. Appl. Polym. Sci.*, vol. 13, pp. 1741–1747, 1969.
- [97] J. Goerke, “Pulmonary surfactant: Functions and molecular composition,” *Biochim. Biophys. Acta, Mol. Basis Dis.*, vol. 1408, no. 2–3, pp. 79–89, 1998.
- [98] J. P. Butler, R. E. Brown, D. Stamenović, J. P. Morris, and G. P. Topulos, “Effect of surface tension on alveolar surface area,” *J. Appl. Physiol.*, vol. 93, no. 3, pp. 1015–1022, 2002.
- [99] E. R. Weibel, *Functional Morphology of Lung Parenchyma*, no. 25. Berne: University of Berne, 2011.
- [100] S. A. Dias, “Réponse des cellules épithéliales pulmonaires à l’exposition au perfluorocarbone dans le contexte des applications de la ventilation liquide totale,” l’Université Paris Est, 2017.
- [101] Wikipedia, “Viscosity,” *Wikipedia*. [Online]. Available: https://en.wikipedia.org/wiki/Viscosity_of_amorphous_materials.
- [102] K. J. Cassidy *et al.*, “A rat lung model of instilled liquid transport in the pulmonary airways rats A rat lung model of instilled liquid transport in the pulmonary airways,” *J. Appl. Physiol.*, vol. 90, pp. 1955–1967, 2001.
- [103] J. C. Anderson *et al.*, “Effect of ventilation rate on instilled surfactant distribution in the pulmonary airways of rats,” *J. Appl. Physiol.*, vol. 97, pp. 45–56, 2004.
- [104] D. M. King, Z. Wang, J. W. Kendig, H. J. Palmer, B. A. Holm, and R. H. Notter, “Concentration-dependent, temperature-dependent non-Newtonian viscosity of lung surfactant dispersions,” *Chem. Phys. Lipids*, vol. 112, pp. 11–19, 2001.
- [105] D. M. King *et al.*, “Bulk shear viscosities of endogenous and exogenous lung surfactants,” *Am. J. Physiol. - Lung Cell. Mol. Physiol.*, vol. 282, no. 2, pp. 277–284, 2002.
- [106] K. W. Lu, J. Pérez-Gil, and H. W. Taesch, “Kinematic viscosity of therapeutic pulmonary surfactants with added polymers,” *Biochim. Biophys. Acta, Rev.*

- Biomembr.*, vol. 1788, no. 3, pp. 632–637, 2009.
- [107] L. P. A. Thai, F. Mousseau, E. K. Oikonomou, and J. Berret, “On the rheology of pulmonary surfactant : effects of concentration and consequences for the surfactant replacement therapy,” pp. 1–28, 2019.
- [108] “Respiratory Distress Syndrome,” *stanfordchildrens.org*. .
- [109] J. W. Kendig, R. H. Notter, C. Cox, L. J. Reubens, J. M. Davis, and W. M. Maniscalco, “A Comparison of Surfactant as Immediate Prophylaxis and as Rescue Therapy in Newborns of Less Than 30 Weeks’ Gestation,” *N. Engl. J. Med.*, vol. 325, no. 11, pp. 783–793, 1991.
- [110] M. S. Dunn, A. T. Shennan, D. Zayack, and F. Possmayer, “Bovine surfactant replacement therapy in neonates of less than 30 weeks' gestation: a randomized controlled trial of prophylaxis versus treatment,” *Pediatrics*, vol. 87, no. 3, pp. 377–386, 1991.
- [111] N. Nouraeyan, A. Lambrinakos-Raymond, M. L. Rrt, and G. S. Anna, “Surfactant administration in neonates : A review of delivery methods,” *Can. J. Respir. Ther.*, vol. 50, no. 3, pp. 91–95, 2014.
- [112] J. Kattwinkel, M. Robinson, B. T. Bloom, P. Delmore, and J. E. Ferguson, “Technique for intrapartum administration of surfactant without requirement for an endotracheal tube,” *J. Perinatol.*, vol. 24, no. 6, pp. 360–365, 2004.
- [113] S. M. Donn and S. K. Sinha, “Aerosolized lucinactant: a potential alternative to intratracheal surfactant replacement therapy,” *Expert Opin. Pharmacother.*, vol. 9, no. 3, pp. 475–8, 2008.
- [114] F. Moya and A. Maturana, “Animal-Derived Surfactants Versus Past and Current Synthetic Surfactants: Current Status,” *Clin. Perinatol.*, vol. 34, no. 1, pp. 145–177, 2007.
- [115] S. Minocchieri, C. A. Berry, and J. J. Pillow, “Nebulised surfactant to reduce severity of respiratory distress: A blinded, parallel, randomised controlled trial,” *Arch. Dis. Child. Fetal Neonatal Ed.*, pp. 15–18, 2018.
- [116] B. K. Walsh, B. Daigle, R. M. DiBlasi, and R. D. Restrepo, “AARC Clinical Practice Guideline. Surfactant Replacement Therapy: 2013,” *Respir. Care*, vol. 58, no. 2, pp. 367–375, 2013.
- [117] T. Sera, H. Fujioka, H. Yokota, and A. Makinouchi, “Three-dimensional visualization and morphometry of small airways from microfocal X-ray

- computed tomography,” *J Biomech*, vol. 36, pp. 1587–1594, 2003.
- [118] D. M. Hyde *et al.*, “Asthma: a comparison of animal models using stereological methods,” *Eur Respir Rev.*, vol. 15, no. 101, pp. 122–135, 2006.
- [119] J. P. Carson, D. R. Einstein, K. R. Minard, M. V Fanucchi, C. D. Wallis, and R. A. Corley, “High-resolution lung airway cast segmentation with proper topology suitable for computational fluid dynamic simulations,” *Comput Med Imaging Graph.*, vol. 34, no. 7, pp. 572–578, 2011.
- [120] R. E. Jacob, S. M. Colby, S. Kabilan, D. R. Einstein, and P. James, “In Situ Casting and Imaging of the Rat Airway Tree for Accurate 3D Reconstruction,” *Exp Lung Res.*, vol. 39, no. 6, pp. 249–257, 2014.
- [121] S. F. Barré, D. Haberthür, T. P. Cremona, M. Stampanoni, and J. C. Schittny, “The total number of acini remains constant throughout postnatal rat lung development,” *Am J Physiol Lung Cell Mol Physiol.*, vol. 311, pp. 1082–1089, 2016.
- [122] V. S. Fernandes *et al.*, “Pulmonary Pharmacology & Therapeutics Role of endogenous hydrogen sulfide in nerve-evoked relaxation of,” vol. 41, pp. 1–10, 2016.
- [123] A. Monteiro and R. L. Smith, “Bronchial tree Architecture in Mammals of Diverse Body Mass,” *Int. J. Morphol.*, vol. 32, no. 1, pp. 312–316, 2014.
- [124] B. Asgharian *et al.*, “Modeling particle deposition in the pig respiratory tract,” *J. Aerosol Sci.*, vol. 99, pp. 107–124, 2016.
- [125] R. F. Phalen, M. J. Oldham, C. B. Beaucage, T. T. Crocker, and J. D. Mortensen, “Postnatal Enlargement of Human Tracheobronchial Airways and Implications for Particle Deposition,” *Anat. Rec.*, vol. 212, pp. 368–380, 1985.
- [126] M. Menache, W. Hofmann, B. Ashgarian, and F. J. Miller, “Airway Geometry Models of Children’s Lungs for Use in Dosimetry Modeling,” *Inhal. Toxicol.*, vol. 20, pp. 101–126, 2008.
- [127] W. Hess, “Das Prinzip des kleinsten Kraftverbrauches im Dienste hamodynamischer Forschung,” *Arch. für Anat. und Physiol. Arch. für Anat. und Physiol.*, pp. 1–62, 1914.
- [128] M. Cecil, “The Physiological Principle of Minimum Work: I. The Vascular System and the Cost of Blood Volume,” *Proc Natl Acad Sci USA*, vol. 12, no. 3, pp. 207–14, 1926.

- [129] M. Filoche, C. F. Tai, and J. B. Grotberg, “Three-dimensional model of surfactant replacement therapy,” *Proc. Natl. Acad. Sci.*, vol. 112, no. 30, pp. 9287–9292, 2015.
- [130] T. Wilson, “Design of the bronchial tree,” *Nature*, vol. 213, pp. 668–669, 1967.
- [131] E. R. Weibel, *Morphometry of the Human Lung*, 1st ed. New York: Springer-Verlag Berlin Heidelberg GmbH, 1963.
- [132] A. Schmidt, S. Zidowitz, A. Kriete, T. Denhard, S. Krass, and H. Peitgen, “A digital reference model of the human bronchial tree,” *Comput Med Imaging Graph.*, vol. 28, pp. 203–211, 2004.
- [133] M. H. Tawhai *et al.*, “CT-based geometry analysis and finite element models of the human and ovine bronchial tree,” *J Appl Physiol.*, vol. 97, pp. 2310–2321, 2004.
- [134] J. M. Davis, G. A. Russ, L. Metlay, B. Dickerson, and B. S. Greenspan, “Short-Term Distribution Kinetics of Intratracheally Administered Exogenous Lung Surfactant,” *Pediatr. Res.*, vol. 31, no. 5, pp. 1–5, 1992.
- [135] N. Gilliard, P. M. Richman, T. A. Merritt, and R. G. Spragg, “Effect of volume and dose on the pulmonary distribution of exogenous surfactant administered to normal rabbits or to rabbits with oleic acid lung injury.,” *Am. Rev. Respir. Dis.*, vol. 141, no. 3, pp. 743–747, 1990.
- [136] Y. Zheng, H. Fujioka, and J. C. Grotberg, “Effects of Inertia and Gravity on Liquid Plug Splitting at a Bifurcation,” *J Biomech Eng.*, vol. 128, pp. 707–716, 2006.
- [137] J. Marín-Corral *et al.*, “Redox Balance and Cellular Inflammation in the Diaphragm, Limb Muscles, and Lungs of Mechanically Ventilated Rats,” *Anesthesiology*, vol. 112, pp. 384–394, 2010.
- [138] S. Roy *et al.*, “Early Airway Pressure Release Ventilation Prevents Ards- a Novel Preventive Approach to Lung Injury,” *Shock*, vol. 39, no. June 2012, pp. 28–38, 2014.
- [139] J. Lipes, A. Bojmehrani, and F. Lellouche, “Low Tidal Volume Ventilation in Patients Without Acute Respiratory Distress Syndrome : A Paradigm Shift in Mechanical Ventilation,” *Crit Care Res Pr.*, vol. 2012, 2012.
- [140] M. Briel *et al.*, “Higher vs Lower Positive End-Expiratory Pressure in Patients With Acute Lung Injury,” *JAMA*, vol. 303, no. 9, pp. 865–873, 2015.

- [141] R. Soll and E. Özek, “Multiple versus single doses of exogenous surfactant for the prevention or treatment of neonatal respiratory distress syndrome,” *Cochrane Database Syst. Rev.*, no. 1, 2009.
- [142] D. Walmrath *et al.*, “Bronchoscopic administration of bovine natural surfactant in ARDS and septic shock: Impact on gas exchange and haemodynamics,” *Eur. Respir. J.*, vol. 19, no. 5, pp. 805–810, 2002.
- [143] K. Raghavendran, D. Willson, and R. Notter, “Surfactant Therapy of ALI and ARDS,” *Crit Care Clin*, vol. 27, no. 3, pp. 525–559, 2012.
- [144] K. Kim, S. Q. Choi, Z. a Zell, T. M. Squires, and J. a Zasadzinski, “Effect of cholesterol nanodomains on monolayer morphology and dynamics.,” *Proc. Natl. Acad. Sci. U. S. A.*, vol. 110, no. 33, pp. E3054-60, 2013.
- [145] J. Arko, “Nursing Procedures and Skills,” <https://nursinginhana.com/tag/lateral-position/>, 2018. .
- [146] M. F. Krause, E. R. Hendrik, D. Gommers, and B. Lachmann, “A new simple method of staining exogenous surfactant in experimental research,” *Eur Respir J.*, vol. 15, no. 5, pp. 949–954, 2000.
- [147] A. Kornecki and R. N. Singh, *Acute Respiratory Distress Syndrome*, Ninth Edit. Elsevier Inc., 2018.
- [148] G. D. Rubenfeld *et al.*, “Incidence and Outcomes of Acute Lung Injury,” *N Engl J Med.*, vol. 353, pp. 1685–93, 2005.
- [149] J. J. Zimmerman, S. R. Akhtar, E. Caldwell, and G. D. Rubenfeld, “Incidence and Outcomes of Pediatric Acute Lung Injury,” *Pediatrics*, vol. 124, no. 1, pp. 87–95, 2009.
- [150] S. Erickson *et al.*, “Acute lung injury in pediatric intensive care in Australia and New Zealand - A prospective, multicenter, observational study,” *Pediatr. Crit. Care Med.*, vol. 8, no. 4, pp. 317–323, 2007.
- [151] A. G. Randolph *et al.*, “The feasibility of conducting clinical trials in infants and children with acute respiratory failure,” *Am. J. Respir. Crit. Care Med.*, vol. 167, no. 10, pp. 1334–1340, 2003.
- [152] Y. López-Fernández *et al.*, “Pediatric acute lung injury epidemiology and natural history study: Incidence and outcome of the acute respiratory distress syndrome in children,” *Crit. Care Med.*, vol. 40, no. 12, pp. 3238–3245, 2012.

- [153] W.-L. Yu *et al.*, “The epidemiology of acute respiratory distress syndrome in pediatric intensive care units in China,” *Intensive Care Med.*, vol. 35, no. 1, pp. 136–143, 2009.
- [154] J. B. Grotberg, M. Filoche, D. F. Willson, K. Raghavendran, and R. H. Notter, “Did Reduced Alveolar Delivery of Surfactant Contribute to Negative Results in Adults with Acute Respiratory Distress Syndrome?,” *Am. J. Respir. Crit. Care Med.*, vol. 195, no. 4, pp. 538–540, 2017.
- [155] N. T. Gnscom and M. E. Wohl, “Dimensions of the growing trachea related to age and gender,” *Am. J. Roentgenol.*, vol. 146, no. 2, pp. 233–237, 1986.
- [156] “2-20 years: Boys Stature-for-age and Weight-for-age percentiles,” *www.cdc.gov*, 2000. [Online]. Available: <https://www.cdc.gov/growthcharts/data/set1clinical/cj411021.pdf>.
- [157] T. F. de Vasconcelos, B. Sapoval, J. S. Andrade, J. B. Grotberg, Y. Hu, and M. Filoche, “Particle capture into the lung made simple?,” *J. Appl. Physiol.*, vol. 110, no. 6, pp. 1664–1673, 2011.
- [158] D. Halpern and D. Gaver, “Boundary Element Analysis of the Time-Dependent Motion of a Semi-infinite Bubble in a Channel,” *J Comput Phys.*, vol. 115, pp. 366–375, 1994.
- [159] H. Fujioka and J. B. Grotberg, “The steady propagation of a surfactant-laden liquid plug in a two-dimensional channel,” *Phys Fluids.*, vol. 17, no. 8, p. 082102, 2005.
- [160] S. L. Waters and J. B. Grotberg, “The propagation of a surfactant laden liquid plug in a capillary tube,” *Phys. Fluids*, vol. 14, no. 2, pp. 471–480, 2002.
- [161] H. Fujioka, S. Takayama, and J. B. Grotberg, “Unsteady propagation of a liquid plug in a liquid-lined straight tube,” *Phys. Fluids*, vol. 20, no. 6, pp. 1–14, 2008.
- [162] J. M. Ryans, H. Fujioka, D. Halpern, and D. P. Gaver, “Reduced-dimension modeling approach for simulating recruitment/de-recruitment dynamics in the lung,” *Ann Biomed Eng.*, vol. 44, no. 12, pp. 3619–31, 2016.
- [163] J. Ryans, H. Fujioka, and D. P. Faver, “Micro-scale to Meso-scale Analysis of Parenchymal Tethering: The Effect of Heterogeneous Alveolar Pressures on the Pulmonary Mechanics of Compliant Airways,” *J Appl Physiol*, vol. 126, no. 5, pp. 1204–13, 2019.
- [164] F. Xu and O. E. Jensen, “Trapping and displacement of liquid collars and plugs

in rough-walled tubes,” *Phys. Rev. Fluids*, vol. 2, no. 9, pp. 1–22, 2017.

List of figures

Figure 1: Example of main respiratory structures [1]	3
Figure 2: Schematic representation of the pulmonary airway system of the human (Weibel [3]).	4
Figure 3: Schematic representation of the respiratory zone, where gas exchange occurs [1].	5
Figure 4: Pig airways extracted from CT images [15]. There is an early airway branching that feeds the top right lung lobe.	7
Figure 5: Three-dimensional representation description of surfactant proteins [92]	16
Figure 6: Surface tension (in mN/m) with air for different percentages of surfactant varying from 1% to 100% diluted by classical aqueous cell feeding culture medium (DMEM) [100].....	18
Figure 7: Viscosity of Infasurf [®] and Survanta [®] versus phospholipid concentration. A) Infasurf [®] determined at 23°C. B) Infasurf [®] at 37°C. C) Survanta [®] determined at 23°C. D) Survanta [®] at 37°C. [106]	20
Figure 8: Values of Curosurf [®] static viscosity as a function of the concentration obtained from Magnetic Rotational Spectroscopy [107].....	21
Figure 9: Geometric description of the airway tree: the airways are described by their diameter (D) and length (L). A bifurcation is characterized by its branching angles (θ_2 and θ_3), and the relation between successive bifurcations by the rotation angles between successive bifurcation planes (ψ).....	30
Figure 10: Schematic representation of the geometry in the conductive and transitory zones of the pulmonary airway system [3].	30
Figure 11: Statistics of the rat lung model built from [6]. A) The number of branches vs. generation. B) Average diameter vs. generation. C) Average length vs. generation.	31
Figure 12: Statistics of the rat lung model built from [6]. A) Histogram of branching angles. B) Histogram of angle to the normal direction of gravity [6].	32
Figure 13: Comparison between measurements of Oakes et al. performed on Wistar rat [11], measurements of Raabe et al. performed on Long-Evans rat [6], and measurements of Lee et al. performed on Sprague-Dawley rat [10] from [11].....	34
Figure 14: Example of a Long-Evans rat respiratory airway tree (31 generations). The color coding corresponds to the value of the diameter. A) Front view, B) Side view, C) Top view, and D) Bottom view.	35

Figure 15: Long-Evans rat pulmonary airway tree. The tree is color-coded according to the generation number.	35
Figure 16: Development of the bronchial tree of the respiratory system of the rat lung at days 4, 10, 21, 36, and 60 [121]. The gray color represents the walls of the conducting airways. The colored spheres represent the entrances of the acini.	37
Figure 17: Bronchial trees of the respiratory airway system of rats. A) Sera et al. [117], B) Einstein et al. [16] C) Counter et al. [14] D) Carson et al. [119] E) Oakes et al. [11] F) Jacob et al. [120].	37
Figure 18: Schematic of an A) in-plane and B) out-of-plane bifurcation.	39
Figure 19: Statistics of the geometry of the pig lung model based on Azad <i>et al.</i> data [15]. A) The number of branches vs. generation. B) Average diameters vs. generation. C) Average length vs. generation.	42
Figure 20: Example of a pig pulmonary airway tree (22 generations) based on Azad <i>et al.</i> [15]. The color-coding represents the diameter value. A) Front view, B) Side view, C) Top view, and D) Bottom view.	43
Figure 21: Example of a pig pulmonary airway tree (22 generations) based on Azad <i>et al.</i> [15]. The color-coding represents the generation number.	43
Figure 22: A) Schematic and nomenclature of the pig bronchial tree (Monteiro <i>et al.</i> [123]). B) Photograph (dorsal aspect) of a 105 kg pig (trachea (a), carina (b), left lung (c), right lung (d), and cranial lobe bronchus (e)) (Judge <i>et al.</i> [26])	44
Figure 23: Pig conducting airways. A) Maina <i>et al.</i> [24] B) Monteiro <i>et al.</i> [123] C) Asgharian <i>et al.</i> [124] D) Azad <i>et al.</i> [15].	45
Figure 24: Symmetric model of the human pulmonary airway tree, four generations plus trachea.	46
Figure 25: Statistics of the human lung model based on the Weibel symmetric model. A) The number of branches vs. generation. B) Average diameter vs. generation. C) Average length vs. generation.	47
Figure 26: Symmetric human pulmonary airway tree based on Weibel's symmetric model [9]. The color coding represents the diameter value.	47
Figure 27: Symmetric human pulmonary airway tree with 15 generations. The color coding represents the diameter value.	48
Figure 28: Asymmetric model of the human pulmonary airway tree. The color coding represents the diameter value.	49
Figure 29: Asymmetric model of the human pulmonary airway tree with a maximum of 15 generations. The color-coding represents the Generation number.	49

Figure 30: A) Raabe's lung airways tree, first three generations plus trachea. B) The asymmetric model of tracheobronchial bifurcation [6].	50
Figure 31: Statistics of Raabe's human lung model [6]. A) The number of branches vs. generation. B) Average diameter vs. generation. C) Average length vs. generation. D) The number of terminals vs. generation.	51
Figure 32: Raabe-based lung airway tree. The color coding corresponds to the value of the diameter.	52
Figure 33: Raabe-based lung airway tree. The color-coding tree representing the generation number.	52
Figure 34: Human airways image and cast. A) Phalen <i>et al.</i> [125] B) Monteiro <i>at al.</i> [123] C) Schmidt <i>et al.</i> [132] D) Tawhai <i>et al.</i> [133].	53
Figure 35: Splitting of a liquid plug across one single bifurcation: the spatial orientation of the bifurcation is characterized by two angles: the rolling angle (φ), and the pitch angle (γ). The roll angle and pitch angle describe the orientation of the bifurcation plates with respect to gravity. A plug of volume V_0 entering the parent branch leaves behind a trailing film of thickness h . The volumes entering the daughter branches are V_2 and V_3 such that $V_2 + V_3 < V_0$.	59
Figure 36: Schematic of the pressure difference between the upstream pressure P_1 in the parent branch and the downstream pressures P_2 and P_3 . Taken from [82].	60
Figure 37: Sketch of the multiple aliquot deliveries. A and B: a liquid plug propagating in an airway with dry walls leaves a trailing film and may end up being entirely deposited on the airway wall. C and D: the same plug propagating into an airway whose walls are already coated with surfactant proceeds without losing its mass, and starts leaving a trailing film only when it reaches the dry portions of the walls.	67
Figure 38: Patient positions. Taken from [145].	70
Figure 39: Schematic of the experimental setup. The roll angle (ϕ) and pitch angle (γ) describe the orientation of the bifurcation plates with respect to the gravity. The branching angle of the daughter tube with respect to the parent tube is indicated by θ . Taken from [82].	71
Figure 40: Comparison of R_ξ vs. Ca_p for $\gamma=0^\circ$ and $\phi=15^\circ$ (experiments: black diamonds, model: black line), $\phi=30^\circ$ (experiments: orange squares, model: orange line), and $\phi=60^\circ$ (experiments: blue triangles, diamond, model: blue line). Experimental data are extracted from [82].	72
Figure 41: Comparison of R_ξ vs. Ca_p for $\phi=30^\circ$ and $\gamma=-15^\circ$ (experiments: black diamonds, model: black line), $\gamma=0^\circ$ (experiments: orange squares, model: orange	

- line), and $\gamma=15^\circ$ (experiments: blue triangles, model: blue line). Experimental data are extracted from [82]..... 73
- Figure 42: Comparison of R_s vs. Ca_p for different values of the Bond number Bo (angles are $\phi=60^\circ$ and $\gamma=0^\circ$): $Bo=1.26$ (experiments: black diamonds, model: black line), and $Bo=0.76$ (experiments: blue triangles, model: blue line). Experimental data are extracted from [82]..... 74
- Figure 43: R_s vs. Re_p for $\gamma=0^\circ$ and $\phi=30^\circ$ (experiments: orange squares, model: orange line) and $\phi=60^\circ$ (experiments: blue triangles, model: blue line). Data are extracted from [136] 76
- Figure 44: Delivery of three surfactant dose volumes into a rat lung (L+R posture). Surfactant (Infasurf®) was tagged with Green Tissue Marking Dye. A) Dose volume per kg = 1.125 mL.kg⁻¹, B) Dose volume per kg = 2.5 mL.kg⁻¹, and C) Dose volume per kg = 5.8 mL.kg⁻¹..... 79
- Figure 45: Simulated distributions of surfactant in the rat. A) 3D Front view representing the distribution of volumes reaching the terminal branches for $V_D=1.125$ mL.kg⁻¹. The efficiency index is $\eta=5.9\%$. B) The same figure, for $V_D=2.5$ mL.kg⁻¹ with $\eta=45.6\%$ and C) the same figure, for $V_D=5.8$ mL.kg⁻¹ with $\eta=76\%$. D) 3D front view displaying the amount of surfactant left coating the airways, in simulation (A). The color-coding represents the left coating volume of each airway. The homogeneity index is $HI=0.2$. E) The same figure as (D), corresponding to simulation (B) with $HI=0.29$, and F) the same figure as (D), corresponding to simulation (C) with $HI=0.28$ 80
- Figure 46: Images of sample experiments (A-D) [102] and our surfactant delivery simulation (E-H) at the end-inspiration. 1st (A, E), 3rd (B, F), 6th (C, G), and 10th (D, H) aliquot..... 83
- Figure 47: A) Liquid dose volume distribution during the 10th breath [102]. (B) Front view of the simulated end distribution of surfactant in a 3D model of rat lung. The color-coding represents the volume coating each airway divided by the initial instilled dose volume. C) The delivered surfactant to the terminal airways. The color of each bubble corresponds to the percentage of the initial dose volume, reaching each terminal airway..... 84
- Figure 48: Comparison between measured Quadrant Homogeneity Index (QHI) (1) and simulated Quadrant Homogeneity Index (SQHI). A) Image computed from the numerical simulation to mimic the images of Figure 46. A sphere is plotted around each terminal branch. Its grayscale goes from white (no surfactant) to black (fully

coated). When two spheres superimpose, their grey levels are added. B) The image obtained in the frame (A) is thresholded to obtain a black and white image (threshold is 90% grey), on which the SQHI can be computed as in [102]. C) Comparison of measured QHI and simulated QHI (SQHI) on 10 consecutive breaths. Equation Chapter (Next) Section 1..... 84

Figure 49: Simulation of surfactant delivery in a symmetric model of the rat airway tree. The simulation is performed on a 0.330-kg rat in the supine position. Surfactant viscosity is $\mu=30$ cP, dose volume per kg is 1 mL.kg⁻¹, and flow rate per kg is 30 mL.kg⁻¹.s⁻¹. A) Front view of the symmetric model of the rat conducting airways. The color-coding represents the diameter value. B) 3D representation of the delivery (gravity is signaled by the red arrow). The color of each bubble corresponds to the volume of the surfactant reaching each terminal branch. The computed efficiency index is $\eta = 26.8\%$ and the homogeneity index of this distribution is $HI = 7.45$ 90

Figure 50: Simulation of surfactant delivery in a realistic model of the rat airway tree. The delivery is performed on a 0.330-kg rat in the supine position. Surfactant viscosity is $\mu = 30$ cP, dose volume per kg is 1 mL.kg⁻¹, and flow rate per kg is 30 mL.kg⁻¹.s⁻¹. The airway tree model has 31 generations and 1457 terminal branches. (A) 3D representation of the delivery. Each bubble represents a terminal branch, and the color of each bubble corresponds to the volume of the surfactant reaching the corresponding terminal branch. The computed efficiency index is $\eta = 4.9\%$. (B) Coating in the tree. The color-coding represents the volume coating each airway. (C) Normalized delivery $V_N(i)$ plotted vs. the terminal branch number. (D) Histogram of normalized delivery. The homogeneity index of this distribution is $HI = 0.32$, which corresponds to a highly inhomogeneous distribution..... 92

Figure 51: Simulated distributions of surfactant delivery in a 0.330-kg rat in the supine position. A) 3D Front view representing the distribution of volumes reaching the acini, for a dose volume of 2 mL.kg⁻¹. The efficiency index is $\eta = 41\%$. B) Same figure, for a dose volume of 5 mL.kg⁻¹. The efficiency index is $\eta = 76\%$. C) 3D front view displaying the amount of surfactant left coating the airways, in simulation (A). The color-coding represents the volume left coating each airway divided by the initial instilled dose volume. The homogeneity index is $HI=0.47$, D) Same figure as (C), corresponding to simulation (B). The homogeneity index is $HI=0.54$ 94

Figure 52: Efficiency index η (solid line, filled symbols) and homogeneity index HI (dashed line, open symbols) vs. dose volume per kg for tracheal flow rates of 10, 20, 30, 40, and 50 mL.kg⁻¹.s⁻¹ in the rat lung. 95

- Figure 53: Total coating cost vs. flow rate for a 0.330-kg rat lung in the supine position. A) The absolute amount of coating volume in the entire tree, B) coating volume divided by the initial instilled dose volume. 96
- Figure 54: Efficiency index η (open symbols) and homogeneity index HI (filled symbols) as a function of dose volume, computed in a 0.330-kg rat lung, for three different flow rates, (viscosity $\mu = 30$ cP). A) Single instillation in the LLD position. B) Single instillation in the RLD position. C) Single instillation in the supine position. D) Single instillation in the prone position. E) Double instillation in supine and prone positions (S+P). F) Three instillations, one-half way between LLD and supine, one-half way between RL and supine, and one in prone posture (SL+SR+P). 98
- Figure 55: Efficiency index η (open symbols with solid line) and homogeneity index HI (filled symbols with the dashed line) as functions of the dose volume for Survanta with two viscosity, 9 cP (concentration: 25 mg of PL/ml, 770 s^{-1} shear rate and 37 °C) and 52 cP (concentration: 35 mg of PL/ml, 70 s^{-1} shear rate and 37 °C). 100
- Figure 56: Efficiency index η (solid line) and homogeneity index HI (dashed line) as functions of the dose volume for 3 different values of the surface tension. 101
- Figure 57: Efficiency index η (filled symbols) and homogeneity index HI (open symbols) computed when changing the number of aliquots for a given initial dose volume, in a 0.330-kg rat lung, (total dose volume: 2 mL.kg⁻¹, flow rate: 30 mL.kg⁻¹.s⁻¹, LLD, viscosity $\mu = 30$ cP). 103
- Figure 58: Normalized deliver vs. terminal branches. A) 4 mL.kg⁻¹ dose volume per kg, 10 mL.kg⁻¹.s⁻¹ flow rate, and 10 cP viscosity in LLD position. B) 1 mL.kg⁻¹ dose volume per kg, 40 mL.kg⁻¹.s⁻¹ flow rate, and 40 cP viscosity in LLD position. 105
- Figure 59: Simulation of surfactant delivery in the pig airway system. (A) 3D Front view representing the distribution of volumes reaching the acini, for a dose volume per kg of 1 mL.kg⁻¹. The computed efficiency index is $\eta = 60\%$. B) Same figure, for a dose volume per kg of 4 mL.kg⁻¹. The calculated efficiency index is $\eta = 90\%$. Each sphere represents a terminal branch, and the color of the sphere gives the volume of surfactant reaching the corresponding terminal branch. (C) 3D front view displaying the amount of surfactant left coating the airways, in simulation (A). The color-coding represents the volume left coating each airway divided by the initial instilled dose volume. D) Same figure as (C), corresponding to simulation (B). (E) Normalized delivery $V_N(i)$ plotted vs. the terminal branch number of simulation (A). (F) Same figure as (F) plotted for simulation (B). 109

- Figure 60: Efficiency index (solid line, filled symbols) and homogeneity index (dashed line, open symbols) vs. the dose volume per kg for tracheal flow rates of 1, 2, 3, and 4 $\text{mL.kg}^{-1}.\text{s}^{-1}$ in the pig lung. All deliveries are performed in the supine position. 110
- Figure 61: Efficiency index (solid line) and homogeneity index (dashed line) vs. the dose volume, computed in a 40-kg pig lung for three different flow rates, (viscosity $\mu = 30$ cP). A) Single instillation in the supine position. B) Single instillation in the LLD position. C) Double instillation in supine and prone positions (S+P). D) Double instillation in LLD and RLD positions (L+R). E) Three instillations, one-half way between LLD and supine, one-half way between RL and supine, and one in prone posture (SL+SR+P). 112
- Figure 62: Simulated delivery in a 40-kg pig (viscosity $\mu = 30$ cP). The airway tree is asymmetric with 21 generations and 1712 acini. The two front views display the fraction of the initial dose volume delivered to each acinus. A) Half-supine and half-prone position (S+P). The computed efficiency index is $\eta = 15\%$ and the homogeneity index is $HI = 0.13$. 876 out of 1712 acini do not receive any surfactant B) Half-LLD and half-RLD positions (L+R). The efficiency index is $\eta = 26\%$ and the homogeneity index is $HI = 0.19$. 241 out of 1712 acini do not receive any surfactant. 113
- Figure 63: Efficiency index (solid line, filled symbols) and homogeneity index (dashed line, open symbols) vs. dose volume for Survanta with two values of the viscosity, 9 cP (Concentration: 25 mg of PL/ml, 770 s^{-1} shear rate and $37 \text{ }^\circ\text{C}$) and 52 cP (Concentration: 35 mg of PL/ml, 70 s^{-1} shear rate and $37 \text{ }^\circ\text{C}$). 114
- Figure 64: Efficiency index (solid line, filled symbols) and homogeneity index (dashed line, open symbols) vs. dose volume for 3 different values of the surface tension. 115
- Figure 65: Efficiency index (filled symbols) and homogeneity index (open symbols) computed in a multiple aliquot delivery with the same initial dose volume, in a 40-kg pig lung, (flow rate: $30 \text{ mL.kg}^{-1}.\text{s}^{-1}$, posture LLD, viscosity $\mu = 30$ cP). A) Total dose volume = 1 mL.kg^{-1} , B) total dose volume = 4 mL.kg^{-1} 116
- Figure 66: A) Front view of the 1-kg neonatal respiratory lower tract. B) Front view of the 70-kg adult respiratory lower tract. C) Normalized delivery of terminals of neonate's lung. D) Normalized delivery of terminals of the Adult lung. E) Histogram of normalized delivery of neonate's lung. F) Histogram of normalized delivery of adult lung. 120
- Figure 67: Efficiency index η (line, filled symbols) and homogeneity index HI (dashed line, open symbols) vs. tracheal flow rate for total dose volumes per kg of 1, 2, 3, and 4 mL.kg^{-1} in the 1-kg neonate lung. For each given dose volume, one-half is delivered in RLD and the other in LLD. 122

Figure 68: Total coating cost vs. flow rate for a 1-kg neonate lung in the L+R position. A) The absolute amount of coating volume in the entire tree, B) coating volume divided by the initial instilled dose volume.	123
Figure 69: Trailing film ratio thickness to the radius at low (blue) and high (red) flow rate in 1 mL.kg ⁻¹ dose volume per kg.....	124
Figure 70: Splitting factor at low (blue) and high (red) flow rate in 1 mL.kg ⁻¹ dose volume per kg.....	124
Figure 71: Efficiency index (solid line, filled symbols) and homogeneity index (dashed line, open symbols) vs. the tracheal flow rate for total dose volumes per kg of 1, 2, 3, and 4 mL.kg ⁻¹ in the 70-kg adult lung. For each value of the dose volume, one-half is delivered in RLD and the other in LLD.	125
Figure 72: Total coating cost vs. flow rate for a 70-kg adult lung in the L+R position. A) The absolute amount of coating volume in the entire tree, B) coating volume divided by the initial instilled dose volume.	126
Figure 73: Efficiency index η (solid line, filled symbols) and homogeneity index HI (dashed line, open symbols) as a function of the flow rate, computed in a human adult lung. A) Single instillation in the LLD position. B) Single instillation in the supine position. C) Double instillation in LLD and RLD positions (L+R). D) Double instillation in supine and prone positions (S+P).	127
Figure 74: Efficiency index η (solid line, filled symbols) and homogeneity index HI (dashed line, open symbols) vs. the dose volume for Survanta® with two different values of the viscosity, 9 cP (concentration: 25 mg of PL/ml, 770 s ⁻¹ shear rate and 37°C) and 52 cP (concentration: 35 mg of PL/ml, 70 s ⁻¹ shear rate and 37°C).....	129
Figure 75: Efficiency index η (solid line, filled symbols) and homogeneity index HI (dashed line, open symbols) vs. the dose volume for 3 different values of the surface tension.	130
Figure 76: Efficiency index (solid line, filled symbols) and homogeneity index (dashed line, open symbols) vs. age for 4 different values of the dose volume, at for a 6 mL.kg ⁻¹ .s ⁻¹ flow rate per kg.....	133
Figure 77: Efficiency (solid line, filled symbols) and homogeneity (dashed line, open symbols) vs. age at 4 dose volumes in 1 mL.kg ⁻¹ .s ⁻¹ flow rate per kg.	134
Figure 78: Simulation of surfactant delivery in a symmetric and asymmetric models of the human airway tree. A) Front view of the symmetric model of the human conducting airways. B) Front view of the asymmetric model of the human conducting airways. The color-coding represents the diameter value. C) 3D front view displaying the amount of surfactant left coating the airways, in simulation (A). The color-coding	

represents the volume left coating each airway divided by the initial instilled dose volume. D) Same figure as (C), corresponding to simulation (B). E) 3D Front view representing the distribution of volumes reaching the acini. F) Same figure, for the asymmetric tree..... 136

Figure 79: Efficiency index (solid line, filled symbols) and homogeneity index (dashed line, open symbols) vs. tracheal flow rate for total dose volumes per kg of 1, 2, 3, and 4 mL.kg⁻¹. A) Weibel-based symmetric respiratory airways tree. B) Weibel-based asymmetric respiratory airways tree. 137

Figure 80: Efficiency index η (solid line, filled symbols) and homogeneity index HI (line, open symbols) vs. dose volume, computed in a 70-kg human lung, at a 4 mL.kg⁻¹.s⁻¹ the flow rate in two single (LLD and supine) and two double (L+R and S+P) instillation. 139

Figure 81: Efficiency index η (solid line, filled symbols) and homogeneity index HI (dashed line, open symbols) vs. dose volume for Survanta® for two different values of the viscosity, 9 cP (Concentration: 25 mg of PL/ml, 770 s⁻¹ shear rate and 37 °C) and 52 cP (Concentration: 35 mg of PL/ml, 70 s⁻¹ shear rate and 37 °C)..... 140

Figure 82: Efficiency index η (solid line, filled symbols) and homogeneity index HI (dashed line, open symbols) vs. dose volume for 3 different values of the surface tension..... 141

Figure 83: Efficiency index η (filled symbols) and homogeneity index HI (open symbols) vs. the number of aliquots in a multiple-aliquot delivery..... 142

Figure 84: Efficiency index η (solid line, filled symbols) and homogeneity index HI (dashed line, open symbols) as functions of the tracheal flow rate for total dose volumes per kg of 1, 2, 3, and 4 mL.kg⁻¹. A) Weibel-based asymmetric model. B) Raabe-based asymmetric model. 144

List of tables

Table 1: Pediatric acute respiratory distress syndrome definition. OI = oxygenation index, OSI = oxygen saturation index [34].	10
Table 2: Overview of case histories and clinical trials demonstrating the benefits of SRT in children/infants/babies with ARDS [60]	12
Table 3: Surfactant properties [114]	23
Table 4: Compared lung geometry between Wistar, Long-Evans, and Sprague-Dawley rats modify from [11].	33
Table 5: Recent research on the morphology of rat conducting airways	36
Table 6: Airway lengths (cm) and diameter ratios (Md. Azad [15]).	40
Table 7: Branching angles and bifurcation plane angles. By default, all data are taken from Md. Azad [15], pig #3, figure 2 C, D and figure 4 A, B. When data were not available for pig #3, other pig data were used. Red color refers to the lack of data for pig #3 and the green bracket refers to the pig number.	41
Table 8: Branching angles for daughter one (θ_1) for main stem bronchi.	41
Table 9: Recent research on the morphology of pig conducting airways	44
Table 10: Research on the morphology of human conducting airways	53
Table 11: Surfactant properties [105][144]	69
Table 12: Mechanical properties of liquids and experimental conditions.	71
Table 13: Mechanical properties of the liquid and experimental conditions.	75
Table 14: Properties and condition of instilled surfactant in simulations and experiments [102].	81
Table 15: Simulated efficiency and homogeneity indices compared with the homogeneity index measured in Cassidy <i>et al.</i> [102].	82
Table 16: Properties and condition of instilled surfactant in simulations	90
Table 17: Computed efficiency and homogeneity indices of instilled surfactant.	93
Table 18: Properties and condition of instilled surfactant	93
Table 19: Computed efficiency and homogeneity indices of instilled surfactant.	94
Table 20: Properties and condition of instilled surfactant	97
Table 21: Properties and condition of instilled surfactant	100
Table 22: Properties and condition of instilled surfactant	101
Table 23: Properties and condition of instilled surfactant	103
Table 24: The efficiency and homogeneity in different applied conditions	104
Table 25: Properties and condition of instilled surfactant	105

<i>Table 26: Properties and conditions of instilled surfactant</i>	108
<i>Table 27: Properties and conditions of instilled surfactant</i>	111
<i>Table 28: Properties and condition of instilled surfactant.....</i>	114
<i>Table 29: The efficiency and homogeneity in different applied conditions</i>	118
<i>Table 30: Properties and conditions of instilled surfactant</i>	119
<i>Table 31: Properties and conditions of instilled surfactant</i>	121
<i>Table 32: Properties and condition of instilled surfactant.....</i>	128
<i>Table 33: Properties and condition of instilled surfactant.....</i>	130
<i>Table 34: The efficiency and homogeneity in different applied conditions</i>	130
<i>Table 35: Properties and conditions of instilled surfactant</i>	132
<i>Table 36: Age-dependent lung size and body weight.....</i>	132
<i>Table 37: Properties and conditions of instilled surfactant</i>	135
<i>Table 38: Model size and body weight.....</i>	135
<i>Table 39: Properties and condition of instilled surfactant.....</i>	138

Titre : Propagation de bouchons liquides dans les poumons humains

Mots clés : Poumon, Arbre trachéo-bronchique, administration de surfactant, dynamique des fluides

Résumé : La Thérapie par Substitution de Surfactant (TSS), qui opère par instillation d'une solution de surfactant directement dans l'arbre bronchique, est un traitement remarquablement efficace chez les prématurés souffrant de syndrome de détresse respiratoire. À l'inverse, son utilisation s'est avérée inexplicablement décevante chez les adultes atteints du syndrome de détresse respiratoire aigu. Dans cette thèse, nous présentons un modèle numérique de la TSS chez l'animal et chez l'homme.

En simulant la TSS dans des modèles 3D réalistes de poumons, nous démontrons la sensibilité de son efficacité vis-à-vis de l'architecture géométrique, de la taille du sujet et des conditions d'administration, et mettons en évidence en particulier les différences profondes entre les modèles animaux et l'homme. Ces travaux permettent aujourd'hui d'envisager une réouverture de cette voie thérapeutique chez l'adulte, guidée par un véritable outil de prédiction de l'administration individualisée chez le patient.

Title: Propagation of liquid plugs into the human lung

Keywords: Lung, Tracheobronchial tree, Fluid dynamics, Surfactant delivery, SRT

Abstract: Surfactant Replacement Therapy (SRT), which operates by instillation of a surfactant solution directly into the bronchial tree, is a remarkably effective treatment for premature infants with respiratory distress syndrome. Disappointingly, its use in adults for treating acute respiratory distress syndrome (ARDS) experienced initial success followed by failures. In this thesis, we present a numerical model of SRT in animals and humans.

By simulating SRT in realistic 3D lung models, we demonstrate the sensitivity of its effectiveness to geometric architecture, subject size and administration conditions, and highlight in particular the profound differences between animal and human models. These studies now make it possible to consider reopening this therapeutic route in adults, guided by a real tool for predicting individualized administration in patients.